Distribution Agreement

In presenting this thesis or dissertation as a partial fulfillment of the requirements for an advanced degree from Emory University, I hereby grant to Emory University and its agents the non-exclusive license to archive, make accessible, and display my thesis or dissertation in whole or in part in all forms of media, now or hereafter known, including display on the world wide web. I understand that I may select some access restrictions as part of the online submission of this thesis or dissertation. I retain all ownership rights to the copyright of the thesis or dissertation. I also retain the right to use in future works (such as articles or books) all or part of this thesis or dissertation.

Signature:

_____ _____

Yang Liu Date

Development of Nanoparticle-based Tools to Investigate Cell Mechanotransduction at the Living/Nonliving Interface

By

Yang Liu

Doctor of Philosophy

Chemistry

_____

Khalid Salaita
Advisor

_____

Tianquan Lian
Committee Member

_____

Vince Conticello
Committee Member

Accepted:

_____

Lisa A. Tedesco, Ph.D.
Dean of the James T. Laney School of Graduate Studies

_____

Date

Development of Nanoparticle-based Tools to Investigate Cell Mechanotransduction at the Living/Nonliving Interface

By

Yang Liu

B.S. Hunan University, 2010

Advisor: Khalid Salaita, Ph.D.

An abstract of

A dissertation submitted to the Faculty of the

James T. Laney School of Graduate Studies of Emory University

in partial fulfillment of the requirements for the degree of

Doctor of Philosophy

in Chemistry

2016

Abstract

Development of Nanoparticle-based Tools to Investigate Cell Mechanotransduction at the Living/Nonliving Interface

By

Yang Liu

Mechanical forces play an essential role in regulating cell functions and cell fate, ranging from proliferation, differentiation to migration and apoptosis. Despite great significance, the lacking of molecular tools to interrogate these forces has hindered the biological community to fully understand the underlying mechanisms of mechanotransduction. In this dissertation, multiple gold nanoparticle (AuNP) tension probes and actuators are introduced for the study of mechanotransduction at the surface of living cells.

Chapter 1 briefly reviews the role of mechanical forces in cell biology and several common techniques that have recently emerged for measuring cell forces. This chapter also emphasizes the design and biological applications of synthetic tension probes for molecular tension fluorescence microscopy (MTFM).

Chapter 2 describes the systematic development of a gold nanoparticle tension probe for visualizing forces exerted by integrin receptors. For the first time, integrin forces were quantified with molecular tension probes during initial cell spreading and focal adhesion maturation.

Chapter 3 reports the technological advancement of a nanopatterned tension probe arrays and its application in understanding how nanoscale clustering of RGD ligands alters the mechano-regulation of their integrin receptors. We found that the mechanism of sensing ligand spacing is force-mediated.

Chapter 4 details the recent development of DNA-based nanoparticle tension probes for studying the mechanism of how chemo-mechanical coupling influences immune function. With unprecedented sensitivity, we provided the first pN tension maps of individual TCR-pMHC complexes during T cell activation. Importantly, naïve CD8 T cells recruit TCRs, co-receptor CD8, and adhesion molecules such as LFA-1 to achieve a force of 12-19 pN, which is indispensable for enhanced antigen fidelity.

Chapter 5 introduces the development of a novel optomechanical acatutor that can specifically deliver pN forces to cell surface receptors. We showed that a variety of cell behaviors, such as cell adhesion, migration and T-cell activation, are mechanosensitive and can be remotely controlled by our optomechanical switch.

Chapter 6 summaries of the thesis and provides a future outlook on developing the next generation of molecular tension probes and actuators. We believe that these optical methods and tools will likely transform the study of mechanotransduction in biology.

Development of Nanoparticle-based Tools to Investigate Cell Mechanotransduction at the Living/Nonliving Interface

By

Yang Liu

B.S. Hunan University, 2010

Advisor: Khalid Salaita, Ph.D.

A dissertation submitted to the Faculty of the

James T. Laney School of Graduate Studies of Emory University

in partial fulfillment of the requirements for the degree of

Doctor of Philosophy

in Chemistry

2016

Acknowledgement

First and foremost, I would like to thank my advisor, Dr. Khalid Salaita, for bringing me to this wonderful and vigorous lab. He is one of the most enthusiastic scientists that I have ever met and the one who triggered my enormous passion for interdisciplinary science. I feel extremely fortunate to have Khalid's mentorship and motivation at this stage of my career. I would also like to thank my committee members, Dr. Vince Conticello and Dr. Tianquan Lian who offered their valuable advice and support for my academic advancement every year.

I would like to thank the current and former members of the Salaita lab for their contribution in the past six years. I have grown so much both in life and in my research by interacting with and learning from them. I thank Dr. Yoshie Nurai and Dr. Kevin Yehl for giving me their priceless guidance in the beginning of my graduate study; senior postdoc members, Dr. Weiwei Zheng and Dr. Zheng Liu for their sincere help and continuous encouragement. I would miss our scientific journal club and gym members including Dr. Zheng Liu, Victor Ma and Hanquan Su, with whom I had countless happiness both in the lab and after work.

I would like to thank my awesome collaborators outside the lab. Dr. Ada Cavalcanti-Adam and Dr. Brian Evavold are absolutely motivating and helpful for my research projects and future career development. Dr. Lori Blanchfield is the sweetest collaborator that I have worked with, who always prioritizes my experimental needs in her daily schedule and even during Christmas!

Finally, special thanks go to my entire family, especially my mom with her unconditional love and my dad for being a role model in my scientific career. Most

importantly, I have to thank my beloved girlfriend, Kornelia, who gives me companion in countless days and nights in the lab, and always gives me confidence in pursuing a higher level in my life.

List of Abbreviations

Abbreviation	Full Name
AFM	atomic force microcopy
AuNP	gold nanoparticle
BFP	biomembrane force probes
cRGDfK	cyclic Arg-Gly-Asp-D-Phe-Lys
ECM	extracellular matrix
EGF	epidermal growth factor
EGFR	epidermal growth factor receptor
FA	focal adhesion
FRET	förster resonance energy transfer
ICAM-1	intercellular adhesion molecule-1
MLCK	myosin light chain kinase
mPADs	micropost array detector
MTFM	molecular tension-based fluorescence microscopy
NSET	nanometal surface energy transfer
OMA	Optomechanical Actuator
PEG	polyethylene glycol
pN	piconewton
QE	quenching efficiency
RICM	reflection interference contrast microscopy
ROCK	Rho-associated protein kinase

Abbreviation	Full Name
SMFS	single molecule force spectroscopy
TFM	traction force microscopy
TIRF	total internal reflection fluorescence
WLC	worm-like chain

Table of Contents

Table of Figures

List of Tables

Chapter 1: Development of molecular tools to study mechanotransduction at the cell surface

Adapted from Liu, Y.; Ma. V.P.; Galior, K.; Chang, Y.; Zhang, Y.; Salaita, K. Synthetic Probes for Molecular Force Imaging in Living Systems. *Accounts of Chemical Research*, to be submitted

1.1 Introduction

1.1.1 Examples of cell mechanotransduction

Living systems are exquisitely sensitive to mechanical cues that influence a broad range of processes such as biofilm formation,[1] embryonic development,[2] immune response,[3] wound healing,[4] cell proliferation and differentiation.[5] Akin to the biochemical information exchange, mechanical interactions constantly and dynamically occur among neighboring cells or between cells and their extracellular matrix (ECM).[6] Therefore, it is not surprising that almost all cells have evolved the ability to detect and converting mechanical information into biochemical signals, a process widely known as mechanotransduction.

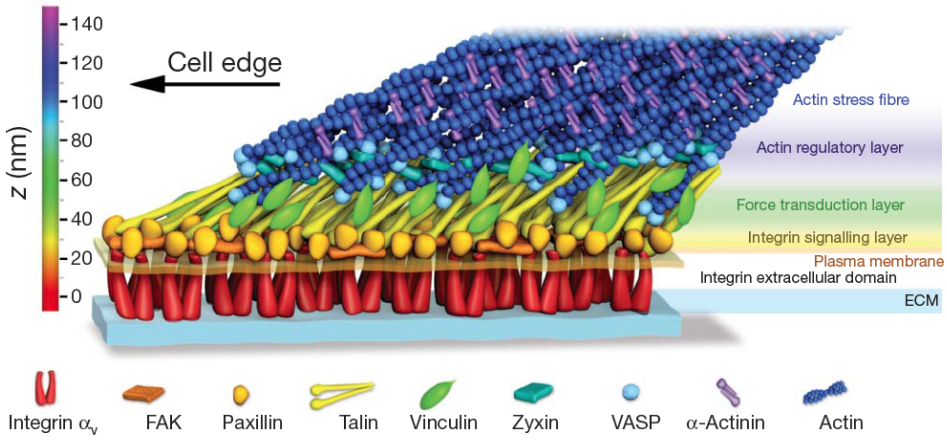

Figure 1.1 Schematic model of integrin-mediated focal adhesion (FA). FAs bridges the cell cytoskeleton and extracellular matrix, which features a defined layer-by-layer architecture at the nanoscale. The protein positions were experimentally determined by using photoactivated localization microscopy (PALM). Reprinted from reference 8 with permission of the publisher.

Many mechanotransduction processes are mediated by receptors residing at the cell surface. For example, integrins are a class of heterodimeric αβ transmembrane receptors that transmit cellular forces bi-directionally between cells and also between cells and

their ECM.[7] In the later case, activated integrin receptors recruit hundreds of other structural and signaling proteins to form a supramolecular assembly known as the focal adhesion (FA) (Figure 1.1).[8-9] Through these structures, cells can mechanically probe the properties of their environment (i.e. rigidity, ligand spacing, dimensions)[10] and consequently direct cell differentiation and migration.[11]

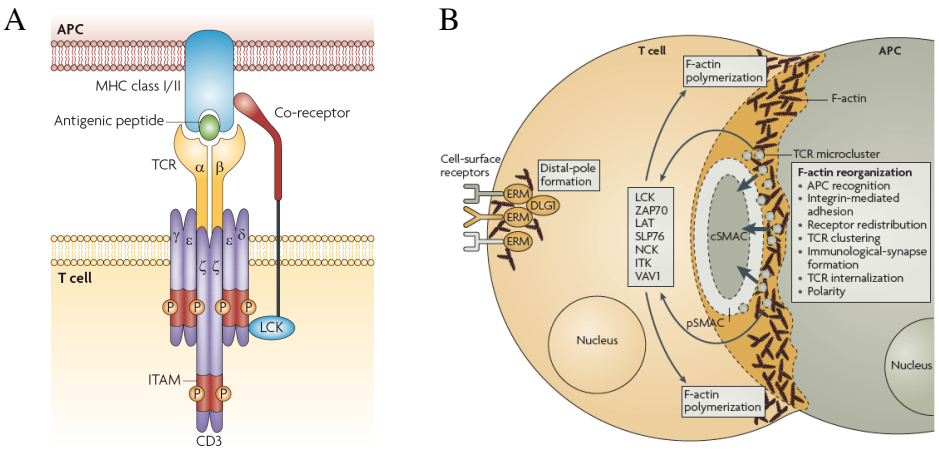

Figure 1.2 Classical model of TCR activation. (A) TCR recognizes the peptide-loaded MHC antigen at the T cell-APC junction, triggering the phosphorylation of immunoreceptor tyrosine-based activation motif for downstream signaling. (B) Activated TCR microclusters are translocated towards the center of the T cell, forming a signaling complex known as the central supramolecular activation cluster (c-SMAC). Reprinted from references 16 and 17 with the permission of the publisher.

Several other surface receptors, such as cadherins,[12] T cell receptor (TCR),[13] B cell receptor (BCR), notch[14] and receptor tyrosine kinases (RTKs),[15] also transmit forces and their activation pathways are mechanosensitive. For example, TCR recognizes and binds to its ligand, the antigenic peptide-major histocompatibility complex (pMHC), which is expressed on the surface of antigen-presenting cells (APCs) (Figure 1.2A).[16] At this cell-cell junction, activated TCR microclusters are translocated across the cell surface to form the central supramolecular activation clusters (cSMAC) (Figure 2B).[17] Extensive research

has shown that this process was coupled to actin retrograde flow and myosin contractility.[18] Both the inhibition of myosin activity and softening of substrate stiffness were found to profoundly lower the activation level of TCR.[3] More recently, single molecule experiments using optical tweezers demonstrated that the TCR was mechanically activated by externally applied forces[19] and the receptor also displayed distinct structural changes in response to ~15 pN forces,[20] thus suggesting a potential physical basis by which T-cells translate mechanical information into immunological functions.

1.1.2 The molecular foundation of mechanotransduction

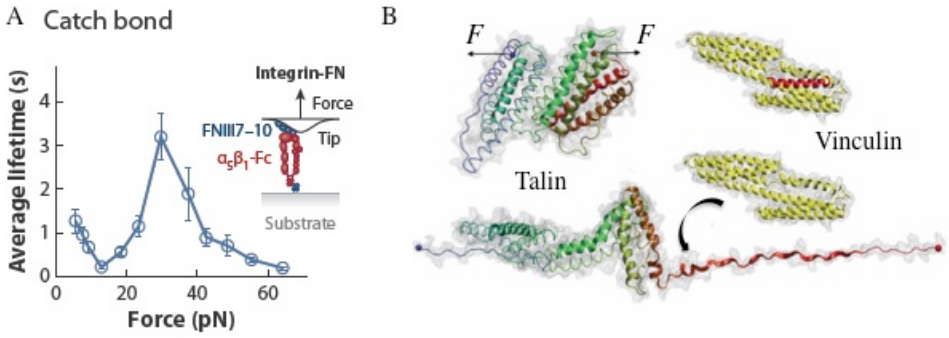

Figure 1.3 General mechanisms of mechanical regulation at the molecular level. (A) Plot showing that integrin receptors display a catch bond feature, where the receptor/ligand bond lifetime peaks at ~30 pN of externally applied forces. (B) Schematic showing mechanical unfolding of talin and exposing its cryptic sites for vinculin binding. Reprinted from references 21 and 26 with the permission of the publisher.

Generally, there are two common mechanisms for the mechanical regulation of a biochemical signal transduction pathway. The first involves modulating the kinetics of protein-protein interactions as a function of force, which either accelerate the dissociation or stabilize the association of the bond.[21] A bond that displays reduced dissociation rates when experiencing a mechanical force is counter-intuitive and described as a catch bond (Figure 1.3A).[21-22] So far, multiple catch bonds have been discovered for structural

proteins within the cytoplasm and also in signaling receptors at the cell membrane.[22-25] The second mechanism involves the mechanical exposure of cryptic sites within a protein thus triggering downstream recruitment events. For example, integrin-mediated forces activate the cryptic sites buried within the α–helix bundles of a talin molecule, leading to vinculin binding and FA reinforcement (Figure 1.3B).[26]

Based on Bell model, an external force (F) not only drastically changes the free energy landscape of an unfolding reaction from G^0 (black curve) to G^0-$F\Delta x$ (red curve), but also lowers the energy barrier $\Delta G^{\ddagger}$ and the G^0 of the unfolded state B (Figure 1.4A).[27-28] Consequently, the reaction rate (k_{off}) and the population distribution of unfolded state B are both increased. Therefore, it is critical to develop tools for force measurement to better understand how mechanics influence binding kinetics, shifting equilibrium distributions of proteins and ultimately controlling signaling pathways within the context of a living cell.

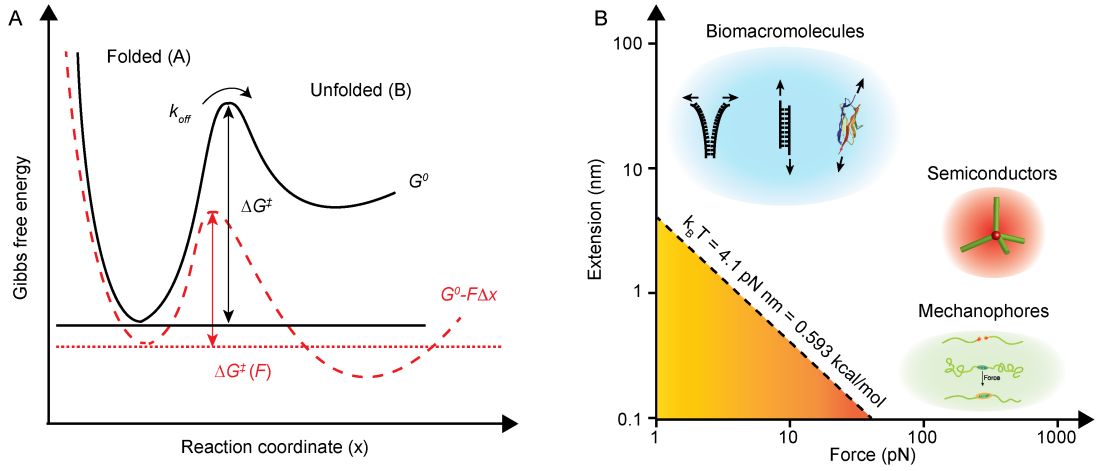

Figure 1.4 Mechanically unfolding of biomolecules. (A) Free energy landscape of a two-state model representative of a biomolecular unfolding event upon force application. (B) Plot showing the force-extension relationship of important biomolecules (blue), semiconductor tetrapod (red) and mechanophores (green).

1.2 Current methods to measure cellular forces

Typically, unfolding a single biological macromolecule involves rupturing non-covalent bonds with energy level on the order of 1-100 kcal/mol. For example, the ΔG of unfolding a typical RNA hairpin is ~35 kcal/mol (blue area, Figure 1.4B).[29] Note that 1 kcal/mol is equivalent to ~6.9 pN•nm and therefore, we can estimate the rupture force of a RNA hairpin at ~ 12.3 pN (assuming a 20 nm extension). Several optical force sensors and mechanophores have been developed to report on mechanical load, however, these types of probes are sensitive to forces of hundreds or thousands of pN (100-1000 kcal/mol). They either rupture a covalent bond[30] or bend a stiff semiconductor tetrapod crystal[31] to report forces (green and red area, Figure 1.4B). Therefore, these probes are unable to report the typical range of molecular forces (1-100 pN) that mediate mechanotransduction pathways in biology.

1.2.1 Polymer network deformation (TFM and mPADs)

In the past two decades, a number of innovative techniques have been developed for measuring forces in living cells. The first class of techniques focused on measuring the deformation of soft polymer networks and this includes methods such as traction force microscopy (TFM) and microfabricated post-array-detectors (mPADs) (Figure 1.5, left).[32-33] Upon cellular traction, the deformation of gels or polymer microposts is detected by using conventional fluorescence microscopy. In the case of TFM, the strain is interpolated for every position on the substrate and further translated into local stress by reversing the calculation of the stress–strain formulation, assuming an ideal and homogeneous hydrogel.[34] The readout for mPADs is the lateral bending of the

microposts, which is more direct and less computationally intensive.[35] Alternatively, Forster resonance energy transfer (FRET) has been utilized to optically estimate strain-induced deformation of fibronectin matrix and synthetic RGD hydrogels, where energy transfer efficiency decreases upon external stretching by integrin receptors.[36-37] Although these techniques have been greatly appreciated by the biomechanics research community, these polymer substrates are crosslinked and only sensitive to forces at nN level, yielding a spatial resolution and force sensitivity that can not reveal mechanics mediated by signaling receptors (Table 1.1). For example, TFM reports cellular forces in units of stress (nN/μm^2), and thus mechanical events during initial cell spreading is largely invisible because only low density of integrin receptors are clustered to form nascent FAs and the transmitted forces are insufficient to yield deformations across the substrate.

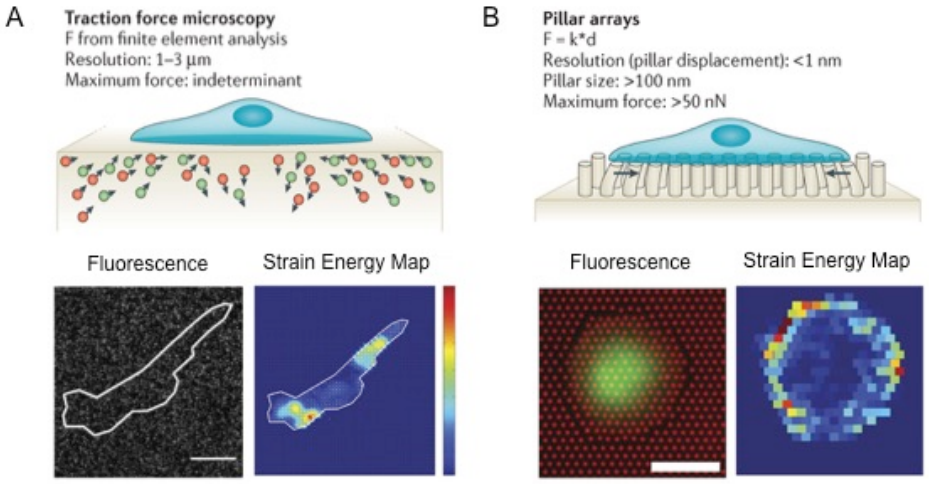

Figure 1.5 Polymer network deformation methods for measuring cellular forces. (A) Traction force microscopy monitors the displacement of fluorescent beads embedded in the synthetic polymer gels and estimate the corresponding forces using finite element analysis. Sacle bar, 50 μm. (B) Micropillar array detectors (mPADs) measure the bending degree of the microposts in response to horizontal forces. Scale bar, 30 μm. Reprinted from references 32 and 33 with the permission of the publishers.

1.2.2 Single molecule force spectroscopy (SMFS)

A second general strategy for measuring molecular forces of a cell is single molecule force spectroscopy (SMFS) that includes atomic force microscopy (AFM), optical/magnetic tweezer and biomembrane force probe (BFP) (Figure 1.6).[38-39] SMFS allows the measurement of forces ranging from below 1 pN to several nN, which provides an appropriate means to investigate the mechanical event of a single biomolecule with extremely high resolution and sensitivity. For example, AFM has been used to measure the catch bond behavior of a ligand-bound integrin receptor under mechanical load.[40] In addition, magnetic tweezers have been used to activate single integrin receptors and to trigger the formation of nascent focal complex *in vitro*.[41] However, these SMFS methods are low throughput and interrogate one bond at a time, thus failing to capture the mechanics of a whole cell or to fully activate surface receptors that require clustering in their physiological conditions.

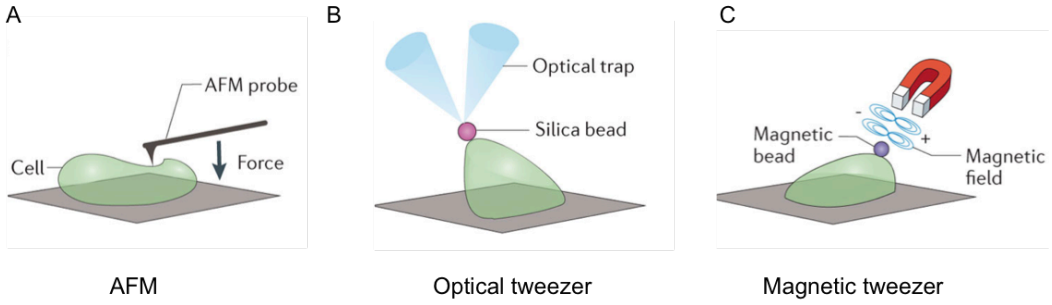

Figure 1.6 Single molecule force spectroscopy for measuring cellular forces. (A) An atomic force microscope (AFM) uses an AFM cantilever or tip to apply or monitor mechanical forces in cells. (B) Optical tweezer utilizes laser beams to control and monitor the movement of a silica bead attached to a cell and thus quantifies the pushing or pulling forces generated cells. (C) Magnetic tweezers uses weak external electromagnetic fields to apply pN forces while measuring and monitoring cell mechanics. Reprinted from references 39 with the permission of the publishers.

1.3 Molecular Tension Probes

1.3.1 Genetically-encoded and immobilized probe

To address the limitations inherent to SMFS, molecular tension probes were recently introduced wherein single elastic molecules function as reporters of cell mechanics.[42-44] Typically, these tension probes consist of a fluorescent donor-acceptor pair separated by a molecular "spring". By using fluorescence microscopy, one can visualize single-molecule mechanical unfolding events across the entire cell, successfully combining the high-throughput of TFM deformation measurements and the pN sensitivity of SMFS (Table 1.1 and Figure 1.7A). This approach was first applied to engineer genetically-encoded tension probes to measure the forces across a protein expressed within a cell. To date, multiple forms of genetically-encoded tension sensors consisting of α-helical, spectrin repeats and flagelliform elastic polypeptides have been reported to estimate pN forces transmitted in proteins such as α-actinin,[45] vinculin,[46] talin[47] and E-cadherin.[12]

	Traction force microscopy/ micro-post array detectors	Single Molecule methods (AFM/BFP/ Tweezers)	Molecular Tension Probes
Force range	*Ensemble (nN)*	*Single molecule* [48]	*Single molecule* [48]
Temporal resolution	*~sec*	*~msec*	*~msec*
Spatial resolution	*~1 μm*	*1-20 nm*	*~20 nm*
Throughput	*High*	*Low*	*High*
Allows for clustering	*Yes*	*No*	*Yes*

Table 1. A comparison of the advantages and disadvantages of polymer network deformation techniques (TFM), single-molecule force spectroscopy (SMFS) and molecular tension probes.

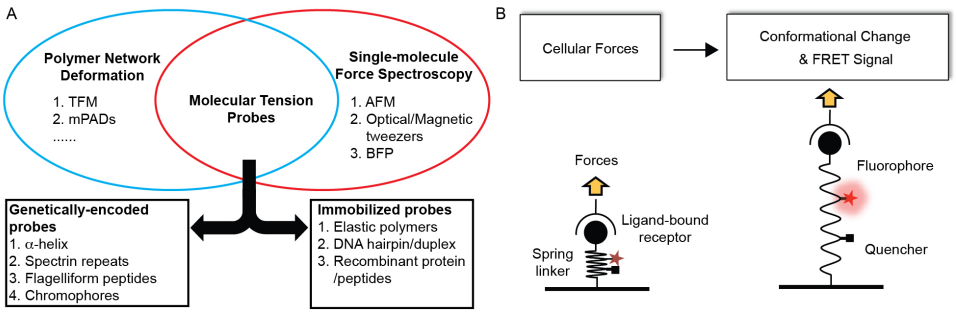

Figure 1.7 Molecular tension probes. (A) Scheme depicting the advantages of molecular tension probes that bridges both polymer network deformation and single-molecule force spectroscopy. Examples of genetically-encoded probes and synthetic probes are included. (B) Flow chart showing that synthetic tension probes detect fluorescence recovery upon cellular forces induced conformational changes.

Another major category of molecular tension probes is the immobilized probes, which consist of an elastic unit flanked by a fluorescent dye and quencher and are immobilized on a surface. Specifically, our lab has pioneered the development of these substrate-immobilized molecular tension probes to quantify forces mediated by surface receptors, a technique we termed molecular tension fluorescence microscopy (MTFM) (Figure 1.7B).[42] In contrast to the cross-linked nature of TFM substrate, each MTFM probe consists of only one elastic molecule that independently reports the mechanical force from its bound receptor. With this strategy, we can map the tension applied by single receptors with molecular specificity, submicron spatial resolution, millisecond temporal resolution and low pN force sensitivity (Table 1.1). This review will focus on the immobilized class of tension probes.

1.3.2 Guidelines for the design of immobilized tension probes

In a typical configuration, the MTFM probes consist of a flexible linker flanked by a fluorophore/quencher pair. The probe is decorated with a biological ligand at one terminus and is immobilized to the substrate through the other terminus. In the resting

state, MTFM probes adopt a relaxed or closed conformation in which the fluorophore is strongly quenched due to proximity to quencher. When forces are transmitted through the ligand-receptor complex, tension increases along the linker extending it from its resting conformation, and thus increasing the distance between the two dyes and restoring the fluorescence. To design an efficient MTFM sensor, a few general rules are critical (Figure 1.8). First, the extendable linker needs a mechanical resistance that is matched to the pN forces under investigation (sensitivity); second, the extension of the linker should exceed the FRET distance of the reporter to maximize the sensitivity; third, the quenching efficiency of the dye should be maximized when the probe is at resting (signal/noise ratio); finally, the MTFM probes must be immobilized onto the substrate through stable chemical bonds to sustain receptor forces without rupturing (mechanical stability).

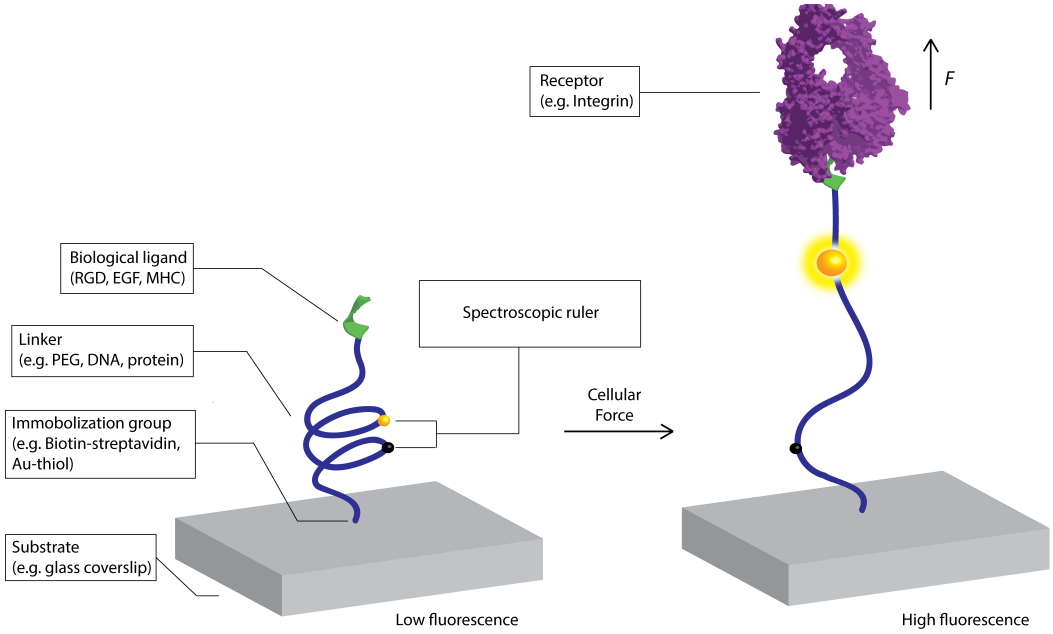

Figure 1.8 Schematic dissecting the key components of immobilized tension probes.

1.3.3 Selecting the key components of immobilized tension probes

1.3.3.1 Mechanical Springs

Different elastic molecules have been utilized as the spring element in molecular tension probes. Here, we classify these molecules into two categories: (i) switch-like spring with defined secondary structure such as DNA hairpins and protein domain; (ii) entropic spring with random coil conformation such as polyethylene glycol (PEG), single-stranded DNA and elastic polypeptide (EP). In the first category, the molecular spring adopts a defined structural motifs (secondary or tertiary structure) such as a DNA hairpin, [49-52] and α-helical or β-sheet protein domain[53]. The stability (ΔG) of these secondary structures is a primary determinant of the magnitude of forces required for mechanical unfolding.[54] For example, the GC content of the stem region in a DNA hairpin structure tunes the rupture force from 2 to 19 pN (Figure 1.9A). Notably, mechanical unfolding of these highly ordered structures is cooperative, displaying a "digital" response to external forces within a narrow window of external forces (*i.e.* conformational change is only observed when the force applied approaches the force threshold).

The second category of springs includes polymer chains that adopt random conformations at zero force.[55-56] In contrast, these entropic springs yield an "analogue" response to forces where their extensions proportionally respond to the magnitude of applied forces (Figure 1.9B). For polymers such as PEG, it has been both theoretically and experimentally proven that the force-extension curve of these springs simply follows the worm-like chain (WLC) model (eq. 1),

$$F = \frac{k_B T}{P}\left\{\frac{1}{4}\left(1-\frac{x}{L_0}\right)^{-2} - \frac{1}{4} + \frac{x}{L_0}\right\} \qquad eq.1$$

where, k_B is Boltzmann constant; T is temperature; P, L_0 and x are the persistence length, contour length and the extension of the polymer chain. Based on this relationship, the dynamic force range of PEG-based springs solely depends on the contour length (L_0) of the polymer (*i.e.* M_w of polymer) and the forces experienced by these polymers can be estimated by measuring their extension (x).

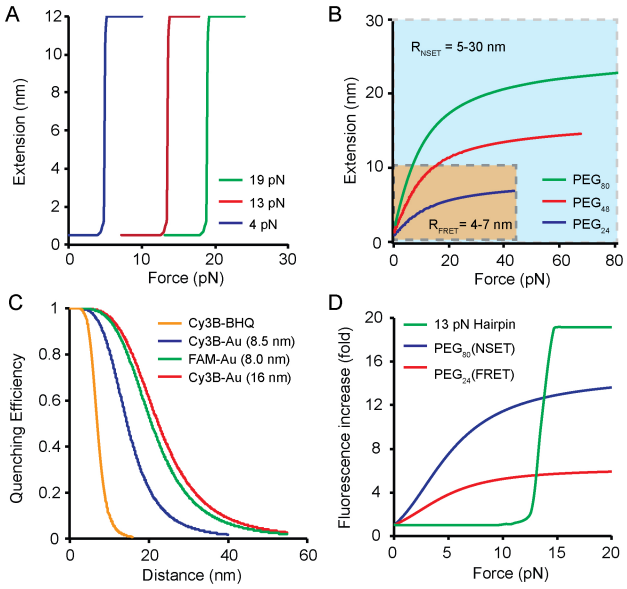

Figure 1.9 Mechanical spring and spectroscopic ruler. (A) Plot showing the expected force-extension curve for DNA hairpins of different GC contents. (B) Theoretical plot showing the force responses of PEG linkers as a function of end-to-end distance. Yellow region highlights the R range of FRET pairs and blue region highlights the R range of NSET pairs. (C) Plot showing the quenching efficiency as a function of PEG extension with different energy transfer mechanisms (parenthesis indicates the radius of AuNP). (D) Plot comparing the fold increase of donor fluorescence as a function of tension applied to different probes.

1.3.3.2 Spectroscopic rulers

To date, the spectroscopic ruler utilized in MTFM is based on energy transfer between a fluorescent donor and acceptor (quencher). Here, two common resonance energy transfer mechanisms are introduced: fluorescence resonance energy transfer (FRET)[57] and nanometal surface energy transfer (NSET)[58].

Similarly, in both FRET and NSET, the emission spectrum of the donor significantly overlaps with the absorption of the acceptor so that the energy of an excited donor is efficiently transferred to a nearby acceptor in a distance-dependent fashion. To unify these two mechanisms, the FRET/NSET efficiency (*E*) as a function of distance (r) has been mathematically described in one general equation (eq. 2),

$$E = \frac{1}{1 + \left(\frac{r}{R}\right)^n} \qquad eq.2$$

where *r* is the actual distance between the donor/acceptor pair and constant *R* is the förster distance at which the energy transfer efficiency is 50%.

Based on eq. 2, the FRET efficiency is governed by an inverse sixth power law (n = 6) and the forster distance *R* depending on the spectral overlap of the FRET pair. Here, a small *R* (typically 4-7 nm) limits the detection of FRET signals within a short range (1-10 nm). However, in NSET, the donor dipole is strongly quenched by multiple dipoles presented on the surface of a gold nanoparticle rather than a single dipole, thus affording NSET with unique quenching capabilities.[59] First, the distance-dependent NSET efficiency follows an inverse forth power law (n = 4), which yields a much broader dynamic range for energy transfer than that of FRET (Figure 1.9B and C). Second, the Forster distance (*R*) of NSET is highly tunable depending on the nanoparticle size and the

degree of spectral overlap between the AuNP and dye (Figure 1.9C). Typically, larger nanoparticles and more spectral overlap provide more superior energy transfer.[60]

As a rule of thumb, the choice of FRET or NSET should always be considered along with the mechanical properties of the spring. For "digital" probes, the most critical parameter is a high value of energy transfer efficiency at the resting states. Without external forces, donor fluorescence should be maximally quenched, thus generating a large enhancement following mechanical unfolding. For example, unzipping of a DNA hairpin labeled with Cy3B/Black Hole Quencher (BHQ) pairs can easily lead to a 20-fold increase in fluorescence intensity (Figure 1.9D).[52] For "analogue" probes employing FRET or NSET, the forster distance R should match one half of the contour length of the polymer linker, such that the polymer extension can be fully visualized by the recovery of donor fluorescence. For example, FRET has been successfully used to monitor the dynamic conformational change of PEG_{24} whose contour length (L_0 = 8.4 nm) falls within the working distance of typical dye/quencher pairs (Figure 1.9D).[61] However, in the case of longer springs such as PEG_{80} (L_0 = 28.0 nm), the change in FRET becomes negligible beyond the initial 10 nm extension (Figure 1.9B), and NSET (R value > 15 nm) is preferred since it provides larger quenching distances and generates a 10-fold enhancement in fluorescence intensity (Figure 1.9B and D).[58]

1.3.3.3 Immobilization strategies

To visualize cell forces mediated by surface receptors, MTFM probes must be immobilized onto a culture substrate. Toward this end, an ideal immobilization strategy should be (i) chemically stable against the biological media and benign to all elements of the probes; (ii) physically robust to withstand mechanical dissociation over the timescale of an experiment; (iii) highly reproducible and facile so that consistent density of molecular force probes are fabricated on different coverslips.

So far, three common coupling strategies have been used to graft MTFM probes onto the surfaces. The first strategy is affinity coupling through which biotinylated probes are bound to streptavidin-modified substrates with extremely high affinity (K_d = 10^{-13} M).[52, 61] The second strategy utilizes chemisorption, where thiolated probes are self-assembled onto a gold surface *via* the formation of gold-sulfur bonds.[58, 62] This coupling provides not only high grafting density but also a semi-covalent linkage stronger than most other non-covalent bonds. In the third strategy, MTFM probes are covalently immobilized to a substrate via chemical reactions, which affords the most stable linkage. For example, Chang *et al.* covalently modified the PEG-based probes to the substrate through "azide/alkyne click chemistry", enabling live-cell imaging of integrin tension for up to 3 days.[63]

All immobilization strategies for molecular tension probes surveyed here have their advantages and drawbacks. On one hand, attaching the molecular tension probes onto surfaces *via* biotin−streptavidin interactions may not be sufficiently stable for long-term imaging or for receptors that apply large magnitudes of forces (e.g. integrins). On the other hand, the surface density of biotinylated probes is highly consistent, *ca.* 400

probes/μm^2 for DNA probes, allowing us to quantify the molecular unfolding by intensometric measurement.[52] The biotin–streptavidin interaction is also compatible with biological systems and minimally influences the structure and function of MTFM probes. Therefore, one must judiciously choose an appropriate attachment strategy depending on their experimental conditions and needs.

1.3.4 Biological applications of immobilized tension probes

In 2011, our lab reported the first generation of PEG-based MTFM probes.[57] As-a-proof-of-concept, these probes were engineered to report the mechanical forces associated with the endocytosis of epidermal growth factor receptor (EGFR), which is known to broadly regulate cell survival, proliferation and differentiation (Figure 1.10A). In this design, Alexa647 fluorophore-tagged EGF ligand was covalently conjugated to one terminus of the PEG spring and a biotin group to the other terminus. In order to quench the fluorescence, the entire construct was then immobilized onto a substrate fully modified with quencher-tagged streptavidin. Upon receptor engagement, an average force of ~ 4 pN was detected and quantified in real-time, and we showed that the recruitment of clathrin was highly associated with tension generation.

Following this success, a similar PEG probe was developed to study integrin-mediated forces.[64] To this end, the biological ligand of the probe was instead modified with a cyclized RGD peptide, which has strong binding affinities to $\alpha v\beta 3$ and $\alpha 5\beta 1$ integrins. Unexpectedly, integrin receptors exerted forces sufficient to dissociate streptavidin-biotin complexes, the highest non-covalent interaction in nature (Figure 1.10B). There are many plausible explanations for this phenomenon, Likely, the “catch bond” feature of integrin receptor, low frequency traction force oscillations and integrin

clustering in mature FAs together contribute to a strengthened and prolonged lifetime of integrin-RGD interaction, which outcompetes a mechanically-weakened streptavidin-biotin bond.[64] Eventually and most importantly, this result prompted us to search for the next generation of tension probes with improved stability, broader dynamic range and higher sensitivity.

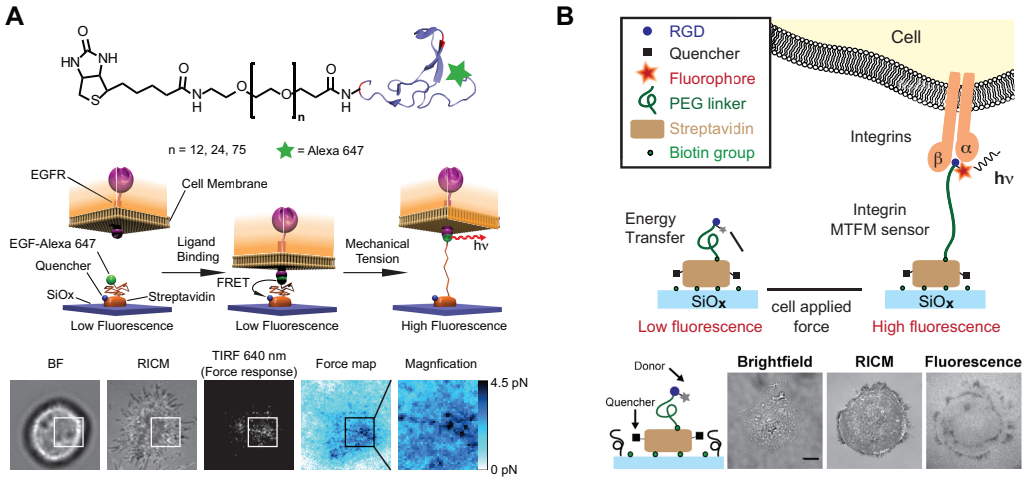

Figure 1.10 First generation of MTFM probes for measuring receptor forces. (A) PEG-based tension probes was used to report forces associated with EGFR signaling pathway. (B) Integrin-mediated forces dissociated the biotin-streptavidin bond that was used to immobilize MTFM probes on the glass coverslip. Reprinted from references 57 and 64 with the permission of the publishers.

1.4 Aim and scope of the dissertation:

Over the past few decades, technological innovations in force measurement and manipulation have revolutionized our understanding of mechanical forces in cell biology, thus starting a completely new era of mechanobiology. However, current techniques still lack the ability to interrogate cellular forces at the single receptor level and with high throughput. This dissertation aims to introduce a series of molecular techniques with specific applications in studying integrin and TCR mediated mechanotransduction pathways. With these tools, some long-standing questions are to be addressed, including:

1. What are the magnitude of forces involved in integrin activation and the maturation of focal adhesions?

2. How does the nanoscale clustering of ligands influence the mechanical forces transmitted by integrin receptors?

3. How do mechanical forces participate in the activation of TCR and regulate immune response?

4. Can cell signaling and functions be mechanically controlled through a high throughput optical method?

In summary, chapter 2 describes the systematic development of a gold nanoparticle tension probe for visualizing forces exerted by integrin receptors. For the first time, integrin forces were quantified with pN sensitivity during initial cell spreading and focal adhesion maturation. Chapter 3 reports the technological advancement of nanopatterned tension probe arrays and carefully explores how nanoscale clustering of RGD ligands alters the mechano-regulation of their integrin receptors. The physical mechanism of how cells measure ligand spacing was revealed. Chapter 4 details the invention of DNA-based

nanoparticle tension probes and explores how chemo-mechanical coupling influences immune function. With the highest sensitivity to date, these sensors provided the first pN tension maps of individual TCR-pMHC complexes during T-cell activation. Significantly, this study showed that CD8+ T cells recruit TCRs, co-receptor CD8, and adhesion molecules such as LFA-1 to achieve a force of 12-19 pN, a level indispensable for enhanced antigen fidelity. Finally, chapter 5 introduces the recent development of a gold nanorod based optomechanical acatutor that specifically deliver pN forces upon optical illumination. A variety of cell behaviors, such as cell adhesion, migration and T-cell activation, were remotely triggered by the activation of corresponding mechanosensitive receptors.

1.5 References:

1. Asally, M.; Kittisopikul, M.; Rue, P.; Du, Y. J.; Hu, Z. X.; Cagatay, T.; Robinson, A. B.; Lu, H. B.; Garcia-Ojalvo, J.; Suel, G. M., Localized cell death focuses mechanical forces during 3D patterning in a biofilm. *Proceedings of the National Academy of Sciences of the United States of America* **2012,** *109* (46), 18891-18896.

2. Mammoto, T.; Ingber, D. E., Mechanical control of tissue and organ development. *Development* **2010,** *137* (9), 1407-1420.

3. Judokusumo, E.; Tabdanov, E.; Kumari, S.; Dustin, M. L.; Kam, L. C., Mechanosensing in T lymphocyte activation. *Biophysical Journal* **2012,** *102* (2), L5-7.

4. Brugues, A.; Anon, E.; Conte, V.; Veldhuis, J. H.; Gupta, M.; Colombelli, J.; Munoz, J. J.; Brodland, G. W.; Ladoux, B.; Trepat, X., Forces driving epithelial wound healing. *Nature Physics* **2014,** *10* (9), 684-691.

5. McBeath, R.; Pirone, D. M.; Nelson, C. M.; Bhadriraju, K.; Chen, C. S., Cell shape, cytoskeletal tension, and RhoA regulate stem cell lineage commitment. *Dev Cell* **2004,** *6* (4), 483-95.

6. Ingber, D. E., Cellular mechanotransduction: putting all the pieces together again. *Faseb Journal* **2006,** *20* (7), 811-827.

7. Schwartz, M. A., Integrins and Extracellular Matrix in Mechanotransduction. *Cold Spring Harbor Perspectives in Biology* **2010,** *2* (12).

8. Kanchanawong, P.; Shtengel, G.; Pasapera, A. M.; Ramko, E. B.; Davidson, M. W.; Hess, H. F.; Waterman, C. M., Nanoscale architecture of integrin-based cell adhesions. *Nature* **2010,** *468* (7323), 580-U262.

9. Wolfenson, H.; Lavelin, I.; Geiger, B., Dynamic Regulation of the Structure and Functions of Integrin Adhesions. *Dev Cell* **2013,** *24* (5), 447-458.

10. Geiger, B.; Spatz, J. P.; Bershadsky, A. D., Environmental sensing through focal adhesions. *Nature Reviews Molecular Cell Biology* **2009,** *10* (1), 21-33.

11. Wozniak, M. A.; Modzelewska, K.; Kwong, L.; Keely, P. J., Focal adhesion regulation of cell behavior. *Biochimica Et Biophysica Acta-Molecular Cell Research* **2004,** *1692* (2-3), 103-119.

12. Borghi, N.; Sorokina, M.; Shcherbakova, O. G.; Weis, W. I.; Pruitt, B. L.; Nelson, W. J.; Dunn, A. R., E-cadherin is under constitutive actomyosin-generated tension that is increased at cell–cell contacts upon externally applied stretch. *Proceedings of the National Academy of Sciences of the United States of America* **2012,** *109* (31), 12568-12573.

13. Liu, Y.; Blanchfield, L.; Ma, V. P. Y.; Andargachew, R.; Galior, K.; Liu, Z.; Evavold, B.; Salaita, K., DNA-based nanoparticle tension sensors reveal that T-cell receptors transmit defined pN forces to their antigens for enhanced fidelity. *Proceedings of the National Academy of Sciences of the United States of America* **2016,** *113* (20), 5610-5615.

14. Gordon, W. R.; Zimmerman, B.; He, L.; Miles, L. J.; Huang, J. H.; Tiyanont, K.; McArthur, D. G.; Aster, J. C.; Perrimon, N.; Loparo, J. J.; Blacklow, S. C., Mechanical Allostery: Evidence for a Force Requirement in the Proteolytic Activation of Notch. *Dev Cell* **2015,** *33* (6), 729-736.

15. Salaita, K.; Nair, P. M.; Petit, R. S.; Neve, R. M.; Das, D.; Gray, J. W.; Groves, J. T., Restriction of Receptor Movement Alters Cellular Response: Physical Force Sensing by EphA2. *Science* **2010,** *327* (5971), 1380-1385.

16. Gascoigne, N. R. J., Do T cells need endogenous peptides for activation? *Nature Reviews Immunology* **2008,** *8* (11), 895-900.

17. Billadeau, D. D.; Nolz, J. C.; Gomez, T. S., Regulation of T-cell activation by the cytoskeleton. *Nature Reviews Immunology* **2007,** *7* (2), 131-43.

18. Yu, Y.; Smoligovets, A. A.; Groves, J. T., Modulation of T cell signaling by the actin cytoskeleton. *Journal of Cell Science* **2013,** *126* (5), 1049-1058.

19. Kim, S. T.; Takeuchi, K.; Sun, Z. Y.; Touma, M.; Castro, C. E.; Fahmy, A.; Lang, M. J.; Wagner, G.; Reinherz, E. L., The alphabeta T cell receptor is an anisotropic mechanosensor. *J Biol Chem* **2009,** *284* (45), 31028-37.

20. Das, D. K.; Feng, Y.; Mallis, R. J.; Li, X.; Keskin, D. B.; Hussey, R. E.; Brady, S. K.; Wang, J. H.; Wagner, G.; Reinherz, E. L.; Lang, M. J., Force-dependent transition in the T-cell receptor beta-subunit allosterically regulates peptide discrimination and pMHC bond lifetime. *Proc Natl Acad Sci U S A* **2015,** *112* (5), 1517-22.

21. Schoen, I.; Pruitt, B.; Vogel, V., The Yin-Yang of Rigidity Sensing: How Forces and Mechanical Properties Regulate the Cellular Response to Materials. *Annual Review of Materials Research* **2012**.

22. Kong, F.; Garcia, A. J.; Mould, A. P.; Humphries, M. J.; Zhu, C., Demonstration of catch bonds between an integrin and its ligand. *Journal of Cell Biology* **2009,** *185* (7), 1275-1284.

23. Buckley, C. D.; Tan, J. Y.; Anderson, K. L.; Hanein, D.; Volkmann, N.; Weis, W. I.; Nelson, W. J.; Dunn, A. R., The minimal cadherin-catenin complex binds to actin filaments under force. *Science* **2014,** *346* (6209), 600-+.

24. Sauer, M. M.; Jakob, R. P.; Eras, J.; Baday, S.; Eris, D.; Navarra, G.; Berneche, S.; Ernst, B.; Maier, T.; Glockshuber, R., Catch-bond mechanism of the bacterial adhesin FimH. *Nature Communications* **2016,** *7*.

25. Liu, B.; Chen, W.; Evavold, Brian D.; Zhu, C., Accumulation of Dynamic Catch Bonds between TCR and Agonist Peptide-MHC Triggers T Cell Signaling. *Cell* **2014,** *157* (2), 357-368.

26. del Rio, A.; Perez-Jimenez, R.; Liu, R.; Roca-Cusachs, P.; Fernandez, J. M.; Sheetz, M. P., Stretching single talin rod molecules activates vinculin binding. *Science* **2009,** *323* (5914), 638-41.

27. Bustamante, C.; Chemla, Y. R.; Forde, N. R.; Izhaky, D., Mechanical processes in biochemistry. *Annu Rev Biochem* **2004,** *73*, 705-48.

28. Bell, G. I., Models for the specific adhesion of cells to cells. *Science* **1978,** *200* (4342), 618-27.

29. Liphardt, J.; Onoa, B.; Smith, S. B.; Tinoco, I., Jr.; Bustamante, C., Reversible unfolding of single RNA molecules by mechanical force. *Science* **2001,** *292* (5517), 733-7.

30. Potisek, S. L.; Davis, D. A.; Sottos, N. R.; White, S. R.; Moore, J. S., Mechanophore-linked addition polymers. *Journal of the American Chemical Society* **2007,** *129* (45), 13808-13809.

31. Choi, C. L.; Koski, K. J.; Sivasankar, S.; Alivisatos, A. P., Strain-Dependent Photoluminescence Behavior of CdSe/CdS Nanocrystals with Spherical, Linear, and Branched Topologies. *Nano Letters* **2009,** *9* (10), 3544-3549.

32. Iskratsch, T.; Wolfenson, H.; Sheetz, M. P., Appreciating force and shape-the rise of mechanotransduction in cell biology. *Nat Rev Mol Cell Biol* **2014,** *15* (12), 825-33.

33. Polacheck, W. J.; Chen, C. S., Measuring cell-generated forces: a guide to the available tools. *Nature Methods* **2016,** *13* (5), 415-423.

34. Munevar, S.; Wang, Y. L.; Dembo, M., Traction force microscopy of migrating normal and H-ras transformed 3T3 fibroblasts. *Biophysical Journal* **2001,** *80* (4), 1744-1757.

35. Fu, J. P.; Wang, Y. K.; Yang, M. T.; Desai, R. A.; Yu, X. A.; Liu, Z. J.; Chen, C. S., Mechanical regulation of cell function with geometrically modulated elastomeric substrates. *Nature Methods* **2010,** *7* (9), 733-U95.

36. Baneyx, G.; Baugh, L.; Vogel, V., Coexisting conformations of fibronectin in cell culture imaged using fluorescence resonance energy transfer. *Proceedings of the National Academy of Sciences of the United States of America* **2001,** *98* (25), 14464-14468.

37. Kong, H. J.; Polte, T. R.; Alsberg, E.; Mooney, D. J., FRET measurements of cell-traction forces and nano-scale clustering of adhesion ligands varied by substrate stiffness. *Proceedings of the National Academy of Sciences of the United States of America* **2005,** *102* (12), 4300-4305.

38. Clausen-Schaumann, H.; Seitz, M.; Krautbauer, R.; Gaub, H. E., Force spectroscopy with single bio-molecules. *Current Opinion in Chemical Biology* **2000,** *4* (5), 524-530.

39. Tyler, W. J., OPINION The mechanobiology of brain function. *Nature Reviews Neuroscience* **2012,** *13* (12), 867-878.

40. Marshall, B. T.; Long, M.; Piper, J. W.; Yago, T.; McEver, R. P.; Zhu, C., Direct observation of catch bonds involving cell-adhesion molecules. *Nature* **2003,** *423* (6936), 190-193.

41. Jiang, G.; Giannone, G.; Critchley, D. R.; Fukumoto, E.; Sheetz, M. P., Two-piconewton slip bond between fibronectin and the cytoskeleton depends on talin. *Nature* **2003,** *424* (6946), 334-7.

42. Jurchenko, C.; Salaita, K. S., Lighting Up the Force: Investigating Mechanisms of Mechanotransduction Using Fluorescent Tension Probes. *Mol Cell Biol* **2015,** *35* (15), 2570-2582.

43. Cost, A. L.; Ringer, P.; Chrostek-Grashoff, A.; Grashoff, C., How to Measure Molecular Forces in Cells: A Guide to Evaluating Genetically-Encoded FRET-Based Tension Sensors. *Cellular and Molecular Bioengineering* **2015,** *8* (1), 96-105.

44. Wang, Y.; Meng, F.; Sachs, F., Genetically encoded force sensors for measuring mechanical forces in proteins. *Commun Integr Biol* **2011,** *4* (4), 385-90.

45. Meng, F. J.; Sachs, F., Visualizing dynamic cytoplasmic forces with a compliance-matched FRET sensor. *Journal of Cell Science* **2011,** *124* (2), 261-269.

46. Grashoff, C.; Hoffman, B. D.; Brenner, M. D.; Zhou, R.; Parsons, M.; Yang, M. T.; McLean, M. A.; Sligar, S. G.; Chen, C. S.; Ha, T., Measuring mechanical tension across vinculin reveals regulation of focal adhesion dynamics. *Nature* **2010,** *466* (7303), 263-266.

47. Austen, K.; Ringer, P.; Mehlich, A.; Chrostek-Grashoff, A.; Kluger, C.; Klingner, C.; Sabass, B.; Zent, R.; Rief, M.; Grashoff, C., Extracellular rigidity sensing by talin isoform-specific mechanical linkages. *Nature cell biology* **2015,** *17* (12), 1597-1606.

48. Louveau, A.; Smirnov, I.; Keyes, T. J.; Eccles, J. D.; Rouhani, S. J.; Peske, J. D.; Derecki, N. C.; Castle, D.; Mandell, J. W.; Lee, K. S.; Harris, T. H.; Kipnis, J., Structural and functional features of central nervous system lymphatic vessels. *Nature* **2015,** *523* (7560), 337-41.

49. Shroff, H.; Reinhard, B. M.; Siu, M.; Agarwal, H.; Spakowitz, A.; Liphardt, J., Biocompatible Force Sensor with Optical Readout and Dimensions of 6 nm3. *Nano Letters* **2005,** *5* (7), 1509-1514.

50. Zhang, Y.; Ge, C.; Zhu, C.; Salaita, K., DNA-based digital tension probes reveal integrin forces during early cell adhesion. *Nat Commun* **2014**, DOI: 10.1038/ncomms6167.

51. Blakely, B. L.; Dumelin, C. E.; Trappmann, B.; McGregor, L. M.; Choi, C. K.; Anthony, P. C.; Duesterberg, V. K.; Baker, B. M.; Block, S. M.; Liu, D. R.; Chen, C. S., A DNA-based molecular probe for optically reporting cellular traction forces. *Nat Meth* **2014**, DOI: 10.1038/nmeth.3145.

52. Zhang, Y.; Ge, C.; Zhu, C.; Salaita, K., DNA-based digital tension probes reveal integrin forces during early cell adhesion. *Nature Communications* **2014,** *5*, 5167.

53. Galior, K.; Liu, Y.; Yehl, K.; Vivek, S.; Salaita, K., Titin-Based Nanoparticle Tension Sensors Map High-Magnitude Integrin Forces within Focal Adhesions. *Nano Letters* **2016,** *16* (1), 341-8.

54. Woodside, M. T.; Behnke-Parks, W. M.; Larizadeh, K.; Travers, K.; Herschlag, D.; Block, S. M., Nanomechanical measurements of the sequence-dependent folding landscapes of single nucleic acid hairpins. *Proc Natl Acad Sci U S A* **2006,** *103* (16), 6190-5.

55. De Gennes, P., Conformations of polymers attached to an interface. *Macromolecules* **1980,** *13* (5), 1069-1075.

56. Bouchiat, C.; Wang, M.; Allemand, J. F.; Strick, T.; Block, S.; Croquette, V., Estimating the persistence length of a worm-like chain molecule from force-extension measurements. *Biophysical Journal* **1999,** *76* (1), 409-413.

57. Stabley, D. R.; Jurchenko, C.; Marshall, S. S.; Salaita, K. S., Visualizing mechanical tension across membrane receptors with a fluorescent sensor. *Nature Methods* **2012,** *9* (1), 64-67.

58. Liu, Y.; Yehl, K.; Narui, Y.; Salaita, K., Tension Sensing Nanoparticles for Mechano-Imaging at the Living/Nonliving Interface. *Journal of the American Chemical Society* **2013,** *135* (14), 5320-5323.

59. Yun, C. S.; Javier, A.; Jennings, T.; Fisher, M.; Hira, S.; Peterson, S.; Hopkins, B.; Reich, N. O.; Strouse, G. F., Nanometal Surface Energy Transfer in Optical Rulers, Breaking the FRET Barrier. *Journal of the American Chemical Society* **2005,** *127* (9), 3115-3119.

60. Breshike, C. J.; Riskowski, R. A.; Strouse, G. F., Leaving Forster Resonance Energy Transfer Behind: Nanometal Surface Energy Transfer Predicts the Size-Enhanced Energy Coupling between a Metal Nanoparticle and an Emitting Dipole. *Journal of Physical Chemistry C* **2013,** *117* (45), 23942-23949.

61. Stabley, D. R.; Jurchenko, C.; Marshall, S. S.; Salaita, K. S., Visualizing mechanical tension across membrane receptors with a fluorescent sensor. *Nature Methods* **2012,** *9* (1), 64-U172.

62. Liu, Y.; Medda, R.; Liu, Z.; Galior, K.; Yehl, K.; Spatz, J. P.; Cavalcanti-Adam, E. A.; Salaita, K., Nanoparticle Tension Probes Patterned at the Nanoscale: Impact of Integrin Clustering on Force Transmission. *Nano Letters* **2014,** *14*, 5539-5546.

63. Chang, Y.; Liu, Z.; Zhang, Y.; Galior, K.; Yang, J.; Salaita, K., A General Approach for Generating Fluorescent Probes to Visualize Piconewton Forces at the Cell Surface. *Journal of the American Chemical Society* **2016,** *138* (9), 2901-2904.

64. Jurchenko, C.; Chang, Y.; Narui, Y.; Zhang, Y.; Salaita, Khalid S., Integrin-Generated Forces Lead to Streptavidin-Biotin Unbinding in Cellular Adhesions. *Biophysical Journal* **2014,** *106* (7), 1436-1446.

Chapter 2: Development of gold nanoparticle-based tension probes for mechano-imaging of integrin-mediated forces

Adapted from Liu, Y.; Yehl, K.; Narui, Y.; Salaita, K. Tension Sensing Nanoparticles for Mechano imaging at the Living/non-Living Interface. *J. Am. Chem. Soc.* **2013**, 135 (14), 5320–5323

2.1 Introduction

One of the most significant challenges pertaining to understanding the interplay between mechanical forces and chemical reactions involves elucidating the magnitude of force experienced by specific molecules as a function of time and space.[1-3] To address this need, several pioneering groups in the area of mechanochemistry have developed force sensitive chromophores, or mechanophores, that respond to mechanical tension by undergoing covalent bond rearrangements that shift absorbance or fluorescence emission.[4] Nonetheless, given the relatively large changes in free energy required to break covalent bonds, current mechanophore probes are sensitive to forces in the range of hundreds to thousands of pN (~10-100 kcal/mol, assuming a 10 Å displacement).[5] Thus, current mechanophores are unable to probe forces in the range of 1-50 pN that can drive conformational changes in macromolecules and molecular assemblies.

Tension-driven conformational rearrangements underpin many of the fundamental processes that regulate living systems. For example, cell division,[6] translation,[7] and transcription[8] require spatially and temporally coordinated low pN range forces to proceed. Accordingly, our group recently developed a method termed Molecular Tension-based Fluorescence Microscopy (MTFM), to measure pN forces exerted by cell surface receptors.[2] MTFM employs a ligand molecule linked to a polymeric "spring" and anchored to a surface. The linker is flanked by a pair of dyes utilizing fluorescence resonance energy transfer (FRET) to report on molecular forces that extend the polymer from its resting position. MTFM offers the only method to visualize pN forces exerted between a membrane receptor and its extracelluar ligand. We rationalized that, by developing a gold nanoparticle-based mechanophore, the force sensitivity of MTFM

could be extended to measure receptor tension magnitudes that are not practically accessible by FRET-based approaches, such as the genetically encoded spider silk construct,[1] and our own FRET-based polyethylene glycol (PEG) tension sensors.[2]

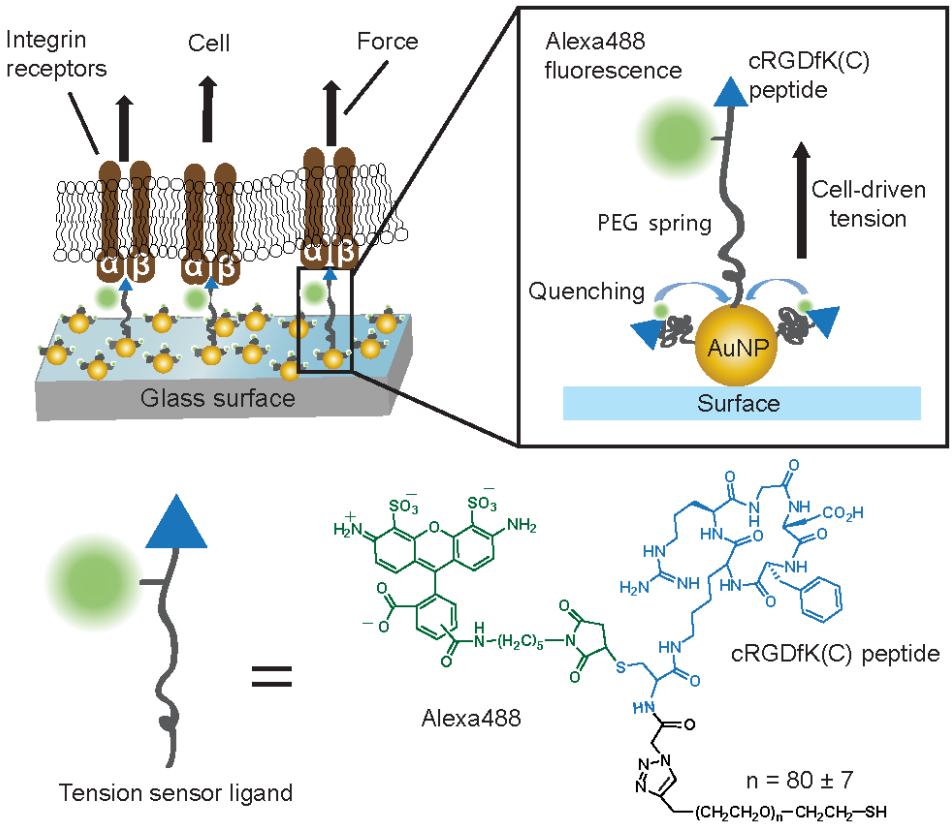

Figure 2. 1 AuNP-based molecular tension fluorescence microscopy

Noble metal nanoparticles have revolutionized the field of chemical sensing due to their unique optical, electrical, electrochemical, and catalytic properties.[9] Moreover, the relatively biocompatible nature of gold nanoparticles (AuNP) has lent itself to biological sensing applications for both *in vivo* and *in vitro* assays.[10] In many of these applications, the superior fluorescence quenching ability of AuNPs is exploited to achieve high sensitivity turn-on detection.[11] Compared to molecular quenchers, the effective quenching distance of AuNP can be as long as several tens of nanometers.[12] Theoretical and

experimental studies have shown that the distance-dependent quenching of 1-20 nm AuNPs follows a $1/r^4$ relationship, termed Nanometal Surface Energy Transfer (NSET),[13] which provides a highly sensitive approach to measuring molecular distances in living systems.[14]

Herein, we report on an AuNP-based sensor for MTFM to visualize the pN-range force dynamics of integrin receptors with high selectivity as cells engage to a substrate (Figure 2.1). As a proof-of-concept, we target the a_Vb_3 integrins using high affinity peptides, because integrins are the primary molecules to sustain large tensile loads supporting cell adhesion and cell migration.[15] The AuNP MTFM sensor utilizes a calibrated NSET response to determine the molecular extension of an entropic polymer "spring"[16] anchored to the AuNP scaffold. This distance information is then used to infer the corresponding molecular tension. Thus, this probe provides the first reversible nanoparticle mechanosensor for imaging integrin molecular tension.

2.2 Results and discussion

2.2.1 Synthesis and characterization of the MTFM probes

Figure 2.1 describes the AuNP-MTFM approach. To synthesize the ligand (Appendix, Figure A2.1), cyclic Arg-Gly-Asp-dPhe-Lys-(Cys) peptide (cRGDfK(C)) was first modified with an NHS-azide in high yield (>90%). This afforded the orthogonal reactive thiol and azide groups for further modification. Maleimide-Alexa488 dye and alkyne-terminated polyethylene glycol (PEG, MW 3400) were further coupled to the thiol and azide, respectively. The purity of the final product was confirmed by HPLC and MALDI-TOF MS (Appendix, Figure A2.2). The mass distribution of the PEG polymer indicated a contour length of 28.0 ± 2.5 nm, assuming a monomer length value of 0.35

nm.[17] Based on the Worm-like Chain (WLC) model for force-induced molecular extension,[18] the fluorophore should rest at 4.9 ± 0.2 nm from the AuNP surface at low packing density (< 29 molecules/AuNP), and can be extended up to ~28 nm away from the gold surface. Thus, the sensor should generate a 10-fold increase in fluorescence signal, if subjected to sufficient tension.

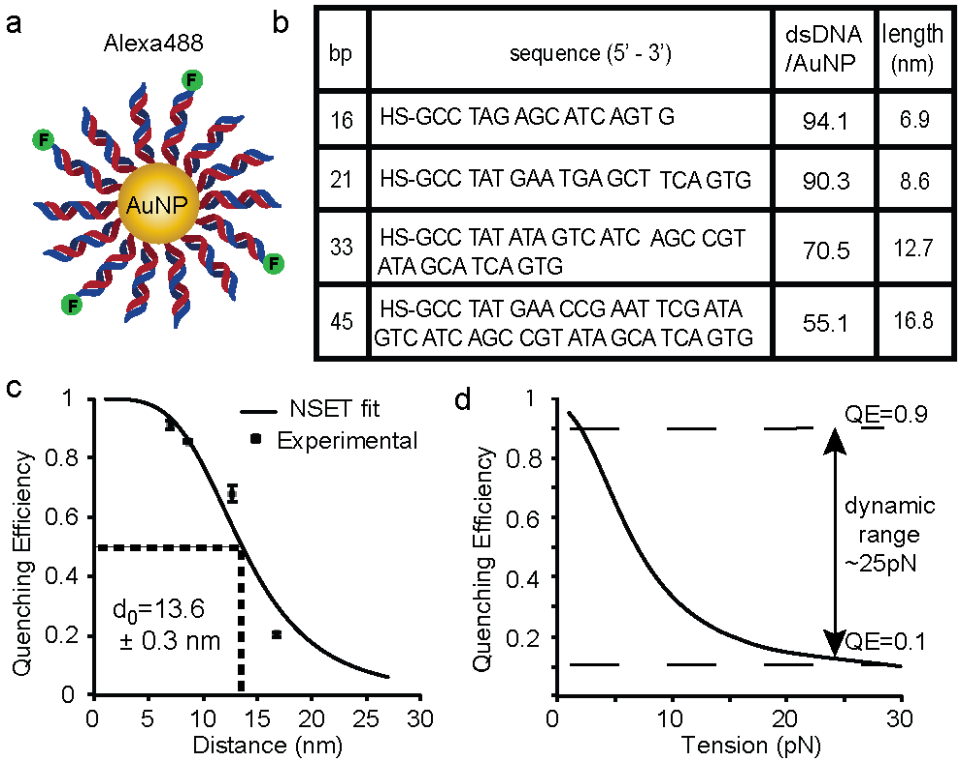

bp	sequence (5' - 3')	dsDNA /AuNP	length (nm)
16	HS-GCC TAG AGC ATC AGT G	94.1	6.9
21	HS-GCC TAT GAA TGA GCT TCA GTG	90.3	8.6
33	HS-GCC TAT ATA GTC ATC AGC CGT ATA GCA TCA GTG	70.5	12.7
45	HS-GCC TAT GAA CCG AAT TCG ATA GTC ATC AGC CGT ATA GCA TCA GTG	55.1	16.8

Figure 2.2 NSET calibration. (a) To determine d_0, particles were functionalized with a binary mixture of 1:9 labeled:unlabeled dsDNA. (b) Table showing the DNA sequences used, their measured density, and predicted lengths. (c) Plot showing the quenching efficiency as a function of distance from the AuNP surface. The data was fitted to the NSET model and d_0 was determined to be 13.6 ± 0.3 nm. (d) A theoretical force-quenching efficiency plot based on combining the WLC and NSET models. The force dynamic range corresponds to quenching efficiency ranging from 0.9 to 0.1.

To quantify the distance between the Alexa488 dye and AuNP surface, we measured the d_0 (distance at which the quenching efficiency = 0.5) by using highly packed duplex DNA as a molecular ruler. Briefly, a series of DNA duplexes conjugated

with 5'Alexa488 at the terminus of one strand and a 5' thiol at the terminus of the complementary strand were immobilized to the AuNP surface while the salt concentration was titrated to 0.3 M NaCl (Figure 2.2a-b). To minimize self-quenching, the dye labeled DNA duplex was diluted in a 1:9 ratio using identical duplexes that lacked the 5' fluorophore. We used the OliGreen assay and the calibrated fluorescence intensity to provide two independent methods to determine the DNA loading number per particle, which is reported in Figure 2.2b and Table A2.1.[19] These values suggest that the duplexes present orientations perpendicular to the gold surface.[20] We then measured the fluorescence intensity of the four AuNP-dsDNA-Alexa488 conjugates before and after dissolution of the AuNP. The quenching efficiency of triplicate AuNP samples was plotted as a function of distance and fitted to the NSET equation (Figure 2.2c), providing a d_0 of 13.6 ± 0.3 nm. This value is in agreement with literature precedents that reported d_0 of 10.4 nm and 15.7 nm for 10 nm AuNPs displaying Atto647, and Cy3, respectively.[12, 21] Importantly, we can combine this calibrated NSET equation and the WLC relation, which has been experimentally and theoretically validated for PEG, to generate a theoretical curve depicting quenching efficiency as a function of applied tension (Figure 2.2d). Based on this plot, the quenching efficiency decreases from 0.9 to 0.1 when a force of 25 pN is applied, affording a wider dynamic range than our reported FRET-based PEG tension sensor,[2] and a 5- to 10-fold improvement in signal-to-background when compared to the genetically encoded spider-silk tension sensors construct.[1, 3]

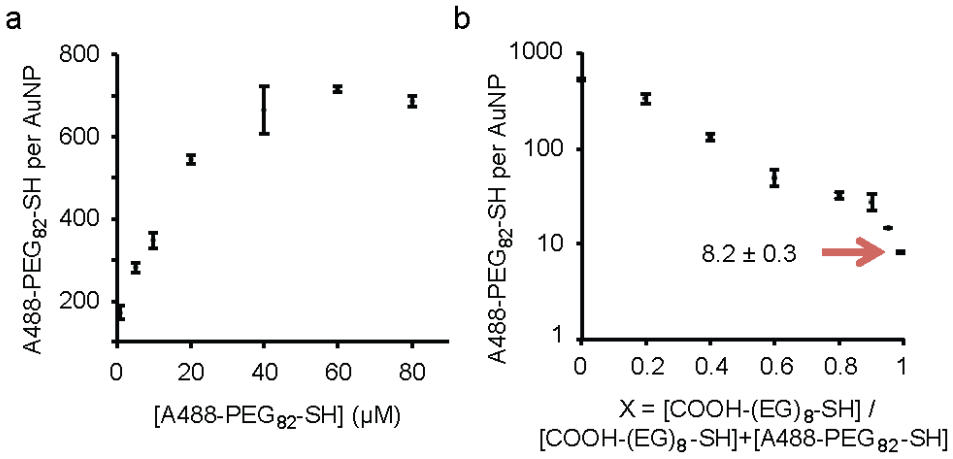

Figure 2.3 PEG conformation on AuNP surface. Plot of A488-PEG_{82}-SH loading as a function of incubation with single ligand (a), and binary mixture of ligands of A488-PEG_{82}-SH and COOH-EG_8-SH (b). The total ligand concentration was maintained at 40 μM, and the ratio was varied from 0 to 0.99.

Given that the ligand density dictates its conformation on the AuNP surface,[22] and consequently influences sensor response, we quantified the density of the ligand as function of its incubation concentration. We found that the number of surface bound ligands per AuNP ranges from 700-100 when the ligand concentration was varied from 80 mM to 1 mM (Figure 2.3a). To passivate the bare gold surface and increase particle stability, we introduced other competing thiolated ethylene glycol molecules to form binary PEG coated AuNPs. Among these, we found that COOH-EG_8-SH to be advantageous due to increased particle stability. The dual PEG modification strategy offered significant improvement in controlling the number of ligand molecules per particle, especially at low ligand densities, eg. 1-10 ligands per NP (Figure 2.3b). This ensured that the polymers adopt their predicted Flory radius of 4.9 nm, thus maintaining the relaxed mushroom conformation and generating a more reproducible response.[17]

We next verified the conformation of the polymer for particles displaying 8.2 ± 0.3 Alexa488-PEG_{82}-SH per NP. Using the measured d_0 of 13.6 nm, the quenching efficiency

data (Appendix, Figure A2.3) indicated that the dye was 8.4 nm from the NP surface. This distance is in general agreement with the predicted dye-AuNP distance of 7.4 nm, which is the sum of the expected contour length of COOH-EG_8-SH (2.8 nm),[23] and the Flory radius of the partially crowded Alexa488-PEG_{82}-SH (4.6 nm). We further verified the PEG conformation using negative staining TEM of samples with different surface loading densities (Appendix, Figure A2.4).

2.2.2 Immobilization and characterization of the AuNP-MTFM sensors on glass substrate

Typically, AuNPs are immobilized to a substrate using primary amines or thiols, which provide sufficient binding for most chemical sensing applications. However, to measure molecular forces, we needed to irreversibly immobilize AuNP conjugates, such that particles would not translocate in response to external tension (Appendix, Figure A2.5). Therefore, we used lipoic acid ligands to provide strong affinity to the gold surface due to multivalent binding.[24] Moreover, this method allowed immobilization of AuNP-based MTFM sensors within a few minutes, thus minimizing the aggregation due to extended incubation times. To generate these surfaces, amine-functionalized substrates were reacted with a mixture of 5% w/v mPEG-NHS (MW 2000) and 0.5% w/v lipoic acid-PEG-NHS (MW 3400) in 0.1 M sodium bicarbonate buffer, overnight. AFM was then used to determine the surface density of anchored AuNPs (Figure 2.4a), and showed that the average inter-particle distance was ~110 nm. Although particle spacing was disordered across the substrate, this type of packing is known to allow cell focal adhesion formation.[25]

2.2.3 Live-cell imaging of integrin-mediated forces

To image the tension exerted by living cells, human breast cancer cells (HCC 1143) were plated onto the AuNP sensor modified glass surfaces for 1 hour to allow the cells to form adhesions. To minimize auto-fluorescence and maximize the signal to background ratio, we performed total internal reflection fluorescence microscopy (TIRFM) using a laser coupled inverted microscope. At the resting state, we observed relatively low and uniform background fluorescence intensity (Appendix, Figure A2.5c). After cells adhered and polarized on the surface, we used brightfield (Figure 2.4b) and reflection interference contrast microscopy (RICM, Figure 2.4c) to observe the binding between the cell and the surface. In the AuNP-MTFM channel (TIRF 488), we observed a strong fluorescence intensity increase (up to 7 fold over background) (Fig. 3d) that was strongly associated with the cell-binding pattern in RICM (Figure 2.4c). The signal to background ratio at the brightest spots of the image was ~20, which allowed direct and facile identification of areas of high tension. In some local regions, rod-like contact patterns formed (Figure 2.4d-f, red arrow, inset) suggesting the formation of mature focal adhesions.[26] Using the bulk quenching efficiency values, and the NSET model, we first determined the average PEG extension at each pixel of the image (Appendix, Figure A2.6). Next, the WLC model was used to estimate the minimum ensemble tension exerted at each sensor ligand, thus providing a tension map (Figure 2.4f). While a number of techniques such as traction force microscopy and PDMS post arrays have been used to measure cell forces, our method detects pN tension, thus representing a 3-order of magnitude sensitivity improvement, and is exclusive to RGD-binding receptor molecules. The temporal and spatial resolution of MTFM are not different from standard fluorescence microscopy

techniques, which exceed that of traction force microscopy, and especially if combined with super-resolution imaging or single molecule imaging approaches.[27]

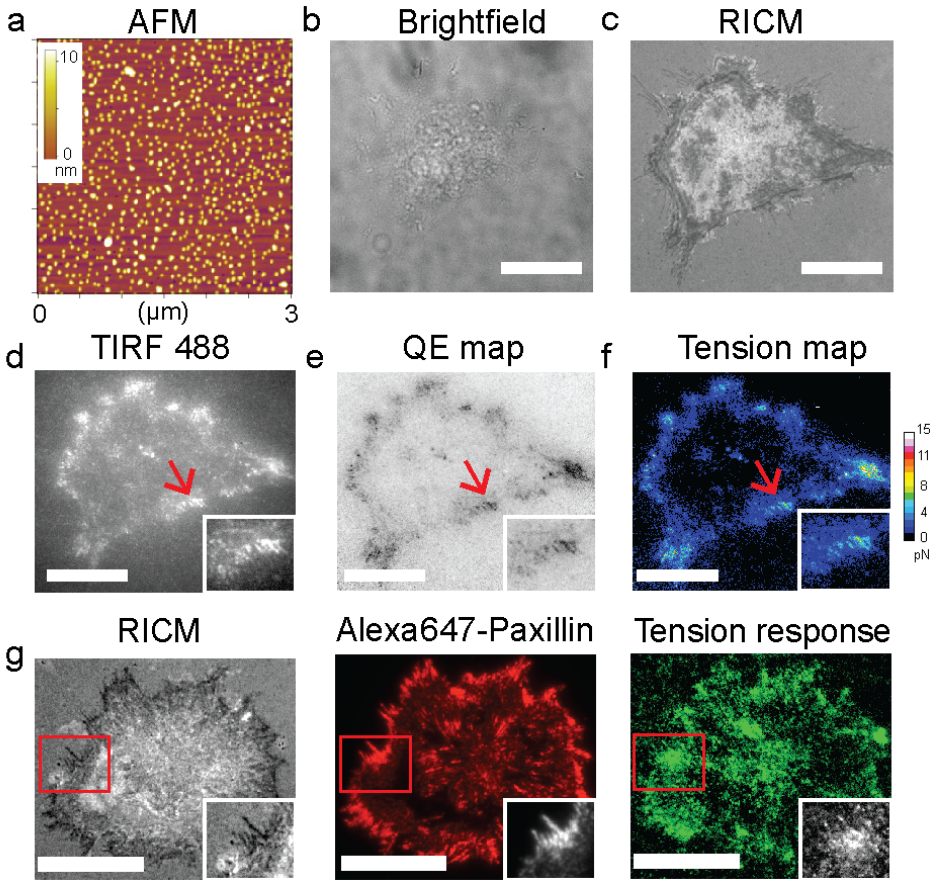

Figure 2.4 Mechano-imaging of integrins in live cell. (a) AFM image showing the typical AuNP sensor distribution. After 1 hr of cell culture on the sensor surface, the brightfield (b) and RICM image (c) were captured to visualize cell adhesion. RICM (c) clearly revealed the adhesion sites (dark region) mostly at the edge of the cell. (d) TIRF image (500 ms acquisition time) of the same cell shown in (b-c). The raw fluorescence data was converted to a quenching efficiency map using bulk quenching efficiency of AuNP sensor. A force map was then calculated using the WLC model. Inset shows rod-like focal adhesions with a high level of force. Scale bar, 20 μm. (g) Representative images showing that paxillin colocalizes with tension signals within focal adhesions. Scale bar, 15 μm.

To validate that the tension signal is due to specific focal adhesion complexes, cells were cultured onto passivated PEG-only surfaces or non-sensing AuNP conjugate surfaces. Minimal cell attachment was observed under our experimental conditions, thus

showing specificity of RGD binding (Appendix, Figure A2.6). In another experiment, we treated the cells on AuNP-MTFM sensor surfaces with 25 μM latrunculin B (LatB), which inhibits actin polymerization, and thus prevents force generation (Appendix, Figure A2.8). After 10 min of treatment with LatB, the increased fluorescence completely dissipated and returned to background levels for all observed cells. In addition, we immunostained for paxillin, a marker of focal adhesions (see Methods in SI). Figure 2.4g shows a high degree of overlap between the AuNP-MTFM response and the paxillin-staining. Note that the tension signal significantly weakens once cells are fixed, likely due to nm scale cytoskeletal and PEG relaxation. Taken together, these experiments clearly show that the reversible fluorescence response is due to mechanical tension exerted by integrins the MTFM sensor.

2.2.4 Visualization of integrin forces initial and mature focal adhesions

To demonstrate dynamic imaging capabilities, we collected time-lapse images of a cell as it contacted a substrate and initiated focal adhesion formation (Figure 2.5). The tension signal rapidly translocated from the center of the cell to its periphery over the span of 10 min. This is the first direct evidence showing the presence of integrin tension during initial cell substrate contact, which was previously inferred by ligand translocation.[28] In another time-lapse video, we captured the tension dynamics of the reverse event, as a cell underwent contraction and the high-tension regions at the cell periphery dissipated (Appendix, Figure A2.9). The alignments of tension signals are clearly perpendicular to the cell edge, corresponding to its distal orientation.[26] Finally, histogram analysis of force distribution within focal adhesions showed a mean tension of ~1.0 pN, which is in agreement with estimates from traction force microscopy and PDMS

post arrays (Appendix, Figure A2.10). Interestingly, some regions displayed tension values that are an order of magnitude greater than the average, which is compatible with integrin-RGD rupture forces measured using atomic force microscopy.[29]

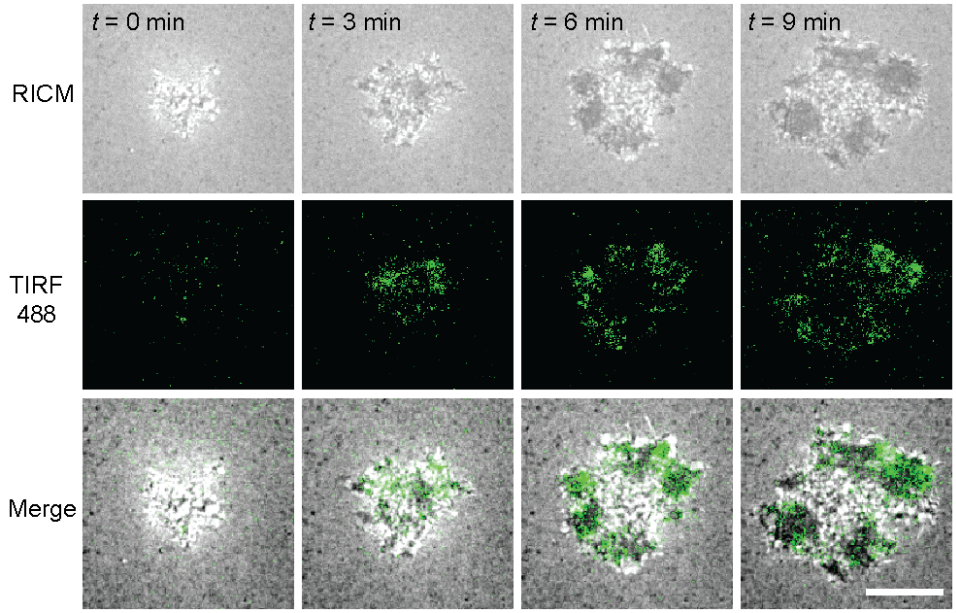

Figure 2.5 Initial tension dynamics during cell adhesion. Time-lapse images recording the first 10 min of cell-substrate interactions after the cell engaged the surface. Tension signal (TIRF 488 channel, 100 ms acquisition time) colocalized with cell binding locations as shown in the RICM channel. Scale bar, 15 μm.

2.3 Conclusion

In summary, we report the first nanoparticle-based molecular tension probe and use it to image the dynamics of integrin adhesions. We calibrated the NSET response and verified the sensor conformation on the AuNP surface. In principle, this sensor reports on molecular tension with a wider dynamic range than is fundamentally allowed by FRET-based methods. Note that the stability of the thiol gold bond exceeds that of integrin-RGD interaction, and thus the MTFM sensor is stable within our experimental conditions.[30] The measured ensemble integrin tension agrees with the expected average values, based on traction force microscopy, but we observe a wide distribution of tension

magnitudes within adhesions. Given that nanoparticles can be spatially patterned onto surfaces, this suggests that one may be able to readily investigate the role of ligand density and topology on force transmission. AuNPs can be also tracked using label-free methods, which should allow for dual force-localization studies in 3D.

2.4 Materials and methods

2.4.1 Materials

(3-Aminopropyl) trimethoxysilane (97%, APTMS), O-(2-carboxyethyl)-O′-(2-mercaptoethyl)heptaethylene glycol (95%, COOH-EG_8-SH), 2,5-dihydroxybenzoic acid (99%, DHB), triethylamine (99%, TEA), dithiothreitol (99.0%, DTT), triethylammonium acetate (TEAA), gold (III) chloride hydrate (99.0%), sodium citrate (99%), paraformaldehyde (95%, PFA), Hank's balanced salts (#H1387) and Triton X-100 were purchased from Sigma-Aldrich (St. Louis, MO) and used without further purification. The heterobifunctional linker azide-NHS (#88902) was purchased from Thermo Fisher Scientific (Rockford, IL). The fluorescent dyes Alexa488-maleimide and Alexa488-NHS, Alexa647 labeled IgG_1 secondary antibody as well as the OliGreen assay were purchased from Life Technologies (Carlsbad, CA). Number two glass coverslips, ascorbic acid (>99.0%), and 96-well plates were purchased from Fisher Chemical & Scientific (Pittsburg, PA). DMF (>99.5%), DMSO (99.5%) and sodium bicarbonate (99.0%) were purchased from EMD chemicals (Philadelphia, PA). Cyclic(RGDfK)C was custom synthesized by Peptides International (Louisville, KY). All DNA strands used were custom synthesized and desalted by Integrated DNA Technologies (Coralville, Iowa). Alkyne-PEG-SH (MW 3400), mPEG-NHS (MW 2000), and lipoic acid-PEG-NHS (MW 3400) were purchased from Nanocs (New York, NY). Amine-PEG-SH (MW 3400) was purchased from Creative PEGworks (Winston Salem, NC). $CuSO_4.5H_4O$ was purchased from Mallinckrodt (St. Louis, MO) and P4 gel size exclusion beads were acquired from Biorad (Hercules, CA). IgG1 paxillin-antibody was EMD Millipore (Billerica, MA). All

DI water was obtained from a Nanopure water purification system with a UV sterilization unit and showed a resistivity of 18.2 MW.

2.4.2 Synthesis of gold nanoparticles

Citrate-stabilized gold nanoparticles (AuNPs, 14.8 ± 0.8 nm) were prepared using published procedures. Briefly, a 500 mL solution of 1 mM hydrogen tetrachloroaurate (III) trihydrate was brought to a vigorous boil, and once boiling, 50 mL of a 38.8 mM sodium citrate tribasic dihydrate solution was added and allowed to reflux for 15 min. The reaction mixture was filtered using a 0.45 μm acetate filter, producing monodisperse AuNPs. The extinction spectrum of the AuNPs was determined using UV-vis spectrometry, and particle size was verified using transmission electron microscopy (TEM).

2.4.3 Negative staining TEM

The polyethylene glycol (PEG) modification of AuNPs was visualized by negative staining TEM. PEG molecules have poor contrast in conventional TEM due to their low electron density. Therefore, negative staining was used to enhance the contrast and identify the PEG shell surrounding the gold core. Specimens were prepared in DI water. The samples were deposited onto glow discharged 300 mesh carbon coated copper grids (Electron Microscopy Sciences). After a 30 seconds incubation period, excess liquid was wicked away and the specimens were stained with 1% methylamine tungstate (Ted Pella, Inc). Excess stain was wicked away after incubating it on the grid for 1 minute. The sample grids were subsequently dried under vacuum. TEM measurements were acquired on a Hitachi H-7500 transmission electron microscope at an accelerating voltage of 75 kV. The micrographs were recorded at magnifications of 200,000×.

2.4.4 Ensemble fluorescence measurement

The ensemble fluorescence emission intensity of Alexa488 dye from all AuNP conjugates was measured by using a Biotek Synergy HT plate reader at λ = 485 nm/528 nm excitation/emission. Each well in the 96-well plate (Fisher scientific) was filled to a volume of 100 µl. All measurements were performed in triplicate, and the reported error bars represent the standard deviation of these measurements.

2.4.5 HPLC

All PEG conjugated products were purified by using a C18 column (diameter: 4.6 mm; length: 250 mm) in a reverse phase binary pump HPLC that was coupled to a diode array detector (Agilent 1100).

2.4.6 MALDI-Mass Spectroscopy

A 10 mM solution of 2,5-dihydroxybenzoic acid (DHB) was prepared in tetrahydrofuran (THF) as the MALDI matrix and 0.1 M sodium chloride was added as cationization agent.[31] All products were also pre-dissolved in THF and then mixed with an equal volume of DHB matrix. 2 µl of this mixture was added to each well on the MALDI plate. After allowing the solution to dry for 20 min, the sample was analyzed by a high performance MALDI time-of-flight mass spectrometer (Voyager STR).

2.4.7 Optical Microscopy

Live cells were imaged in standard cell imaging buffer (Hank's balanced salt, pH 7.4, 10 mM HEPES without phenol red) at 37 °C, and fixed cells were imaged in 1% BSA in 1× PBS at room temperature. During imaging, physiological temperature was maintained with a warming apparatus consisting of a sample warmer and an objective warmer (Warner Instruments 641674D and 640375). The microscope was Nikon Eclipse Ti

driven by the Elements software package. The microscope features an Evolve electron multiplying charge coupled device (CCD; Photometrics), an Intensilight epifluorescence source (Nikon), a CFI Apo 100× (numerical aperture (NA) 1.49) objective (Nikon) and a TIRF launcher with two laser lines: 488 nm (10 mW) and 638 nm (20 mW). This microscope also includes the Nikon Perfect Focus System, an interferometry-based focus lock that allowed the capture of multipoint and time-lapse images without loss of focus. The microscope was equipped with the following Chroma filter cubes: TIRF 488, TIRF 640, FITC and reflection interference contrast microscopy (RICM).

2.4.8 AFM imaging

The density of AuNP tension sensor on the functionalized glass coverslip was measured by using an atomic force microscope mounted on an anti-vibration stage (Asylum Research, CA). Silicon AFM tips (MikroMasch) with a force constant (5.4-16 N/m) were used to image the sample in tapping mode at a scan rate of 1 Hz. All images were processed and rendered using IgorPro.

2.4.9 Cell culture

HCC1143 cells were cultured in RPMI 1640 medium (Mediatech) supplemented with 10% FBS (Mediatech), HEPES (9.9 mM, Sigma), sodium pyruvate (1 mM, Sigma), L-glutamine (2.1 mM, Mediatech), penicillin G (100 IU ml^{-1}, Mediatech) and streptomycin (100 μg ml^{-1}, Mediatech) and were incubated at 37 °C with 5% CO_2. Cells were passaged at 90–100% confluency and plated at a density of 50% using standard cell culture procedures. All experiments were conducted with HCC1143 cells that had been serum-starved for ~12 h.

2.4.10 Paxillin-immunostaining

Paxillin-immunostaining was used to image the location of mature focal adhesion sites at the cell membrane. After allowing HCC1143 cells to engage the surface, cells were fixed by incubation in 1 ml of 4% w/v paraformaldehyde [15] for 10 min. The PFA was subsequently rinsed off using 25 ml of 1 X PBS, and then cells were permeated by incubation with 0.1% (v/v) Triton X-100 for 5 min in PBS. The cells were then rinsed with 25 ml 1 X PBS, and then blocked for 1 hr using 1% w/v BSA. Note that the force signal gradually weakens as a function of time after fixation, and therefore, overnight blocking is not recommended. 10 μg/mL of primary IgG_1 anti-paxillin antibody was incubated for 1 hr and then rinsed using 25 ml of 1 X PBS. The cells were then incubated using an Alexa647 labeled secondary antibody (Life Technologies) for 1 hr. After thorough rinsing, TIRF microscopy was then immediately used to image paxillin.

2.4.11 Synthesis and quantification of dsDNA-AuNP for NSET calibration

5' Disulfide-modified oligonucleotides were custom synthesized by Integrated DNA Technologies (IDT). The disulfide group was reduced by incubation with 5 nmol of lyophilized oligonucleotide with 100 μL of disulfide cleavage buffer (0.1 M dithiothreitol (DTT), 170 mM phosphate buffer at pH 8.0) for 3 hr at room temperature. The reduced oligonucleotides were then purified using a NAP-5 column (GE Healthcare, Piscataway, NJ) using DI water as the eluent.

5' Amine-modified oligonucleotides were custom synthesized by IDT and used without further purification. 10 nmol of the oligonucleotide was reacted with 100 nmol of Alexa488-NHS ester dye in 1X PBS (pH 7.4) for 12 hr at room temperature. The product was subsequently purified by reverse phase HPLC (flow rate 1 ml/min, solvent A: 0.1M

DI TEAA, solvent B: 100% acetonitrile, initial condition was 10% B with a gradient of 1% per min). The final concentration was determined by using a Nanodrop spectrophotometer.

Equal amounts of 5'SH-DNA and 5' Alexa488-DNA were mixed together at ~25 μM concentrations in 1XPBS and hybridized by heating to 95 ºC for 5 min, then cooling at a rate of 3.3 °C/min over a period of 20 min. Afterwards, 8.7 μM of dsDNA was then added to 3.0 mL of 15 nm diameter gold nanoparticles (8.4 nM), bringing the concentration of oligonucleotide and gold nanoparticles to ~2.7 μM, and ~5.8 nM, respectively. The pH of the solution was adjusted to pH 7.4 by adding 296.3 μL of 100 mM phosphate buffer, thus bringing the phosphate buffer concentration to 9 mM. The particles were then stabilized by adding sodium dodecyl sulfate (SDS) to the solution and bringing its final concentration to 0.1% (g/mL) by using a stock solution of 10% SDS. The particles were successively salted with eight NaCl additions that were spaced 20 min apart using a stock solution of 2.0 M NaCl. The final NaCl concentration of the DNA-AuNP solution was increased to 0.3 M. The first NaCl addition increased the concentration to 0.05 M, while the remaining three NaCl additions increased the NaCl concentration by 0.1 M increments. The fully salted particles were then incubated overnight, in the dark and at room temperature. The following day, the particles were centrifuged five times and reconstituted in DI water for each wash.

The number of dsDNA loaded per AuNP was subsequently quantified using two independent assays, the commercial OliGreen assay kit, and by conventional fluorescence measurement using a calibration curve following KCN dissolution of the Au. In the table below, the results of these two assays are listed and compared. Based on the results of

these two measurements, the average number of dsDNA loaded per particle indicated a densely packed DNA surface.

2.5 References

1. Grashoff, C.; Hoffman, B. D.; Brenner, M. D.; Zhou, R.; Parsons, M.; Yang, M. T.; McLean, M. A.; Sligar, S. G.; Chen, C. S.; Ha, T., Measuring mechanical tension across vinculin reveals regulation of focal adhesion dynamics. *Nature* **2010,** *466* (7303), 263-266.

2. Stabley, D. R.; Jurchenko, C.; Marshall, S. S.; Salaita, K. S., Visualizing mechanical tension across membrane receptors with a fluorescent sensor. *Nature Methods* **2012,** *9* (1), 64-67.

3. Borghi, N.; Sorokina, M.; Shcherbakova, O. G.; Weis, W. I.; Pruitt, B. L.; Nelson, W. J.; Dunn, A. R., E-cadherin is under constitutive actomyosin-generated tension that is increased at cell–cell contacts upon externally applied stretch. *Proceedings of the National Academy of Sciences of the United States of America* **2012,** *109* (31), 12568-12573.

4. Caruso, M. M.; Davis, D. A.; Shen, Q.; Odom, S. A.; Sottos, N. R.; White, S. R.; Moore, J. S., Mechanically-Induced Chemical Changes in Polymeric Materials. *Chemical Reviews* **2009,** *109* (11), 5755-5798.

5. Kryger, M. J.; Munaretto, A. M.; Moore, J. S., Structure–Mechanochemical Activity Relationships for Cyclobutane Mechanophores. *Journal of the American Chemical Society* **2011,** *133* (46), 18992-18998.

6. Fink, J.; Carpi, N.; Betz, T.; Bétard, A.; Chebah, M.; Azioune, A.; Bornens, M.; Sykes, C.; Fetler, L.; Cuvelier, D., External forces control mitotic spindle positioning. *Nature cell biology* **2011,** *13* (7), 771-778.

7. Chicurel, M. E.; Singer, R. H.; Meyer, C. J.; Ingber, D. E., Integrin binding and mechanical tension induce movement of mRNA and ribosomes to focal adhesions. *Nature* **1998,** *392* (6677), 730-733.

8. Yin, H.; Wang, M. D.; Svoboda, K.; Landick, R.; Block, S. M.; Gelles, J., Transcription against an applied force. *Science* **1995,** *270* (5242), 1653-7.

9. Saha, K.; Agasti, S. S.; Kim, C.; Li, X.; Rotello, V. M., Gold Nanoparticles in Chemical and Biological Sensing. *Chemical Reviews* **2012,** *112* (5), 2739-2779.

10. Murphy, C. J.; Gole, A. M.; Stone, J. W.; Sisco, P. N.; Alkilany, A. M.; Goldsmith, E. C.; Baxter, S. C., Gold nanoparticles in biology: beyond toxicity to cellular imaging. *Accounts of Chemical Research* **2008,** *41* (12), 1721-1730.

11. Dubertret, B.; Calame, M.; Libchaber, A. J., Single-mismatch detection using gold-quenched fluorescent oligonucleotides. *Nat Biotech* **2001,** *19* (4), 365-370.

12. Chhabra, R.; Sharma, J.; Wang, H.; Zou, S.; Lin, S.; Yan, H.; Lindsay, S.; Liu, Y., Distance-dependent interactions between gold nanoparticles and fluorescent molecules with DNA as tunable spacers. *Nanotechnology* **2009,** *20* (48), 485201.

13. Yun, C.; Javier, A.; Jennings, T.; Fisher, M.; Hira, S.; Peterson, S.; Hopkins, B.; Reich, N.; Strouse, G., Nanometal surface energy transfer in optical rulers, breaking the FRET barrier. *Journal of the American Chemical Society* **2005,** *127* (9), 3115-3119.

14. Chen, Y.; O'Donoghue, M. B.; Huang, Y. F.; Kang, H.; Phillips, J. A.; Chen, X.; Estevez, M. C.; Yang, C. J.; Tan, W., A surface energy transfer nanoruler for measuring binding site distances on live cell surfaces. *Journal of the American Chemical Society* **2010,** *132* (46), 16559-16570.

15. Pfaff, M.; Tangemann, K.; Müller, B.; Gurrath, M.; Müller, G.; Kessler, H.; Timpl, R.; Engel, J., Selective recognition of cyclic RGD peptides of NMR defined conformation by alpha IIb beta 3, alpha V beta 3, and alpha 5 beta 1 integrins. *Journal of Biological Chemistry* **1994,** *269* (32), 20233-20238.

16. Shroff, H.; Reinhard, B. M.; Siu, M.; Agarwal, H.; Spakowitz, A.; Liphardt, J., Biocompatible Force Sensor with Optical Readout and Dimensions of 6 nm3. *Nano Letters* **2005,** *5* (7), 1509-1514.

17. De Gennes, P., Conformations of polymers attached to an interface. *Macromolecules* **1980,** *13* (5), 1069-1075.

18. Bouchiat, C.; Wang, M.; Allemand, J. F.; Strick, T.; Block, S.; Croquette, V., Estimating the persistence length of a worm-like chain molecule from force-extension measurements. *Biophysical Journal* **1999,** *76* (1), 409-413.

19. Yehl, K.; Joshi, J. P.; Greene, B. L.; Dyer, R. B.; Nahta, R.; Salaita, K., Catalytic Deoxyribozyme-Modified Nanoparticles for RNAi-Independent Gene Regulation. *ACS nano* **2012,** *6* (10), 9150-9157.

20. Dulkeith, E.; Ringler, M.; Klar, T.; Feldmann, J.; Javier, A. M.; Parak, W., Gold nanoparticles quench fluorescence by phase induced radiative rate suppression. *Nano Letters* **2005,** *5* (4), 585-589.

21. Acuna, G. P.; Bucher, M.; Stein, I. H.; Steinhauer, C.; Kuzyk, A.; Holzmeister, P.; Schreiber, R.; Moroz, A.; Stefani, F. D.; Liedl, T.; Simmel, F. C.; Tinnefeld, P., Distance Dependence of Single-Fluorophore Quenching by Gold Nanoparticles Studied on DNA Origami. *ACS nano* **2012,** *6* (4), 3189-3195.

22. Levin, C. S.; Bishnoi, S. W.; Grady, N. K.; Halas, N. J., Determining the conformation of thiolated poly (ethylene glycol) on Au nanoshells by surface-enhanced Raman scattering spectroscopic assay. *Analytical Chemistry* **2006,** *78* (10), 3277-3281.

23. Harder, P.; Grunze, M.; Dahint, R.; Whitesides, G.; Laibinis, P., Molecular conformation in oligo (ethylene glycol)-terminated self-assembled monolayers on gold and silver surfaces determines their ability to resist protein adsorption. *Journal of Physical Chemistry B* **1998,** *102* (2), 426-436.

24. Mei, B. C.; Susumu, K.; Medintz, I. L.; Mattoussi, H., Polyethylene glycol-based bidentate ligands to enhance quantum dot and gold nanoparticle stability in biological media. *Nature Protocols* **2009,** *4* (3), 412-423.

25. Huang, J.; Gräter, S. V.; Corbellini, F.; Rinck-Jahnke, S.; Bock, E.; Kemkemer, R.; Kessler, H.; Ding, J.; Spatz, J. P., Impact of order and disorder in RGD nanopatterns on cell adhesion. *Nano Letters* **2009,** *9* (3), 1111-1116.

26. Gardel, M. L.; Schneider, I. C.; Aratyn-Schaus, Y.; Waterman, C. M., Mechanical integration of actin and adhesion dynamics in cell migration. *Annual Review of Cell and Developmental Biology* **2010,** *26*, 315-333.

27. Muzzey, D.; van Oudenaarden, A., Quantitative Time-Lapse Fluorescence Microscopy in Single Cells. *Annual Review of Cell and Developmental Biology* **2009,** *25* (1), 301-327.

28. Yu, C.; Law, J. B. K.; Suryana, M.; Low, H. Y.; Sheetz, M. P., Early integrin binding to Arg-Gly-Asp peptide activates actin polymerization and contractile movement that stimulates outward translocation. *Proceedings of the National Academy of Sciences of the United States of America* **2011,** *108* (51), 20585-20590.

29. Lehenkari, P. P.; Horton, M. A., Single Integrin Molecule Adhesion Forces in Intact Cells Measured by Atomic Force Microscopy. *Biochemical and Biophysical Research Communications* **1999,** *259* (3), 645-650.

30. Grandbois, M.; Beyer, M.; Rief, M.; Clausen-Schaumann, H.; Gaub, H. E., How Strong Is a Covalent Bond? *Science* **1999,** *283* (5408), 1727-1730.

31. Pasch, H.; Schrepp, W., *MALDI-TOF mass spectrometry of synthetic polymers*. Springer: 2003.

32. Dulkeith, E.; Morteani, A.; Niedereichholz, T.; Klar, T.; Feldmann, J.; Levi, S.; Van Veggel, F.; Reinhoudt, D.; Möller, M.; Gittins, D., Fluorescence quenching of dye molecules near gold nanoparticles: radiative and nonradiative effects. *Physical review letters* **2002,** *89* (20), 203002.

33. Staros, J. V.; Bayley, H.; Standring, D. N.; Knowles, J. R., Reduction of aryl azides by thiols: implications for the use of photoaffinity reagents. *Biochemical and biophysical research communications* **1978,** *80* (3), 568.

34. Chen, Y.; Kamlet, A. S.; Steinman, J. B.; Liu, D. R., A biomolecule-compatible visible-light-induced azide reduction from a DNA-encoded reaction-discovery system. *Nature chemistry* **2011,** *3* (2), 146-153.

2.6 Appendix

DNA duplex length	16 bp	21 bp	33 bp	45 bp
Number of dsDNA/AuNP using the OliGreen assay	93.3 ± 3.7	86.6 ± 4.5	60.0 ± 2.2	53.3 ± 3.9
Number of dsDNA/AuNP using Alexa488 fluorescence	95.0 ± 1.3	94.3 ± 0.5	81.2 ± 0.8	57.0 ± 0.8
Average	94.1	90.3	70.5	55.1

Table A2.1 Determination of dsDNA loading per AuNP using OliGreen assay and standard Alexa488 fluorescence calibration curve assay.

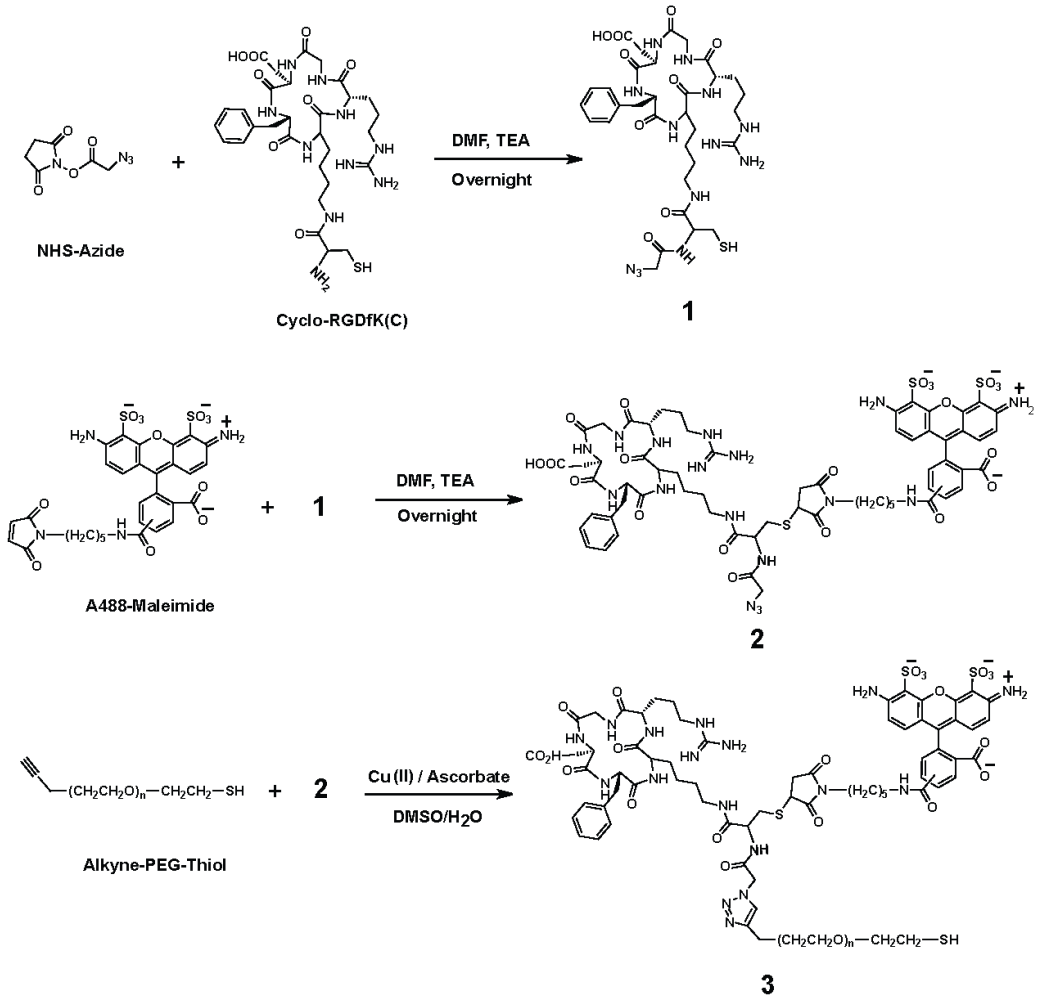

Figure A2.1 Synthesis of tension sensor ligand

Synthesis of **1**. 200 μg of cRGDfK(C) peptide (MW: 706.81) was reacted with 0.1 mg azide-NHS linker (MW: 198.14) in 15 μL DMF. To this reaction mixture, 0.1 μL of neat triethylamine [32] was added as an organic base and the reaction was allowed to proceed for 12 hr. The product, **1**, of this reaction was purified by reverse phase HPLC (flow rate 1 ml/min; solvent A: 99.5% DI water, 0.5% TFA; solvent B: 99.5% acetonitrile 0.5% TFA; initial condition was 10% B with a gradient of 1% per min). The yield of the reaction was determined to be 49% by integrating the HPLC peaks. Note that the yield was low due to the formation of dimer products formed by oxidation of the thiol. Although 0.1 M dithiothreitol (DTT) treatment of the oxidized product **1** minimized dimer formation, DTT was found to inadvertently reduce the azide group to an amine group.[33-34] Thus, the (cRGDfK)C starting peptide was typically pre-treated with 0.1 M DTT before use in order to minimize the dimer starting material.

Synthesis of **2**. A 10-fold molar excess of maleimide-Alexa488 dye in 10 μL DMF was mixed with purified **1** (~1-10 mM) and 0.1 μL of neat TEA overnight. The product of this reaction, **2**, was subsequently purified by HPLC using the same method that was described for purification of **1**. The molecular weight of the product was measured using MALDI-TOF as 1493 m/z, which was consistent with a calculated m/z of 1501. The concentration of purified product **2** was determined by UV-vis absorbance of Alexa488 dye and the sample was then dried in a Speedvac for 6 hr.

Synthesis of **3**. A 0.7 molar ratio of alkyne-PEG-SH (~1 mM) to **2** was dissolved in 10 μL DMSO and 5 μL DI water. 2 μL of 2 M TEAA buffer and 2 μL of 5 mM ascorbic acid was then added to this solution. Finally, 1 μL of $Cu(II)SO_4$ was added to the solution and vortexed. The reaction was incubated overnight at room temperature with foil to protect from ambient light. The reaction mixture was then treated with 0.1 M DTT in phosphate buffer for 1 hr to reduce disulfides that formed overnight. Afterwards, size exclusion chromatography was performed with a spin column (cutoff: 4000 MW) to remove all other by-products except the final product **3.** HPLC (method was the same as the one used for **1** and **2**), and MALDI-TOF were used to confirm the synthesis of **3** with a near 99% purity, which was based on HPLC peak integration.

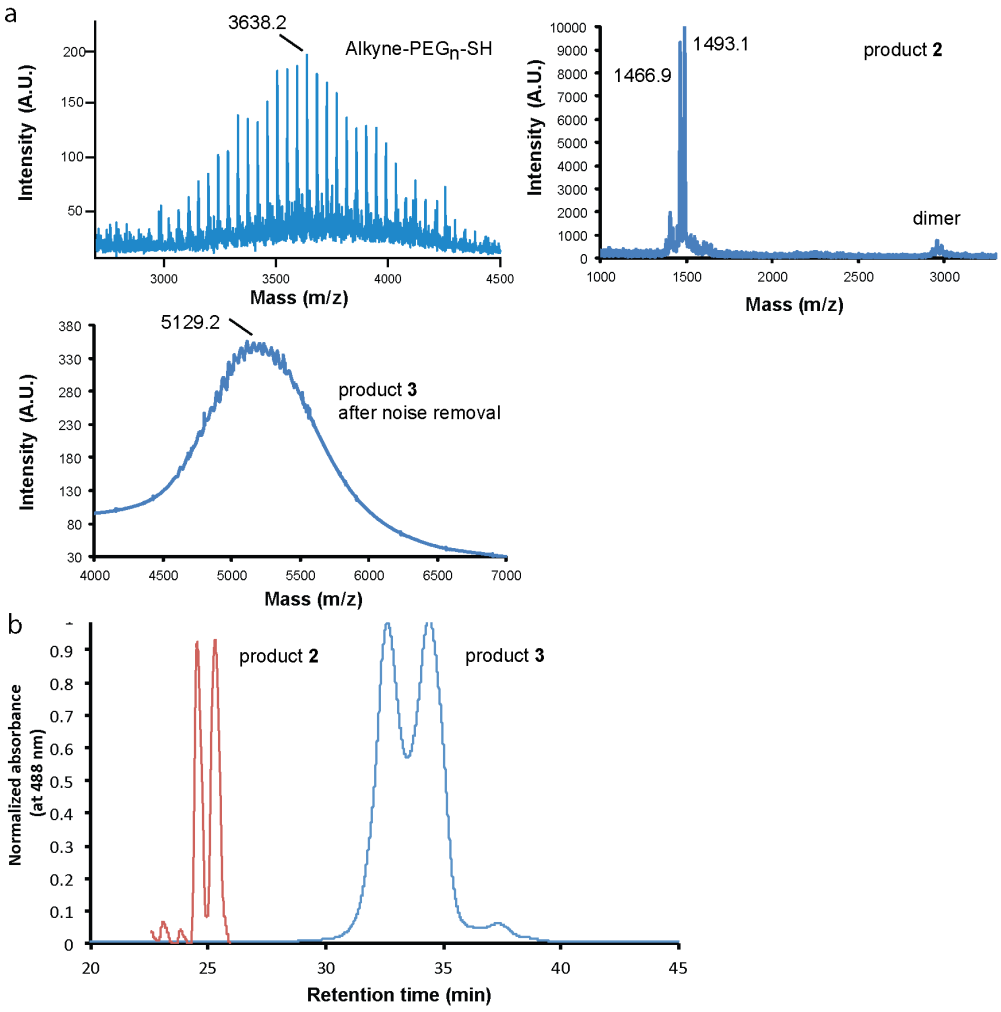

Figure A2.2 HPLC and MALDI characterization. (a) MALDI-TOF mass spectra for alkyne-PEG-SH and Alexa488-RGD-azide **2** and final sensor ligand **3**. (b) HPLC purification of **2** and **3**.

The mass of the alkyne-PEG$_n$-SH reagent was obtained using MALDI-TOF, and found to be polydisperse with a maximum intensity at 3638.2 m/z (Figure A2.2a). In the mass spectrum of the PEG polymer, we observed peak to peak spacings of 44 m/z, corresponding to the mass of one ethylene glycol monomer. Using this value, we determined the average number of the monomers in this PEG molecule to be 80, after subtracting the mass of the alkyne and thiol functional groups along with one sodium ion.[31] The FWHM of the mass peak was determined to be 14, which indicates a standard deviation in the number of monomers corresponding to 80±7 ethylene glycol units per polymer. The mass of **3** was measured at 5129.2 m/z. The difference between the mass of **2** and **3** is 3636.1 m/z, which agrees with the average mass of the alkyne-PEG$_{80}$-SH starting material (Figure A2.2a). In the mass spectrum of product **2**, the peak at 1493.1 is

the product peak, while the peak at 1466.9 is equal to the molecular ion peak minus the mass of N_2. The loss of N_2 from the azide is likely due to the MALDI laser excitation.

Importantly, the HPLC chromatograph of **2** and **3** shows a significant shift in the retention times. This is due to the conjugation with alkyne-PEG_{80}-SH, which markedly increase the molecular weight of the product. Moreover, the doublet in the chromatograph of **2** and **3** is likely due to the isomers of the maleimide group in Alexa488 dye molecule.

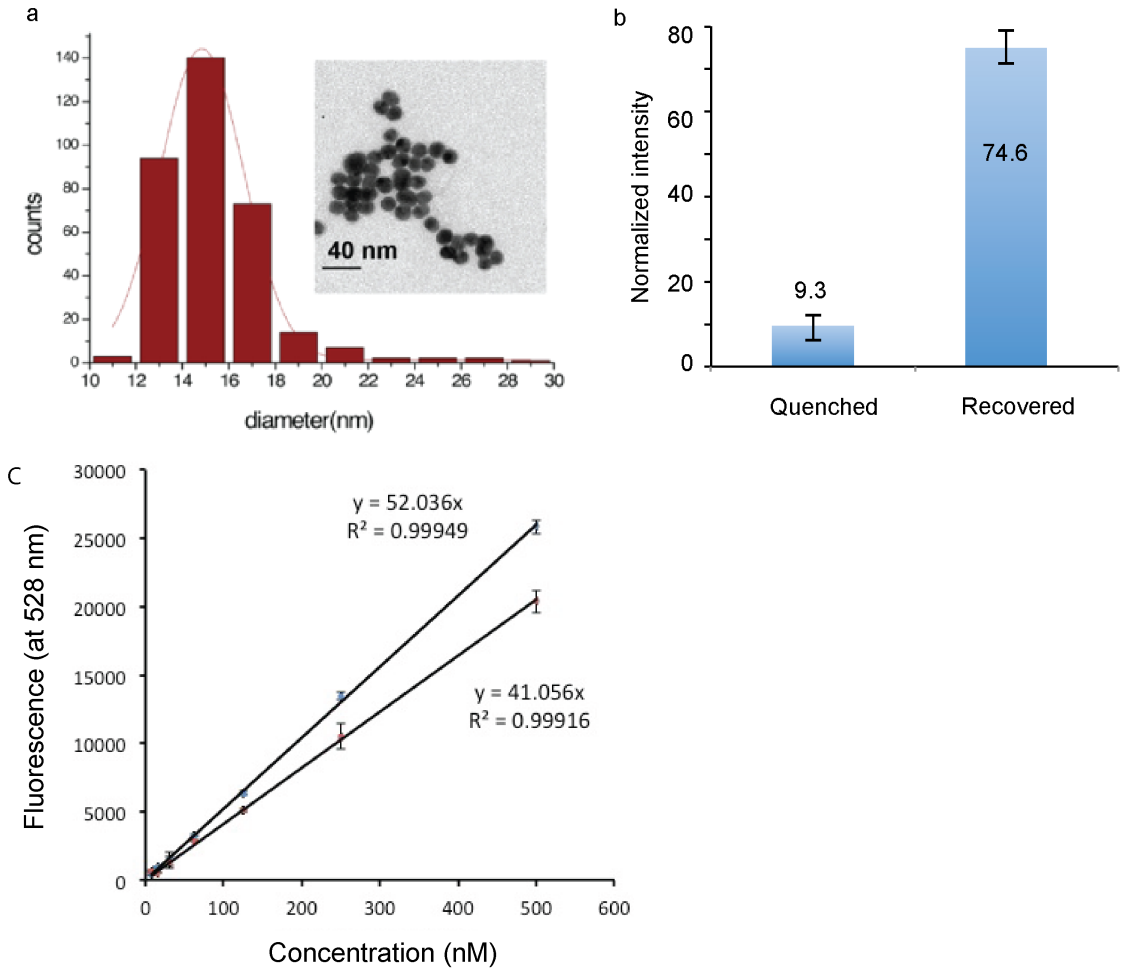

Figure A2.3 Characterization of gold nanoparticles. (a) Histogram showing the diameter distribution of AuNPs as measured by TEM. (b) The normalized fluorescence intensity of AuNP tension sensors before and after 50 mM KCN treatment. (c) Plot showing a fluorescence calibration curve of Alexa 488 in the presence of 50 mM KCN (blue) and in the presence of 2 nM AuNPs (red).

A 4.1 nM solution of citrate-stabilized AuNPs (15 nm) was incubated with 39.6 μM of COOH-EG_8-SH and 0.4 μM of tension sensor ligand (**3**) to form AuNP-sensor. After 12 hr of incubation at room temperature, the AuNP-sensors were purified from excess of unbound ligands by using six rounds of centrifugation (13500 rpm, 25 min each) and washing with DI water.

To determine the quenching efficiency of Alexa488 in **3** by the AuNP, we measured the fluorescence intensity from these nanoparticle conjugates before and after treatment with 50 mM KCN.

Two corrections were applied to ensure the validity of this assay. The first was to account for KCN-induced quenching of Alexa488. The first calibration curve was generated by addition of 50 mM KCN to a range of Alexa488 solutions. This calibration

plot is shown in Figure A2.3(c). The second type of correction accounted for the AuNP filter effect, since AuNPs will block some of the fluorescence excitation source at λ = 490 nm. To measure the filter effect, we doped 2 nM of COOH-EG_8-SH modified AuNP to a series of Alexa488 solutions. By comparing the slope shift, we calculated the filter effect to be 1.3.

Based on this analysis, we determined that the experimental quenching efficiency to be 87.5% for Alexa 488.

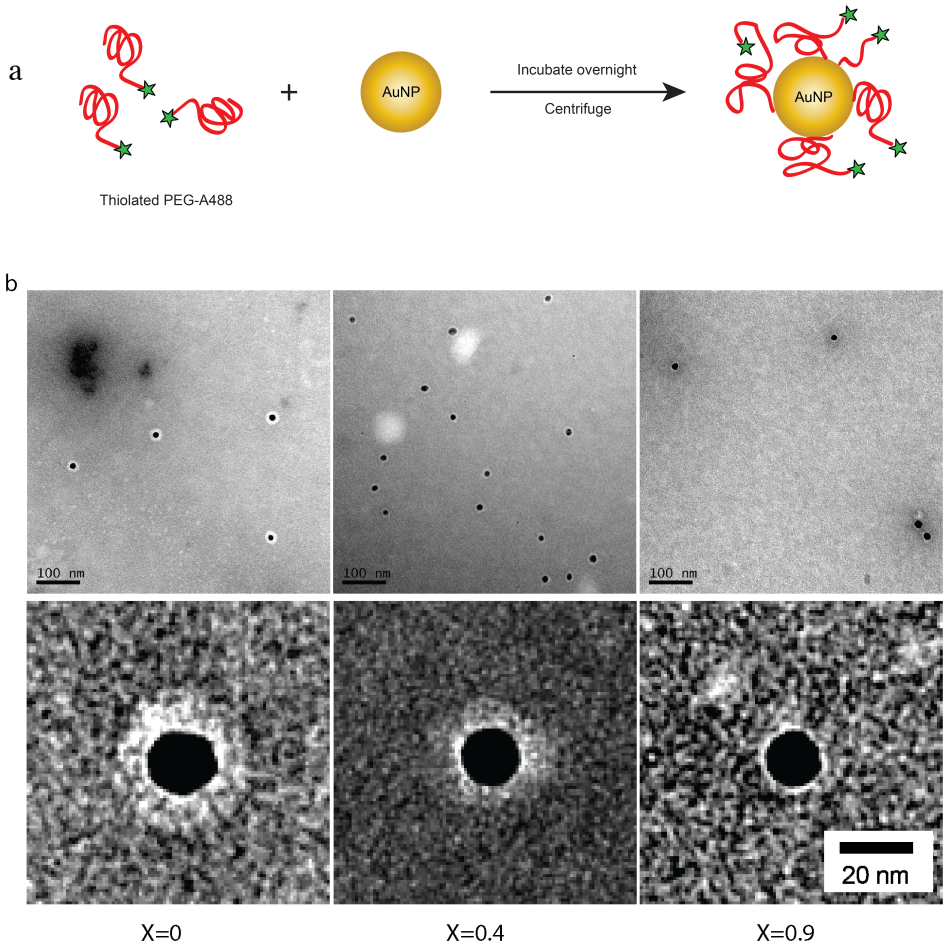

Figure A2.4 Synthesis of AuNP-PEG-Alexa488 for PEG conformation study. (a) Scheme showing the steps in AuNP conjugate synthesis. (b) Representative negative staining TEM micrographs of particles with X from 0 to 0.9, indicating the effect of polymer density on PEG conformation (Upper, raw image; lower, zoom in image).

10 mM of amine-PEG_{82}-thiol was mixed with 30 mM Alexa488-NHS ester in DMF with 0.1 µl TEA. The reaction was carried out for 12 hr and followed by size exclusion chromatography with a 4000 MW cutoff (P4 gel). The purity of the final product was confirmed by HPLC to be 98%. A series of SH-PEG-A488 solutions ranging in concentration from 1 to 80 µM were then mixed with a 4.1 nM solution of citrate-capped AuNPs for 12 hr (see Figure 2.3). After purification by six rounds of centrifugation and washing, we performed negative staining TEM to analyze each of these samples.

To generate the plot in main Figure 2.3B, we used a binary PEG system to modify the particles. In these experiments, the total PEG concentration was maintained at 40 µM and the ratio between the COOH-EG_8-SH and A488-PEG_{82}-SH was varied from 0 to 0.99. Also, negative stain TEM was performed to verify the molecular conformation of the PEG_{82} as it transitions from mushroom to brush (see Figure A2.4b).

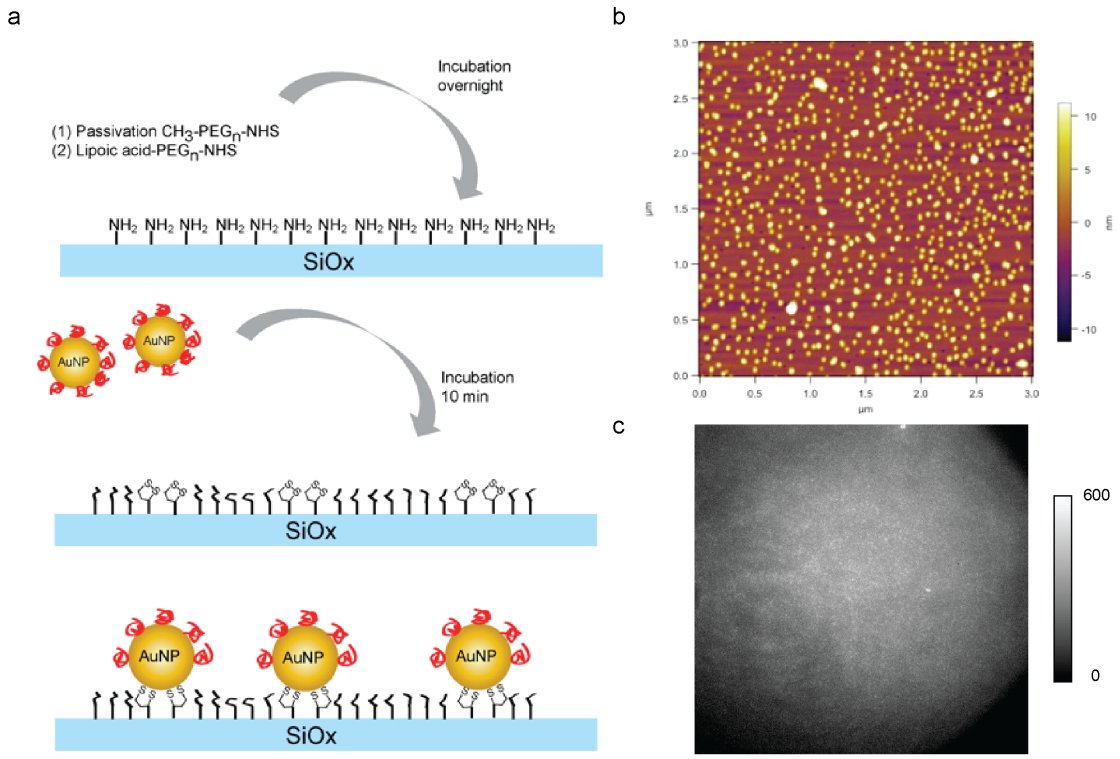

Figure A2.5 Substrate modification with densely packed AuNP sensors. (a) Scheme showing the reaction scheme used in the modification of the substrate. (b) Representative AFM showing AuNP-sensor distribution on substrate. (c) An average image of 10 quenched fluorescence images of AuNP-sensor modified surface without cells.

To functionalize the slides with the amine group, No.2 glass coverslips were cleaned with DI water twice, sonicated in DI water, and then sonicated with acetone for 15 min. The cleaned slides were then dried under a stream of high purity N_2. Fresh piranha solution (7:3 v/v = H_2SO_4: H_2O_2) was mixed and then used to clean the substrates for 15 min. Afterwards, the substrates were rinsed with copious amount of DI water. The substrates were then sonicated in acetone to remove excess water and to further clean the substrate. Subsequently, 1% v/v APTMS solution in acetone was added to the slides and incubated for 2 hr.

The slides were then thermally annealed for 4 hr at 80 °C. The surface was then passivated with 5% w/v mPEG-NHS (MW 2000) and 0.5% w/v lipoic acid-PEG (MW 3400) in 200 μL of 0.1 M fresh sodium bicarbonate solution. After overnight incubation at 4 °C, the excess unreacted PEG molecules were rinsed with DI water. This strategy affords a glass surface with sufficient lipoic acid groups to irreversible anchor AuNP MTFM sensors. Finally, 2 nM of AuNP-sensor solution was incubated for 10 min and then rinsed with DI water to remove nonspecifically bound particles.

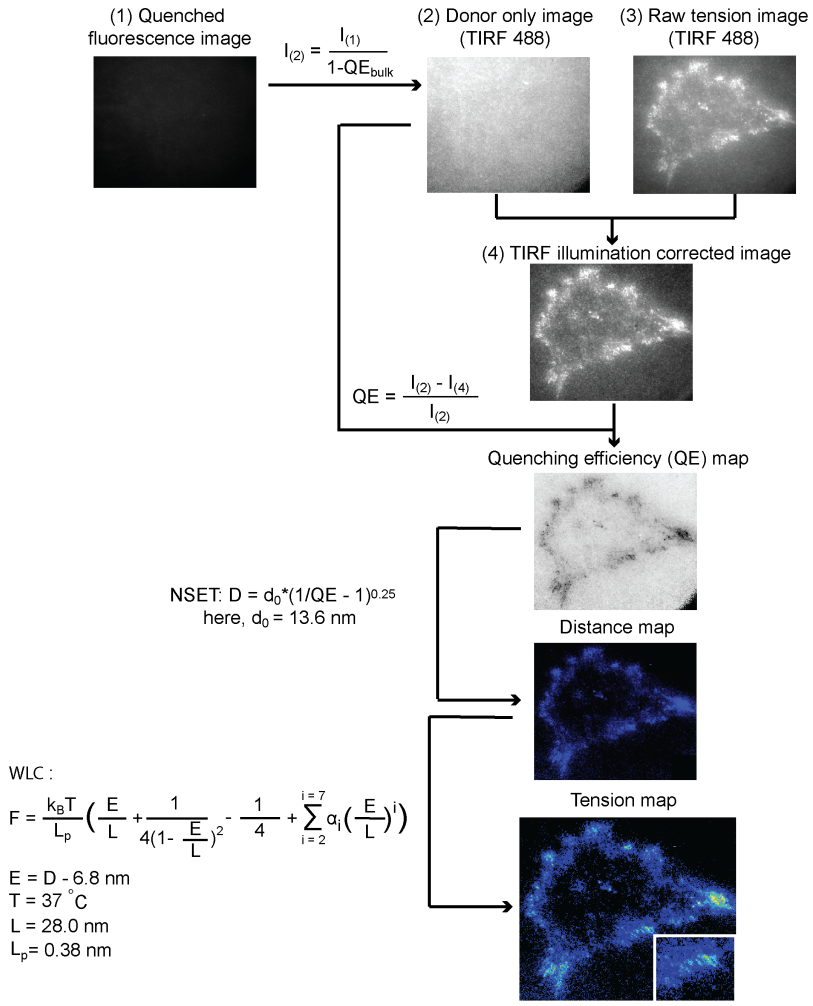

Figure A2.6 Stepwise image analysis of cell tension by using NSET and WLC model.[18]

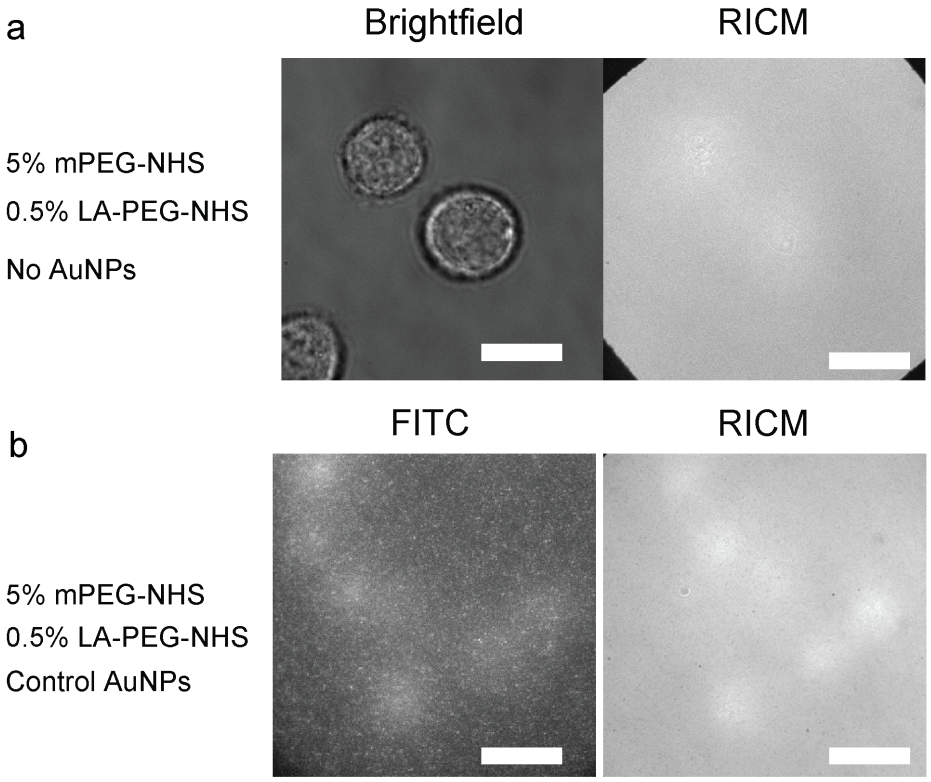

Figure A2.7 Control experiment for non-specific interactions between cells and passivated substrate

To demonstrate that cells exclusively interact with the (cRGDfK)C peptide at the terminus of the AuNP-sensor within the experimental time frame of 1 hr, we performed two control experiments. In the first control experiment, the surface was functionalized with 5% w/v mPEG-NHS and 0.5% w/v lipoic acid-PEG-NHS but not incubated with the AuNP-sensor. In this case, cells failed to interact or engage with the surface. Therefore, cells do not bind to defect sites nor the PEG passivation layer.

In the second set of controls, we incubated the same substrate as in Figure A2.7a along with AuNPs that were modified with 100% COOH-EG8-SH (rather than 99% COOH-EG8-SH and 1% **3** that are typically used in experiments). In this case, we wanted to investigate whether cells engaged the AuNP or the terminal COOH groups presented on the AuNP. As in the previous control, cells were unable to engage the surface within the 1 hr experimental time window (Figure A2.7b). These experiments also allowed to determine the amount of background fluorescence (including instrumental noise and AuNP scattering) and cellular autofluorescence.

Taken together, this data shows that cell surface integrin receptors directly interact with the cRGDfK(C) peptide with molecular specificity.

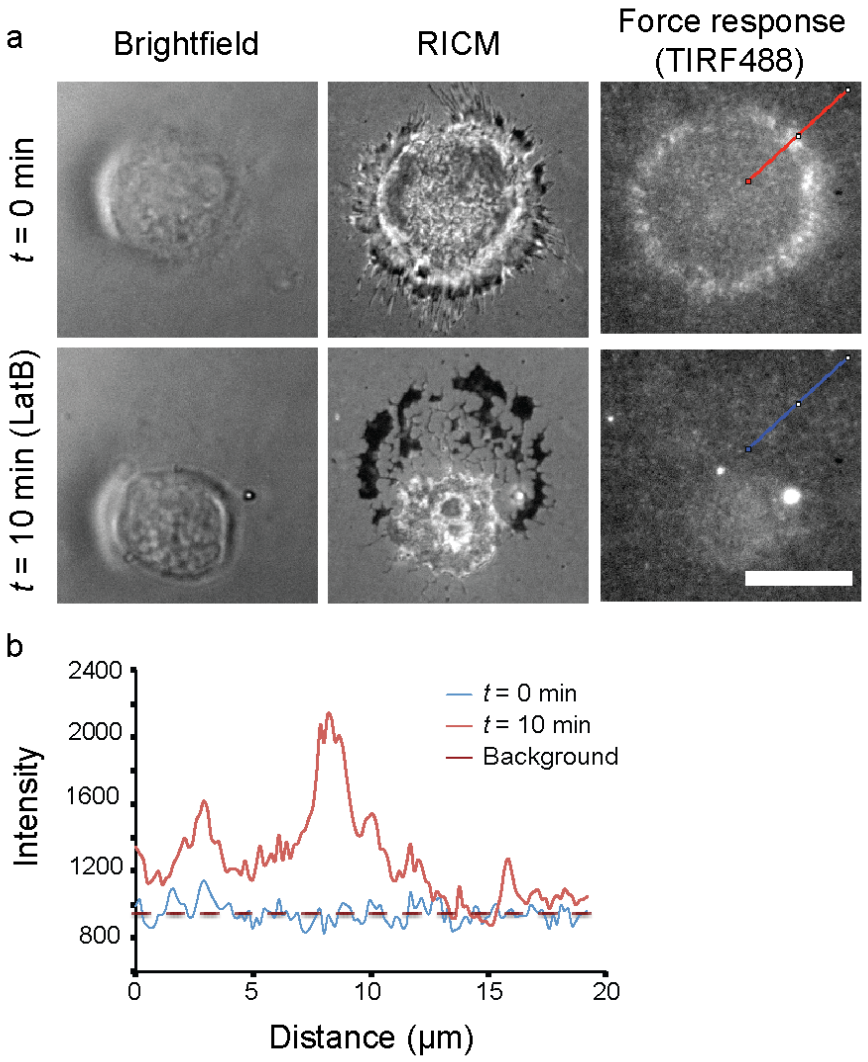

Figure A2.8 Sensor reversibility (a) Tension signal was monitored before and after treatment with 25 μM LatB. At t = 0 min, the cell adhered to the surface (upper panel) and triggered the force response. After 10 min incubation with LatB, the cell moved (lower panel) and the force response also disappeared and recovered to background level. Scale bar, 15 μm. (b) The corrected intensity profile of the linescan in force response images (T488).

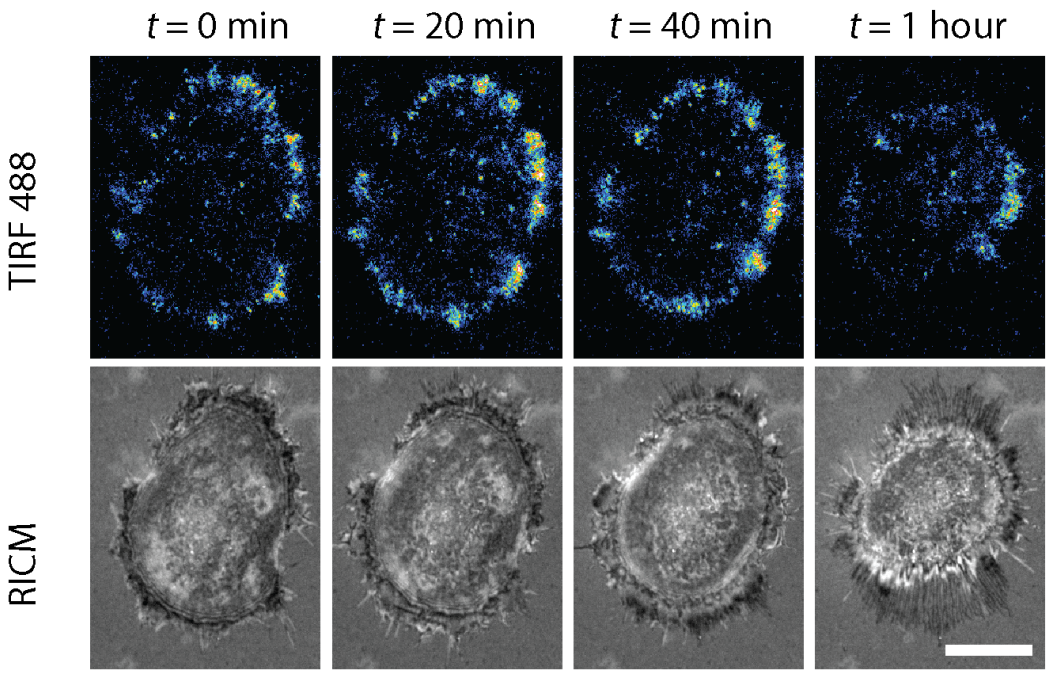

Figure A2.9 Real-time imaging of cell contraction. TIRF488 channel and RICM channel were used to record integrin tension and cell spreading simultaneously for over 1h. Scale bar, 20 μm

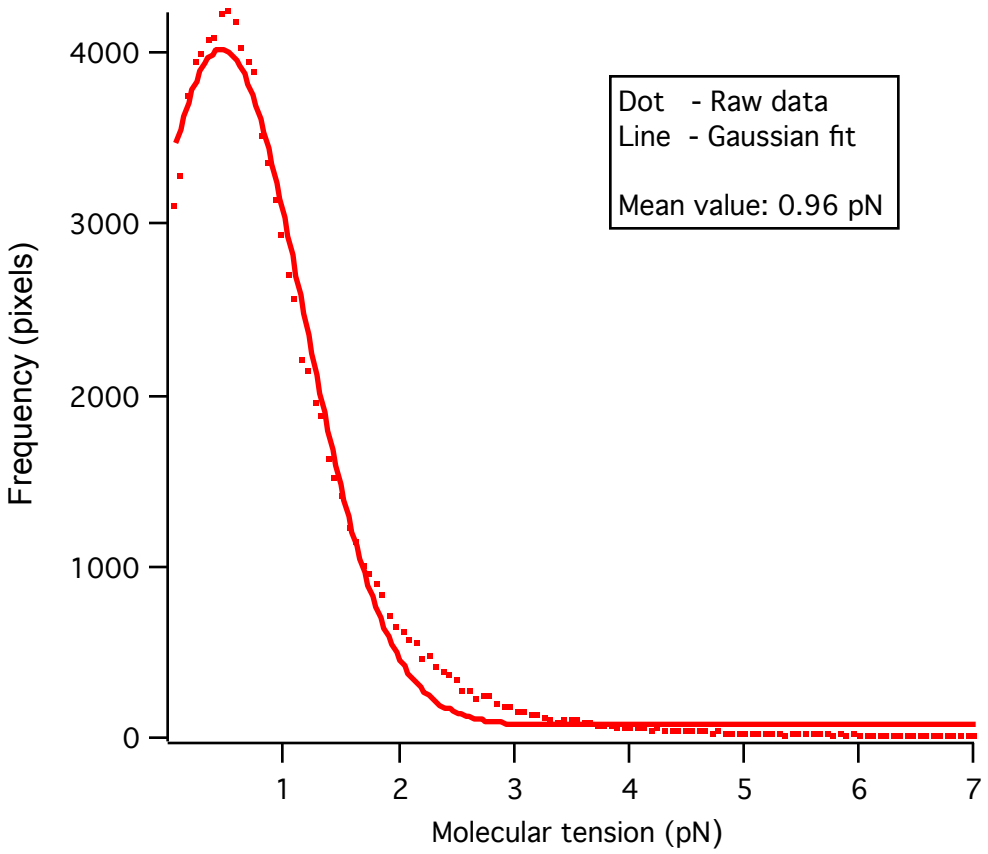

Figure A2.10 Histogram analysis of tension distribution within cellular adhesions. The data was accumulated from three different cells and displayed after background subtraction and conversion as shown in Figure A2.6. Most cell adhesions display a tension of 0.5-3 pN, in agreement with literature estimates using bulk polymer traction force microscopy methods.

Chapter 3: Utilizing nanopatterned MTFM to investigate the impact of integrin clustering on force transmission

Adapted from Liu, Y.; Medda, R.; Liu, Z.; Galior, K.; Yehl, K.; Cavalcanti-Adam, E.A.; Spatz, J.P.; Salaita, K. Nanoparticle Tension Probes Patterned at the Nanoscale: Impact of integrin clustering on force transmission. *Nano Letters* **2014**, 14(10), 5539-5546

3.1 Introduction

Because cell membrane receptors reside at the interface between a cell and its external surroundings, these molecules have evolved to sense and transduce both chemical and physical cues with high fidelity. One common mechanism to trigger or modulate surface receptor activation involves ligand-induced clustering, which in turn contributes to a robust biochemical response. For example, T-cell receptors,[1-2] Fc-ε receptors,[3] EphA2 receptor tyrosine kinases,[4] Notch receptors[5] and epidermal growth factor receptors (EGFR)[6] oligomerize at the plasma membrane upon activation. Intriguingly, the majority of oligomerized ligand-receptor complexes subsequently couple with the cytoskeleton, and are actively transported by retrograde flow.[4, 7-8] Many of these assemblies experience resistance during active transport through the plasma membrane, resulting in mechanical tension which is likely to modulate signaling outcome. Accordingly, the coupling between receptor clustering, mechanical tension, and signal transduction at the plasma membrane is receiving increased interest.[9-13] However, one of the greatest challenges in this area pertains to the lack of methods that can control clustering while also reporting on molecular tension during the signaling activity of live cells. In this paper, we report the development and application of an approach to address this need, thus showing the ability to simultaneously control receptor clustering with nanometer precision while also recording receptor mechanical forces with pN force resolution.

Integrins are α-, β- heterodimeric cell surface receptors that span the plasma membrane and recognize specific ligand molecules within the extracellular matrix (ECM).[14] At the sites of activated integrin receptors, hundreds of different structural and adapter proteins will assemble into a three-dimensional cross-linked structure that spans

many microns in length and is described as the focal adhesion (FA).[15] Importantly, FAs regulate many cellular processes such as migration, differentiation and proliferation.[16] By providing a physical linkage bridging the FA and the ECM, integrins experience mechanical forces that are exerted by the cell and countered by the ECM.[17] These forces play critical roles in integrin function and activation, allowing cells to recognize and respond to specific physical features of their microenvironment.[18-19] Another essential parameter that modulates integrin activation is ligand spacing, where it has been shown that the inter-ligand spacing needs to be at least 60-70 nm in order for FA maturation to proceed.[20-22] Therefore, it seems intuitive to conclude that there is an intimate connection between integrin receptor clustering and force transmission,[23] but the details remain obscure.

To visualize the forces exerted by cell surface receptors, we recently developed molecular tension fluorescence microscopy (MTFM), which generates pN-range force maps with high spatial and temporal resolution.[24] The probe in MTFM is comprised of a flexible linker molecule flanked by a donor fluorophore and ligand at one terminus, and a quencher or a second fluorophore at the other terminus. The MTFM probe is typically immobilized onto a surface, such that the flexible linker is in a collapsed resting state, where the donor fluorophore is highly quenched. Upon the application of mechanical tension, the linker is extended, thus separating the fluorophore from the quencher and increasing the fluorescence intensity by 10 to 20 fold. Recently, we developed integrin-specific MTFM probes by conjugating a fluorescent cyclized Arg-Gly-Asp-dPhe-Lys (c(RGDfK)) peptide at one terminus of a polyethylene glycol (PEG)-linker and using a thiol at the other terminus to immobilize this probe onto a 15 nm gold nanoparticle

(AuNP).[25] The AuNP provides a physical scaffold to anchor the probe, and also efficiently quenches fluorescence when the PEG is in a relaxed conformation. To our surprise, we also found that integrin-specific MTFM probes immobilized through biotin-streptavidin are ruptured due to integrin-mediated forces that dissociate the biotin-streptavidin complex.[26] Therefore, the use of thiol-gold binding minimizes the possibility of force-induced dissociation of these probes. To the best of our knowledge, MTFM[24] and its recent variants[25-27] provide the only known method to visualize the pN forces exerted by cell surface receptors.

To test the relationship between integrin tension and ligand spacing, it is necessary to nanopattern MTFM probes. In principle, this could be achieved using a number of methods ranging from micro-contact printing[28] to dip-pen nanolithography[29] and e-beam lithography[30]. However, few approaches are amenable to rapid prototyping, soft matter patterning, high-end fluorescence microscopy compatibility, as well as sub-10 nm resolution registry over cm^2 areas.[31] Fulfilling these requirements is needed to control integrin spacing at the relevant nanometer length scales, while also providing the throughput necessary to study the inherent heterogeneity of cells and to permit simultaneous biochemical analysis.

Addressing this need, Spatz and colleagues have developed elegant methods to nanopattern RGD ligands.[32] This approach, named block copolymer micellar nanolithography (BCMN), generates arrays of immobilized AuNPs with tunable spacings that range from ~30 nm up to ~300 nm across the entire substrate (cm-scales). RGD-decorated AuNPs confine the integrin receptors to minimum distances defined by the inter-particle spacing. Herein, we combine MTFM with BCMN (Figure 3.1) to provide

evidence showing that the mechanism of ligand density sensing is force-mediated; only sufficiently spaced ligands (<60-70 nm) allow for the transmission of myosin-generated tension to individual integrin receptors.

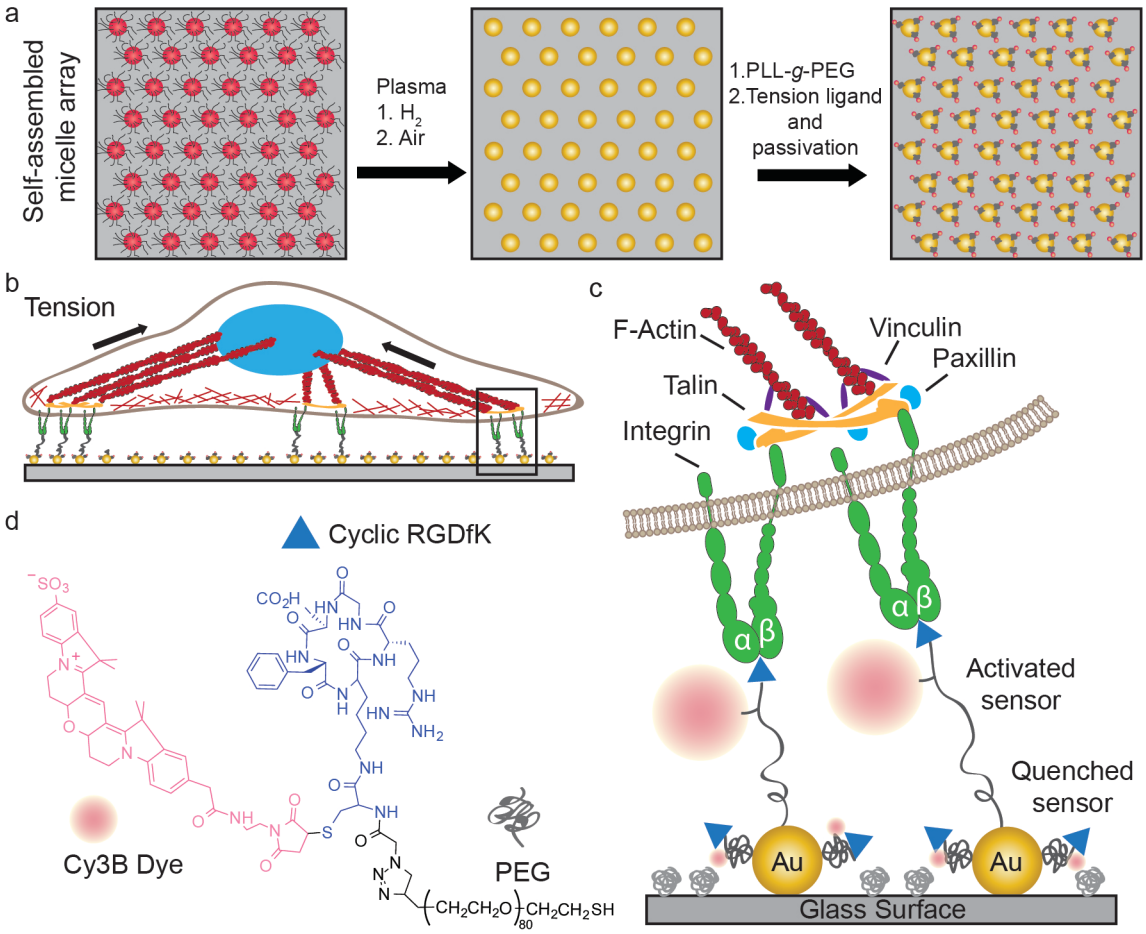

Figure 3.1 Combining block copolymer micellar nanolithography (BCMN) with AuNP-based molecular fluorescence tension microscopy (AuNP-based MTFM) for investigating the role of ligand density in modulating integrin tension. (a) Illustration showing the procedure used to generate BCMN patterned MTFM tension probes. (b-c) Schematic showing the expected mechanism of how cell-generated forces activate the tension probe. (d) Chemical structure of the MTFM tension probe ligand that was synthesized (see *methods* and appendix for details) and used in this work.

3.2 Results and discussion

3.2.1 Fabrication and characterization of the nanopatterned AuNP-MTFM probes

Given that the 50 and 100 nm interparticle spacings are known to promote and destabilize FA formation, respectively, we tuned the dip-coating speed in BCMN to generate substrates with these AuNP spacings.[20] The hexagonal arrangement of the AuNP pattern as well as the interparticle distances and heights were evaluated by atomic force microscopy (AFM) (Figure 3.2a, b) and scanning electron microscopy (*Appendix,* Figure A3.1). Based on this analysis, the AuNPs height was 8.4 ± 1.0 nm (*Appendix,* Figure A3.2), and the spacing on the two types of substrates was determined to be 99 nm ± 12 nm and 49 nm ± 9 nm.

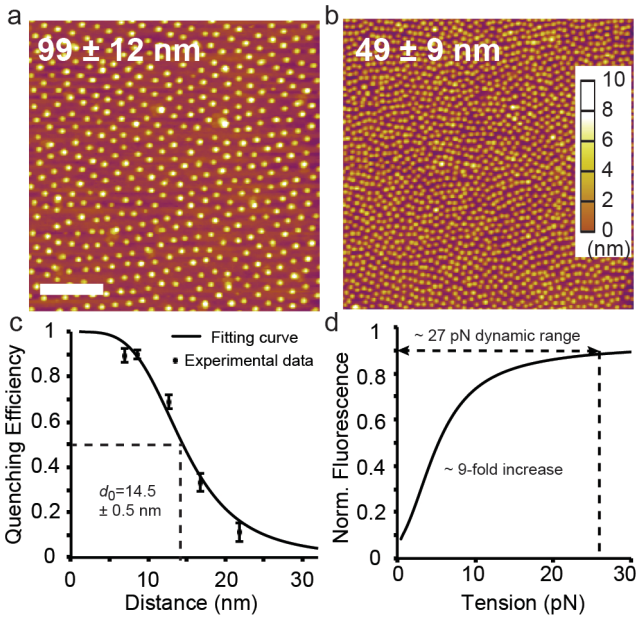

Figure 3.2 Characterization of nanopatterned AuNP-MTFM probes. (a, b) Representative AFM topography images of BCMN-patterned 9 nm AuNP arrays with a mean spacing of 99 ± 12 nm and 49 ± 9 nm. Scale bar, 500 nm. (c) NSET calibration plot showing quenching efficiency of Cy3B fluorophore as a function of distance from AuNP surface as set by a range of DNA duplexes (*Appendix,*Table A3.1). The data was fit to the R^4 NSET model and d_0 (50% quenching distance) was determined to be 14.5 ± 0.5 nm. (d) Theoretical plot showing the change in fluorescence as a function of applied tension based on combining the WLC and NSET models. The dynamic range of the probe corresponds to quenching efficiency values ranging from 90% to 10%.

Although it is known that AuNPs with greater diameters are more efficient at quenching fluorescence,[33] we avoided larger AuNPs because of the potential for multiple integrin binding to each particle. Based on structural data and previous literature reports, we selected 9 nm AuNPs because this is the most efficient quenching AuNP that would still ensure a maximum of one integrin engaged to each particle.[32] Accordingly, we measured the nanometal surface energy transfer (NSET) radius between a 9 nm AuNP and Cy3B dye and found this to be 14.5 ± 0.5 nm by using highly packed duplex DNA as a molecular ruler (Figure 3.2c, Table A3.1 and *Appendix,* Figure A3.3). This NSET radius is in agreement with a value of 14.7 nm that was reported for 8 nm AuNPs and Cy3B dye.[33] Note that the Cy3B dye was used in this work to leave the enhanced green fluorescent protein (eGFP) fluorescence channel available for genetically encoding markers of FAs. Based on this NSET radius and the predicted worm-like chain (WLC) model of PEG_{80},[34] we would expect a force dynamic range that saturates at 27 pN, assuming the ability to detect quenching efficiency values from 90% to 10% (Figure 3.2d).

To prevent non-specific protein adsorption and cell binding, the plasma-treated AuNP array substrate was passivated using a 0.1 mg/ml solution of poly(L-lysine)-*graft*-poly(ethylene glycol) (PLL-*g*-PEG)(PLL(20 kDa)-*g*[3.5]-PEG(2 kDa)) in 0.1M HEPES buffer for 1 h. Subsequently, unbound PLL-*g*-PEG was removed by rigorously rinsing with DI water. We found that this protocol minimized the non-specific interaction of NIH/3T3 fibroblasts to substrate (*Appendix,* Figure A3.4).

The final step of substrate fabrication involves modifying AuNPs with the molecular tension ligand. To maintain the collapsed mushroom conformation of the tension ligand,

it was necessary to functionalize the AuNP with low densities of the fluorescent probe. It was also important to block the remaining AuNP surface, thus minimizing potential non-specific protein interactions. Accordingly, the AuNP was modified with a binary mixture of the tension ligand and the short thiolated PEG, $SH(CH_2)_2(OCH_2CH_2)_8COOH$. The synthesis of the SH-PEG_{80}-c(RGDfK)-Cy3B molecular tension ligand was adapted from our previous work (*Appendix,* Figure A3.5 and A3.6). Briefly, a terminal cysteine residue that presents an amine and thiol was incorporated in the c(RGDfK) peptide. The amine group was initially modified with an NHS-azide with high yield (>90%). In the following two steps, the maleimide-Cy3B dye and alkyne-terminated polyethylene glycol (Alkyne-PEG_{80}-SH, MW 3400) were further coupled to the thiol and azide groups, respectively. After HPLC purification, thiolated MTFM ligands were allowed to self-assemble onto the surface of the AuNP. By varying the concentration of tension ligands from 400 nM to 20 nM, while maintaining a constant thiol concentration of 40 μM using $SH(CH_2)_2(OCH_2CH_2)_8COOH$, we tuned the density of tension probe ligands per AuNP. By empirically testing the cell adhesion onto these different substrates, we found that the 200 nM ligand concentration was the minimum concentration sufficient for allowing significant cell adhesion and spreading (*Appendix,* Figure A3.4). Given that lower ligand densities are desirable for minimizing background signal, we selected this concentration for subsequent cell studies.

To quantify the number of molecular tension ligands per AuNP, we performed a quantitative fluorescence calibration and found that particles incubated with a 200 nM concentration of tension probe (39.8 μM $SH(CH_2)_2(OCH_2CH_2)_8COOH$) had an average of 5.1 ± 0.5 probes per AuNP (*Appendix,* Figure A3.7). Due to the significant excess of the

thiol ligand compared to the concentration of AuNPs, this average number is valid for both 50 and 100 nm spaced substrates. When these particles are immobilized onto the glass coverslip, only part of the Au surface is available for sensor modification due primarily to the steric blocking of the surface bound PLL-*g*-PEG brush. The estimated thickness of the PLL-*g*-PEG layer in the hydrated state is approximately 4-6 nm,[35] which is comparable to the size of AuNP radius. Therefore, we assumed that at most only half of the AuNP surface area was available for binding tension sensors; thus allowing a maximum average number of 2.5 probes per particle. This number strongly suggests that each AuNPs was loaded with a low density of the tension probe, thus ensuring that the PEG was in the collapsed mushroom conformation at resting.[36]

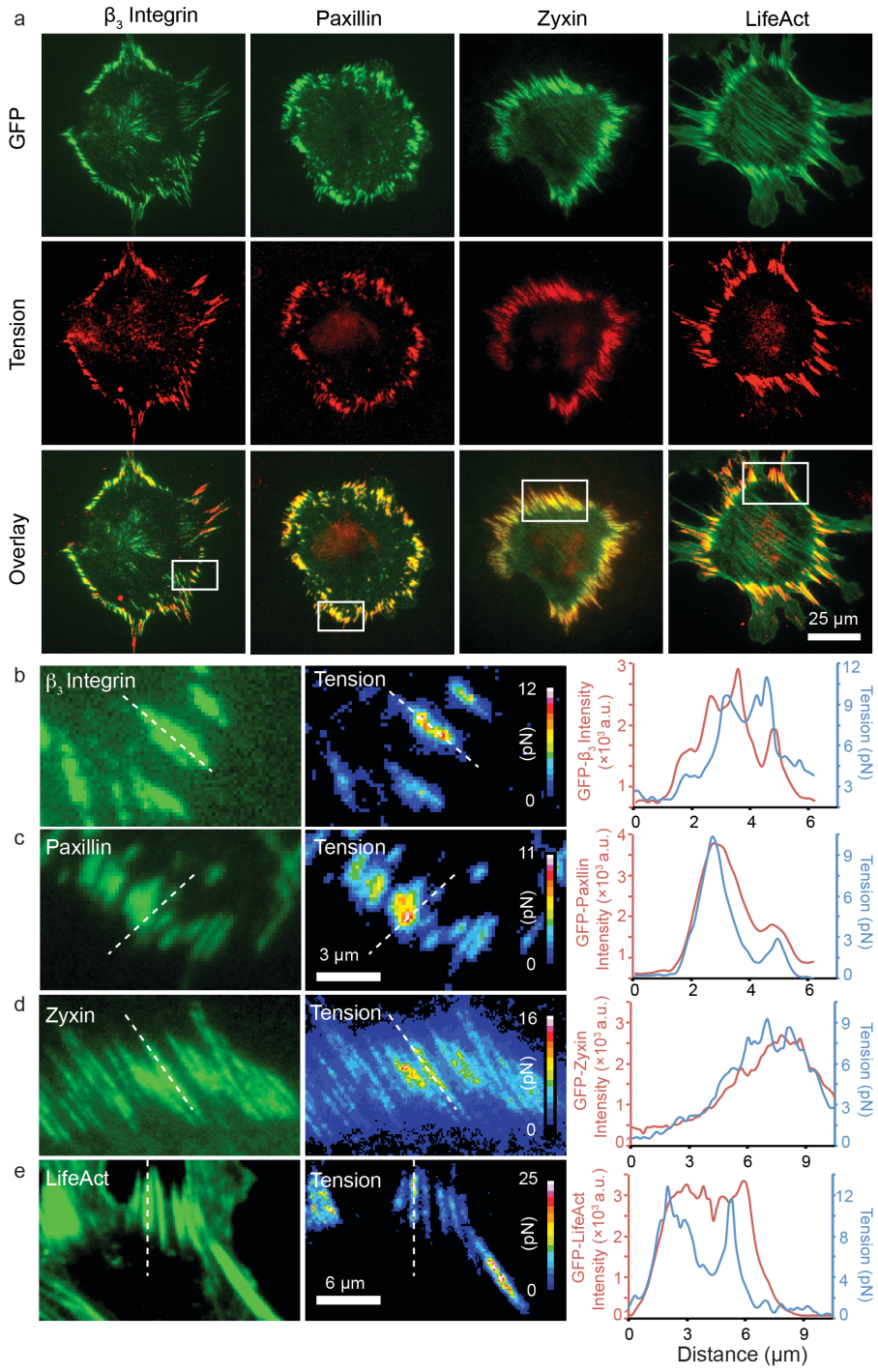

Figure 3.3 Analysis of FA proteins and integrin tension colocalization. a) Representative TIRFM-488 (GFP channel, green) and Cy3B epifluorescence (integrin-tension channel, red) images of NIH/3T3 fibroblast cells cultured on randomly arranged AuNP sensor substrates for 1-2 hr. The cells were transiently transfected to express GFP β_3-integrin, paxillin, zyxin and LifeAct, and this signal was found to colocalize with the integrin tension signal. (b-e) Representative zoom-in images showing the distribution of

GFP-tagged β_3-integrin, paxillin, zyxin and LifeAct with the integrin-tension signal. The integrin tension signal was quantified and found to highly co-localize with FA markers (see line scan analysis). Tension values were dynamic (see below) and varied across subcellular regions reaching maxima that ranged from ~10-20 pN. Note that the reported tension values represent the average minimum tension per ligand, thus likely underestimating the forces applied by integrins.

3.2.2 Co-localizing different FA markers with integrin tension

Toward investigating the relationship between force transmission and FA formation, we next demonstrated the compatibility of MTFM with genetically-encoded tagging of FA markers. NIH/3T3 fibroblast cells were transiently transfected with β_3-integrin, paxillin, zyxin, and LifeAct, and then cultured onto substrates modified with randomly arranged 9 nm diameter AuNP tension sensors for ~1-2 hr and subsequently imaged using total-internal reflection fluorescence microscopy (TIRFM) (Figure 3.3a). The density of disordered AuNP sensors on these substrates is ~100 nm, which is sufficiently broad to allow FA maturation and force transmission.[22] In all cases, we found strong integrin tension colocalization with the early markers of FAs such as β_3-integrin, and paxillin. In contrast, the zyxin and LifeAct signals were distributed across the entire cell but preferentially localized to the actin bundles, in agreement with previous reports.[37] The integrin tension signal was mainly detected at the cell perimeter, coinciding with the greatest zyxin and LifeAct intensities at the tips of the actin bundles. In some cases, the signal observed at the center of cell was due to autofluorescence from the nucleus. However, in other cases the signal was due to focal adhesion generated forces. The distinction between the two types of signal is clearer upon examination of the β_3-integrin-GFP channel.

Upon analysis of sub-cellular regions (Figure 3.3b-e), we found that the maximum integrin tension within each FA typically appeared near the center of the rod-shaped

elongated structure. Note that in these zoom-in images we observed that the peak position of tension can be offset from the peak position of the focal adhesion, either proximal or distal, by sub-micron distances, or in some cases, it may perfectly overlap with the peak position of the focal adhesion marker, thus demonstrating the dynamic tension fluctuations during FA formation.[38] By quantifying the quenching efficiency of the tension ligands at resting and employing the ligand density of 2.5 per AuNP, we were also able to estimate the minimum average force per ligand, which ranged from 1-20 pN (Figure A3.8, Appendix), which is consist with the observation of integrin force mediated biotin-streptavidin dissociation.[26] Note that this value is significantly greater than that reported by Dunn and colleagues (1-5 pN), and may be due to the limited dynamic range of their spider-silk based probes or the nature of the linear RGD peptide used in their studies.[27]

3.2.3 The impact of ligand spacing on integrin tension

We next investigated the relationship between integrin clustering and tension by culturing GFP-paxillin transfected cells onto MTFM-patterned substrates with 50 and 100 nm spacing. The cells were continuously monitored using TIRFM (GFP-paxillin) and epi-fluorescence microscopy (integrin tension) for over 5 hr. Representative cell images are shown in Figure 3.4a, and the data indicated that the footprint of the cells cultured on the 100 nm spacing remained small (300 ~ 1000 μm^2) in contrast to cells grown on the substrate with 50 nm spacing (2000 ~ 5000 μm^2). The difference in cell spreading was observed at the earliest time points (~30 min) and became more pronounced at all later time points (Figure 3.4a). Although cells start spreading almost immediately upon plating on the 50 nm spaced AuNP arrays, only a few cells spread onto the 100 nm spaced

substrate before the 30 min time point, in agreement with literature.[20] Surprisingly, both the average FA size (as measured by GFP-paxillin, Figure 3.4b) and the average tension per integrin receptor (Figure 3.4c) were similar for the cells cultured on both substrate spacings at the early time point of 30 min (each data point represents n=10 cells). At later time points, FA area and the average tension per integrin ligand diverged; cells on the 50 nm spacing formed significantly larger FAs with greater values of tension per integrin ligand (Figure 3.4b-c, and *Appendix,* Figure A3.9). It is notable that for the substrate of 50 nm spacing, the average size of FAs continues to grow over the time course of the experiment (from nascent focal adhesion to mature and elongated focal adhesion). However, the average tension per integrin ligand only rises to a threshold level that is maintained across the 5 hr experiment. To verify this observation, we added 30 μM Oleoyl-L-α-lysophosphatidic acid (LPA), a stimulant of myosin-contractility, to cells that have been cultured for 5.5 hr in serum supplemented media (*Appendix,* Figure A3.10). Statistical analysis showed no significant increase in mean tension per integrin or total traction per cells. In contrast, addition of LPA to serum starved fibroblasts led to a significant increase in tension and FA area, recovering to levels similar to that of cells cultured in serum-supplemented conditions. This data clearly indicates that although the total tension generated by the cell is growing, the tension per integrin ligand is maintained at a constant value; thus, individual integrin tension does not increase continuously during FA maturation and cell spreading. Our finding has two implications. First, it suggests that the mechanism of how cells continuously increase the exerted traction force is through increasing the number of surface-engaged integrins (and cell

area) rather than mounting greater force per ligand.[39] Second, this observed level of force maybe related to the universal peak tension that was recently reported by Wang and Ha.[40]

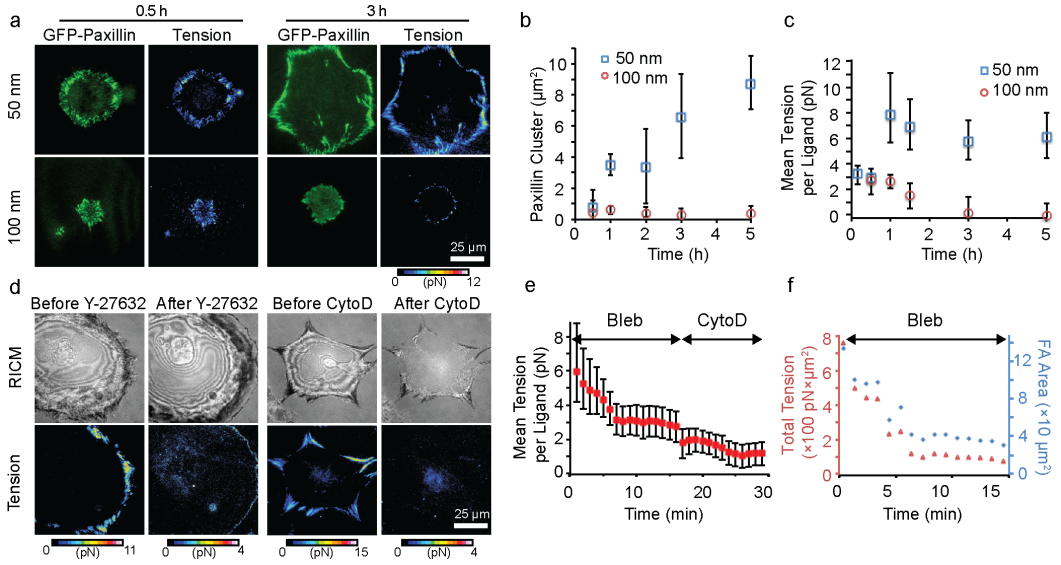

Figure 3.4 Nanoscale clustering modulates integrin forces. (a) Representative images of GFP-paxillin expressing NIH/3T3 cells seeded onto the 50 and 100 nm spaced AuNP substrates. Images are shown for the 0.5 and 3 hr time-points, highlighting the differences in integrin tension, cell shape, and FA size at these two time points. (b) Plot of GFP-paxillin cluster size (which is indicative of FA size) as a function of time for n=10 cells. The plot shows a steady increase in FA size over 5 hr after cell seeding on the 50 nm-spaced substrate, in contrast to the 100-nm spaced substrate, which shows limited FA maturation. (c) Plot showing the average tension per integrin ligand across the entire cell for n=10 cells. Integrin tension increased rapidly within the first hour and was then maintained for cells cultured on AuNP arrays spaced at 50 nm. This is in contrast to cells cultured on the AuNP arrays spaced at 100 nm where tension decreased by the later time points. (d) Representative images showing the change in integrin tension before and after treating the same cell with Y-27632 (40 μM) and cytochalasin D (10 μM). (e) Stepwise blebbistatin and cytochalasin D treatment of cells (n = 4) led to significant reduction of mean integrin ligand tension. (f) Blebbistatin treatment of cells (n = 4 cells) led to over 80% reduction in the total cell traction force and FA area.

The results also suggest that at early time points (~30 min), the mechanism of integrin force generation is independent of integrin clustering, and increasing the average magnitude of tension per integrin ligand beyond 2-3 pN requires a greater ligand density (<~60 nm spacing). Based on previous literature, the early time point forces are likely generated by actin polymerization, rather than myosin contraction.[41] To distinguish the

contributions of actin polymerization and myosin contractility to integrin tension, we imaged NIH 3T3 fibroblasts before and after treatment with the Rho kinase inhibitor Y-27632, and cytochalasin D (Figure 3.4d and *Appendix,* Figure A3.11). Analysis from n = 5 cells treated with Y-27632 for 30 min shows that integrin tension signal generated by mature FAs decreased significantly to values of ~2-3 pN per ligand, and were exclusively localized to a sub-micron structure at the cell edge. In contrast, addition of 10 μM cytochalasin D rapidly (~5 min) abolished all integrin tension signal to background levels, likely due to the disruption of actin polymerization. To further confirm that actin polymerization and myosin contractility are the two main contributors to integrin tension, we performed a stepwise inhibition of both processes in the same cells. We first performed timelapse imaging on fibroblasts (n = 4 cells) that were treated with a myosin II inhibitor (25 μM blebbistatin). In this experiment, the average integrin ligand tension was reduced from ~6 pN to ~3 pN and reached a steady state value within 5 min of adding the drug, which is similar to the effect of Y-27632 and suggests the loss of myosin-driven tension at this time point. Interestingly, this level of tension coincides with the magnitude of integrin ligand tension during initial cell spreading (Figure 3.4c, t = 30 min). When these cells were further treated with 10 μM cytochalasin D, the mean integrin ligand tension was immediately reduced (within 1 min) to approximately 2 pN and was gradually reduced to ~1 pN within 15 min (Figure 3.4e). This ~2 pN decrease in integrin ligand tension is likely due to the loss of actin-driven forces and associated membrane tension. Exclusively treating cells with blebbistatin led to an 80% decrease in FA size as well as >80% decrease in the total tension per cell (Figure 3.4f), in agreement with literature precedent.[42] When comparing the total decrease in cell tension with the

loss of tension per ligand, it is clear that myosin-inhibition leads to a decrease in the number of engaged integrins and not only a decrease in integrin tension. Taken together, this data suggests that during initial FA formation, actin polymerization drives integrin tension to an average of 1-3 pN per ligand. This is closely followed by actomyosin-contractility that increases the average tension to ~6-8 pN, and is associated with FA maturation. Note that this value of mean ligand tension was also observed in two additional cell lines, Rat Embryonic Fibroblasts (REFs) and Human Bone Osteosarcoma Epithelial Cells (U2OS) (*Appendix,* Figure A3.12).

To better understand the relationship between FA maturation and force transmission for the high ligand density substrate, we captured timelapse movies of integrin tension with F-actin dynamics (Figure 3.5a-b). At initial time points, we observed diffuse integrin tension over the lamellipodium, which was similar to the intensity of tension in cells grown on the 100-nm spaced substrate. At subsequent time points, we observed high integrin tension puncta that localized to the tips of f-actin bundles (Figure 3.5b, white arrow), which is the location of the linkage between the FA and cytoskeleton.[43] We tracked a single integrin tension puncta (white arrow, Fig. 4b), and observed that within the time frame (from t = 25 to 41 min) the maximum integrin ligand tension within the single FA increased one order of magnitude, from ~3 pN to ~12 pN. For this single FA, we found that integrin tension increased concomitantly with FA growth (*Appendix,* Figure A3.13). Interestingly, micron-scale actin fiber assembly coincides with the increase of integrin tension (*Appendix,* Figure A3.14), in agreement with literature suggesting the importance of stress fibers as a template for tension mounting and FA maturation.[44]

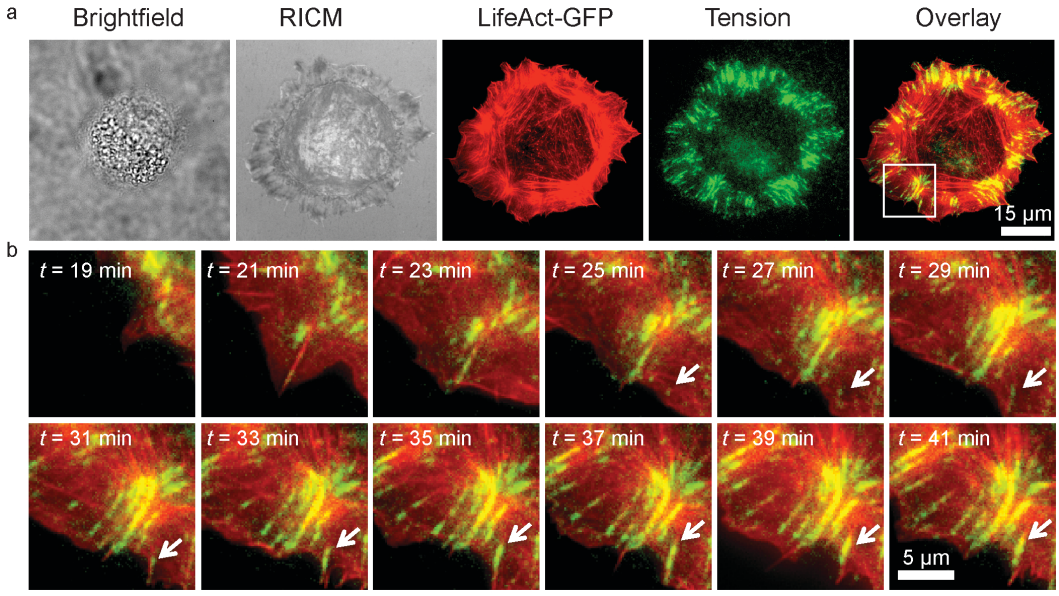

Figure 3.5 Integrin tension and actin dynamics during early FA maturation. (a) Representative brightfield, reflection-interference contrast microscopy (RICM), LifeAct GFP (TIRFM 488, red), integrin tension (epifluorescence Cy3B, green), and overlay of GFP and tension signals for a single NIH/3T3 fibroblast cells adhered on sensor substrate immediately following cell seeding. (b) Zoom-in timelapse overlay images of integrin tension for t = 19 min to 41 min.

3.3 Conclusion

We have combined BCMN with MTFM to simultaneously control ligand spacing with sub-5 nm resolution while also recording integrin tension with pN force sensitively and high temporal resolution in living cells. We found that integrin receptors placed 100 nm apart displayed significantly reduced tension as well as diminished capacity for FA formation compared to receptors with 50 nm spacing. Based on our data, we propose that integrin ligand sensing occurs by the following steps: 1) F-actin polymerization drives an increase in integrin tension to 1-3 pN during nascent adhesion formation; 2) optimal ligand spacing (< 60-70 nm) allows bound integrins to harness actomyosin-driven tension to increase their average tension to ~6-8 pN, thus facilitating FA maturation. This

physical model of FA matruation complements structural models of integrin clustering that relate dimensions of α-actinin and talin1 to the minimal ligand spacing.[45-47] We also show that the mechanism of increasing cell traction force occurs through the recruitment of a greater number of integrins under tension rather than maintaining a constant number of integrin receptors and ramping the tension per receptor.

Note that the reported values of integrin tension represent the mean per molecule and this does not preclude that some receptors will experience greater values of force. For example, each pixel of an image collected from cells on the 50 nm spacing reports on the average force for 9 MTFM probes, and it is unlikely that all of these probes are engaged by integrin receptors. Therefore, the values of tension reporter here represent the lower bound estimate of force, and this is not inconsistent with our recent finding of integrin force-driven biotin-streptavidin dissociation[26] and the recent report of 40 pN universal peak tension for integrin activation.[40] It would be of interest to compare forces exerted onto more physiological integrin ligands such as fibronectin and collagen that can engage different classes of adhesion receptors and thus may display important differences in force magnitude and dynamics.

Combining MTFM with BCMN-based patterning is highly modular and adaptable, and thus this technique can be applied to study the complex relationships between receptor clustering and mechanical tension in many other receptor signaling pathways, such T cell receptor activation and the EGFR pathway. Our approach is certainly more facile than the most commonly used approaches to measure receptor tension, such as traction force microscopy (TFM)[48] and PDMS micropost arrays,[39] both of which employ elastomeric substrates that deform under mechanical stress. Therefore, we expect that this

strategy will likely become a workhorse tool in studying the molecular biophysics of cell receptor signaling.

3.4 Materials and methods

3.4.1 Materials

(3-Aminopropyl) trimethoxysilane (97%, APTMS), O-(2-carboxyethyl)-O'-(2-mercaptoethyl) heptaethylene glycol (95%, COOH-EG8-SH), 2,5-dihydroxybenzoic acid (99%, DHB), triethylamine (99%, TEA), dithiothreitol (99.0%, DTT), triethylammonium acetate (TEAA), Oleoyl-L-α-lysophosphatidic acid (LPA) sodium salt (>98%), Y-27632 Dihydrochloride (>98%), cytochalasin D (≥ 98%) were purchased from Sigma-Aldrich (St. Louis, MO) and used without further purification. The heterobifunctional linker azide-NHS (product #: 88902) was purchased from Thermo Fisher Scientific (Rockford, IL). The fluorescent dye Cy3B-maleimide was purchased from GE healthcare Bio-Science (Pittsburgh, PA). Lipofectamine® LTX with Plus™ Reagent for cell transfection and Dulbecco's Modified Eagle's Medium (DMEM) were purchased from Life Technologies (Carlsbad, CA). Number two glass coverslips, ascorbic acid (>99.0%), and 96-well plates were purchased from Fisher Chemical & Scientific (Pittsburgh, PA). DMF (>99.5%), DMSO (99.5%) and sodium bicarbonate (99.0%) were purchased from EMD chemicals (Philadelphia, PA). Cyclic(RGDfK)C was custom synthesized and HPLC purified by Peptides International (Louisville, KY). All DNA strands used were custom synthesized and desalted by Integrated DNA Technologies (Coralville, Iowa). Alkyne-PEG-SH (MW 3400) was purchased from Nanocs (New York, NY). CuSO4.5H4O was purchased from Mallinckrodt (St. Louis, MO) and P4 gel size exclusion beads were

acquired from Biorad (Hercules, CA). DI water was obtained from a Nanopure water purification system with a UV sterilization unit and showed a resistivity of 18.2 MW.

The AuNPs that were used to generate the randomly immobilized gold particle arrays, and to calibrate the NSET distance were custom synthesized and characterized by TEM by Nanocomposix (San Diego, CA). Based on TEM analysis that was provided by the manufacturer, the mean diameter of these particles was 8.6 ± 0.6 nm. This diameter was intentionally selected to match the average size of BCMN-generated AuNP that had a 8.4 ±1.0 nm diameter (based on SEM and AFM, Fig. S1-2).

3.4.2 Fabrication of BCMN patterned gold nanoparticle (AuNP) arrays.

The protocol for deposition of 9 nm gold nanoparticles (AuNPs) on surfaces by block copolymer micelle nanolithography (BCMN) using polystyrene-*block*-poly (2-vinylpyridine) (PS-*b*-P2VP) is based on the work by Glass et al.[49] Prior to BCMN, glass surfaces were activated in oxygen plasma (0.4 mbar, 150 W) for 10 min. The micelle solution used to fabricate the 49 nm interparticle distance substrate was prepared by dissolving polymer '1056' (consisting of 1056 polystyrene units and 671 vinyl pyridine units) at a concentration of 9 mg/ml in *o*-xylene and adding $HAuCl_4$ to the polymer solution to obtain a gold loading of 0.3 ($HAuCl_4$*$3H_2O$ from Sigma, Germany). The micelle solution used to fabricate the 99 nm distance substrate was prepared similarly using a polymer concentration of 5 mg/ml and a gold loading of 0.25. In this work, we used dip-coating to obtain the 99 nm distance by using a constant retraction speed of approximately 25 mm/min, whereas in the case of the 49 nm distance samples we employed spin coating with a speed of 7000 rpm. It should be noted that either method could be used for the generation of small or large interparticle distances by only adjusting

the retraction, or the spinning velocity. The organic compounds were removed by hydrogen plasma treatment (0.4 mbar, 150 W) for 45 min, which also results in the coalescence of the AuNPs.

3.4.3 Scanning Electron Microscopy

The quasi-hexagonal AuNP pattern was analyzed with scanning electron microscopy SEM (LEO 1530 Gemini, Carl Zeiss, Germany). To enhance electron scattering, thus enhancing contrast, carbon was sputtered on the surfaces prior to SEM imaging.

3.4.4 Ensemble fluorescence measurements

The fluorescence intensity of Cy3B was recorded using a Biotek Synergy HT plate reader operated using a filter set with excitation/emission λ = 565 nm/610 nm. Each well in the 96-well plate (Fisher scientific) was filled to a volume of 100 µl. All measurements were performed in triplicate, and the reported error bars represent the standard deviation of these measurements.

3.4.5 HPLC

Reaction products were purified using a C18 column (diameter: 4.6 mm; length: 250 mm) in a reverse phase binary pump HPLC that was coupled to a diode array detector (Agilent 1100).

3.4.6 MALDI-Mass Spectrometry

A 10 mM solution of 2,5-dihydroxybenzoic acid (DHB) was prepared in tetrahydrofuran (THF) as the MALDI matrix and 0.1 M sodium chloride was added as cationization agent.[50] All products were also pre-dissolved in THF and then mixed with an equal volume of the DHB matrix. 2 µl of this mixture was then added to each well on

the MALDI plate. After allowing the solution to dry for 20 min, the sample was analyzed by a high performance MALDI time-of-flight mass spectrometer (Voyager STR).

3.4.7 Optical Microscopy

Live cells were imaged in phenol red free Dulbecco's Modified Eagle's Medium (DMEM) at 37 °C. During imaging, physiological temperature was maintained with a warming apparatus consisting of a sample warmer and an objective warmer (Warner Instruments 641674D and 640375). The microscope was a Nikon Eclipse Ti driven by the Elements software package. The microscope features an Evolve electron multiplying charge coupled device (EMCCD; Photometrics), an Intensilight epifluorescence source (Nikon), a CFI Apo 100× (numerical aperture (NA) 1.49) objective (Nikon) and a TIRF launcher with two laser lines: 488 nm (10 mW) and 647 nm (20 mW). This microscope also includes the Nikon Perfect Focus System, an interferometry-based focus lock that allowed the capture of multipoint and time-lapse images without loss of focus. In all the reported experiments, we used the following Chroma filter cubes: TIRF 488, TRITC, and reflection interference contrast microscopy (RICM).

3.4.8 AFM imaging

The density of AuNP tension sensor on the functionalized glass coverslip was measured by using an atomic force microscope mounted on an anti-vibration stage (MFP-3D, Asylum Research, CA). Silicon AFM tips (MikroMasch) with a force constant (5.4-16 N/m) were used to image the sample in tapping mode at a scan rate of 1 Hz. All images were processed and rendered using IgorPro.

3.4.9 Cell culture and transfection

NIH/3T3 fibroblast cells were cultured in Dulbecco's Modified Eagle's Medium (DMEM) supplemented with 10% Cosmic Calf Serum (Mediatech), HEPES (9.9 mM, Sigma), sodium pyruvate (1 mM, Sigma), L-glutamine (2.1 mM, Mediatech), penicillin G (100 IU ml−1, Mediatech) and streptomycin (100 μg ml−1, Mediatech) and were incubated at 37 °C with 5% CO2. Cells were passaged at 60-80% confluency and plated at a density of 10% using standard cell culture procedures. All cell transfection was performed in a 24-well plate. All procedures are based on a standard protocol provided by Life Technologies (Carlsbad, CA). Briefly, 4×104 cells were plated in each well one day before transfection. During transfection, 0.5-1 mg DNA was mixed with Lipofectamine® LTX with Plus™ Reagent for each well and incubated for 24-48 hr before imaging.

3.5 References

1. O'Donoghue, G. P.; Pielak, R. M.; Smoligovets, A. A.; Lin, J. J.; Groves, J. T., Direct single molecule measurement of TCR triggering by agonist pMHC in living primary T cells. *Elife* **2013,** *2*.

2. Deeg, J.; Axmann, M.; Matic, J.; Liapis, A.; Depoil, D.; Afrose, J.; Curado, S.; Dustin, M. L.; Spatz, J. P., T Cell Activation is Determined by the Number of Presented Antigens. *Nano Letters* **2013,** *13* (11), 5619-5626.

3. Wu, M.; Holowka, D.; Craighead, H. G.; Baird, B., Visualization of plasma membrane compartmentalization with patterned lipid bilayers. *Proceedings of the National Academy of Sciences of the United States of America* **2004,** *101* (38), 13798-13803.

4. Salaita, K.; Nair, P. M.; Petit, R. S.; Neve, R. M.; Das, D.; Gray, J. W.; Groves, J. T., Restriction of Receptor Movement Alters Cellular Response: Physical Force Sensing by EphA2. *Science* **2010,** *327* (5971), 1380-1385.

5. Narui, Y.; Salaita, K., Membrane Tethered Delta Activates Notch and Reveals a Role for Spatio-Mechanical Regulation of the Signaling Pathway. *Biophysical Journal* **2013,** *105* (12), 2655-2665.

6. Stabley, D.; Retterer, S.; Marshall, S.; Salaita, K., Manipulating the lateral diffusion of surface-anchored EGF demonstrates that receptor clustering modulates phosphorylation levels. *Integrative Biology* **2013,** *5* (4), 659-668.

7. Lidke, D. S.; Nagy, P.; Heintzmann, R.; Arndt-Jovin, D. J.; Post, J. N.; Grecco, H. E.; Jares-Erijman, E. A.; Jovin, T. M., Quantum dot ligands provide new insights into

erbB/HER receptor–mediated signal transduction. *Nature biotechnology* **2004,** *22* (2), 198-203.

8. Yu, Y.; Smoligovets, A. A.; Groves, J. T., Modulation of T cell signaling by the actin cytoskeleton. *Journal of Cell Science* **2013,** *126* (5), 1049-1058.

9. Groves, J. T.; Kuriyan, J., Molecular mechanisms in signal transduction at the membrane. *Nature Structural & Molecular Biology* **2010,** *17* (6), 659-665.

10. Smoligovets, A. A.; Smith, A. W.; Groves, J. T., Ratiometric Imaging of the T-Cell Actin Cytoskeleton Reveals the Nature of Receptor-Induced Cytoskeletal Enrichment. *Biophysical Journal* **2013,** *105* (3), L11-L13.

11. Bakker, G. J.; Eich, C.; Torreno-Pina, J. A.; Diez-Ahedo, R.; Perez-Samper, G.; van Zanten, T. S.; Figdor, C. G.; Cambi, A.; Garcia-Parajo, M. F., Lateral mobility of individual integrin nanoclusters orchestrates the onset for leukocyte adhesion. *Proceedings of the National Academy of Sciences of the United States of America* **2012,** *109* (13), 4869-4874.

12. Lohmuller, T.; Xu, Q.; Groves, J. T., Nanoscale obstacle arrays frustrate transport of EphA2-Ephrin-A1 clusters in cancer cell lines. *Nano Letters* **2013,** *13* (7), 3059-64.

13. Yu, C.; Law, J. B. K.; Suryana, M.; Low, H. Y.; Sheetz, M. P., Early integrin binding to Arg-Gly-Asp peptide activates actin polymerization and contractile movement that stimulates outward translocation. *Proceedings of the National Academy of Sciences of the United States of America* **2011,** *108* (51), 20585-20590.

14. Shattil, S. J.; Kim, C.; Ginsberg, M. H., The final steps of integrin activation: the end game. *Nature Reviews Molecular Cell Biology* **2010,** *11* (4), 288-300.

15. Kanchanawong, P.; Shtengel, G.; Pasapera, A. M.; Ramko, E. B.; Davidson, M. W.; Hess, H. F.; Waterman, C. M., Nanoscale architecture of integrin-based cell adhesions. *Nature* **2010,** *468* (7323), 580-U262.

16. Burridge, K.; ChrzanowskaWodnicka, M., Focal adhesions, contractility, and signaling. *Annual Review of Cell and Developmental Biology* **1996,** *12*, 463-518.

17. Friedland, J. C.; Lee, M. H.; Boettiger, D., Mechanically activated integrin switch controls alpha5beta1 function. *Science* **2009,** *323* (5914), 642-4.

18. Geiger, B.; Spatz, J. P.; Bershadsky, A. D., Environmental sensing through focal adhesions. *Nature Reviews Molecular Cell Biology* **2009,** *10* (1), 21-33.

19. Balaban, N. Q.; Schwarz, U. S.; Riveline, D.; Goichberg, P.; Tzur, G.; Sabanay, I.; Mahalu, D.; Safran, S.; Bershadsky, A.; Addadi, L.; Geiger, B., Force and focal adhesion assembly: a close relationship studied using elastic micropatterned substrates. *Nature cell biology* **2001,** *3* (5), 466-472.

20. Cavalcanti-Adam, E. A.; Volberg, T.; Micoulet, A.; Kessler, H.; Geiger, B.; Spatz, J. P., Cell spreading and focal adhesion dynamics are regulated by spacing of integrin ligands. *Biophysical Journal* **2007,** *92* (8), 2964-2974.

21. Schvartzman, M.; Palma, M.; Sable, J.; Abramson, J.; Hu, X. A.; Sheetz, M. P.; Wind, S. J., Nanolithographic Control of the Spatial Organization of Cellular Adhesion Receptors at the Single-Molecule Level. *Nano Letters* **2011,** *11* (3), 1306-1312.

22. Huang, J.; Gräter, S. V.; Corbellini, F.; Rinck, S.; Bock, E.; Kemkemer, R.; Kessler, H.; Ding, J.; Spatz, J. P., Impact of Order and Disorder in RGD Nanopatterns on Cell Adhesion. *Nano Letters* **2009,** *9* (3), 1111-1116.

23. de Beer, A. G. F.; Cavalcanti-Adam, E. A.; Majer, G.; Lopez-Garcia, M.; Kessler, H.; Spatz, J. P., Force-induced destabilization of focal adhesions at defined integrin spacings on nanostructured surfaces. *Physical Review E* **2010,** *81* (5).

24. Stabley, D. R.; Jurchenko, C.; Marshall, S. S.; Salaita, K. S., Visualizing mechanical tension across membrane receptors with a fluorescent sensor. *Nature Methods* **2012,** *9* (1), 64-U172.

25. Liu, Y.; Yehl, K.; Narui, Y.; Salaita, K., Tension Sensing Nanoparticles for Mechano-Imaging at the Living/Nonliving Interface. *Journal of the American Chemical Society* **2013,** *135* (14), 5320-5323.

26. Jurchenko, C.; Chang, Y.; Narui, Y.; Zhang, Y.; Salaita, K. S., Integrin-generated forces lead to streptavidin-biotin unbinding in cellular adhesions. *Biophysical Journal* **2014,** *106* (7), 1436-46.

27. Morimatsu, M.; Mekhdjian, A. H.; Adhikari, A. S.; Dunn, A. R., Molecular Tension Sensors Report Forces Generated by Single Integrin Molecules in Living Cells. *Nano Letters* **2013,** *13* (9), 3985-3989.

28. Thery, M.; Piel, M., Adhesive micropatterns for cells: a microcontact printing protocol. *Cold Spring Harb Protoc* **2009,** *2009* (7), pdb prot5255.

29. Giam, L. R.; Massich, M. D.; Hao, L. L.; Wong, L. S.; Mader, C. C.; Mirkin, C. A., Scanning probe-enabled nanocombinatorics define the relationship between fibronectin feature size and stem cell fate. *Proceedings of the National Academy of Sciences of the United States of America* **2012,** *109* (12), 4377-4382.

30. Kolodziej, C. M.; Maynard, H. D., Electron-Beam Lithography for Patterning Biomolecules at the Micron and Nanometer Scale. *Chemistry of Materials* **2012,** *24* (5), 774-780.

31. Glass, R.; Arnold, M.; Blummel, J.; Kuller, A.; Moller, M.; Spatz, J. P., Micro-nanostructured interfaces fabricated by the use of inorganic block copolymer micellar monolayers as negative resist for electron-beam lithography. *Advanced Functional Materials* **2003,** *13* (7), 569-575.

32. Arnold, M.; Cavalcanti-Adam, E. A.; Glass, R.; Blummel, J.; Eck, W.; Kantlehner, M.; Kessler, H.; Spatz, J. P., Activation of integrin function by nanopatterned adhesive interfaces. *Chemphyschem* **2004,** *5* (3), 383-388.

33. Breshike, C. J.; Riskowski, R. A.; Strouse, G. F., Leaving Forster Resonance Energy Transfer Behind: Nanometal Surface Energy Transfer Predicts the Size-Enhanced Energy Coupling between a Metal Nanoparticle and an Emitting Dipole. *Journal of Physical Chemistry C* **2013,** *117* (45), 23942-23949.

34. Bouchiat, C.; Wang, M.; Allemand, J. F.; Strick, T.; Block, S.; Croquette, V., Estimating the persistence length of a worm-like chain molecule from force-extension measurements. *Biophysical Journal* **1999,** *76* (1), 409-413.

35. Feuz, L.; Strunz, P.; Geue, T.; Textor, M.; Borisov, O., Conformation of poly(L-lysine)-graft-poly(ethylene glycol) molecular brushes in aqueous solution studied by small-angle neutron scattering. *European Physical Journal E* **2007,** *23* (3), 237-245.

36. De Gennes, P., Conformations of polymers attached to an interface. *Macromolecules* **1980,** *13* (5), 1069-1075.

37. Yoshigi, M.; Hoffman, L. M.; Jensen, C. C.; Yost, H. J.; Beckerle, M. C., Mechanical force mobilizes zyxin from focal adhesions to actin filaments and regulates cytoskeletal reinforcement. *Journal of Cell Biology* **2005,** *171* (2), 209-215.

38. Plotnikov, S. V.; Pasapera, A. M.; Sabass, B.; Waterman, C. M., Force Fluctuations within Focal Adhesions Mediate ECM-Rigidity Sensing to Guide Directed Cell Migration. *Cell* **2012,** *151* (7), 1513-1527.

39. Fu, J. P.; Wang, Y. K.; Yang, M. T.; Desai, R. A.; Yu, X. A.; Liu, Z. J.; Chen, C. S., Mechanical regulation of cell function with geometrically modulated elastomeric substrates. *Nature Methods* **2010,** *7* (9), 733-U95.

40. Wang, X. F.; Ha, T., Defining Single Molecular Forces Required to Activate Integrin and Notch Signaling. *Science* **2013,** *340* (6135), 991-994.

41. Borisy, G. G.; Svitkina, T. M., Actin machinery: pushing the envelope. *Current Opinion in Cell Biology* **2000,** *12* (1), 104-112.

42. Wolfenson, H.; Bershadsky, A.; Henis, Y. I.; Geiger, B., Actomyosin-generated tension controls the molecular kinetics of focal adhesions. *Journal of Cell Science* **2011,** *124* (9), 1425-1432.

43. Pellegrin, S.; Mellor, H., Actin stress fibres. *Journal of Cell Science* **2007,** *120* (20), 3491-3499.

44. Oakes, P. W.; Beckham, Y.; Stricker, J.; Gardel, M. L., Tension is required but not sufficient for focal adhesion maturation without a stress fiber template. *The Journal of Cell Biology* **2012,** *196* (3), 363-374.

45. Coussen, F.; Choquet, D.; Sheetz, M. P.; Erickson, H. P., Trimers of the fibronectin cell adhesion domain localize to actin filament bundles and undergo rearward translocation. *Journal of Cell Science* **2002,** *115* (12), 2581-2590.

46. Meyer, R. K.; Aebi, U., Bundling of Actin-Filaments by Alpha-Actinin Depends on Its Molecular Length. *Journal of Cell Biology* **1990,** *110* (6), 2013-2024.

47. Roca-Cusachs, P.; del Rio, A.; Puklin-Faucher, E.; Gauthier, N. C.; Biais, N.; Sheetz, M. P., Integrin-dependent force transmission to the extracellular matrix by alpha-actinin triggers adhesion maturation. *Proceedings of the National Academy of Sciences of the United States of America* **2013,** *110* (15), E1361-E1370.

48. Legant, W. R.; Choi, C. K.; Miller, J. S.; Shao, L.; Gao, L.; Betzig, E.; Chen, C. S., Multidimensional traction force microscopy reveals out-of-plane rotational moments about focal adhesions. *Proceedings of the National Academy of Sciences of the United States of America* **2013,** *110* (3), 881-886.

49. Glass, R.; Moller, M.; Spatz, J. P., Block copolymer micelle nanolithography. *Nanotechnology* **2003,** *14* (10), 1153-1160.

50. Pasch, H.; Schrepp, W., *MALDI-TOF mass spectrometry of synthetic polymers*. Springer: 2003.

3.6 Appendix

bp	DNA Duplex Length (nm)	DNA sequences (5' to 3')
16	6.9	HS-$(CH_2)_6$-GCC TAG AGC ATC AGT G
21	8.6	HS-$(CH_2)_6$-GCC TAT GAA TGA GCT TCA GTG
33	12.7	HS-$(CH_2)_6$-GCC TAT ATA GTC ATC AGC CGT ATA GCA TCA GTG
45	16.8	HS-$(CH_2)_6$-GCC TAT GAA CCG AAT TCG ATA GTC ATC AGC CGT ATA GCA TCA GTG
60	21.9	HS-$(CH_2)_6$-GCC TAT GAA GGA GCT CGC CTA CTA CCG AAT TCG ATA GTC ATC AGC CGT ATA GCA TCA GTG

Table A3.1 DNA strands used to generate the NSET calibration plot to determine d_0. The table displays the number of bases, the calculated end-to-end distance of the duplex, and the composition (shown in 5'-3' orientation) of the thiolated DNA sequence. These strands were hybridized with their fluorescently tagged complements prior to surface immobilization. The calculated length of each DNA duplex assumed a 0.34 nm rise per bp as well as a 1.5 nm length for the two C_6 linkers.

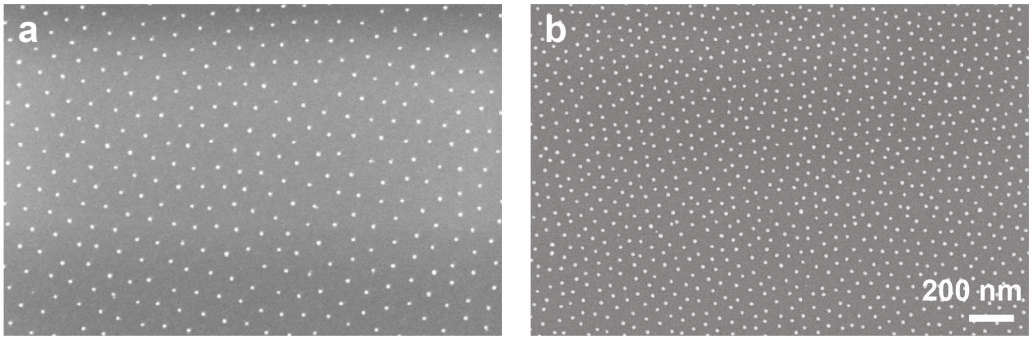

Figure A3.1 Characterization of BCMN patterned AuNP arrays. Representative SEM images of BCMN-patterned 9 nm AuNP arrays with a mean spacing of (a) 99 ± 12 nm and (b) 49 ± 9 nm.

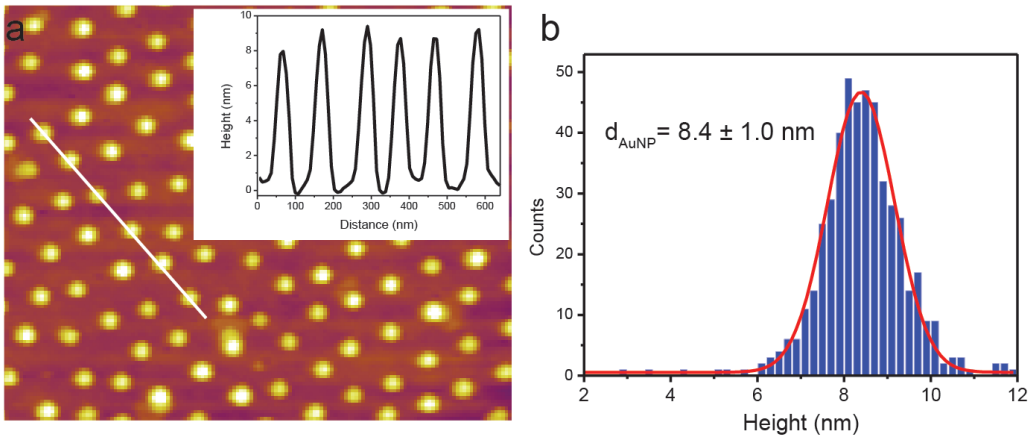

Figure A3.2 Analysis of BCMN-generated AuNP heights using AFM. (a) Representative AFM image of the 99 nm-spaced AuNP array. The white line indicates the region of the image where a linescan analysis was performed on six particles (inset). (b) Histogram showing the height distribution of ~ 400 AuNPs. The histogram was generated by using the IgorPro software package provided with the Asylum MFP-3D AFM system.

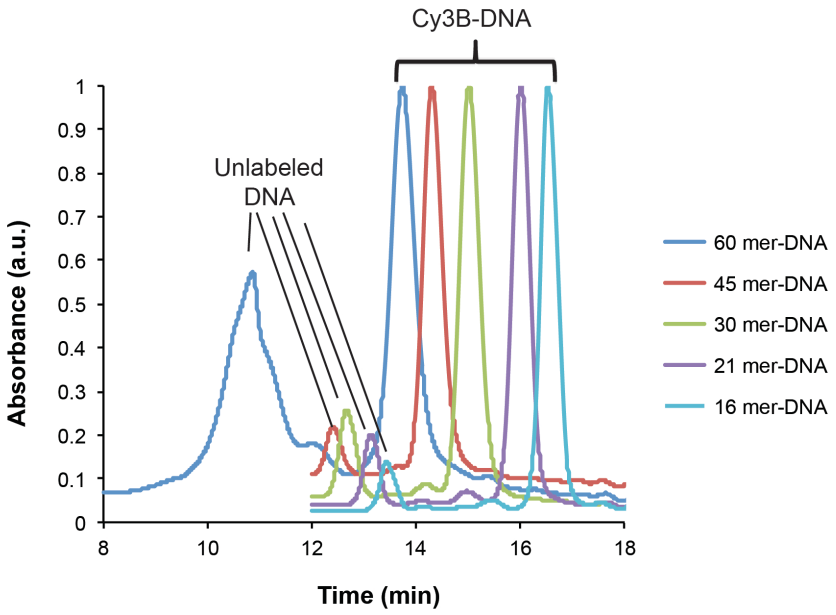

Figure A3.3 Quantification of the value of d_0 in NSET model. A series of overlaid RP-HPLC chromatograms of the products of the reaction between Cy3B-succinimidyl ester and 5 different amine-modified DNA strands in PBS with 0.1 M sodium bicarbonate. The reaction was allowed to proceed overnight, and then the product was initially purified through a size-exclusion column loaded with P-4 gel (Biorad, 4000 M_w cutoff). The reaction product was then injected into the HPLC using the protocol described below.

5' Disulfide-modified oligonucleotides (modification code: /5ThioMC6-D/) were custom synthesized by Integrated DNA Technologies (IDT). The disulfide group was reduced by incubation with 5 nmol of lyophilized oligonucleotide with 100 µL of disulfide cleavage buffer (0.1 M dithiothreitol (DTT), 170 mM phosphate buffer at pH 8.0) for 3 hr at room temperature. The reduced oligonucleotides were then purified using a NAP-5 column (GE Healthcare, Piscataway, NJ) using DI water as the eluent.

5' Amine-modified oligonucleotides (modification code: /5AmMC6/) were custom synthesized by IDT and used without further purification. 10 nmol of the oligonucleotide was reacted with 100 nmol of Cy3B-NHS ester dye in 1X PBS (pH 7.4) for 12 hr at room temperature. The product was subsequently purified by reverse phase HPLC (flow rate 1 ml/min, solvent A: 0.1M DI TEAA, solvent B: 100% acetonitrile, initial condition was 10% B with a gradient of 1% per min). The final concentration was determined by using a Nanodrop spectrophotometer.

Equal amounts of 5'SH-DNA and 5' amine-modified complementary DNA (10% Cy3B labeled, 90% unlabeled) were mixed together at ~25 μM concentrations in 1XPBS and hybridized by heating to 95ºC for 5 min, then cooling at a rate of 3.3 °C/min over a period of 20 min. Afterwards, 8.7 μM of dsDNA was then added to 3.0 mL of 9 nm diameter gold nanoparticles (8.4 nM), bringing the concentration of oligonucleotide and gold nanoparticles to ~2.7 μM, and ~5.8 nM, respectively. The pH of the solution was adjusted to pH 7.4 by adding 296.3 μL of 100 mM phosphate buffer, thus bringing the phosphate buffer concentration to 9 mM. The particles were then stabilized by adding sodium dodecyl sulfate (SDS) to the solution and bringing its final concentration to 0.1% (g/mL) by using a stock solution of 10% SDS. The particles were successively salted with four NaCl additions that were spaced 20 min apart using a stock solution of 2.0 M NaCl. The final NaCl concentration of the DNA-AuNP solution was increased to 0.3 M. The first NaCl addition increased the concentration to 0.05 M, while the remaining three NaCl additions increased the NaCl concentration by 0.1 M increments. The fully salted particles were then incubated overnight, in the dark and at room temperature. The following day, the particles were centrifuged five times and reconstituted in PBS for each wash

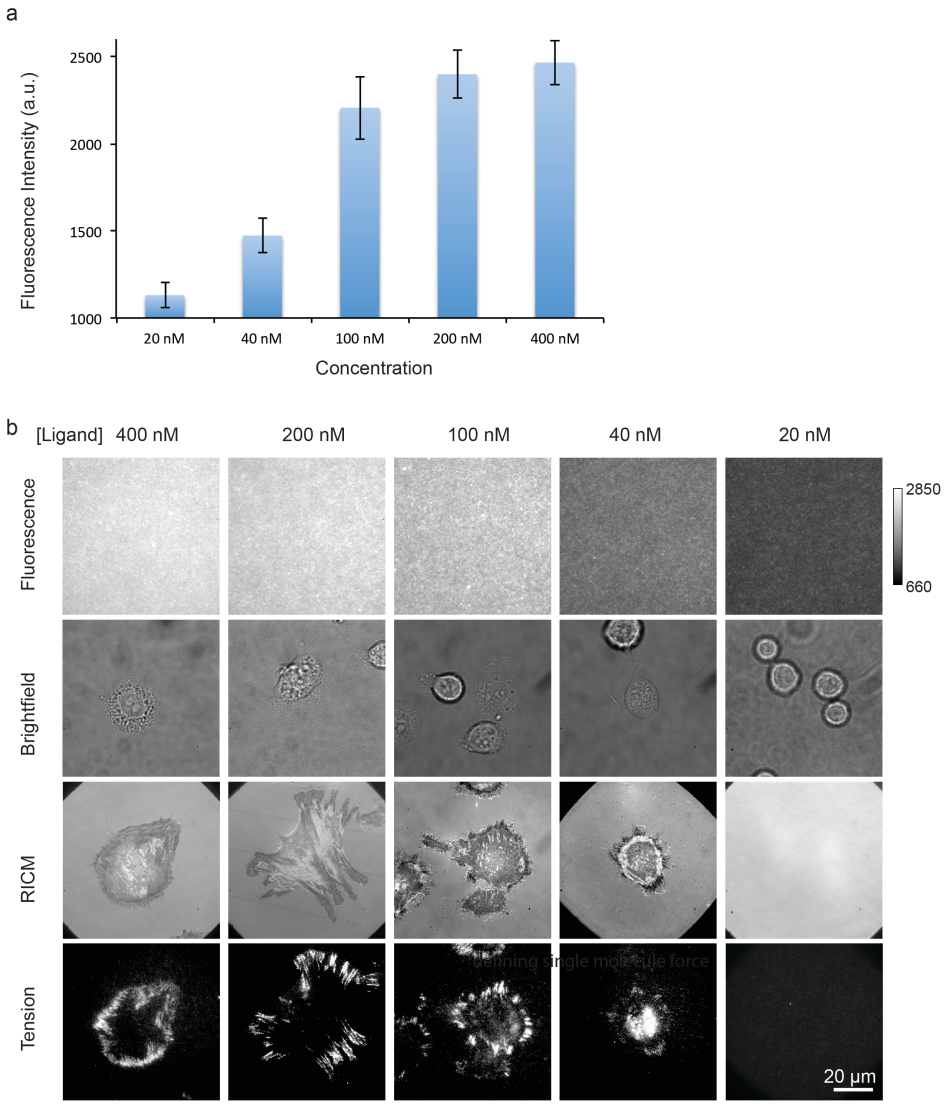

Figure A3.4 Determination of minimal tension ligand concentration. (a) Plot displaying the average substrate fluorescence intensity as a function of incubation concentration of the fluorescent tension ligand. Note that in all incubations, the total thiol concentration was maintained at 40 µM by using a passivating PEG thiol ($SH(CH_2)_2(OCH_2CH_2)_8COOH$). (b) The first row shows representative fluorescence images of the substrate prior to the addition of cells. The brightfield, RICM and tension rows of images show cell adhesion as a function of tension ligand concentration. This data indicates that incubating the substrate with 200 nM of tension ligand along with 39.8 mM of passivating PEG thiol is sufficient for producing robust cell adhesion with minimal fluorescence background intensity.

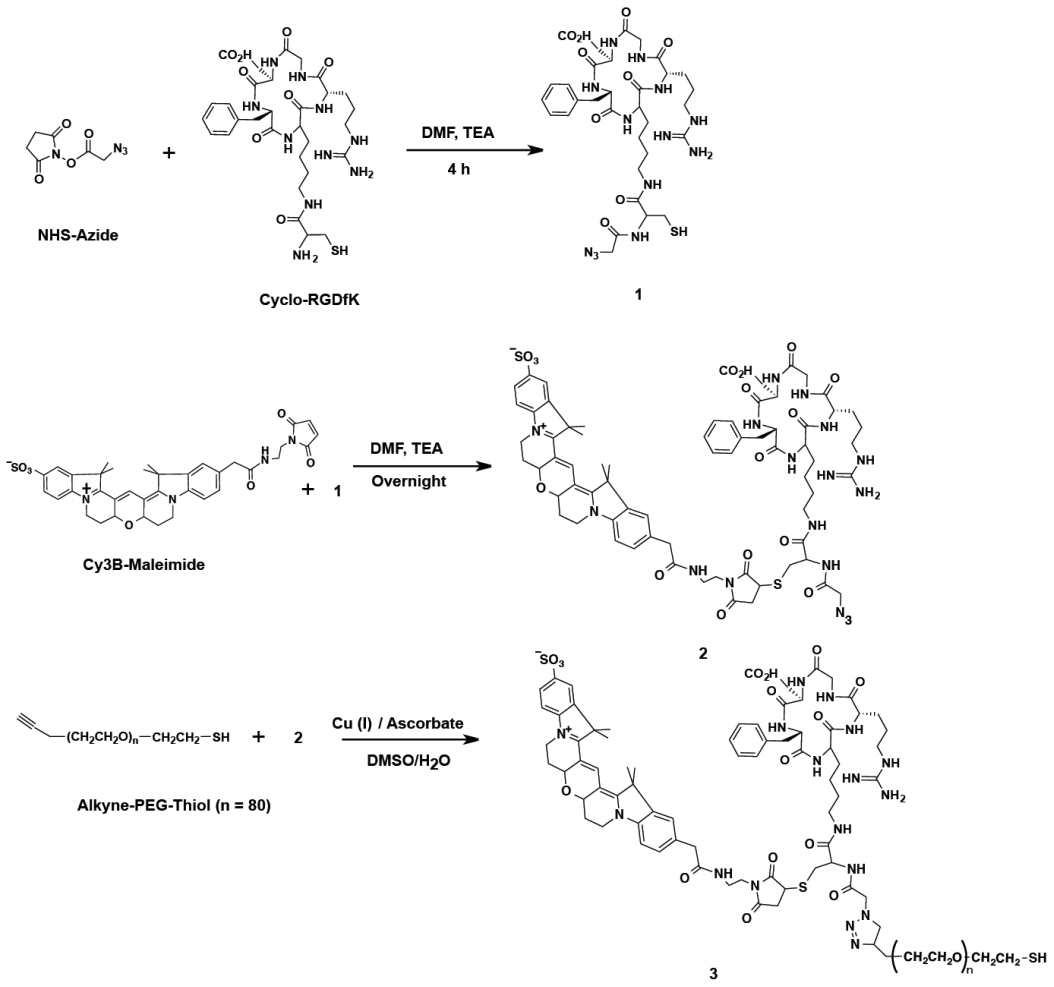

Figure A 3.5 Schematic of chemical synthesis of Cy3B tagged tension sensor ligand.

Synthesis of **1**. 200 μg of cRGDfK(C) peptide (MW: 706.81) was reacted with 0.1 mg azide-NHS linker (MW: 198.14) in 15 μL DMF. To this reaction mixture, 0.1 μL of neat triethylamine was added as an organic base and the reaction was allowed to proceed for 4 hr.

Synthesis of **2**. A 10-fold molar excess of Cy3B-maleimide dye in 10 μL DMF was directly added to eppendorf tube that contained the products of the reaction to generate **1.** 0.1 μL of neat TEA was added and the reaction was allowed to proceed overnight. The product of this reaction, **2**, was subsequently purified by reverse phase HPLC (flow rate 1 ml/min; solvent A: 99.5% DI water, 0.05% TFA; solvent B: 99.5% acetonitrile 0.05% TFA; initial condition was 10% B with a gradient of 1% per min). The sample was then dried in a Speedvac for 6 hr.

Synthesis of **3**. A 0.7 molar ratio of alkyne-PEG-SH (~1 mM) to **2** was dissolved in 10 μL DMSO and 5 μL DI water. 2 μL of 2 M TEAA buffer and 2 μL of 5 mM ascorbic acid was then added to this solution. Finally, 1 μL of Cu(II)SO_4 was added to the solution

and vortexed. The reaction was incubated overnight at room temperature with foil to protect from ambient light. The reaction mixture was then treated with 0.1 M DTT in phosphate buffer for 1 hr to reduce disulfides that formed overnight. Afterwards, size exclusion chromatography was performed with a spin column (cutoff: 4000 MW) to remove all other by-products except the final product **3.** HPLC (method was the same as the one used for **1** and **2** and the chromatogram shown below), and MALDI-TOF (observed mass = 5204.32; calculated mass = 5206.44) were used to confirm the synthesis of **3** with a near 99% purity, which was based on HPLC peak integration.

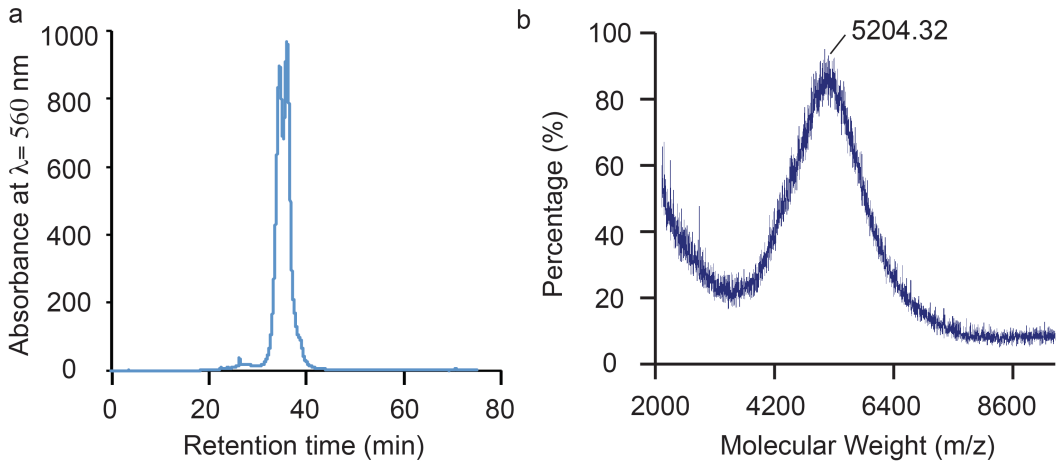

Figure A3.6 HPLC chromatogram (a) and MALDI-TOF spectrum (b) of the final product 3

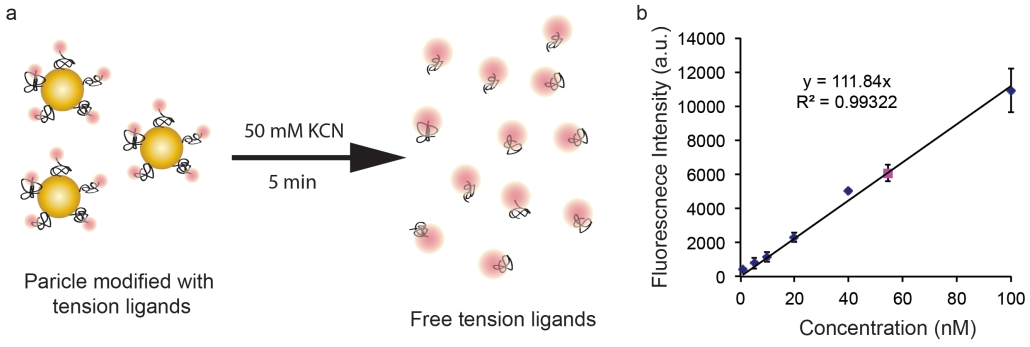

Figure A 3.7 Quantification of the average number of tension sensor ligands per AuNP and the quenching efficiency of Cy3B. (a) Scheme showing the approach used to determine the average stoichiometry between Cy3B-labeled tension probe ligands and AuNP. Briefly, the concentration of AuNP was determined from the absorbance at λ=520 nm. Subsequently, AuNPs were dissolved by treating the sample with 50 mM KCN, which released Cy3B-labeled tension probe ligands within 5 min. The fluorescence intensity of the released Cy3B dye was then used to determine the number of dye molecules in the sample. Note that the quenching efficiency of Cy3B was determined by measuring the fluorescence intensity of the sample before and after AuNP dissolution and using the following relation: $1 - I_{quenched}/I_{de\text{-}quenched}$, and this was determined to be 0.91 in our experiments, indicating an average distance of 8.1 nm between Cy3B dye and AuNP surface. (b) The calibration curve used to quantify the number of tension sensor ligands per AuNP. Blue diamonds represents the calibration curve, while the purple box represents the unknown sample containing the released Cy3B ligands from AuNP-tension probes. All measurements were performed in triplicate.

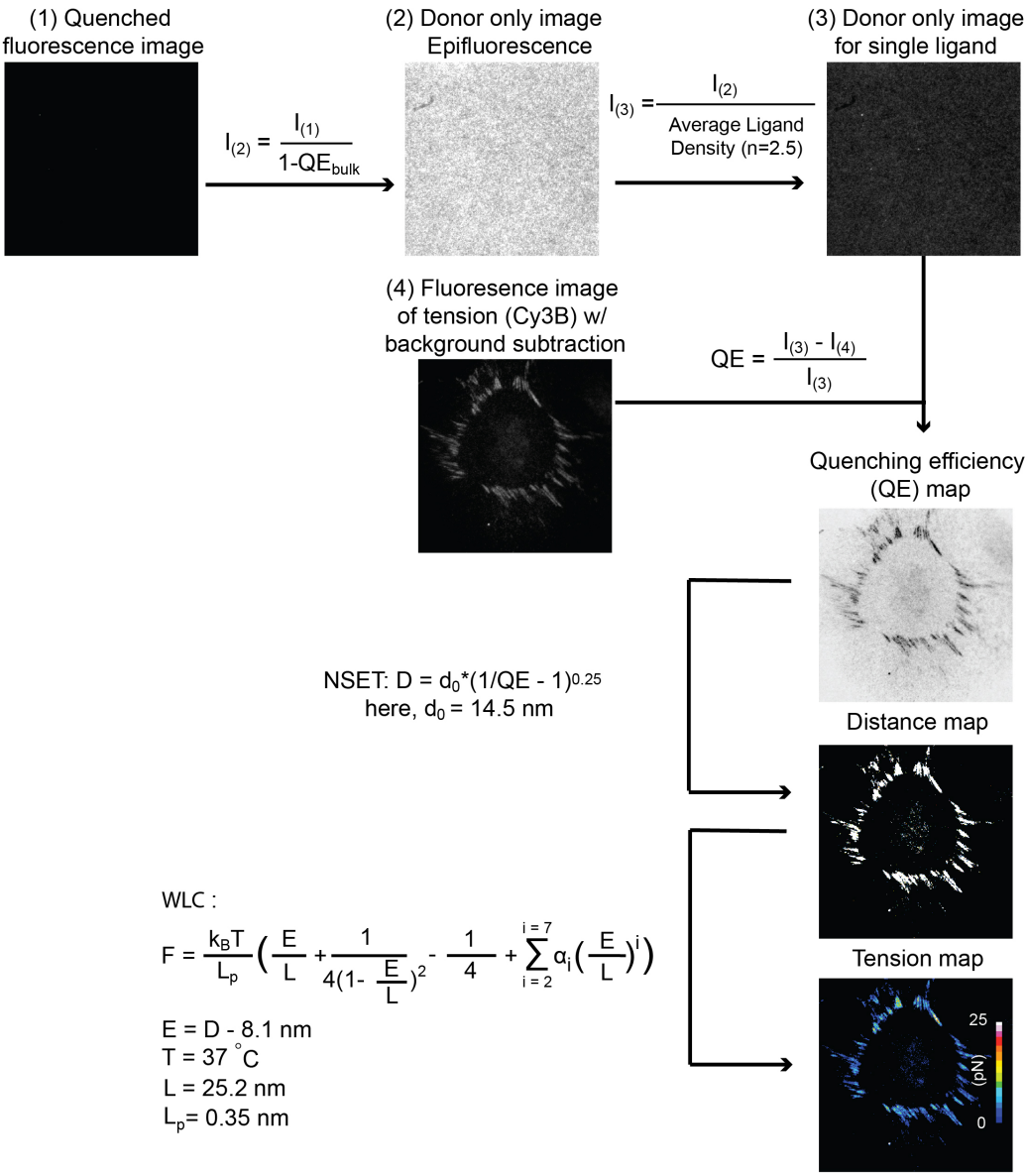

Figure A3.8 Image Analysis. Stepwise image analysis used to relate the raw fluorescence images to a calculated force per integrin. The image analysis employed the NSET and extended WLC models[34].

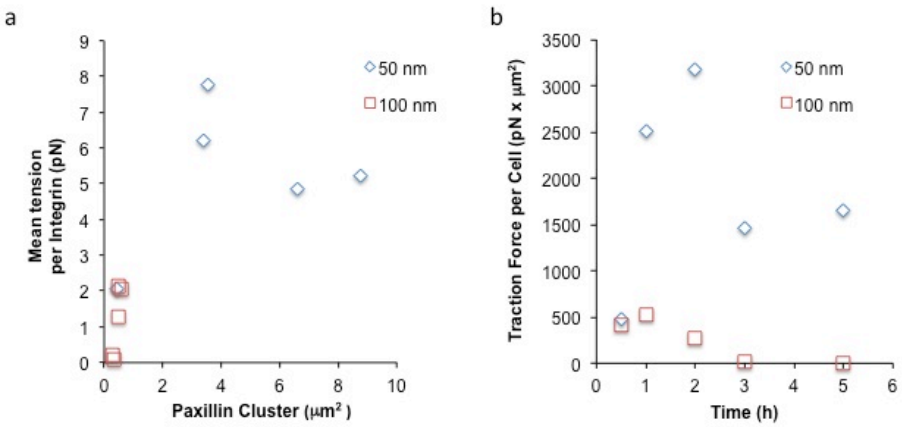

Figure A3.9 Additional analysis for patterned MTFM experiment. (a) Plot showing mean tension per integrin as a function of FA sizes, as indicated by paxillin cluster sizes. (b) Plot showing total traction force per cell as a function of time.

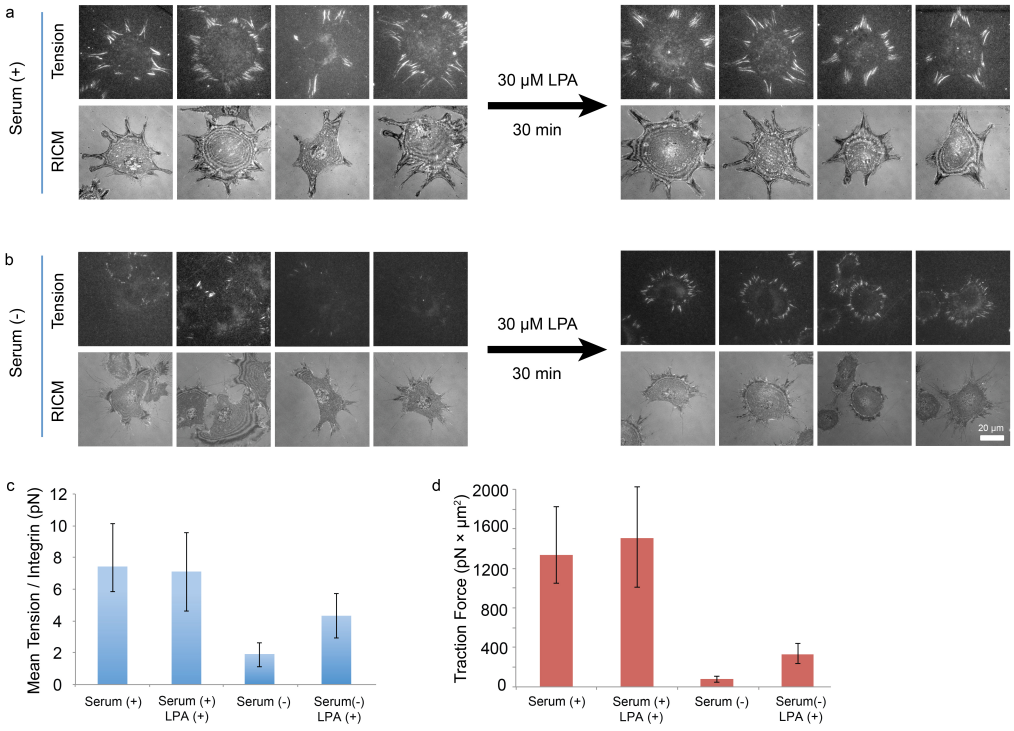

Figure A3.10 LPA Experiment for Testing Tension Saturation. (a) Representative images showing that the addition of 30 μM of Oleoyl-L-α-lysophosphatidic acid (LPA) can enhance the myosin-driven integrin tension as well as FA sizes for NIH/3T3 fibrobalsts cultured in serum-free DMEM medium for overnight. (b-c) Mean integrin tension and total traction force has been measured for cells cultured 5.5 hr in 10% FBS enriched DMEM medium, serum-free medium and serum-free medium with addition of 30 μM LPA for 30 min. Total traction force is calculated as mean integrin tension multiplying the area under tension. Cells are cultured in randomly arranged AuNP-MTFM substrates.

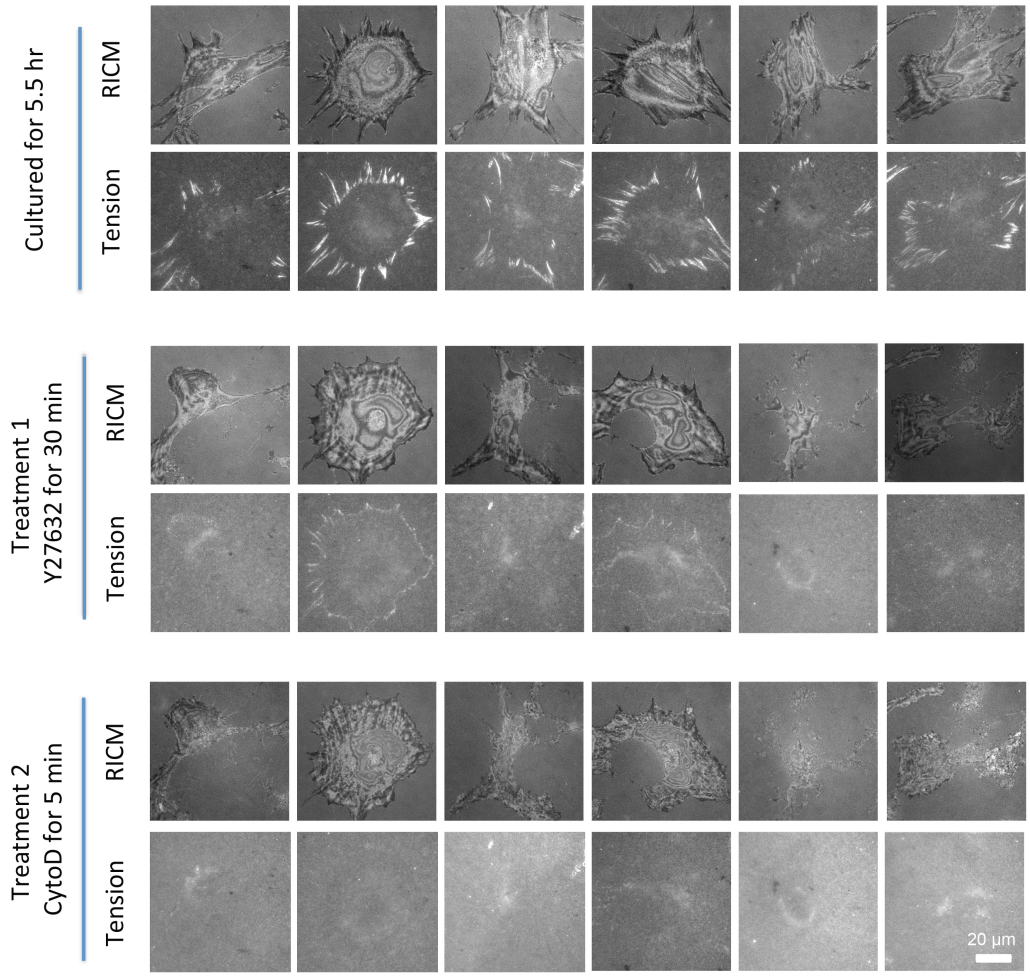

Figure A3.11 Stepwise Inhibition of Integrin Tension Using Pharmacological Drugs. Representative images showing stepwise decrease in tension for 6 NIH/3T3 cells from being cultured for 5.5 hr (top two rows), then with 40 μM ROCK inhibitor (Y-27632) treatment for 30 min (middle two rows) and finally with 10 mM CytoD treatment for 5 min (bottom two rows). Clearly, after ROCK inhibitor treatment, high integrin tension has been reduced to a much lower tension due to cell membrane-driven forces, which have been completely depleted after cytoD treatment.

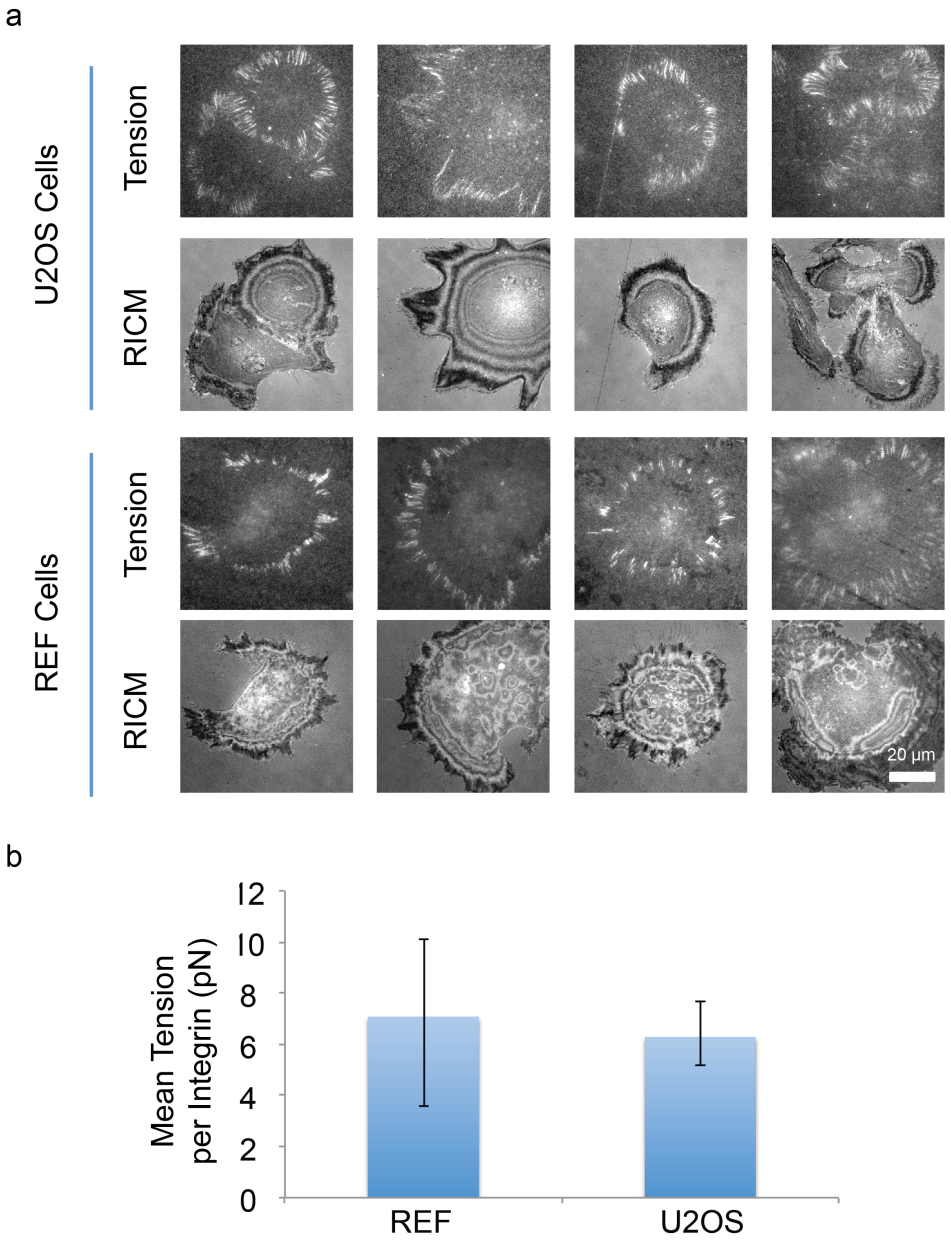

Figure A3.12 Analysis of integrin tension in different cell lines. (a) Representative images showing Rat Embryonic Fibroblasts (REFs) and Human Bone Osteosarcoma Epithelial Cells (U2OS) generated similar level of integrin tension after 1 hr culture on randomly arranged AuNP-MTFM substrates. (b) Quantification of integrin tension for U2OS and REF.

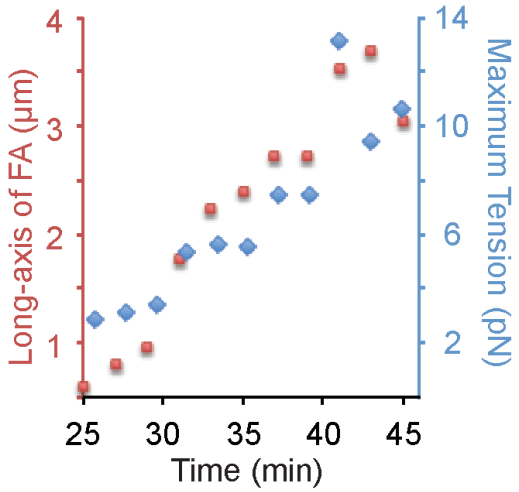

Figure A 3.13 Quantification of FA maturation and integrin tension within single FA. Plot showing the dynamic relationship between the maximum integrin tension within a single FA (right y-axis, blue) and the length of its long-axis (left y-axis, red). The data is analyzed for the highlighted FA shown in Figure 3.5 of main text. The data shows a high correlation between integrin tension and FA size. This finding is in agreement with traction force microscopy-derived for mature FA that is typically several microns in length.

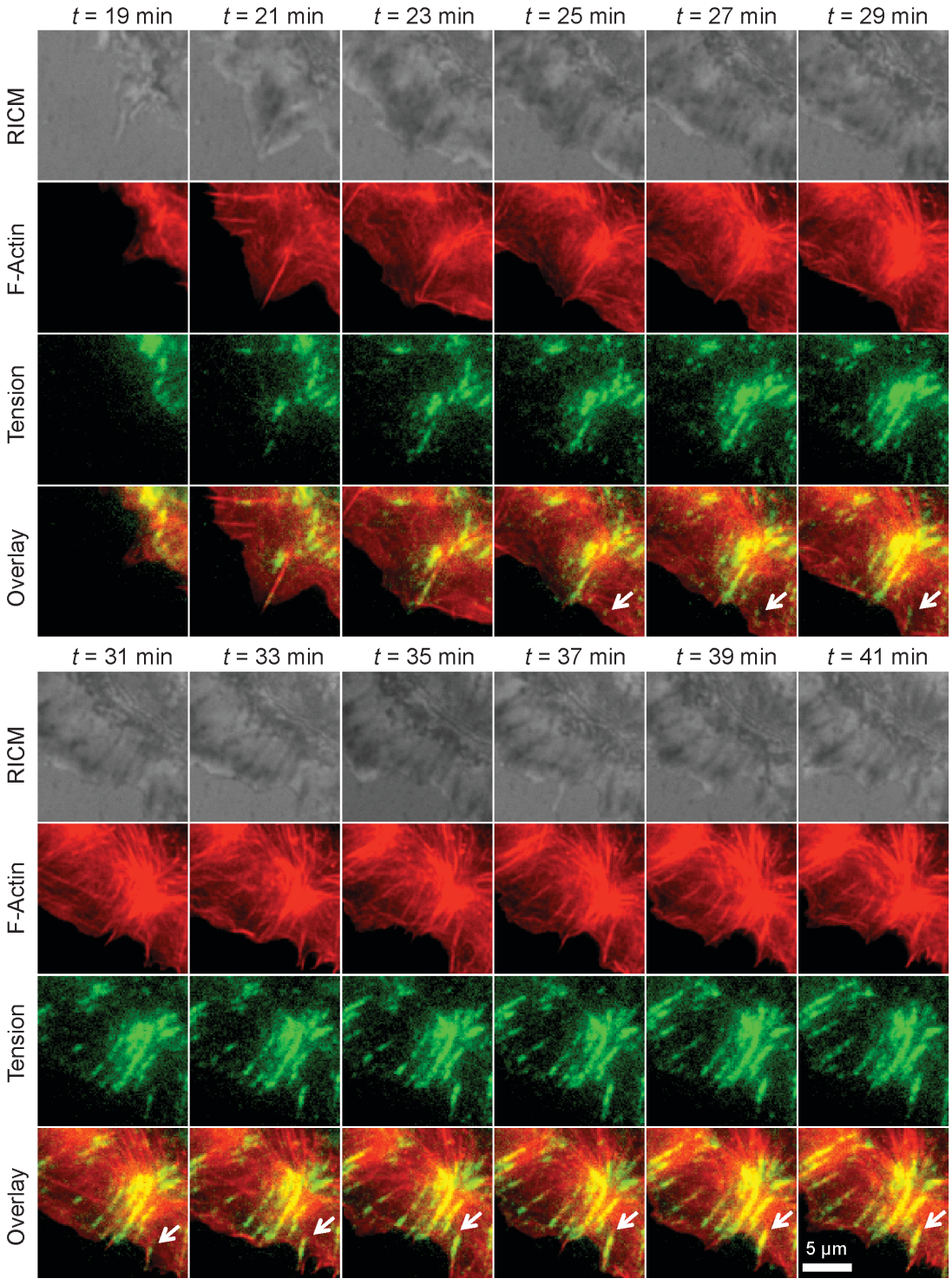

Figure A3.14 Concurrent growth of F-actin template and integrin tension. Timelapse RICM, GFP-lifeAct, integrin tension, and overlay actin-tension images recorded for a 3T3 NIH fibroblast during the initial stages of cell spreading and adhesion. The overlay is shown in the main text in Fig. 4, but here we display the individual fluorescence channels for references.

Chapter 4: Investigating T-cell mechanics with DNA-based AuNP tension probes

Adapted from Liu, Y.; Blanchfield, J. L.; Ma, V.P.; Andargachew, R.; Galior, K.; Liu, Z.; Evavold, B.; Salaita, K. DNA-based Nanoparticle Tension Sensors Reveal that T-cell Receptors Transmit Defined pN Forces to Their Antigens for Enhanced Fidelity. *Proc. Natl. Acad. Sci. USA,* **2016**, 113 (20), 5610-5615

4.1 Introduction

T cell activation is a crucial step in adaptive immunity, offering defense against pathogens and cancer.[1] During activation, the T-cell receptor (TCR) recognizes and binds to its ligand, the antigenic peptide-major histocompatibility complex (pMHC), which is expressed on the surface of antigen presenting cells (APCs). Because T cells are continuously moving and scanning the surfaces of APCs for evidence of antigens, and TCR-ligand binding occurs at the junction between two cells, it is likely that the TCR experiences mechanical forces during normal T cell function. Therefore, an important question in this area pertains to whether the TCR-pMHC complex experiences defined forces during T cell activation and whether these forces influence immune function.[2]

An elegant body of single molecule experiments further underscore the connection between TCR signaling and mechanics. For example, Lang and Reinherz used optical tweezers to demonstrate that the TCR responds to physical forces applied using an optically trapped bead.[3] This team also showed that the TCR undergoes distinct structural transitions within its FG-loop when the pMHC-TCR complex is strained at ~15 pN.[4] Complementary single molecule force spectroscopy measurements using the biomembrane force probe by Zhu and Evavold showed that the average TCR–pMHC bond lifetime ($1/k_{off}$ rate) is enhanced when ~10 pN of tension is applied through a specific antigen.[5] Enhancement of bond lifetime under the influence of antigen mechanical strain (~10 pN) was further demonstrated in CD4+ T cells [6] and for preTCR-pMHC interactions [7]. These experiments specifically demonstrate an inherent TCR sensitivity to pN forces transmitted through its cognate pMHC ligand.[3-8] The role of forces in modulating bond lifetimes is particularly striking, since the most widely

accepted model of TCR activation invokes a kinetic proofreading mechanism, which emphasizes the importance of the TCR-pMHC dissociation rate in boosting antigen specificity.[2, 9] The implicit model is that a T cell actively regulates forces transmitted to its TCR-pMHC complex to fine tune bond lifetimes, thus enhancing selective and differential levels of TCR activation and regulating antigen discrimination and T cell selection.

However, the role of mechanics in T cell activation still remains controversial. Specifically, does the T-cell itself transmit 10-15 pN of tension to its engaged TCR-pMHC complexes during the early stages of antigen proofreading? While traction force microscopy methods demonstrate that T cells generate contractile forces ~5 minutes following activation,[10-11] there is no evidence showing that the TCR-pMHC complex experiences pN forces during initial antigen encounters. Such forces are beyond the spatial and temporal resolution of traction force microscopy. Therefore, new molecular approaches are needed to investigate intrinsic TCR mechanics and to determine the physical basis and physiological consequences of mechanics in immunology.

4.2 Results

4.2.1 Fabrication and characterization of the DNA-based nanoparticle tension sensors

Here, we developed a new type of fluorescent tension probe to directly image and quantify the innate forces mediated by individual TCR complexes upon ligand binding (Figure 4.1A and *Appendix*, Figure A4.1). These probes provide unprecedented sensitivity (see Supplementary Note 1), generating a ~100-fold fluorescence increase in response to pN forces (Figure 4.1B and *Appendix*, Figure A4.2). This sensitivity is essential given the transient nature and the limited number of TCR-pMHC antigens sufficient to activate T cells.[12-13] Briefly, each tension probe consists of a DNA hairpin labeled with a fluorophore-quencher pair, and is immobilized onto a gold nanoparticle (AuNP). The mean interparticle spacing was 48 ± 8 nm (Figure 4.1C), which is physiologically optimal for antigen-mediated T cell adhesion and functional responses.[14-15] Each particle presented an average of 4 ± 1 DNA hairpins (*Appendix*, Figure A4.3). The fluorophore is dual quenched by both the molecular quencher through fluorescence resonance energy transfer (FRET) and the plasmon of the AuNP via nanometal surface energy transfer (NSET) pathway, thus reducing the background signal and boosting sensitivity over conventional molecular tension sensors.[16-22] DNA hairpins generate fluorescence when the applied force exceeds the unfolding force, $F_{1/2}$ (defined as the force at equilibrium for which a hairpin has a 50% probability of unfolding). Note that the probability of mechanical unfolding depends on the loading rate and the duration of the force, and thus the reported $F_{1/2}$ values serve as a lower bound of the applied force given that the physiological loading rates and bond lifetimes are unknown. Importantly,

the $F_{1/2}$ can be tuned from ~2.4 to 19.0 pN through the GC content and stem-loop structure of the hairpin[23] (Table A4.1). Each probe exclusively responds to forces transmitted through a single TCR molecule (*Appendix*, Figure A4.4).

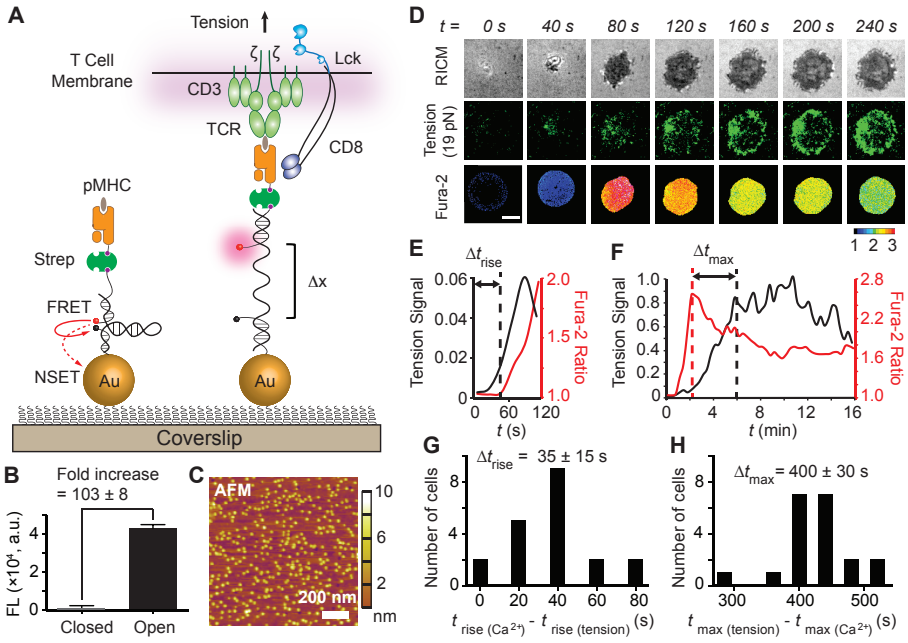

Figure 4.1 T cells apply pN forces to the TCR preceding the rise in Ca^{2+}. (A) Schematic of DNA-based AuNP sensor for mapping TCR-mediated tension. The fluorescence of the Cy3B dye (pink dot) is dequenched upon mechanical unfolding of the hairpin, which separates the dye from the black hole quencher 2 (BHQ2, block dot) and AuNP surface (Δx = ~16.9 nm). (B) Plot showing the fluorescence intensity of the closed and open forms of the hairpin. There is a 103 ± 8 fold increase in fluorescence upon opening of hairpins (error bars indicate standard deviation (SD), n = 3). (C) AFM image showing the immobilized AuNP sensors on a glass coverslip. (D) Simultaneous imaging of cell spreading (Reflection interference contrast microscopy, RICM), 19 pN TCR forces (tension) and T cell activation (fura-2) for a representative OT-1 cell encountering α-CD3 antigen. Unless otherwise noted, all experiments were performed at 23 °C, the temperature at which $F_{1/2}$ values were experimentally determined. Scale bar, 3 mm. (E-F) Representative plots of tension signal and fura-2 ratio showing temporal differences between the initial rise of $[Ca^{2+}]$ and the initial rise in TCR tension (Δt_{rise}) and between the maximum $[Ca^{2+}]$ and the maximum TCR tension signal (Δt_{max}), and for cell shown in D (normalized y-axis applies to E, F). (G-H) Histogram analysis of Δt_{rise} and Δt_{max} (n = 20 cells).

4.2.2 Piconewton forces are transmitted by individual TCR complexes prior to T cell activation

As a proof-of-concept, we used anti-CD3 antibody (α-CD3) modified $F_{1/2}$ =19 pN probes to map TCR forces during the activation of naïve OT-1 cells (Figure 4.1D, $F_{1/2}$ determined at 23 °C, see Supplementary Note 2). Within seconds of encountering the α-CD3 ligand surface, T cells started spreading until reaching ~8-10 mm in diameter. Punctate 19 pN tension signal was also generated within seconds of initial surface contact and progressively increased becoming enriched at the periphery of the contact area in a ring-like pattern. This result provides the first demonstration that the T cell innately transmits pN forces to its TCR complex in a defined spatial and temporal pattern.

Simultaneous tracking of TCR triggering by using a ratiometric fura-2 Ca^{2+} indicator showed that the initial appearance of forces precedes the rise in [Ca^{2+}] by 35 ± 15 s (Figure 4.1D, E, G; n = 20 cells). The initial Ca^{2+} flux was observed ~1 min after initial cell contact, and peaked at ~2 min (Figure 4.1F). Interestingly, the tension signal continued to rise even after the initial Ca^{2+} flux started to subside with a 400 ± 30 s delay between the maximum [Ca^{2+}] and the maximum TCR tension signal (Figure 4.1F and H, n = 20 cells). Therefore, initial TCR triggering is tightly associated with its mechanics, and downstream signaling, such as Ca^{2+} flux, further amplify TCR forces.

Although several lines of evidence demonstrate that actin-mediated cytoskeleton dynamics are crucial in T cell biomechanics [24-26], it remains unclear what cytoskeletal factors specifically initiate the rise of TCR-ligand forces. To address this question, we treated naïve OT-1 cells with a library of cytoskeletal inhibitors and measured cell

spreading and TCR-ligand forces (*Appendix*, Figure A4.5). We found that the GTPase Cdc42 is critical in initiating the rise of TCR-ligand forces. Myosin light chain kinase and Arp2/3 were found to be important in maintaining TCR-ligand forces and their inhibition caused a drastic cell retraction and ring-shaped condensation of tension signals. This result mirrors the disruptive reorganization of F-actin after blebbistatin and Jasplakinolide treatment of Jurkat cells, where actin retrograde flow is hypothesized to exert pushing and pulling forces.[25] Furthermore, immunostaining showed that TCR forces highly co-localized with F-actin and were further surrounded by a slightly inward ring-pattern of myosin light chain kinase (*Appendix*, Figure A4.6). This is consistent with the actomyosin-enriched contraction arc in the lamella.[25] Therefore, TCR-ligand forces are highly regulated by precise coordination between actin dynamics and actomyosin contractility.

4.2.3 TCR-ligand tension requires co-receptor engagement and is modulated by adhesion molecules

Next, we aimed to define the magnitude of innate T cell forces transmitted through the TCR-pMHC bond. We used two DNA tension probes with $F_{1/2}$ = 12 pN or 19 pN and monitored the hairpin unfolding in response to the wild-type N4 ligand, the most potent of the ovalbumin (OVA) antigenic ligands (Figure 4.2A). After allowing naïve OT-1 T lymphocytes to engage the surface for 15 min, cells generated a strong tension signal on the 12 pN probe surface. In contrast, OT-1 T cells failed to unfold the 19 pN sensor (N4 antigen), despite fully spreading on this surface, as determined by reflection interference contrast microscopy (RICM). Since shear flow is known to generate TCR forces,[27] we applied external flow to cells immobilized through the 19 pN probe (with N4 antigen)

and observed a rapid and robust increase in tension signal (*Appendix*, Figure A4.7). This experiment demonstrates that the pMHC-TCR bond can withstand forces greater than 19 pN in the presence of CD8 co-receptor but the innate TCR forces fall within the 12-19 pN range. Thus, TCR mechanics are precisely tuned with an accuracy of a few ~kcal/mol.

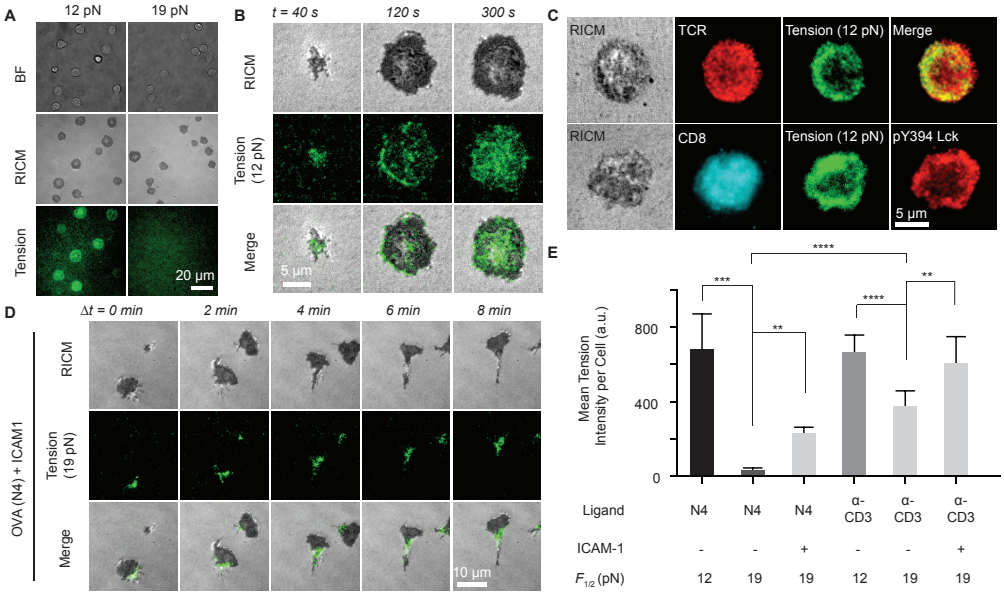

Figure 4.2 The magnitude and spatial organization of TCR-antigen forces are highly dependent on antigen and adhesion receptor binding. (A) Representative brightfield, RICM and tension (12 pN and 19 pN) images of OT-1 cells cultured on tension probe surfaces modified with N4 pMHC. (B) Representative RICM and tension (12 pN) images taken from a timelapse movie for an OT-1 cell upon N4 ligand stimulation (*Appendix*, Movie S3). (C) Representative immunostaining images showing co-localization between TCR and 12 pN tension (top row) and co-localization between active Lck (pY 394), CD8 and 12 pN TCR tension (bottom row) at t = 5min. (D) Representative RICM and 19 pN TCR tension images taken from a timelapse movie for an OT-1 cell upon N4 and ICAM-1 stimulation. (E) Bar graph showing the TCR tension intensity upon ligand stimulation with N4, α-CD3 and ICAM-1. (Error bars represent SD, n = 20 cells, $^{**}P < 0.01$; $^{***}P < 0.001$ and $^{****}P < 0.0001$.)

To determine the characteristic time course of initiating TCR-pMHC forces, we next imaged the surface immediately following culture of naïve OT-1 cells onto 12 pN tension probes. The T cells generated punctate fluorescence tension signal within 40 s of cell-surface contact (Figure 4.2B). This tension signal increased in intensity and spread until it

reached a steady state coinciding with cell spreading as determined by the RICM channel. Spatial analysis at t = 2 min showed that forces were generally concentrated in a ring-like structure 1-2 μm wide at the cell periphery (*Appendix*, Figure A4.8). However, this ring-like distribution was short-lived, becoming diffuse across the junction 2-5 min after cell-surface contact. Subsequently (>5 min), tension was enriched at the center of the contact zone, reminiscent of the central supramolecular activating cluster (c-SMAC).[28]

We further analyzed the spatial colocalization between tension, TCR, CD8 (co-receptor), and lymphocyte-specific kinase (Lck), which are essential for T cell activation.[29-30] In contrast to the tension signal near the cell edge, TCRs were uniformly distributed across the cell-substrate interface (Figure 4.2C). Therefore, the T cell applies force only to a subset of its TCRs. Notably, CD8 was also homogeneously distributed across the cell membrane, while phosphorylated (active) Lck (pY394) was highly co-localized with TCR tension (Pearson correlation = 0.84 ± 0.04, n = 20 cells, Figure 4.2B and *Appendix*, Figure A4.9), further supporting the relationship between mechanics and early signaling. Probing this relation, we treated T cells with a Lck-specific inhibitor [31] before and after cell plating (*Appendix*, Figure A4.10). Inhibition of Lck after cell plating led to a ~20-30% reduction in tension signals, while pre-treatment with Lck inhibitor abolished tension and cell spreading. This abolishment was also achieved by antibody blocking of CD8 co-receptor or with a mutant pMHC that inhibits co-receptor binding (*Appendix*, Figure A4.10). Therefore, the generation of TCR forces > 12 pN requires CD8 co-receptor and its associated Lck.

TCR-pMHC binding is the first step in the TCR triggering cascade that includes a variety of ligand-receptor pairs during T cell-APC contact. For example, adhesion

receptors such as LFA-1 and other co-stimulatory receptors also bind to their ligands at the intercellular junction, which has been proposed to modulate TCR-pMHC forces.[32] A binary surface co-presenting ICAM-1 ligands and the N4 ligands was engineered using orthogonal chemistry such that TCR forces were exclusively visualized and quantified through the N4 antigen and without convolution from adhesion-mediated forces (Figure 4.2D and *Appendix*, Figure A4.11). Our results show that the incorporation of ICAM-1 not only led to enhanced TCR forces beyond 19 pN, but it also triggered a profound change in T cell morphology and motility. Shortly after engaging the surface (1-5 min), OT-1 cells polarized, forming a kinapse structure that coincided with cell migration at velocities of ~1-2 mm/min. TCR forces were primarily observed at the trailing edge (focal zone) of the T cell, which agrees with a recent model integrating cell motility (surveillance) and TCR signaling.[33-34] Figure 4.2E summarizes the average TCR forces with N4 and a-CD3 ligands and also the role of ICAM-1 in modulating this force (n = 20 cells per group). These data unambiguously show that TCR forces are regulated by antigen and adhesion ligand engagement.

4.2.4 T cells harness mechanical forces as a checkpoint of antigen quality

A key property of T cells is their ability to differentiate nearly identical pMHC ligands with distinct levels of response.[35-36] We asked whether TCR mechanics contribute to the specificity of its response to antigen. To answer this question, we used the less potent ligands Q4 and V4, differing by single amino acid mutations at the fourth position [36] and compared tension signals with that of the OVA N4 antigen. As an initial test, time-lapse imaging showed that the TCR mechanically interrogates the less potent V4 ligand with > 12 pN forces, albeit at differing time scales (*Appendix*, Figure A4.12A). TCR-pMHC

forces were more transient and punctate for V4, in contrast to the greater mechanical response to N4 ligand (*Appendix*, Figure A4.12B). Moreover, the delay between the rise in [Ca^{2+}] and the rise in tension exceeds 5 min for V4, further confirming that TCR-pMHC mechanics are associated with early antigen discrimination.

To relate TCR mechanics with T cell functional response, we plated naïve OT-1 cells onto 12 pN tension sensors displaying N4, Q4, and V4 OVA pMHCs as well as α-CD3. Simultaneously, T cell activation was measured by quantifying the immunofluorescence of Zap70 phosphorylation (pY319) when Cdc42-mediated tension was chemically inhibited and compared to the DMSO control (Figure 4.3A). The tension signal and ligand potency decreased from a-CD3, to N4, Q4, and V4 (Figure 4.3B-C, red bars). Ligand potency was consistent with literature values determined using interferon gamma (IFNg) production.[36] When the Cdc42 inhibitor (ML141) was used, there was a marked reduction of TCR tension and T cell activation (Figure 4.3B-C, blue bar). Plotting the total TCR tension against Zap70 phosphorylation showed a strong correlation (Figure 4.3D, Pearson correlation = 0.99), further supporting a strong relationship between TCR tension and T cell activation. Importantly, the range of T cell responses are dampened upon Cdc42 inhibition, indicating that TCR tension and ligand discrimination are related.

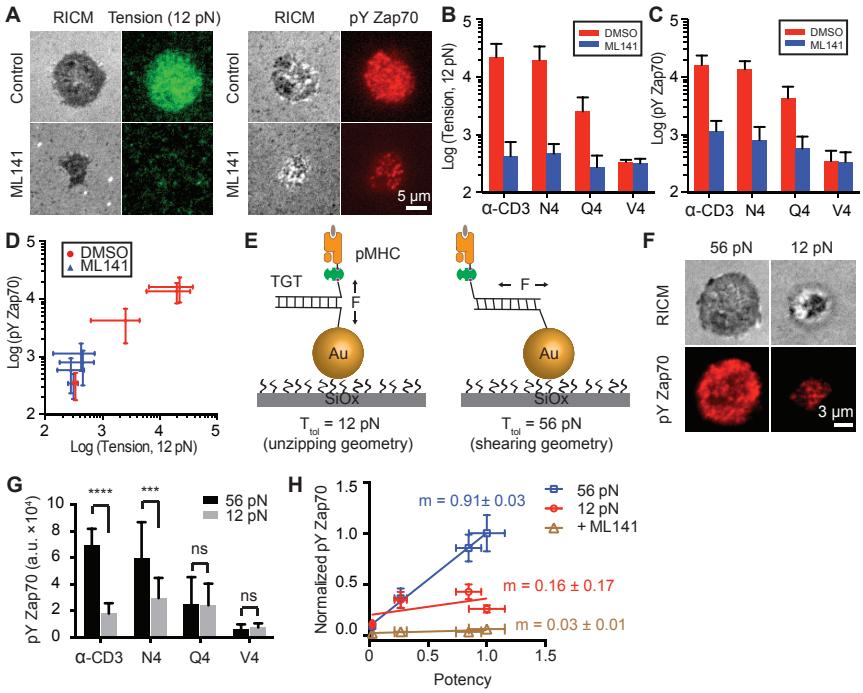

Figure 4.3 TCR forces enhance antigen specificity. (A) Representative images showing TCR tension and pYZap70 upon N4 stimulation with or without ML141 treatment for 30 min. (B-C) Bar graphs quantifying TCR tension signal (b) and pYZap70 staining levels (c) for single OT-1 cells upon ligand stimulation with α-CD3, N4, Q4, and V4 antigens. (Error bars represent SD, n = 20 cells for each group). (D) Plot showing the correlation between TCR tension signal and pYZap70 levels for different ligands. (E) Schematic showing TGTs for modulating TCR forces and T cell activation. TGTs in an unzipping mode (12 pN) or in a shearing mode of TGT (56 pN) were immobilized onto the 9 nm AuNP through Au-thiol interaction. Different ligands were conjugated to the TGTs through biotin-streptavidin binding. (F) Representative images showing differential T cell activation on N4 pMHC modified 12 pN TGT compared to the 56 pN TGT. (G) Bar graph showing pYZap70 levels upon stimulation with pMHCs anchored through the 12 or 56 pN TGT at 37 °C. (Error bars represent SD, from n = 20 cells for each group, ***P < 0.001 and ****P < 0.0001). (H) Plot of pYZap70 levels in response to ligands with increasing potency. The slope (m) indicates the T cell specificity to different ligands. (Error bars represent SEM, n = 20 cells from triplicate measurements).

We next adapted the recently reported DNA tension gauge tether (TGT) [37-38] into our AuNP platform to physically modulate TCR forces (Figure 4.3E). The TGT is a DNA duplex tailored to dissociate at force levels that exceed its mechanical tolerance, T_{tol} (defined as the rupture force when a constant force is applied for 2 sec). In this way, the chemical recognition (affinity) between the TCR and antigenic ligand is maintained,

however the TGT sets the upper limit of forces experienced between a cell-surface receptor and its ligand. Given that TCR forces are in the range of 12-19 pN for the N4 antigen (Fig. 2D), we designed ligands anchored through previously validated TGTs with T_{tol} of 56 pN and 12 pN (Table A4.1), which provide the largest possible difference in mechanical resistance (T_{tol} determined at 37 °C, see Supplementary Note 2). Indeed, the 12 pN TGT presenting a-CD3 displayed greater dissociation compared to the 56 pN TGT (*Appendix*, Figure A4.13). After culturing naïve OT-1 cells for 30 min onto the 12 pN and 56 pN TGTs surface decorated with N4, Q4, and V4 OVA pMHCs as well as a-CD3, T cell activation was quantified using pYZap70 (pY319) (Figure 4.3F-G). Note that all TGT experiments were performed at 37 °C, the temperature at which T_{tol} values were determined. Interestingly, the most potent ligands a-CD3 and N4 displayed the greatest pYZap70 levels when tethered through the 56 pN TGT and displayed a significant reduction in activation for the 12 pN TGT. Thus more potent ligands display enhanced T cell triggering by pulling force >12 pN. The less potent Q4 and V4 antigens did not show differential response to force (Figure 4.3G). Therefore, T cell activation levels are sensitive to the amount of self-generated force transmitted to the different TCR-pMHC bonds, allowing for the optimal (more potent) ligands to selectively benefit from intensified mechanical tension. With the 12 pN TGT, ligand potency is statistically similar across the different antigens. Capping TCR-pMHC force to 12 pN likely leads to dampening differences in TCR-pMHC dwell times.[39] When the cell is allowed to intensify TCR-pMHC tension before it dissociates, the tested ligands further resolve with different levels of pYZap70 and functional responses. This is shown graphically by plotting the pYZap70 levels against ligand potency (Figure 4.3H). Taken together, these

experiments demonstrate that cell-generated forces transmitted to the TCR-pMHC bond amplify the specificity of antigen recognition, which is a required feature of T cell function.

4.3 Discussion and Conclusion

We imaged TCR forces with the highest spatial and temporal resolution reported to date using a new class of molecular tension sensors. For the first time, we reveal that naïve T cells generate forces in the 12-19 pN range during initial antigen recognition (Figure 4.2 and *Appendix*, Figure A4.12). Importantly, our results complement and further validate the physiological relevance of a significant body of single-molecule measurements showing that external forces, in the ~10-20 pN range, drive structural transitions in the TCR and enhance the TCR-pMHC bond lifetime for strong agonists.[4-5, 7] It is no coincidence that the T-cell strains its TCR-pMHC complexes to tension values that are similar to those that achieve maximal "catch bond" behavior (a counter-intuitive enhancement in bond lifetime that occurs when a bond experiences mechanical strain) as determined in single molecule experiments. Our results also suggest that agonists, both strong and weak, experience a pN mechanical stringency test, but strong agonists selectively display enhanced activation presumably due to enhancement in bond lifetime. T cells harness mechanical forces to aid in discrimination between strong and weak agonists by inducing differential phosphorylation level of Zap70 (Figure 4.3), further supporting the force-dependent mechanisms of T cell activation.[40] Given that LFA-1 engagement is not required to generate TCR-pMHC tension, mechanical testing of antigen seems to be independent of T-cell migration processes.

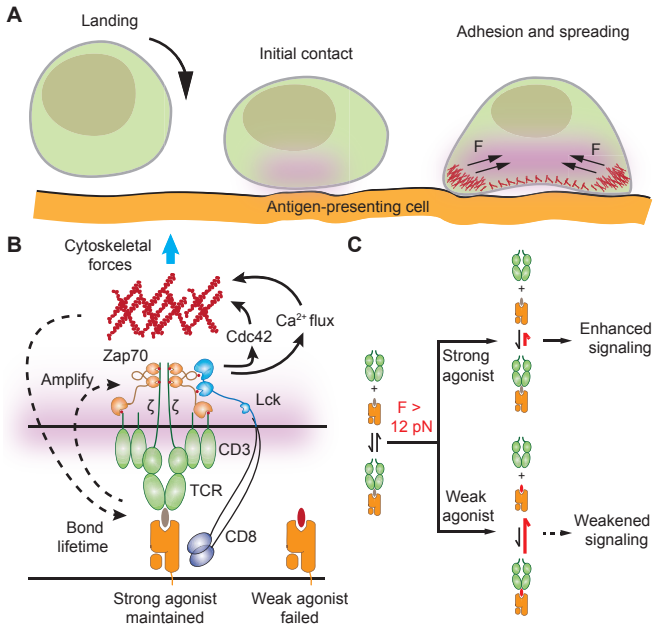

Figure 4.4 Proposed model for T cell force generation and antigen discrimination. (A) Initial ligand-receptor engagement occurs when a T cell physically encounters an antigen-presenting cell. If strong pMHC agonists are encountered, the TCR is triggered and the initial signal is amplified, leading to cell adhesion, spreading and force enhancement. (B) Speculative model depicting how T cells harness a chemo-mechanical feedback mechanism to increase the specificity of TCR signaling and distinguish between strong and weak agonists. The chemical triggering of TCR activates cytoskeletal processes which further enhance mechanical testing of the TCR-pMHC bond. (C) Our data shows that TCR-pMHC complexes experience tension greater than 12 pN during initial ligand-receptor sampling and engagement. Moreover, we find that TCR-pMHC forces greater than 12 pN lead to greater levels of downstream signaling for strong agonists compared to the levels achieved through weaker agonists. The mechanism of differential response to force is likely through catch bond behavior as shown in Liu et al.'s work.[5]

Our data also points to a dual role for mechanics in T cell function (Figure 4.4). First, TCR-pMHC forces are involved in initial ligand discrimination as a fidelity checkpoint. As discussed above, T-cells likely harness mechanics to maximize the TCR-pMHC bond lifetime for cognate ligands. Second, following T cell triggering and Ca^{2+} flux, myosin contractility is enhanced, thus further mounting TCR forces which leads to cell spreading. This, in turn, will increase the number of TCR-pMHC engagements at the T cell-APC junction by simply flattening the cell-cell interface (Figure 4.4A). This chemo-

mechanical feedback maximally amplifies the distinct TCR signaling levels between strong and weak agonists, demonstrating a mechanically regulated model for antigen discrimination (Figure 4.4B and C).

By decorating the tension sensor with different ligands, we show that the magnitude of TCR forces are significantly lower in response to cognate N4 antigen compared to the a-CD3 ligand (Fig. 2) and this conclusion is not simply a result of selective bond rupture, rather T cells selectively transmits forces to a subset of engaged receptors (*Appendix*, Figure A4.10B). These data suggest the existence of a self-regulatory mechanism for fine-tuning of force generation. The observations that CD8 binding and Lck kinase activity are essential in mediating force generation (*Appendix*, Figure A4.9), suggest chemical mechanisms of force regulation.

LFA-1/ICAM-1 binding results in a migratory phenotype of OT-1 cells and also generates a higher level of TCR-pMHC tension within the focal zone (Fig. 2 and *Appendix*, Movie S4), where adhesion molecules including CD2,[41] talin [42] and Rho-associated kinase (ROCK) [43] are enriched. Our data supports the emerging motile synapse model in migratory OT-1 cells [33] and further demonstrates an active crosstalk between TCR signaling and LFA-1 activation. Since T cell migration relies on LFA-1 mediated detachment of the trailing edge (focal zone), our observation points to an idea that TCR signaling is coupled to and modulated by mechanics in the kinapse during lymphocyte surveillance and immune function.

Lastly, our method provides the first platform to decouple the specific forces transmitted through the TCR from those forces that are mediated by LFA-1/ICAM-1 interactions (Figure 4.2C and *Appendix*, Figure A4). In principle, the high modularity of

the method should permit a generalization to investigate the mechanics of any specific surface receptors in the context of other intercellular interactions (e.g. receptor-ligand and glycan-glycan interactions), which normally show synergistic effects at the cellular level. This novel design of molecular tension sensor better resembles the complex nature of cell-cell junctions and provides a readout of mechanics with molecular specificity that is beyond the capabilities of conventional traction force microscopy and single-molecule force spectroscopy methods.

4.4 Materials and methods

4.4.1 Chemical reagents

(3-Aminopropyl) trimethoxysilane (97%, APTMS), triethylammonium acetate (TEAA), hank's balanced salts, $NiSO_4.6H_2O$, Lck inhibitor (7-cyclopentyl-5-(4-phenoxyphenyl)-7H-pyrrolo[2,3-d]pyrimidin-4-ylamine), ROCK inhibitor (Y-27632), MLCK inhibitor (ML-7), F-actin inhibitor (Cytochalasin D), Arp2/3 inhibitor (CK-666), Rac1 inhibitor (NSC23766) were purchased from Sigma-Aldrich (St. Louis, MO) and used without further purification. Cdc42 inhibitor (ML141) was purchased from Santa Cruz Biotech (Dallas, Texas). The fluorescent dye Cy3B-NHS ester was purchased from GE healthcare Bio-Science (Pittsburgh, PA). Number two glass coverslips, ascorbic acid (>99.0%), and 96-well plates were purchased from Fisher Chemical & Scientific (Pittsburgh, PA). DMF (>99.5%), DMSO (99.5%) and sodium bicarbonate (99.0%) were purchased from EMD chemicals (Philadelphia, PA). P2 gel size exclusion beads were acquired from Biorad (Hercules, CA). Lipoic Acid-PEG-NHS (MW 3400) and mPEG-NHS (MW 2000) were purchased from Nanocs (New york, NY). NTA-SAM reagent was purchased from Dojindo (Rockville, Maryland). Recombinant mouse ICAM-1 Fc histag

protein (catalog # 83550) was purchased from biorbyt (San Francisco, CA). AuNPs were custom synthesized and characterized by TEM by Nanocomposix (San Diego, CA). Based on TEM analysis that was provided by the manufacturer, the mean diameter of these particles was 8.6 ± 0.6 nm.

4.4.2 Antibodies

Alexa fluor 647 conjugated anti-TCR antibody (catalog # HM3621) and phalloidin (A22287) was purchased from Life technologies (Grand Island, NY). Anti-Myosin light chain kinase antibody (EP1458Y) was purchased from Abcam (Cambridge, MA). Alexa fluor 647 conjuagted anti-Zap70 (pY319) was purchased from BD Bioscience (catalog # 557817). p-Lck (Tyr 394) rabbit polyclonal IgG was purchased from Santa Cruz (catalog # sc-101728). Anti-mouse CD3 epsilon antibody (catalog # 16-0031) was purchased from ebioscience (San Diego, CA). Anti-mouse CD8a blocking antibody (catalog # CL168AP) was purchased from Cedarlane (Burlington, NC). Secondary antibodies, including Alexa fluor 488 goat anti-rat IgG (H+L), Alexa fluor 488 goat anti-rabbit IgG (H+L) and Alexa fluor 647 goat anti-rabbit IgG (H+L), were purchased from Life technologies (Grand Island, NY).

4.4.3 MHC

Biotinylated H-2K(b) monomers were provided by the National Institutes of Health Tetramer Core Facility at Emory University. Monomers are comprised of the designated peptide loaded in the alpha chain of mouse H-2K(b) that is complexed with beta-2-microglobulin (b2m) from either mouse or human origin. In some experiments, the H-2K(b) alpha chain was mutated to prevent the binding of the CD8 co-receptor and these

monomers are designated mut to distinguish them from wild type H-2K(b). Specifically, the mouse alpha 3 domain of H-2K(b) was substituted with the alpha 3 domain of human HLA-A2. The peptides folded into the monomers include the cognate chicken ovalbumin 257-264 epitope SIINFEKL (N4) as well as altered forms of the peptide SIIQFEKL (Q4) and SIIVFEKL (V4); more specifically the monomers are designated wild type mouse b2m N4, mut mouse b2m N4, wild type mouse b2m V4 and mouse or human b2m Q4. As a negative control to show specificity, we used the wild type H-2K(b) with human b2m and the GP33-41 epitope of lymphocytic choriomeningitis virus (LCMV).

4.4.4 OT-1 cell harvesting and purification

OT-1 T cell receptor transgenic mice were housed and bred in the Division of Animal Resources Facility at Emory University in accordance with the Institutional Animal Care and Use Committee. OT-1 T cells express the CD8 co-receptor and specifically recognize chicken ovalbumin epitope 257–264 (SIINFEKL) in the context of the MHC allele H-2K^{b}. Naïve OT-1 T cells were enriched from the spleen using magnetic activated cell sorting according to manufacturer instructions provided with the CD8a+ T cell Isolation Kit (Miltenyi Biotec). Briefly, a single cell suspension of splenocytes was obtained and incubated with biotinylated antibodies specific for unwanted splenic cell populations. These populations were separated from the OT-1 T cells following incubation with anti-biotin magnetic beads and enrichment on a magnetic column. Purified T cells were washed in complete RPMI media [1x RPMI 1640 (Corning), 10% heat-inactivated fetal bovine serum albumin, 10 mM HEPES buffer (Corning), 50mg/mL gentamicin solution (Corning), 5 x 10^{-5} M 2-mercaptoethanol and 2 mM L-glutamine (Sigma-Aldrich) and analyzed for purity on the same day.

4.4.5 DNA sequences

All DNA strands used were custom synthesized and desalted by Integrated DNA Technologies (Coralville, Iowa), except that quencher strand was synthesized by Biosearch technologies (Petaluma, CA) (*Appendix,* Table A4.1).

4.4.6 $F_{1/2}$ calculation for 35% GC content hairpin (12 pN)

The following $F_{1/2}$ calculation was primarily based on the assumptions and measurements used by Woodside et al.[23] The total free energy of the hairpin can be described as follows:

$$\Delta G(F,x) = \Delta G_{fold} + \Delta G_{stretch} + F \times x \qquad \text{(eq. 1)}$$

, where ΔG_{fold} is the free energy of unfolding the hairpin at $F = 0$, F is the externally exerted force, x is the hairpin extension and $\Delta G_{stretch}$ is the free energy of stretching the ssDNA from $F = 0$ to $F = F_{1/2}$, and can be calculated from worm-like chain model as follows:

$$\Delta G_{stretch} = \frac{k_B T}{L_p} \frac{L_0}{4\left(1-\frac{x}{L_0}\right)} \left[3\left(\frac{x}{L_0}\right)^2 - 2\left(\frac{x}{L_0}\right)^3 \right] \qquad \text{(eq. 2)}$$

where L_p is the persistence length of ssDNA (~ 1.3 nm), L_0 is the contour length of ssDNA (~ 0.63 per nucleotide and ~ 27.7 nm for 44 nucleotides), x is the hairpin extension from equilibrium and was calculated by using (0.44 - (n-1)) nm, and k_B is the Boltzmann constant and T is temperature. To use these equations and estimate the $F_{1/2}$ for each hairpin probe, we determined the sum of ΔG_{fold} and $\Delta G_{stretch}$, and estimated the hairpin displacement needed for unfolding, Δx, by using ((0.44 × (n -1))-2) nm, where n represents the number of bases comprising the hairpin. Note that we subtract a distance of

2 nm because this corresponds to the initial separation between the hairpin termini, which is set by the diameter of the hairpin stem duplex (effective helix width). When $F = F_{1/2}$, then the free energy of the transition equals zero and the $F_{1/2}$ can be rearranged as follows:

$$F_{1/2} = \frac{(\Delta G_{fold} + \Delta G_{stretch})}{\Delta x} \qquad \text{(eq. 3)}$$

In our calculations, $\Delta G_{stretch}$ was determined using equation 2 without modification. ΔG_{fold} was determined using nearest neighbour free energy parameters obtained from the IDT oligoanalyzer 3.1, which uses the UNAfold software package. Eq. 3 was used to infer the $F_{1/2}$ (12.0 pN, see *Appendix*, Table A4.2)for tension probes at experimental conditions (23 °C, 137.3 mM Na^+ and 0.8 mM Mg^{2+}).

$F_{1/2}$ calculation for 100% GC content hairpin (19 pN) is 19.9 pN. However, this hairpin has been experimentally tested and reported[19, 23]. The experimental calibration indicates a $F_{1/2}$ of 19.3 pN. Therefore, we refer to this as the 19 pN hairpin throughout the paper.

4.4.7 Surface Preparation

No.2 glass coverslips were rinsed and sonicated with nanopure water (18.2 MΩ cm^{-1}) for 30 min, and then sonicated with acetone for 15 min. The cleaned slides were then dried in an oven set at 80 °C for 10 min. Fresh piranha solution (7:3 v/v = H_2SO_4: H_2O_2) was mixed and then used to clean the substrates for 30 min. Afterwards, the substrates were rinsed with copious amount of nanopure water. The substrates were then sonicated in acetone to remove excess water and to further clean the substrate. Subsequently, 1% v/v APTMS solution in acetone was added to the slides and incubated for 2 h. The amine-modified coverslips were then rinsed in acetone and water and dried under a stream of N_2.

The slides were then annealed for 1 h at 80 °C. The surface was then passivated with 5% w/v mPEG-NHS (MW 2000) and 0.5% w/v lipoic acid-PEG (MW 3400) in 200 μl of 0.1 M fresh sodium bicarbonate solution. After overnight incubation at 4 °C, the excess unreacted PEG molecules were rinsed with nanopure water. This strategy affords a glass surface with sufficient lipoic acid groups to irreversibly anchor AuNP MTFM sensors at appropriate densities. Finally, coverslips were incubated with 20 nM of unmodified 9 nm AuNP solution for 30 min and then rinsed with nanopure water to remove nonspecifically bound particles.

The DNA tension probe hairpins were assembled in 1X PBS by mixing the Cy3B labeled A21B strand (0.33 μM), quencher strand (0.33 μM) and hairpin strand (0.3 μM) in the ratio of 1.1: 1.1: 1. The solution was then heated to 95 °C for 5 min by using a heat block and cooled back to room-temperature over a period of 30 min. Afterwards, an additional 2.7 mM of BHQ2 strands were introduced into the DNA assembly solution in 1 M NaCl. 100 μl of this final solution was added between two AuNP functionalized coverslips and incubated overnight at 4 °C.

DNA tension probe modified coverslips were rinsed in 1X PBS before further functionalization with 40 μg/ml of streptavidin in 1X PBS. After 1 h incubation, the coverslips were rinsed in 1 X PBS to remove the unbound streptavidin, which was followed by the final modification with 40 mg/ml of biotinylated ligands (pMHC or α-CD3) in 1X PBS for 1 h. These modified coverslips were then assembled into cell imaging chambers (Attofluor, Life Technologies) filled with hank's balanced salt imaging buffer and immediately used for cell experiments.

In the case of tension gauge tether (TGT), a 75 x 25 mm glass slide was cleaned and functionalized with amine groups using the aforementioned method. A 6 channel μ-Slide was then mounted to the glass slide to create 6 well flow chambers, which was then passivated with 5% w/v mPEG-NHS (MW 2000) and 0.5% w/v lipoic acid-PEG (MW 3400) in 0.1 M fresh sodium bicarbonate solution at 4 °C for overnight. Surfaces were washed extensively with nanopure water and then 20 nM AuNP solution was introduced and incubated for 30 min. After thorough rinsing, the hybridized TGTs were dissolved in 1 M sodium chloride solution and were incubated overnight at 4 °C with 10 μM of HS-$(CH_2)_{11}$-$(OCH_2CH_2)_6$-OCH_3 passivating polyethylene glycol. Excess DNA and PEG were removed with three washes of 1X PBS. Afterwards, 40 μg/mL of streptavidin was added and incubated for 1 h. The surfaces were then washed with 1X PBS and subsequently 40 μg/ml of biotinylated ligands (pMHC or a-CD3) was added and allowed to bind to the streptavidin modified duplexes for 1 h. Unbound ligand was washed away with 1X PBS and the surfaces were used within the same day of preparation.

4.4.8 Bulk fluorescence measurement

The fluorescence intensity of Cy3B was recorded using a Biotek Synergy HT plate reader operated using a filter set with excitation/emission λ = 565 nm/610 nm. Each well in the 96-well plate (Fisher scientific) was filled to a volume of 100 μl. All measurements were performed in triplicate, and the reported error bars represent the standard deviation of these measurements.

4.4.9 HPLC

Reaction products were purified using a C18 column (diameter: 4.6 mm; length: 250 mm) in a reverse phase binary pump HPLC that was coupled to a diode array detector (Agilent 1100).

4.4.10 MALDI-mass spectrometry

Concentration of the purified oligonucleotide conjugate was determined by measuring its A_{260} value on Nanodrop 2000 UV-Vis Spectrophotometer (Thermo Scientific). MALDI-TOF mass spectrometry was performed on a high performance MALDI time-of-flight mass spectrometer (Voyager STR). The matrix for all experiments was prepared by freshly dissolving excess of 3-hydroxypicolinic acid (3-HPA) in the matrix solvent (50% MeCN/H_2O, 1% TFA, 10% of 50 mg/ml ammonium citrate).

4.4.11 Calcium imaging

Freshly purified OT1 cells (n = 1×10^6) were centrifuged to remove the RPMI media and re-suspended in 3 ml of hank's imaging buffer. 10 μl of 1 mM of fura-2/Am in DMSO was added into the cell suspension. The mixture solution was kept at 37 °C for 30 min. Afterwards, cells were pelleted by centrifugation at 1200 rpm for 4 min and re-suspended in 3 ml of imaging buffer for additional 15 min incubation. This step is to ensure full de-esterification of the fura-2/Am. Then, the cells were again pelleted in previous described condition and re-suspended in 1 ml of imaging buffer and prepared for seeding.

Nikon CFI S Fluor 100x oil objective, a Chroma 340 excitation filter set (ET340x, T400lp and ET510/80m) and Chroma 380 excitation filter set (ET380x, T400lp and ET510/80m) was used to image and quantify the 510 nm fluorescence intensity with

excitation at both 340 nm and 380 nm of fura-2 dye. During an experiment, the fluorescence images were acquired by using 340 and 380 filter sets sequentially. Afterwards, ImageJ was used to generate a cell mask for both channels excited by 340 nm and 380 nm. Final fura-2 ratio (I_{340}/I_{380}) was calculated by using the image calculator function in ImageJ.

4.4.12 Fluorescence immunostaining

Naïve OT1 cells were seeded onto the tension probe surfaces decorated with different stimulatory ligands. After cell spreading and activation, 4% of paraformaldehyde was gently added to the imaging chamber for 30 min. After thoroughly rinsing with 1X PBS, 0.1% Triton-X was added to the chamber for 10 min. Subsequently, 1X PBS was used to rinse the chamber, which is followed by 2% w/v BSA passivation for 24 h at 4 °C. Without rinsing, primary antibody was directly added into the chamber for targeting the protein of interests and incubate for 1 h at room temperature. Optionally, fluorescently labeled secondary antibody was also added and incubated for 1 h for visualization when primary antibody was not labeled. The standard manufacture recommended concentrations and conditions were used for immunostaining.

4.4.13 Drug Inhibition

For Lck inhibition, 30 μM of Lck inhibitor was incubated with OT1 cells either before or after cell plating. In probing cytoskeletal activities, 40 μM ROCK inhibitor (Y-27632), 40 μM MLCK inhibitor (ML-7), 20 μM F-actin inhibitor (Cytochalasin D), 50 μM Arp2/3 inhibitor (CK-666) was added after 30 min cell plating, respectively. In probing GTPase activities, 200 μM Rac1 inhibitor (NSC23766) and 10 μM Cdc42 inhibitor

(ML141) was pretreated with freshly purified OT1 cells (n = 1×10^6), respectively, for 30 min before cell plating.

4.4.14 AFM imaging

The density of AuNP tension sensor on the functionalized glass coverslip was measured by using an atomic force microscope mounted on an anti-vibration stage (MFP-3D, Asylum Research, CA). Silicon AFM tips (MikroMasch) with a force constant (5.4-16 N/m) were used to image the sample in tapping mode at a scan rate of 1 Hz. All images were processed and rendered using IgorPro.

4.4.15 DNA labeling

A mixture of A21B (10 nmol) and excess Cy3B NHS ester in 0.1 M sodium bicarbonate solution was allowed to react at room temperature overnight. The mixture was then subjected to P2 gel filtration to remove salts, organic solvent and unreacted reactants, and was further purified by reverse phase HPLC (solvent A: 0.1 M TEAA, solvent B: 100% MeCN; initial condition was 10% B with a gradient of 1%/min, flow rate: 1 mL/min). The desired product was characterized by MALDI-TOF mass spectrometry.

4.4.16 Optical microscopy

Live cells were imaged in hank's balanced salt imaging buffer at 23 °C. In TGT experiments, cells were incubated in the imaging buffer at 37 ºC for 30 min before fixation. The microscope was a Nikon Eclipse Ti driven by the Elements software package. The microscope features an Evolve electron multiplying charge coupled device (EMCCD; Photometrics), an Intensilight epifluorescence source (Nikon), a CFI Apo 100× (numerical aperture (NA) 1.49) objective (Nikon) and a TIRF launcher with three

laser lines: 488 nm (10 mW), 561 nm (50 mW), and 638 nm (20 mW). This microscope also includes the Nikon Perfect Focus System, an interferometry-based focus lock that allowed the capture of multipoint and time-lapse images without loss of focus. In all the reported experiments, we used the following Chroma filter cubes: TIRF 488, TRITC, and reflection interference contrast microscopy (RICM).

4.5 References

1. Smith-Garvin, J. E.; Koretzky, G. A.; Jordan, M. S., T Cell Activation. *Annual Review of Immunology* **2009,** *27*, 591-619.

2. Chakraborty, A. K.; Weiss, A., Insights into the initiation of TCR signaling. *Nature Immunology* **2014,** *15* (9), 798-807.

3. Kim, S. T.; Takeuchi, K.; Sun, Z. Y.; Touma, M.; Castro, C. E.; Fahmy, A.; Lang, M. J.; Wagner, G.; Reinherz, E. L., The alphabeta T cell receptor is an anisotropic mechanosensor. *J Biol Chem* **2009,** *284* (45), 31028-37.

4. Das, D. K.; Feng, Y.; Mallis, R. J.; Li, X.; Keskin, D. B.; Hussey, R. E.; Brady, S. K.; Wang, J. H.; Wagner, G.; Reinherz, E. L.; Lang, M. J., Force-dependent transition in the T-cell receptor beta-subunit allosterically regulates peptide discrimination and pMHC bond lifetime. *Proc Natl Acad Sci U S A* **2015,** *112* (5), 1517-22.

5. Liu, B.; Chen, W.; Evavold, Brian D.; Zhu, C., Accumulation of Dynamic Catch Bonds between TCR and Agonist Peptide-MHC Triggers T Cell Signaling. *Cell* **2014,** *157* (2), 357-368.

6. Hong, J.; Persaud, S. P.; Horvath, S.; Allen, P. M.; Evavold, B. D.; Zhu, C., Force-Regulated In Situ TCR-Peptide-Bound MHC Class II Kinetics Determine Functions of CD4+ T Cells. *Journal of Immunology* **2015,** *195* (8), 3557-64.

7. Mallis, R. J.; Bai, K.; Arthanari, H.; Hussey, R. E.; Handley, M.; Li, Z.; Chingozha, L.; Duke-Cohan, J. S.; Lu, H.; Wang, J. H.; Zhu, C.; Wagner, G.; Reinherz, E. L., Pre-TCR ligand binding impacts thymocyte development before alphabetaTCR expression. *Proc Natl Acad Sci U S A* **2015,** *112* (27), 8373-8.

8. Liu, Z.; Liu, Y.; Chang, Y.; Seyf, H. R.; Henry, A.; Mattheyses, A. L.; Yehl, K.; Zhang, Y.; Huang, Z.; Salaita, K., Nanoscale optomechanical actuators for controlling mechanotransduction in living cells. *Nat Meth* **2016,** *13* (2), 143-146.

9. McKeithan, T. W., Kinetic proofreading in T-cell receptor signal transduction. *Proc Natl Acad Sci U S A* **1995,** *92* (11), 5042-6.

10. Bashour, K. T.; Gondarenko, A.; Chen, H. Q.; Shen, K. Y.; Liu, X.; Huse, M.; Hone, J. C.; Kam, L. C., CD28 and CD3 have complementary roles in T-cell traction forces. *Proceedings of the National Academy of Sciences of the United States of America* **2014,** *111* (6), 2241-2246.

11. Hui, K. L.; Balagopalan, L.; Samelson, L. E.; Upadhyaya, A., Cytoskeletal forces during signaling activation in Jurkat T-cells. *Molecular Biology of the Cell* **2015,** *26* (4), 685-695.

12. Huppa, J. B.; Axmann, M.; Mortelmaier, M. A.; Lillemeier, B. F.; Newell, E. W.; Brameshuber, M.; Klein, L. O.; Schutz, G. J.; Davis, M. M., TCR-peptide-MHC interactions in situ show accelerated kinetics and increased affinity. *Nature* **2010,** *463* (7283), 963-967.

13. O'Donoghue, G. P.; Pielak, R. M.; Smoligovets, A. A.; Lin, J. J.; Groves, J. T., Direct single molecule measurement of TCR triggering by agonist pMHC in living primary T cells. *Elife* **2013,** *2*.

14. Deeg, J.; Axmann, M.; Matic, J.; Liapis, A.; Depoil, D.; Afrose, J.; Curado, S.; Dustin, M. L.; Spatz, J. P., T Cell Activation is Determined by the Number of Presented Antigens. *Nano Letters* **2013,** *13* (11), 5619-5626.

15. Delcassian, D.; Depoil, D.; Rudnicka, D.; Liu, M. L.; Davis, D. M.; Dustin, M. L.; Dunlop, I. E., Nanoscale Ligand Spacing Influences Receptor Triggering in T Cells and NK Cells. *Nano Letters* **2013,** *13* (11), 5608-5614.

16. Liu, Y.; Yehl, K.; Narui, Y.; Salaita, K., Tension Sensing Nanoparticles for Mechano-Imaging at the Living/Nonliving Interface. *Journal of the American Chemical Society* **2013,** *135* (14), 5320-5323.

17. Liu, Y.; Medda, R.; Liu, Z.; Galior, K.; Yehl, K.; Spatz, J. P.; Cavalcanti-Adam, E. A.; Salaita, K., Nanoparticle Tension Probes Patterned at the Nanoscale: Impact of Integrin Clustering on Force Transmission. *Nano Letters* **2014,** *14*, 5539-5546.

18. Zhang, Y.; Ge, C.; Zhu, C.; Salaita, K., DNA-based digital tension probes reveal integrin forces during early cell adhesion. *Nature Communications* **2014,** *5*, 5167.

19. Blakely, B. L.; Dumelin, C. E.; Trappmann, B.; McGregor, L. M.; Choi, C. K.; Anthony, P. C.; Duesterberg, V. K.; Baker, B. M.; Block, S. M.; Liu, D. R.; Chen, C. S., A DNA-based molecular probe for optically reporting cellular traction forces. *Nat Methods* **2014,** *11*, 1229-1232.

20. Galior, K.; Liu, Y.; Yehl, K.; Vivek, S.; Salaita, K., Titin-Based Nanoparticle Tension Sensors Map High-Magnitude Integrin Forces within Focal Adhesions. *Nano Letters* **2016,** *16* (1), 341-8.

21. Jurchenko, C.; Chang, Y.; Narui, Y.; Zhang, Y.; Salaita, Khalid S., Integrin-Generated Forces Lead to Streptavidin-Biotin Unbinding in Cellular Adhesions. *Biophysical Journal* **2014,** *106* (7), 1436-1446.

22. Chang, Y.; Liu, Z.; Zhang, Y.; Galior, K.; Yang, J.; Salaita, K., A General Approach for Generating Fluorescent Probes to Visualize Piconewton Forces at the Cell Surface. *Journal of the American Chemical Society* **2016,** *138* (9), 2901-2904.

23. Woodside, M. T.; Behnke-Parks, W. M.; Larizadeh, K.; Travers, K.; Herschlag, D.; Block, S. M., Nanomechanical measurements of the sequence-dependent folding landscapes of single nucleic acid hairpins. *Proc Natl Acad Sci U S A* **2006,** *103* (16), 6190-5.

24. Yu, Y.; Fay, N. C.; Smoligovets, A. A.; Wu, H. J.; Groves, J. T., Myosin IIA modulates T cell receptor transport and CasL phosphorylation during early immunological synapse formation. *Plos One* **2012,** *7* (2), e30704.

25. Yi, J.; Wu, X. F. S.; Crites, T.; Hammer, J. A., Actin retrograde flow and actomyosin II arc contraction drive receptor cluster dynamics at the immunological synapse in Jurkat T cells. *Molecular Biology of the Cell* **2012,** *23* (5), 834-852.

26. Babich, A.; Li, S.; O'Connor, R. S.; Milone, M. C.; Freedman, B. D.; Burkhardt, J. K., F-actin polymerization and retrograde flow drive sustained PLCgamma1 signaling during T cell activation. *J Cell Biol* **2012,** *197* (6), 775-87.

27. Li, Y. C.; Chen, B. M.; Wu, P. C.; Cheng, T. L.; Kao, L. S.; Tao, M. H.; Lieber, A.; Roffler, S. R., Cutting Edge: mechanical forces acting on T cells immobilized via the TCR complex can trigger TCR signaling. *Journal of Immunology* **2010,** *184* (11), 5959-63.

28. Grakoui, A.; Bromley, S. K.; Sumen, C.; Davis, M. M.; Shaw, A. S.; Allen, P. M.; Dustin, M. L., The immunological synapse: A molecular machine controlling T cell activation. *Science* **1999,** *285* (5425), 221-227.

29. Lee, K. H.; Holdorf, A. D.; Dustin, M. L.; Chan, A. C.; Allen, P. M.; Shaw, A. S., T cell receptor signaling precedes immunological synapse formation. *Science* **2002,** *295* (5559), 1539-42.

30. Casas, J.; Brzostek, J.; Zarnitsyna, V. I.; Hong, J.-s.; Wei, Q.; Hoerter, J. A. H.; Fu, G.; Ampudia, J.; Zamoyska, R.; Zhu, C.; Gascoigne, N. R. J., Ligand-engaged TCR is triggered by Lck not associated with CD8 coreceptor. *Nature Communications* **2014,** *5*, 5624.

31. Hui, E.; Vale, R. D., In vitro membrane reconstitution of the T-cell receptor proximal signaling network. *Nature Structural & Molecular Biology* **2014,** *21* (2), 133-42.

32. Beemiller, P.; Krummel, M. F., Mediation of T-Cell Activation by Actin Meshworks. *Cold Spring Harbor Perspectives in Biology* **2010,** *2* (9), 002444.

33. Beemiller, P.; Jacobelli, J.; Krummel, M. F., Integration of the movement of signaling microclusters with cellular motility in immunological synapses. *Nature Immunology* **2012,** *13* (8), 787-95.

34. Choudhuri, K.; Llodra, J.; Roth, E. W.; Tsai, J.; Gordo, S.; Wucherpfennig, K. W.; Kam, L. C.; Stokes, D. L.; Dustin, M. L., Polarized release of T-cell-receptor-enriched microvesicles at the immunological synapse. *Nature* **2014,** *507* (7490), 118-123.

35. Evavold, B. D.; Allen, P. M., Separation of IL-4 production from Th cell proliferation by an altered T cell receptor ligand. *Science* **1991,** *252* (5010), 1308-10.

36. Zehn, D.; Lee, S. Y.; Bevan, M. J., Complete but curtailed T-cell response to very low-affinity antigen. *Nature* **2009,** *458* (7235), 211-214.

37. Wang, X. F.; Ha, T., Defining Single Molecular Forces Required to Activate Integrin and Notch Signaling. *Science* **2013,** *340* (6135), 991-994.

38. Ma, P. V.; Liu, Y.; Yehl, K.; Galior, K.; Zhang, Y.; Salaita, K., The Mechanically-induced Catalytic Amplification Reaction for Readout of Receptor-Mediated Cellular Forces. *Angewandte Chemie International Edition* **2016**.

39. Klammt, C.; Novotna, L.; Li, D. T.; Wolf, M.; Blount, A.; Zhang, K.; Fitchett, J. R.; Lillemeier, B. F., T cell receptor dwell times control the kinase activity of Zap70. *Nature Immunology* **2015,** *16* (9), 961-9.

40. Depoil, D.; Dustin, M. L., Force and affinity in ligand discrimination by the TCR. *Trends in Immunology* **2014,** *35* (12), 597-603.

41. Tibaldi, E. V.; Salgia, R.; Reinherz, E. L., CD2 molecules redistribute to the uropod during T cell scanning: implications for cellular activation and immune surveillance. *Proc Natl Acad Sci U S A* **2002,** *99* (11), 7582-7.

42. Smith, A.; Carrasco, Y. R.; Stanley, P.; Kieffer, N.; Batista, F. D.; Hogg, N., A talin-dependent LFA-1 focal zone is formed by rapidly migrating T lymphocytes. *The Journal of Cell Biology* **2005,** *170* (1), 141-151.

43. Smith, A.; Bracke, M.; Leitinger, B.; Porter, J. C.; Hogg, N., LFA-1-induced T cell migration on ICAM-1 involves regulation of MLCK-mediated attachment and ROCK-dependent detachment. *Journal of Cell Science* **2003,** *116* (Pt 15), 3123-33.

44. Jennings, T.; Singh, M.; Strouse, G., Fluorescent lifetime quenching near d= 1.5 nm gold nanoparticles: probing NSET validity. *Journal of the American Chemical Society* **2006,** *128* (16), 5462-5467.

4.6 Appendix

Strand ID	DNA Sequences (5' to 3')
A21B	/5AmMC6/ - CGC ATC TGT GCG GTA TTT CAC TTT - /3Bio/
Quencher	/5ThiolMC6-D/ - TTT GCT GGG CTA CGT GGC GCT CTT - /3BHQ_2/
Hairpin (12 pN)	GTG AAA TAC CGC ACA GAT GCG TTT GGG TTA ACA TCT AGA TTC TAT TTT TAG AAT CTA GAT GTT AAC CCT TTA AGA GCG CCA CGT AGC CCA GC
Hairpin (19 pN)	GTG AAA TAC CGC ACA GAT GCG TTT CGC CGC GGG CCG GCG CGC GGT TTT CCG CGC GCC GGC CCG CGG CGT TTA AGA GCG CCA CGT AGC CCA GC
Scrambled hairpin	GTG AAA TAC CGC ACA GAT GCG TTT ATC GTC AAT ATA TAC GAT ATT TTT TAG AAT CTA GAT GTT AAC TTT TTA AGA GCG CCA CGT AGC CCA GC
Complement to the scrambled hairpin	AAA AAG TTA ACA TCT AGA TTC TAA AAA ATA TCG TAT ATA TTG ACG ATA AA
TGT thiol anchor strand	/5ThiolMC6-D/TTT TTT TTT TCA CAG CAC GGA GGC ACG ACA C
TGT biotin strand (12 pN)	/5Biosg/GT GTC GTG CCT CCG TGC TGT G
TGT biotin strand (56 pN)	GT GTC GTG CCT CCG TGC TGT G/3Bio/

Table A4.1. DNA sequences. Underscore indicates the stem-loop forming region within hairpins.

Strand ID	ΔG_{fold} (kJ/mol)	$\Delta G_{stretch}$ (kJ/mol)	Δx (nm)	$F_{1/2}$
Hairpin (12 pN)	90.83	31.69	16.92	12.0

Table A4.2. $F_{1/2}$ **calculation for 12 pN DNA probe**

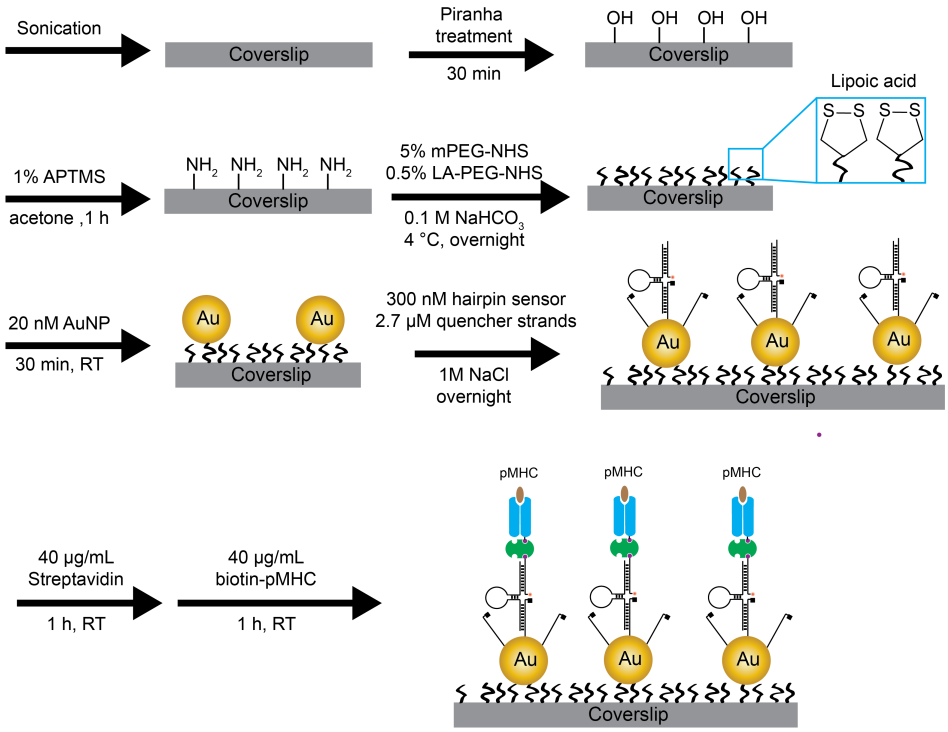

Figure A4.1 Fabrication of DNA-based gold nanoparticle tension sensor surface. Flow chart showing the step-wise fabrication of DNA-based gold nanoparticle tension probes (see *methods* for more description).

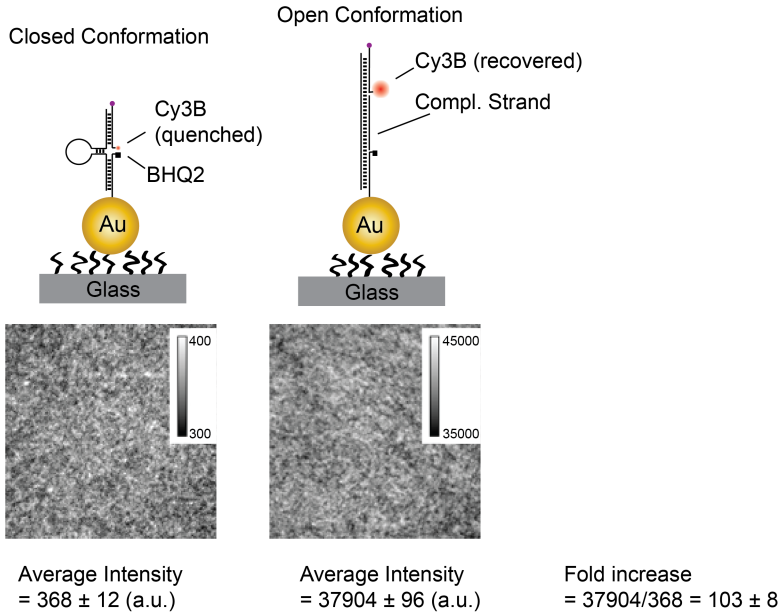

Figure A4.2 Quenching efficiency calibration of DNA-AuNP tension probes. Scheme and representative images of the experiments used to determine the quenching efficiency of DNA tension probes on the AuNP surface. The closed conformation probe sample was prepared as descibed in the Figure A4.1. The open conformation probe used a complementary strand to the scrambled hairpin at 0.3 μM (for sequences see Table A4.1 in methods section). This complementary strand generated a duplex, thus separating the dye from AuNP surface and the molecular quencher. This approach was adapted from energy transfer efficiency calibration experiments reported previously.[16, 44] The calculated fold increase is 103 ± 8.

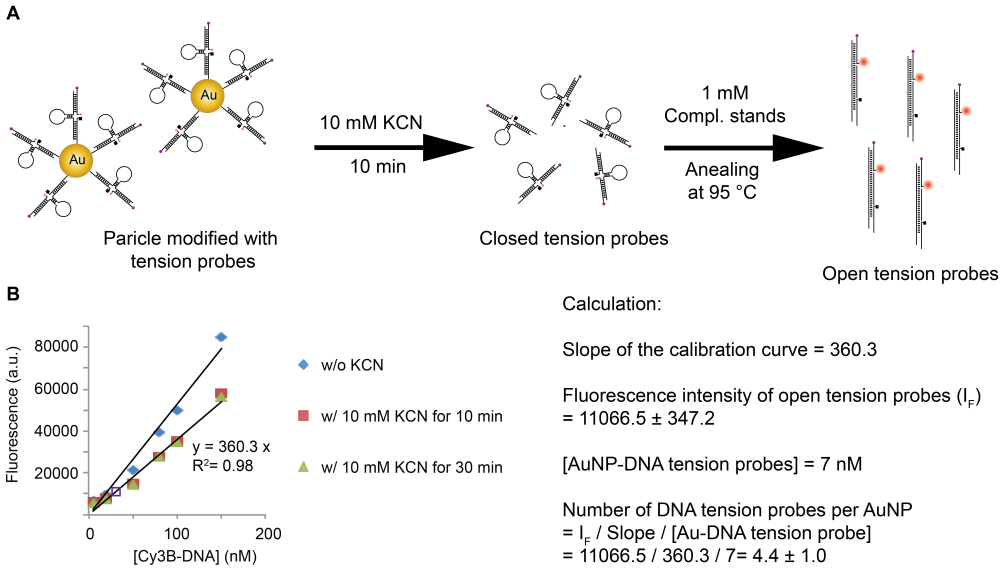

Figure A4.3 Quantification of the average number of DNA sensors per gold nanoparticle. (A) Scheme showing the approach used to determine the average stoichiometry between Cy3B-labeled tension probes and AuNP. Briefly, the concentration of AuNP was determined from the absorbance at λ=520 nm. Subsequently, AuNPs were dissolved by treating the sample with 10 mM KCN, which released Cy3B-labeled tension probes within 10 min. 1 mM of complementary DNA was then added into the solution and heated up to 95°C for hybridization and opening of the hairpin. The fluorescence intensity of the released Cy3B dye was then used to determine the number of dye molecules in the sample. (B) Plots showing the calibration curve used to quantify the number of tension sensor ligands per AuNP. The blue diamonds represent the calibration curve for Cy3B without addition of KCN. The red squares and green triangles represent the calibration curve at different time points with KCN, while the purple box represents the sample containing the released Cy3B ligands from AuNP-tension probes. All measurements were performed in triplicate.

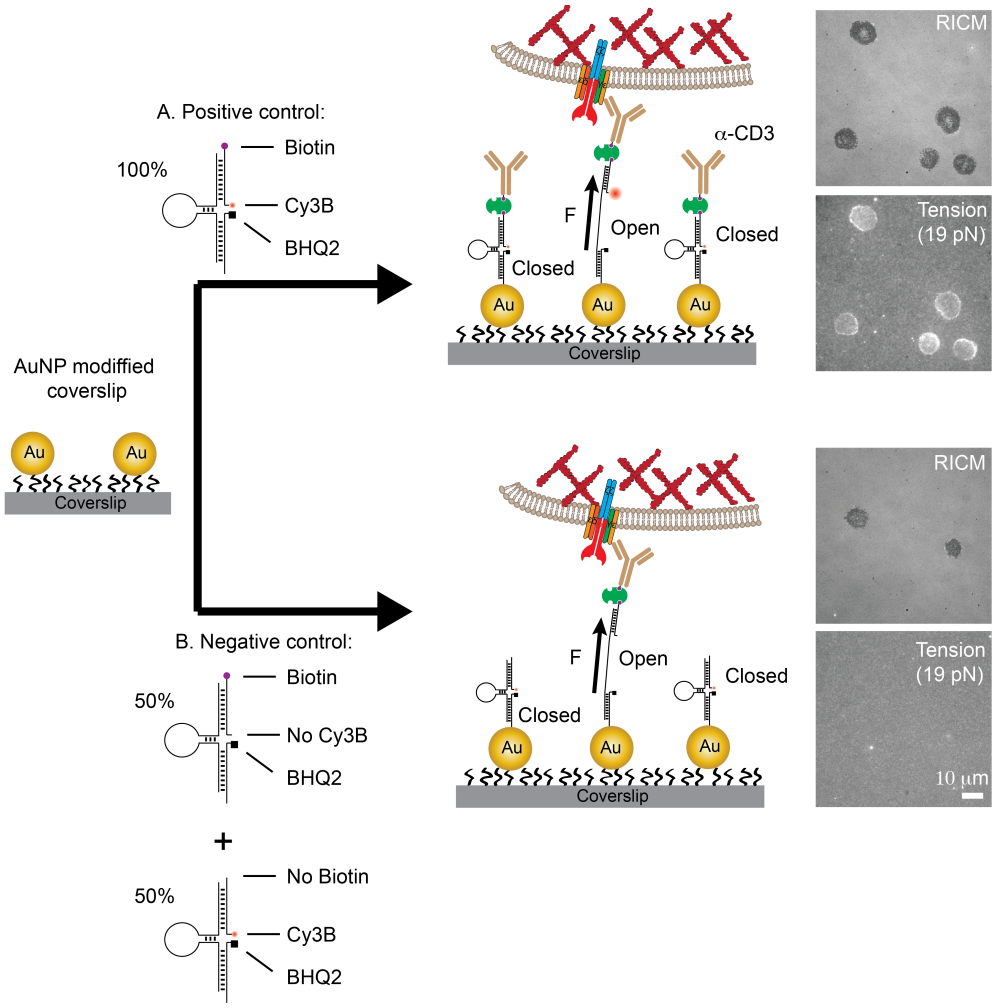

Figure A4.4 Tension signals are specifically generated through TCR-ligand interactions. (A) Schematic representation of the procedure used to generate the positive control sample containing the DNA-based AuNP tension probes modified with α-CD3. The images show representative RICM and 19 pN tension signal for OT-1 cells cultured on the surface for 15 min. (B) Schematic representation of procedure used to generate the negative control sample which included AuNP modified with two types of hairpins at equal concentration. The first hairpin incorporated the Cy3B dye-BHQ2 quencher pair but lacked the biotin group at the terminus of the A21B strand. The second hairpin incorporated the biotin group but lacked the Cy3B dye on the A21B strand. Cell spread on these substrates. However, no detectable fluorescence signal was observed, showing that only specific interaction between TCR and its ligand leads to tension signal.

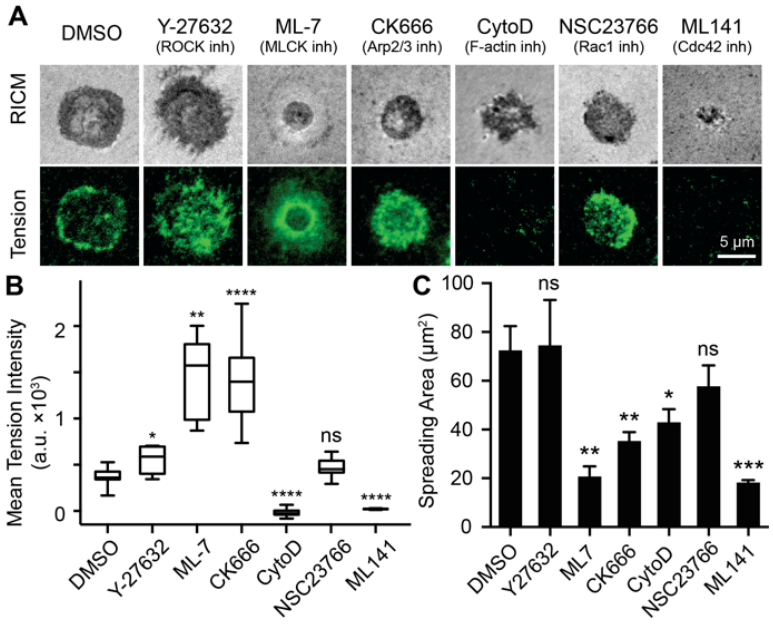

Figure A4.5 Investigation of cytoskeletal elements mediating TCR forces. (A) Representative RICM and 19 pN TCR tension images of T cell treated with different cytoskeletal inhibitors. (B-C) Statistical analysis of 19 pN TCR tension (B) and cell spreading area (C) for T cells treated with different cytoskeletal inhibitors (n = 20 cells for each condition). All error bars represent s.d., *P-value < 0.1; **P < 0.01; ***P < 0.001 and ****P < 0.0001.

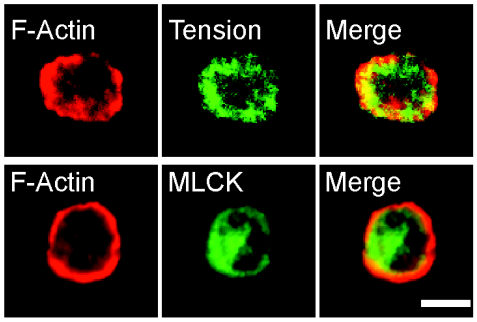

Figure A4.6 Colocalization of TCR tension with F-actin, and F-actin colocalization with myosin light chain kinase. Representative immunostaining images of OT1 cells showing the co-localization between TCR tension (19 pN) and F-Actin assembly (top row) and F-actin co-localization with MLCK (bottom row). In general, F-actin and tension were highly colocalized, while we observed a spatial offset between the F-actin structure and the MLCK at the cell edge. Scale bar: 10 μm.

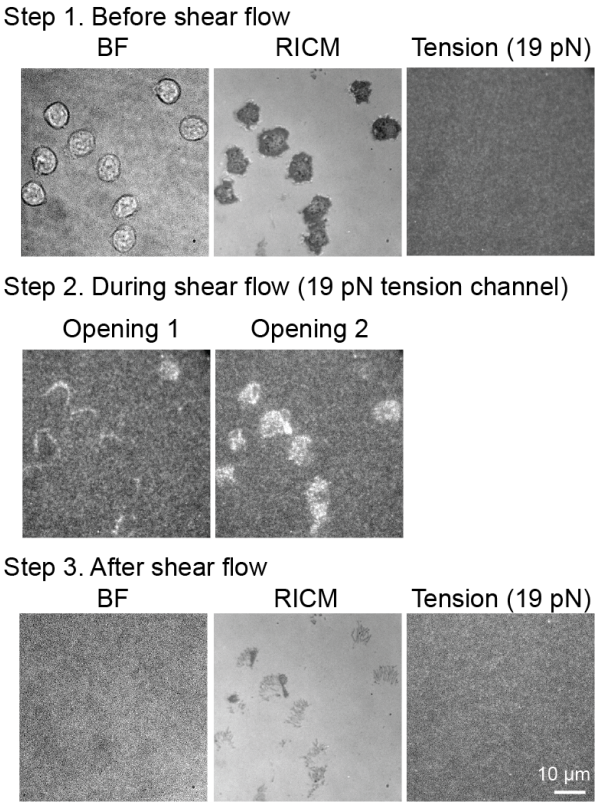

Figure A4.7 Induction of 19 pN sensor by shear flow. Representative images showing that OT1 cells spread and generated no observable tension signals when they were plated onto the N4 decorated 19 pN tension probe surface (step 1). A strong shear flow was generated by pipetting a stream of imaging buffer into the cell chamber, which led to a step-wise increase in fluorescence intensity both at the edge and center (step 2). Eventually, the cells were removed from the surface (RICM) and tension probes recovered back to background levels (step 3).

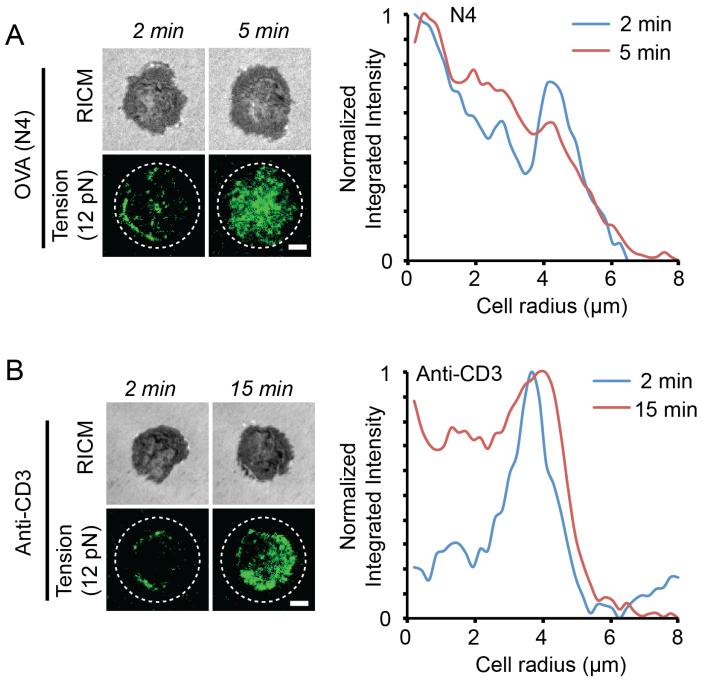

Figure A4.8 Radial distribution function analysis of TCR tension upon ligand stimulation. (A) Representative RICM and 12 pN TCR tension images for OT-1 cells plated onto the N4 pMHC 2 and 5 min after cell-surface contact. The dotted circle represents the ROI used for radial distribution analysis using radial profile plugin in ImageJ. Plots show cell radius (r) vs fluorescence intensity for this cell at t =2 min and 5 min following cell-surface contact. Analysis of tension at t = 2 min showed that forces were generally concentrated in a ring-like structure at the cell periphery. However, a peak at t = 4-5 min was observed in the central area. (B) Represnetative RICM and 12 pN TCR tension images for OT-1 cells plated onto the α-CD3 2 and 15 min after cell-surface contact. TCR tension at t = 2 min were concentrated in a ring-like structure. The characteristic ring-like structure was maintained for 15-60 min. Scale bar: 3 mm.

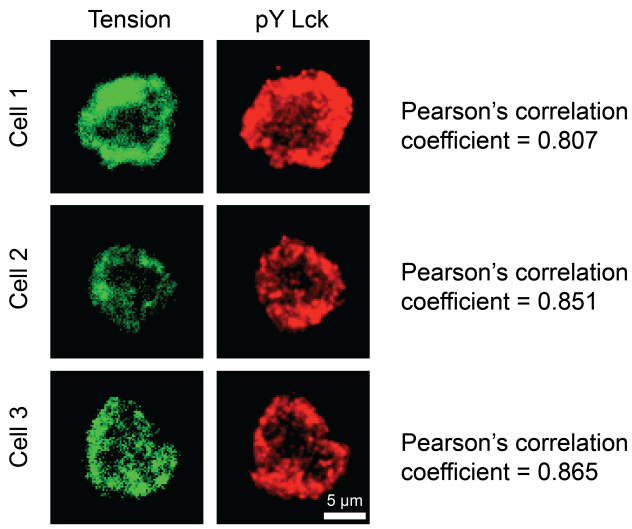

Figure A4.9 Spatial correlation analysis between TCR tension and active Lck. Representative images of 19 pN TCR tension and phosphorylated Lck (pY394). Pearson's correlation coefficients were analyzed using the JACoP plugin implemented in Fiji. Briefly, individual cells acquired from each fluorescence channnel were fed into the JACoP plugin, and the result of this analysis are reported here. n = 20 cells from 3 different chambers were analyzed and an average coefficient of 0.84 ± 0.04 was reported here.

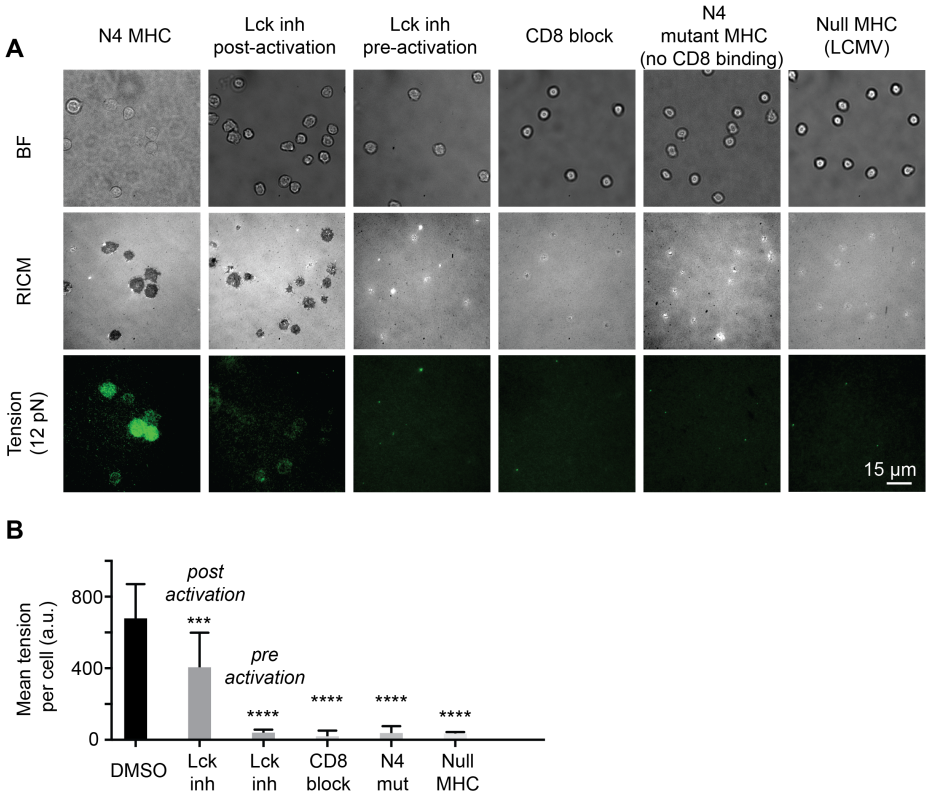

Figure A4.10 Quantification of TCR tension upon perturbation of TCR, CD8 and Lck activities. (A) Representative brightfield, RICM and tension images showing differential T cell responses to different Lck inhibitors before (pre-activation) and after (post-activation) cell plating, CD8 blocking with antibody, mutant N4 pMHC with abolished CD8 binding, and null pMHC presenting the GP33-41 epitope from LCMV. (B) Bar graph quantifying the mean fluorescence tension signal per cell in responses to treatments described in (A). Error bars represent the standard deviation (S.D.) from n = 20 cells for each group. ***$P < 0.001$ and ****$P < 0.0001$.

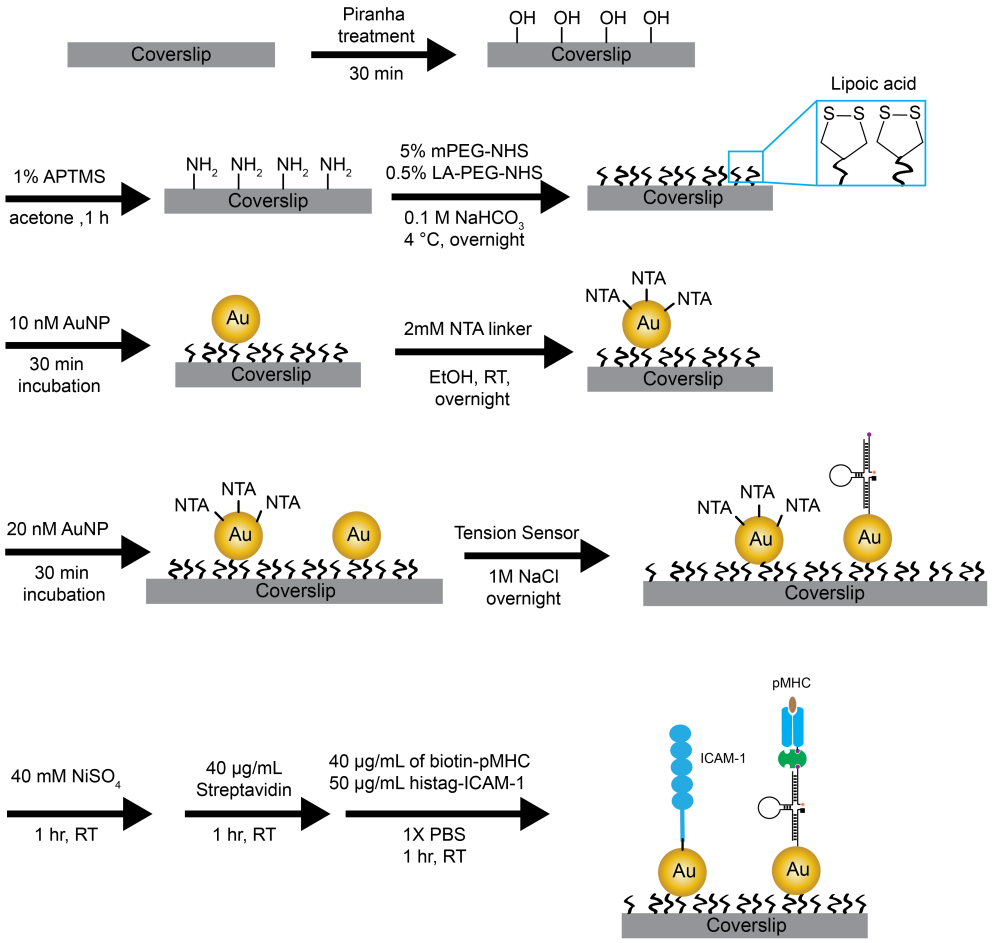

Figure A4.11 Co-presentation of ICAM-1 and DNA tension sensor-pMHC ligands on AuNP. Flow chart showing the step-wise fabrication of AuNP surfaces co-presenting ICAM-1 and DNA tension sensor-pMHC ligands.

No.2 glass coverslips were rinsed and sonicated with nanopure water (18.2 MΩ cm^{-1}) for 30 min, and then sonicated twice with acetone for 15 min. The slides were then dried in an oven set at 80°C for 10 min. Fresh piranha solution (7:3 v/v = H_2SO_4: H_2O_2) was mixed and then used to clean the substrates for 30 min. Afterwards, the substrates were rinsed with a copious amount of nanopure water. The substrates were then sonicated in acetone to remove excess water and for further cleaning. Subsequently, 1% v/v APTMS solution in acetone was added to the slides and incubated for 2 h. The amine-modified coverslips were then rinsed in acetone and water and dried under stream of N_2.

The slides were then annealed for 1 h at 80 °C. The surface was then passivated with 5% w/v mPEG-NHS (MW 2000) and 0.5% w/v lipoic acid-PEG (MW 3400) in 200 μl of 0.1 M fresh sodium bicarbonate solution. After overnight incubation at 4 °C, the excess unreacted PEG molecules were rinsed with nanopure water. This strategy affords a glass surface with sufficient lipoic acid groups to irreversible anchor AuNP MTFM sensors at appropriate densities. Next, 10 nM of unmodified 9 nm AuNP solution was incubated for 30 min and then rinsed with nanopure water to remove nonspecifically bound particles.

400 μl of 2 μM of NTA-SAM reagent in pure ethanol was incubated with the AuNP modified coverslips overnight at RT. The coverslips were then placed in a petri dish containing pure ethanol to prevent sample from drying. After rinsing with copious ethanol, the coverslips were air-dried and incubated with 40 mM of $NiSO_4$ solution for 1 h. Afterwards, an additional 20 nM solution of unmodified AuNPs was incubated with the coverslip for 30 min before modification of tension probes.

The DNA tension probe hairpins were assembled in 1X PBS by mixing the Cy3B labeled A21B strand (0.33 μM), quencher strand (0.33 μM) and hairpin strand (0.3 μM) in the ratio of 1.1: 1.1: 1. The solution was then heated to 95 °C for 5 min by using a heat block and cooled back to room-temperature over a period of 30 min. Afterwards, an additional 2.7 mM of BHQ2 strands were introduced into the DNA assembly solution in 1 M NaCl. 100 μl of this final solution was added between two AuNP functionalized coverslips and incubated overnight at 4°C.

DNA tension probe modified coverslips were rinsed in 1X PBS before further functionalization with 40 mg/ml of streptavidin in 1X PBS. After 1 h incubation, the coverslips were rinsed in 1 X PBS to remove the unbound streptavidin, which was followed by the final modification with a mixture of 40 mg/ml of biotinylated ligands (pMHC or α-CD3) and 50 μg/ml of histag-ICAM-1 in 1X PBS for 1 h.

These modified coverslips were then assembled into cell imaging chambers (Attofluor, Life Technologies) filled with hank's balanced salt imaging buffer and immediately used for cell experiments.

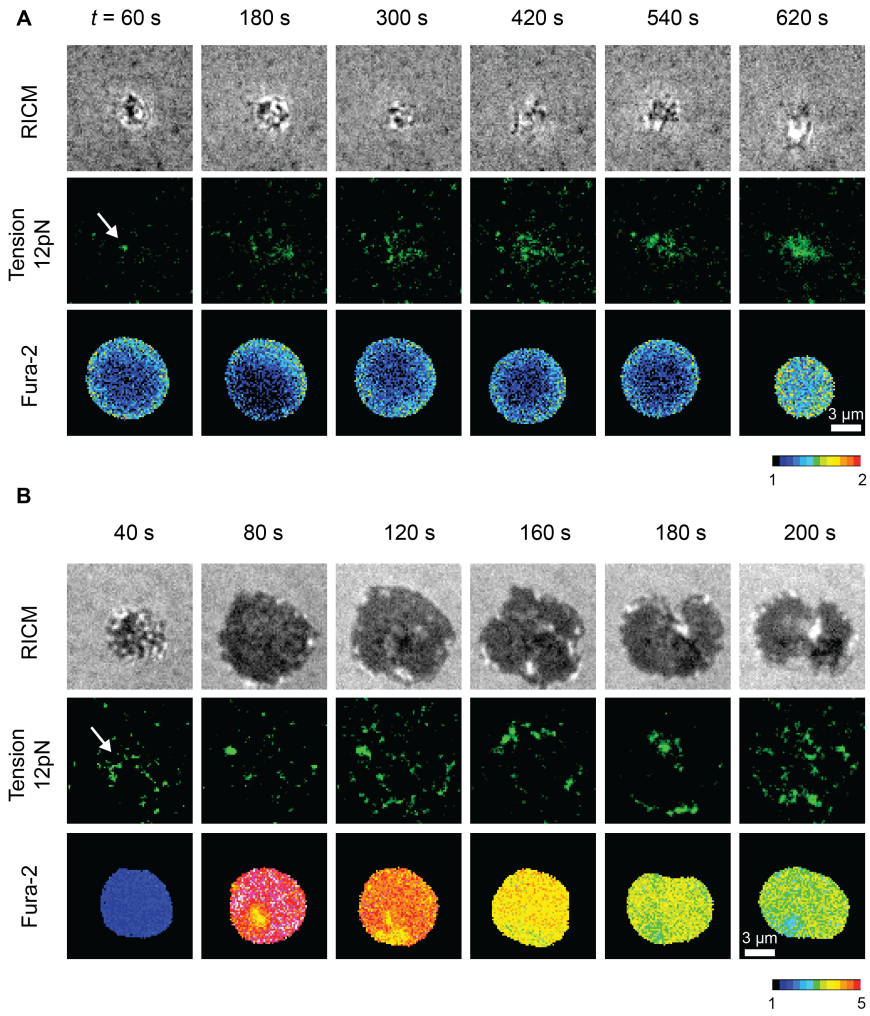

Figure A4.12 Comparison of TCR forces and calcium flux between V4 and N4 ligand. Simultaneous imaging of cell spreading (Reflection interference contrast microscopy, RICM), 12 pN TCR forces (tension) and T cell activation (fura-2) for a representative OT-1 cell encountering V4 pMHC (A) and N4 pMHC (B). White arrow indicates the initial appearance of tension signals within 1 min of cell-substrate contact.

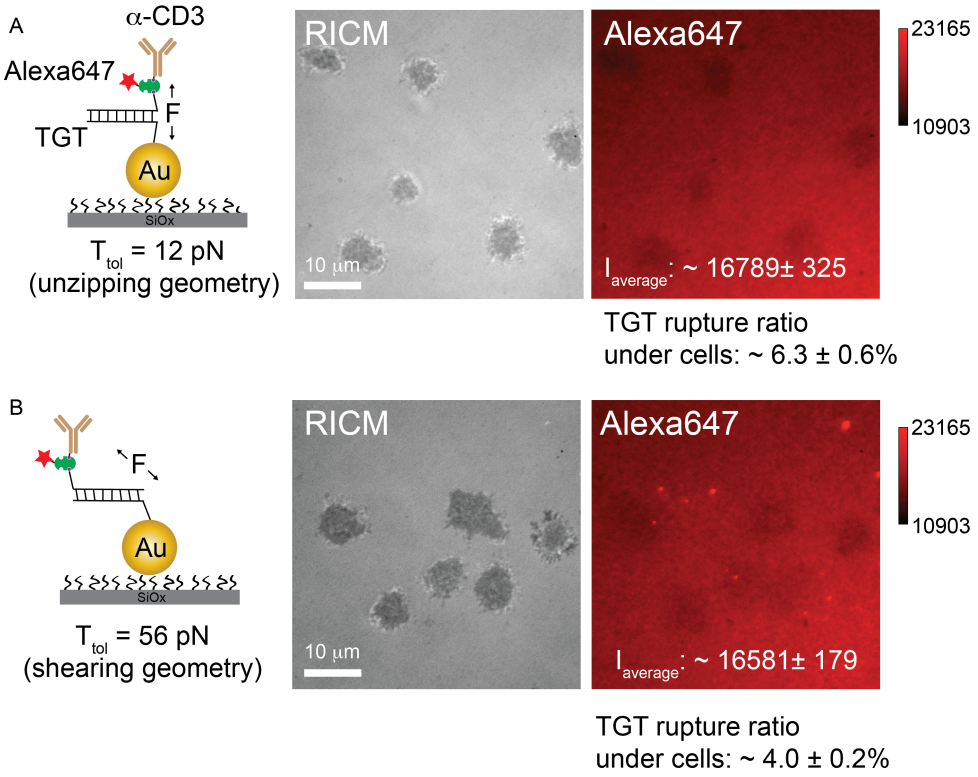

Figure A4.13 Comparison of TGT rupturing between 12 pN and 56 pN probes. (A) Schematic representation of 12 pN TGT modified with α-CD3. RICM and fluorescence images show the result of T cells cultured on this surface for 30 min. T cells spread and generated mechanical forces that dissociate the TGT duplex, leaving an area with decreased fluorescence intensity. Quantification analysis showed a 6.3 ± 0.6 % decrease in fluorescence due to DNA rupturing. (B) Schematic representation of 56 pN TGT modified with α-CD3. Upon plating, OT1 cells spread and generated mechanical forces that reduced the streptavidin intensity by 4.0 ± 0.2 %. These results confirmed the model that 56 pN TGT provided greater mechanical resistance than the 12 pN TGT. n = 20 cells were analyzed.

4.7 Supplementary Note 1

The DNA-based nanoparticle tension probes displayed a 103-fold increase in fluorescence increase upon unfolding (Fig. 1B). Based on AFM analysis, the density of gold nanoparticles sensors is approximately 11 AuNPs per EMCCD pixel area (160 nm × 160 nm). Bulk fluorescence measurements indicate that an average of 4.4 DNA hairpins are bound per AuNP. Given that the maximum fluorescence signal associated with the fully opened hairpin sensors is 37900 a.u. per pixel, we estimate that each activated tension sensor contributes a value of 783 a.u. in fluorescence. This analysis indicates that a minimum of ~31 DNA hairpins ($F_{1/2}$ = 19 pN) are mechanically unfolded per mm^2 based on the αCD3 stimulation data shown in Fig. 2E. Note that only a subset of bound TCR molecules transmit mechanical forces sufficient to unfold the DNA hairpins. In principle, these AuNP-DNA based tension probes provide sufficient sensitivity for single molecule detection.

4.8 Supplementary Note 2

All the DNA tension probes used in this study are either experimentally calibrated (19 pN) using single molecule spectroscopy methods (1, 2) or theoretically calculated based on literature precedent for the $F_{1/2}$ = 12 pN at 23 ^{o}C (see Table S2 in SI methods). Therefore, T cell experiments were performed at the room temperature rather than 37 ^{o}C. We acknowledge that this temperature choice may lead to suboptimal cell activity such as delayed calcium flux. Nonetheless, we observed significant phosphorylation of Lck and Zap70 within a few minutes following cell seeding (Fig. 2C), which is in agreement with the rates of T cell activation in other reported work (3). This suggests that T cell response is not compromised in our experimental conditions.

In experiments using TGTs to physically limit the maximum TCR-pMHC force, we cultured T-cells at 37 ^{o}C for 30 min prior to cell fixation and staining. This is because TGT tension tolerance values for both the 12 and 56 pN probes were previously calculated at 37 ^{o}C (4). Moreover, the 12 and 56 pN TGT probes were selected based on the tension sensor results shown in Fig. 2A and E. The 56 pN probe is expected to provide the most mechanically stable tether, and thus remain hybridized to the surface resisting TCR forces that exceed ~19 pN. In contrast, the 12 pN TGT probes provide a labile tether that is expected to dissociate in response to TCR forces exceeding 12 pN. Thus, these two TGTs cap TCR forces at the most relevant critical thresholds of tension.

Chapter 5: Development of Nanoscale Optomechanical Actuators for Controlling Mechanotransduction in Living Cells

Adapted from Liu, Z.*; Liu, Y.*; Yuan, Y.; Seyf, H.; Henry, A.; Mattheyses, A.; Yehl, K.; Zhang, Y.; Huang, Z.; Salaita, K. Nanoscale Optomechanical Actuators for Controlling Mechanotransduction in Living Cells. *Nature Methods* **2016**, 13, 143-146

5.1 Introduction

By virtue of having a set morphology and architecture, the majority of cells within multicellular organisms experience forces that are highly orchestrated in space and time.[1] To study the dynamic interplay between chemical and mechanical signals at the cell surface, a number of techniques have been developed to investigate cell response to spatially confined physical perturbations.[2] For example, micropipettes[3] and single molecule techniques[4-5] have been used to prod the apical side of individual cells and record biochemical responses, but such approaches are challenging, low-throughput and highly serial.[2] Another general approach involves using magnetic actuation of nanoparticles[6-7] and micropillars[8] to trigger signaling pathways. Controlling magnetic fields with high spatial resolution requires either a sparse density of magnetic elements or sophisticated micro fabricated magnetic structures that focus an external magnetic field. Therefore, magnetic stimulation of mechanotransduction circuits remains specialized and is not widely employed. In the absence of methods for manipulating forces with molecular specificity and high spatio-temporal resolution, elucidating the local biochemical response to mechanics remains a hurdle.[2]

In principle, the most desirable approaches for manipulation within biological systems are optical-based. This is evidenced by the rapid proliferation of photo-stimulation techniques employing caged or photoswitchable molecules, and optogenetic constructs.[9-11] Therefore, the development of methods to harness light for delivering precise physical inputs to biological systems could potentially transform the study of mechanotransduction.

Toward this goal, we develop optomechanical actuator (OMA) nanoparticles to manipulate receptor mechanics with high spatial and temporal resolution using low intensity near-infrared (NIR) illumination (Figure 5.1**a**). OMA nanoparticles are programmed to rapidly shrink upon illumination, thus applying a mechanical load to receptor-ligand complexes decorating the immobilized particle. The NIR optical pulse train controls the amplitude, duration, repetition and loading rate of mechanical input. OMAs are immobilized onto standard glass coverslips allowing cell imaging and manipulation using a conventional fluorescence microscope equipped with an inexpensive NIR laser diode. Therefore, live cell response to mechanical stimulation can be characterized with unprecedented spatial and temporal resolution. Importantly, because mechanical stimulation can be rapidly deployed across arbitrary patterns at the cell surface, we were able to demonstrate the first example of opto-mechanical control of focal adhesion (FA) formation, cell protrusions, cell migration, and T cell activation.

5.2 Results and discussion

5.2.1 Fabrication and characterization of OMA nanoparticles

OMA nanoparticles are comprised of a Au nanorod (25 nm × 100 nm) coated with a thermo-responsive polymer shell (poly(N-isopropylmethacrylamide, pNIPMAm) (Figure 5.1b and *Appendix*, Figure A5.1). The Au nanorod functions as a photothermal transducer, converting a NIR pulse to localized heat that drives a transient collapse of the polymer shell. OMA particles can be immobilized onto virtually any type of support and can also be functionalized with a wide variety of small molecule, peptide, and protein ligands specific to a receptor of interest. Thus, mechanical actuation is molecularly

selective in that only receptors that are directly engaged to ligands on the OMA nanoparticles experience the mechanical input.

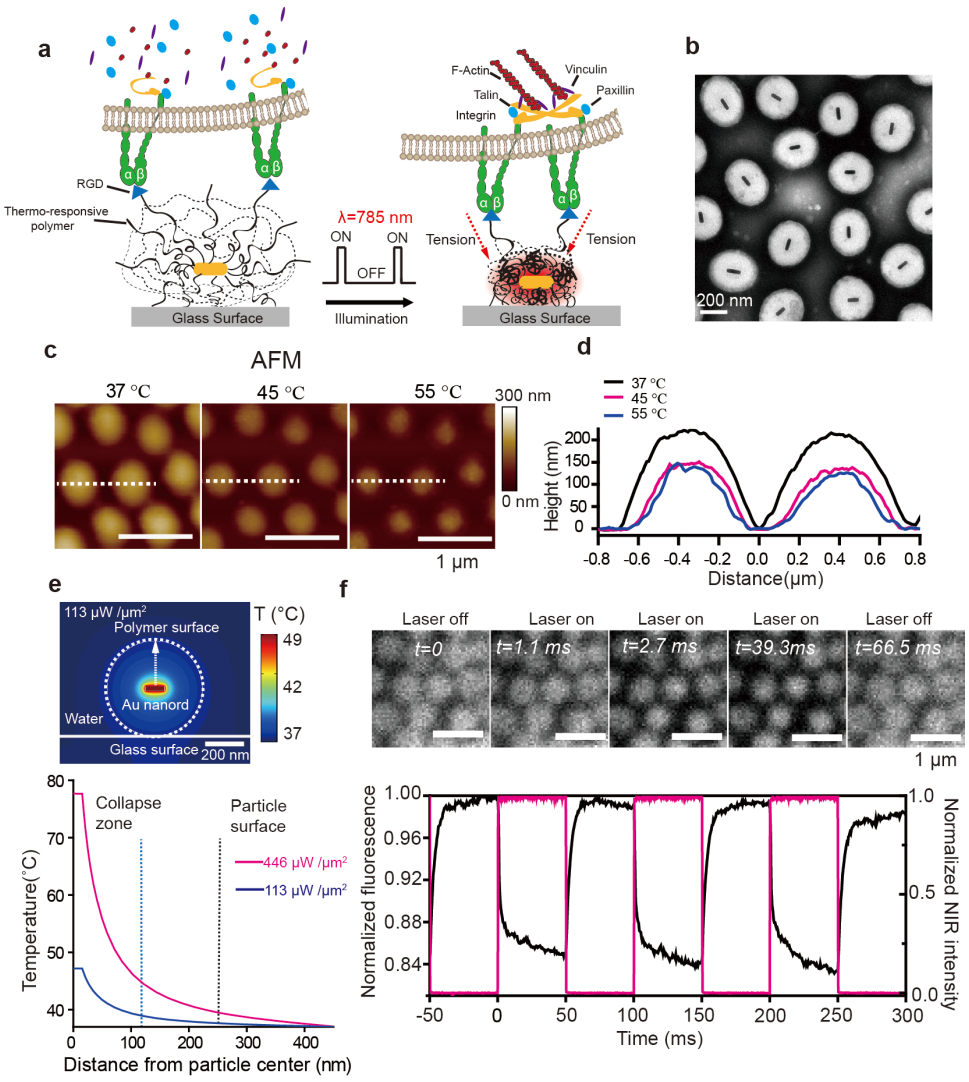

Figure 5.1 Schematic and characterization of optomechanical actuator (OMA) nanoparticles. (a) Schematic showing the general design and proposed mechanism of OMA nanoparticles. (b)Representative TEM image of OMA nanoparticles. (c) Representative AFM images of the OMA nanoparticles at T = 37, 45, and 55 °C in DI water. (d) Plot represents the temperature-dependent height profile across two nanoparticles indicated by the dashed white line. (e) Top: Finite element simulation of the heat distribution in a OMA nanoparticle irradiated with 785 nm IR laser beam at a power density of 113 μW μm^{-2} in water. Bottom: Plot showing the OMA particle temperature as a function of distance from the Au nanorod core irradiated with 785 nm laser for two different power densities (446 and 113 μW μm^{-2}). Note that the power density (113 μW μm^{-2}) is 10 fold greater than that used for cell stimulation because a 100% duty cycle

(steady state illumination) is assumed for the energy input calculation. The details of the simulation are included in the *Methods* and *Appendix*, Figure A5.4. (f) Top: Representative fluorescence images of OMA nanoparticles labeled with Alexa 488 and captured by a sCMOS camera (Andor Zyla sCMOS) at 1800 fps while chopping the NIR laser source at 10 Hz (50% duty cycle). Data was collected in DI water at 37°C. Bottom: The average normalized fluorescence intensity (black curve) of OMA nanoparticles as the NIR laser (red curve) is modulated with a 10 Hz frequency and 50% duty cycle. The dynamics of fluorescence was used to estimate the time constant of particle collapse and relaxation. The ~15% decrease in fluorescence was primarily due to quenching by the Au nanorod upon particle collapse (*Appendix*, Figure A5.5g and h).

TEM of OMA nanoparticles confirms the core-shell structure, monodispersity, and dimensions of the inorganic core (Figure 5.1b and *Appendix*, Figure A5.2). Dynamic light scattering showed that the average hydrodynamic diameter of the particles is 480 ± 20 nm at room temperature (RT), shrinking to a 270 ± 10 nm diameter upon heating to great than 42 °C (*Appendix*, Figure A5.2e). Vis-NIR spectra of OMA particles as a function of temperature confirmed the phase transition temperature and provided characterization of the NIR absorption band (*Appendix*, Figure A5.2f). Temperature-controlled AFM showed that immobilized particles (at 37 °C) displayed a flattened morphology with a mean height and width of 220, and 700 nm, respectively (Figure 5.1c and d). The AFM data also revealed that OMA particles collapsed both in the lateral and vertical directions at $T > 42$ °C, indicating that force vectors point inward toward the particle center with a vertical and horizontal component. Particles displayed a ~70 nm decrease in height and a ~120 nm reduction in particle diameter (Figure 5.1d). Structured illumination microscopy (SIM) measurement of particle diameter also showed a ~100 nm decrease following NIR illumination (*Appendix*, Figure A5.3a–c and Table A5.1). The reduction in particle size represents the maximum receptor displacement during NIR illumination. In principle, the magnitude of receptor displacement can be further tuned by changing particle size and the NIR illumination profile.

Key to the optomechanical actuation strategy is that particle heating is transient and confined to the core. Heat is dissipated as a 1/distance function from the Au nanorod core, and thus sufficiently large OMA particles display negligible surface heating. In contrast, mechanical energy is more efficiently transmitted from the particle core to its surface because of the crosslinked nature of the polymer. 3D simulations mapping the heat distribution around the Au nanorod (Figure 5.1e and *Appendix*, Figure A5.4) confirmed that it is possible to collapse the OMA particle core without significantly altering its surface temperature, thus minimizing thermal effects to cells.

To examine the dynamics of OMAs, we conjugated the particles with Alexa 488, and recorded fluorescence at 1800 frames per second (fps) during pulsed NIR-stimulation at 37 °C in water (Figure 5.1f and *Appendix*, Figure A5.5). Particles were illuminated at 785 nm with a continuous laser pulsed at a 10 Hz frequency and 50% duty cycle. Under these conditions, both the size of OMA particles and their emission intensity decreased upon illumination (Figure 5.1f). Particle actuation was highly reversible and could be sustained for at least 10^6 cycles (*Appendix*, Figure A5.5). The collapse and swelling time constants were 1.3 ± 0.1 msec, and 3.3 ± 0.2 msec, respectively (*Appendix*, Figure A5.5e and f). These time constants indicate that one can mechanically stimulate cells with rates 1-2 orders of magnitude greater than can be achieved with magnetic actuation.[6-8]

To estimate the force applied by OMAs, we used DNA-based fluorescence tension probes that were recently developed in our group (*Appendix*, Figure A5.6).[12] We observed a reversible increase in fluorescence that coincided with NIR illumination; therefore, particle collapse exerts a force per ligand that is greater than 13 pN, but below ~50 pN (*Appendix*, Figure A5.6 and *Methods*).

5.2.2 Optical modulation of integrin-mediated cell adhesion, protrusion and migration

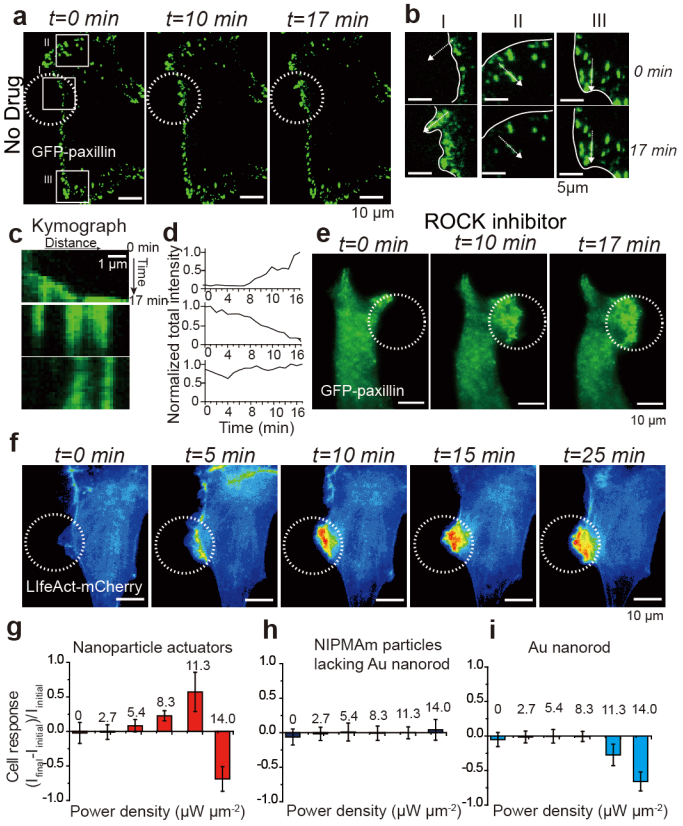

Figure 5.2 Optomechanical actuation of integrins leads to GFP-paxillin and LifeAct-mCherry recruitment. (a) Representative time-lapse TIRF images of GFP-paxillin transiently transfected NIH/3T3 cells that were cultured on OMA nanoparticles displaying the RGD peptide, n≥5 cells. Scale bars, 10 μm. (a, b) NIR illumination (white dashed circle, 10 Hz, 10% duty cycle, power density = 11.3 μW μm^{-2}) leads to rapid recruitment of GFP-paxillin, ROI I. White line indicates cell edge. Adjacent regions showed a loss of GFP-paxillin, ROI II, while distant regions did not show substantial change in GFP-paxillin, ROI III. (c) The kymograph (measured across dashed white arrow) and total paxillin intensity over time (d) within these regions (I, II, and III) of interest confirm the trends noted above. (e) Cells treated with ROCK inhibitor showed a similar increase in GFP-paxillin following force-driven integrin stimulation. Scale bars,10 μm. (f) Representative time-lapse fluorescence images of LifeAct-mcherry transiently transfected 3T3 cells upon NIR illumination (identical conditions to those used in Fig. 2a), n≥20 cells. Scale bars,10 μm. (g-i) Plots of average cellular response for cells cultured on OMA nanoparticles (g), pNIPMAm particles lacking the gold rod core (h), and gold rods lacking the polymer shell (i), when the surface was excited by different NIR laser power intensities (10Hz, 10% duty cycle). The error bar for each data point represents the standard deviation of cell response from at least *n*= 6 cells.

Given that integrin adhesion receptor forces within FAs are estimated within the ~5 pN to 50 pN range,[12-14] OMAs are likely well-suited to trigger integrin activation within FAs. To test this, we transfected NIH/3T3 cells with a plasmid encoding for GFP-paxillin, a widely used surrogate marker for FAs.[3, 15] Cells were then cultured onto a monolayer of OMA nanoparticles modified with cyclic Arg-Gly-Asp-D-Phe-Lys, c(RGDfK), with a density of 2,000 peptides μm^{-2} for 12 hr (*Appendix*, Figure A5.7–10). We illuminated the sample with a pulsed NIR source while recording GFP-paxillin dynamics (Figure 5.2a). No detectable increase in surface temperature was observed at these illumination conditions (*Appendix*, Figure A5.11). Before stimulation, the GFP-paxillin was localized primarily in punctate regions at the cell edge (Figure 5.2a). Representative time-lapse TIRF images showed rapid growth of the total FA size from ~1 μm^2 to 5 μm^2 after stimulation for t = 17 min within region of interest [16] I, coinciding with the NIR illumination area (Figure 5.2a and 2b). In contrast, the average FA size at ROI II, adjacent to the region of NIR stimulation, was reduced by 50% during the same time period. FAs in ROI III, 20 mm away from the NIR source, did not display a detectable change in FA size or organization within the 20 min illumination duration. Kymograph analysis and plots of total paxillin intensity over time within these ROIs confirmed this conclusion (Figure 5.2c and 2d). Other markers of FAs, such as F-actin and vinculin were also rapidly recruited upon identical NIR illumination (*Appendix*, Figure A5.12), demonstrating FA assembly. Dual color imaging of F-actin (mCherry) and paxillin (GFP) upon OMA stimulation showed that F-actin polymerization precedes the recruitment of paxillin and FA maturation, in agreement with existing models (*Appendix*, Figure A5.13). 3D-SIM and total internal reflection fluorescence microscopy (TIRFM) nanometry

showed that the actin network was mechanically displaced by ~100 nm following the collapse of OMA particles (*Appendix*, Figure A5.3 and A5.14). Taken together, these results indicate that particle collapse in the *x*-*y* and *z* directions mechanically strains integrin receptors and this force is transmitted across the cell membrane activating mechanosensitive proteins, such as talin and vinculin, actin polymerization and triggering FA maturation.[3, 8]

Other contributing mechanisms by which OMA collapse could lead to FA maturation may be related to cellular rigidity sensing of the collapsed polymer and increased ligand density in the dehydrated particles. These contributions are likely minimal considering the transient (10% duty cycle) nature of the collapsed particle (Supplementary Note). Moreover, NIR illumination is tuned such that OMA particle are only partially collapsed within the 10 msec illumination window. To further test the role of stiffness sensing and ligand density sensing in cell response, we treated GFP-paxillin expressing cells with the Rho kinase inhibitor Y-27632 for 30 min (blocking myosin II contractility). Based on the literature, ROCK treatment attenuates stiffness sensing mechanisms and ligand density-driven FA maturation.[3, 17-18] Within 5 min of particle actuation, cells rapidly protruded toward the source of the stimulus and increased GFP-paxillin density (Figure 5.2e). Thus, OMA-driven cell stimulation is independent of myosin contractility, and FA growth is primarily attributed to OMA-generated integrin forces, bypassing the requirement for ROCK activity.

To quantify cell response to the NIR intensity and frequency, we transiently transfected cells with LifeAct-mCherry, an F-actin probe, and recorded actin intensity, $I=(I_{final} - I_{initial})/I_{final}$, where $I_{initial}$ is the total actin fluorescence in the ROI prior to

stimulation, and I_{final} is the total fluorescence in the same ROI following stimulation at t = 20 min. This readout allowed us to benchmark the response of cells under different conditions. Although appropriate NIR illumination conditions led to a drastic enhancement in F-actin localization (Figure 5.2f), this was not uniform across all conditions tested. We found that cell response was optimal and similar at frequencies of 10 and 100 Hz (*Appendix*, Figure A5.15). In contrast, there was limited cell response at 1 Hz and 0 Hz (*Appendix*, Figure A5.15–16), which indicated enhanced integrin activation upon cyclic stimulation. Therefore, for controlling FA formation, OMA nanoparticles require the application of cyclic mechanical stimulation rather than sustained force.

At lower NIR intensities (2.7 mW μm^{-2}), where ~20% of effectively bound ligands experience >13 pN (*Appendix*, Figure A5.6), cells did not display a measurable response, indicating that at those force levels, the OMA particles failed to trigger actin polymerization (Figure 5.2g). At greater NIR intensities ranging from 5.4 to 11.3 mW μm^{-2}, corresponding to a range from 60% to 100% of effectively bound ligands experiencing >13 pN of tension, we observed an enhancement in F-actin enrichment. In contrast, at average powers equal to or greater than 14.0 $\mu W\ \mu m^{-2}$, the particle actuation led to cell retraction (*Appendix*, Figure A5.17), which is due to thermal heating.[19] This is supported by thermal measurements showing a 6 ± 1.2 °C increase at this power (*Appendix*, Figure A5.11). Importantly, particles that lacked the Au rod core (Figure 5.2h), rods lacking the polymer shell (Figure 5.2i), or rods coated with a thermally insensitive polymer shell (*Appendix*, Figure A5.18) failed to display any increase in actin localization regardless of the NIR intensity tested. These experiments further confirm that cell response is primarily driven by optical manipulation of integrin tension.

Given that FA formation ultimately controls cell protrusion and migration,[20] we explored whether OMA stimulation could be used to guide cell movement. To test this, we stimulated FA formation in LifeAct-mCherry transfected cells for 2 hrs. (Figure 5.3a show the results from a representative cell. Initially (within 9 min), new protrusions formed in the illumination area. Subsequently (within 40 min), the cell migrated to maximize its overlap with the region of mechanical actuation. Note that the regions of greatest F-actin intensity always coincided with particle actuation. The NIR illumination area was then moved in a stepwise fashion such that at least one part of the cell maintained exposure to the mechanical stimulus. In this way, the cell was mechanically guided across the field of view. Based on kymograph analysis, the average speed of cell migration was approximately 0.33 μm min^{-1} (Figure 5.2b). A plot of the response of six cells stimulated using this approach is shown in (Figure 5.3c, and indicates that while the approach is robust, there is cell to cell variability in response to the mechanical stimulus (*Appendix*, Figure A5.19). Nonetheless, this experiment represents the first example of controlling cell migration by using active mechanical forces.

5.2.3 Actuation of T-cell receptors with OMA nanoparticles

Recent single molecule experiments demonstrate that mechanical stimulation of the T cell receptor leads to T cell activation,[21-22] and thus we next aimed to use OMA particles to optically control T cell activation. As a proof-of-concept, we modified OMA particles with a specific peptide-major histocompatibility complex (pMHC) from the OVA model. These pMHC decorated particles were used to mechanically stimulate TCR in naïve OT-I T lymphocytes (Figure 5.2d). Upon stimulation (*t*=3 min, dotted white circle), T cells were effectively activated within one minute as indicated by a calcium flux measured

with the fura-2 dye (Figure 5.2e, *Appendix*, Figure A5.20a). OT-I cells optically stimulated on a pMHC monolayer on the glass coverslip showed no response (Figure 5.2f and g and *Appendix*, Figure A5.20b). Note that T cells rapidly respond to mechanical stimuli (within 1 min) in contrast to cell adhesions, which typically require ~10 min for initial actin polymerization. Therefore, OMA particles can be used to mechanically trigger T cells, demonstrating applications in studying the role of mechanical forces in different biological systems.

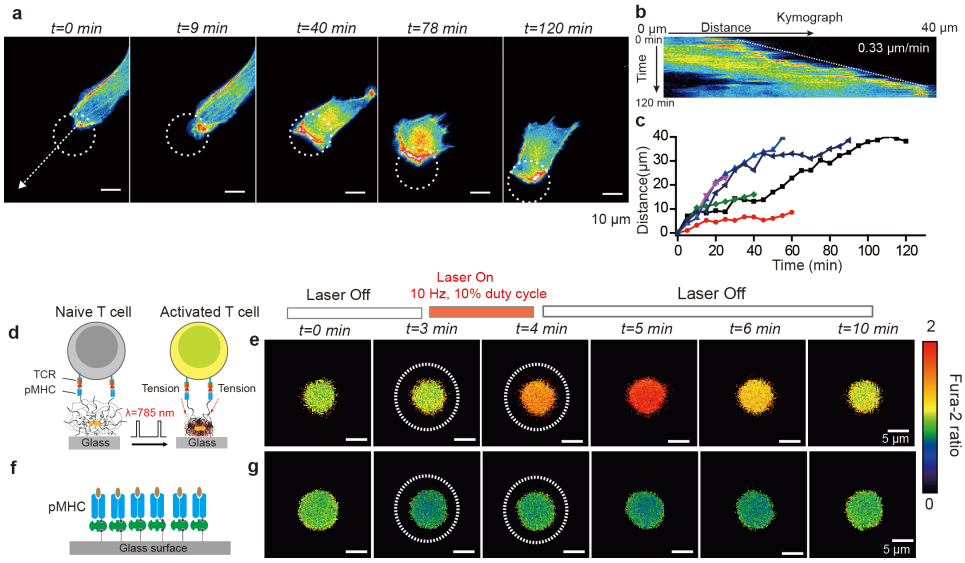

Figure 5.3 Optical control of cell migration and T cell activation by OMA nanoparticles. (a)Representative time-lapse images showing control NIH/3T3 cell migration over long distances by OMA stimulation. The white dashed circle represents the region of NIR illumination. Scale bars,10 µm. (b) Kymograph analysis of cell migration obtained using white dashed arrow shown in (a). (c) Plot showing the cell migration distance as a function of time upon OMA stimulation for *n*= 6 cells. Cell tracking was stopped when cells ceased to respond to NIR illumination or if cells displayed phototoxicity from fluorescence imaging. Supplementary Figure 19 shows representative images of cell migration from these experiments. (d) Schematic showing OMA nanoparticles functionalized with the OVA peptide-major histocompatibility complex (pMHC) and illuminated to mechanically stimulate T cell receptors on the membrane of OT-I Tlymphocytes. (e) Fluorescence images of the ratiometric intensity of the fura-2 calcium indicator dye. Upon stimulation (*t*=3 min, dotted white circle), T cells were effectively activated within a 1min as indicated by the increase of fura-2 emission ratio when excited by 340 nm / 380 nm. Scale bars, 5 µm. (f) Schematic of control

experiments, where OT-I cells were stimulated on a pMHC monolayer that was directly modified on the glass coverslip. (g) Upon stimulation (white circle), no calcium flux was observed and the calcium signal continued to fluctuate at basal levels. Scale bars, 5 μm.

5.3 Conclusion

In summary, we developed a new class of optomechanical actuator nanoparticles that allow one to optically manipulate receptor tension with optical spatial resolution and 5 msec temporal resolution using low intensity NIR illumination. We demonstrate that nanoparticle-generated forces induce F-actin polymerization, recruitment of paxillin and vinculin into FAs, and ultimately controlling cell migration. Note that control of cell migration using light has been achieved using optogenetic tools,[9-10] but unlike these past examples, our approach precludes the need for genetic modification of target cells. Optomechanical stimulation represents a yet unexplored avenue for controlling signaling activity in living cells that may have important applications in a broad range of cell types including neurons, platelets, and T-cells. Moreover, the non-toxic nature of thermo-responsive polymers and gold nanoparticles suggests potential for *in vivo* applications.

5.4 Materials and methods

5.4.1 Gold nanorod preparation

To generate OMA nanoparticles, we first synthesized the gold nanorod (NR) inorganic core using an improved seeded growth synthesis procedure, recently published by Murray and colleagues.[23] The synthesis of AuNRs employed a binary surfactant mixture composed of hexadecyltrimethylammonium bromide (CTAB) and sodium oleate (NaOL) to grow Au seed crystals into NRs. Briefly, the seed solution was prepared as follows: 5 mL of 0.5 mM $HAuCl_4$ was mixed with 5 mL of 0.2 M CTAB solution in a 20 mL scintillation vial. 0.6 mL of fresh 0.01 M $NaBH_4$ was diluted to 1 mL with water and was then injected into the Au(III)-CTAB solution under vigorous stirring (1,200 rpm). The color of the solution changed from yellow to brownish yellow and the stirring was stopped after 2 min. The seed solution was aged at room temperature for 30 min prior to use.

We adapted the general guidelines presented by Murray et al.[23] to control the dimensions of the NR such that the NIR plasmon peak was approximately 800 nm. In our protocol, we prepared a growth solution comprised of 3.6 g of CTAB and 0.4936 g of NaOL dissolved in 100 mL of warm water (~50 °C) in a 250 ml Erlenmeyer flask. The solution was allowed to cool down to 30 °C, and then 8.5 mL of 4 mM $AgNO_3$ solution was added. The mixture was kept undisturbed at 30 °C for 15 min after which 100 mL of 1 mM $HAuCl_4$ solution was added. The solution became colorless after 90 min of stirring (700 rpm), and then 0.6 ml of HCl (37 wt. % in water, 12.1 M) was introduced to adjust the pH and acidify the solution. After 15 min of slow stirring at 400 rpm, 0.6 mL of 0.064 M ascorbic acid was added and the solution was vigorously stirred for 30 s. Finally, 80

μL of seed solution was injected into the growth solution. The resultant mixture was stirred for 30 s and left undisturbed at 30 °C for 12 h to complete NR growth. The products were isolated by centrifugation at 5,000 rpm for 60 min followed by removal of the supernatant; the final solution was concentrated to 90 ml and characterized using UV-vis-NIR and TEM.

5.4.2 Polymerization and encapsulation of AuNRs with pNIPMAm

The procedure for polymerization and encapsulation of the AuNRs with pNIPMAm[24] was adapted from methods noted by Contreras-C´aceres et al.[25] and F. Tang et al.[26] employing Au and Ag spherical nanoparticles, respectively. First, the CTAB and NaOL surfactants coating the AuNRs were replaced with a thiolated and vinyl terminal (C=C) ligand by adding 20 mg of *N,N′*-bis(acryloyl)cystamine to a 90 ml AuNR solution along with 10 ml ethanol while vigorously stirring at 700 rpm for 12 hours. Subsequently, the AuNR solution was purified by centrifugation at 5,000 rpm for 60 min, removing the supernatant, and then redispersing in 15 mL of deionized water. This solution could be stored at 4 °C for several months without adversely affecting quality of OMAs.

The polymerization of pNIPMAm on the Au nanorods surface was carried out as follows: 0.1 g of N-isopropylmethacrylamide, 0.01 g of the crosslinking agent *N,N′*-methylenebisacrylamide were dissolved in 15 ml Milli-Q water in a three neck flask. The mixture was heated to 70 °C under continuous stirring and purged with continuous N_2 flow. Subsequently, 1 ml of the AuNR solution modified with the thiolated vinyl group (described above) was added to the three-neck flask. After 1 min, pNIPMAm polymerization was initiated with the addition of 80 μl (0.1 M) of the free radical initiator

2,2′azobis(2-methylpropionamidine) dihydrochloride (AAPH) and the polymerization was allowed to proceed for 2 hr at 70 °C. In some cases, we aimed to decorate the OMA particles with the alkyne functional group. This was achieved by adding 30 µl of propargyl methacrylate monomer dissolved in 1 mL ethanol at the 100 min time point of reaction and allowing the free-radical polymerization to proceed for the full 2 hr. Please note that vigorous stirring (1,200 rm) was used in every step in the OMA particle synthesis, and no additional detergent was used in the synthetic protocol. After the reaction was complete, the sample was allowed to gradually cool to room temperature while stirring. To remove gold-free nanoparticles, the dispersion was diluted with water, centrifuged, then the supernatant was removed and the resulting pellet was redispersed in water. The procedure was repeated at least three times, yielding OMAs with ~95% purity based on TEM analysis.

The synthesis of the control pNIPMAm particles with 50% crosslinking density used 40 mg of N-isopropylmethacrylamide and 40 mg of the crosslinking agent *N,N′*-methylenebisacrylamide, however, all other steps were identical to the protocol described above for the 10% crosslinking density pNIPMAm-coated particles. The synthesis of the control pNIPMAm particles lacking the inorganic Au NR core was identical to the protocol described above, with a single exception in that the 1 mL AuNR solution was not added.

5.4.3 Characterization of OMAs

Temperature controlled dynamic light scattering (DLS) was performed on a Zetasizer Nano ZS90 (Malvern Instruments, Malvern UK). Negative staining transmission electron microscopy(TEM) was carried out on a Hitachi H-7500 transmission electron microscope

at an accelerating voltage of 75 kV. AFM measurements were performed on a "FastScan Bio" AFM (Bruker, USA) in a closed liquid cell with the ability to control the temperature of the solution from room temperature to 55 °C. Silicon AFM tips (Bruker)with a tip radius of curvature = 12 nm were used to image the sample in *peak-force* tapping mode.

5.4.4 Determination of dynamics of OMA nanoparticles

To determine the collapse and relaxation dynamics of OMA nanoparticles in response to light, we functionalized the particles with a fluorescent dye and used pulsed NIR excitation coupled with fluorescence imaging to monitor particle dynamics. Note that Alexa488 was selected to record particle dynamics because of its known temperature independence, which was verified in *Appendix*, Figure A5.5g and h. Therefore, changes in fluorescence quantum yield (intensity) could be ascribed to OMA particle collapse rather than to local heating. The OMA nanoparticles were immobilized onto azide modified coverslips (as described in the surface preparation section). However, rather than modifying the remaining alkyne functional groups with the cRGDfK peptide, the OMA nanoparticles were conjugated with an azide-modified fluorescent dye. Briefly, a 50 μL solution containing 2.5 μL of 2 nM Alexa Fluor 488-cRGDfK- azide (Note: the synthesis of this molecule was adapted from Liu et al.(Liu, 2013 #11)). 2.5 μL of 10 mM ascorbic acid, 5 μL of 10 mM Cu(II)-TBTA (55% DMSO), and 40 μL of 55% (v/v) DMSO was placed between two OMA-modified coverslips. The sandwiched coverslips were sealed in a secondary petri dish, and the reaction was allowed to proceed for 12 hr at room temperature. The coverslips were then rinsed with ethanol and dried under a stream of nitrogen. The samples with Alexa488-OMA particles were then simultaneously

imaged using epifluorescence microscopy while chopping the NIR laser source at 10 Hz (50% duty cycle). A standard FITC cube was used for fluorescence imaging. In addition, two filters (product number: 87-745,47-291, Edmund optics, USA) were included in the optical path to block the NIR illumination. The fluorescence images were captured by a sCMOS camera (Zyla 4.2 sCMOS, Andor Technologies Ltd., UK) at 1800 fps.

5.4.5 Determination of cRGDfK peptide density on OMA nanoparticles

The value of the extinction coefficient for the cRGDfK peptide was too small for absorption spectrometry to quantify the peptide loading density. Instead, to estimate the peptide density, azide dye was coupled to the alkyne terminal group of the OMA nanoparticles using click chemistry. Based on the assumption that the dye and the cRGDfK peptide have similar coupling efficiencies, we quantified the dye loading density to approximate the peptide loading density.

5.4.6 Quantitative fluorescence calibration curve using supported lipid bilayers

In order to quantify the dye loading density, a quantitative fluorescence supported lipid bilayer calibration curve was constructed to relate fluorescence to dye density.[27] To establish the linear relationship between the observed fluorescence intensity and the fluorophore density, we prepared lipid bilayers with predefined concentrations of fluorescent lipid molecules. Non-fluorescent DOPC supported lipid membranes were doped with DPPE-fluoresce in lipids with ratios ranging from 0 to 1 mol% and then imaged under the same conditions used in live cell imaging (*Appendix*, Figure A5.9a and b). The number of fluorophore molecules per unit area was directly calculated from the footprint of a DOPC lipid, which was reported at 0.72 nm.[27]

5.4.7 Determination of the F factor

The scaling factor F represents the ratio ofFAM emission versus the DPPE-fluorescein emission and is defined as: $F = I_{\text{bulk(FAM-azide)}}/I_{\text{bulk(DPPE-fluorescein)}}$, where $I_{\text{bulk(FAM-azide)}}$ and $I_{\text{bulk(DPPE-fluorescein)}}$ are the intensity of the ligand and lipid molecules in solution after being normalized for concentration, respectively. This value was measured on the fluorescence microscope by moving the focal plane (~200 μm) into the center of the sample (*Appendix*, Figure A5.9d).

5.4.8 Determination of FAM density on OMA nanoparticles surface

To exclude fluorescence quenching by the Au NR core, 50 mM KCN was used to dissolve the gold NR core prior to covalent immobilization of the OMAs nanoparticles onto the glass substrate. After gold dissolution, OMA nanoparticles were washed 5 times with DI water by centrifugation (8000 rpm, 10 min) to wash away the KCN. Subsequently, OMA nanoparticles without the AuNR core were covalently immobilized onto the azide functionalized glass substrates using the click reaction. In order to exclude fluorescence self-quenching, the FAM-azide concentration was ten times lower than the cRGDfK peptide concentration when functionalizing OMA particles. Briefly, a 50 μL solution containing 2.5 μL of 30 mM FAM-azide, 2.5 μL of 10 mM ascorbic acid, 5 μL of 10 mM Cu (II)-TBTA (55% DMSO, 45% H_2O), and 40 μL of 55% by volume DMSO were added to an OMA(Au NR free)-functionalized coverslip and sandwiched with a second OMA(Au NR free)-functionalized glass coverslip. This reaction was allowed to proceed at 50 °C for 3 h prior to rinsing with ethanol and drying with nitrogen. The surface was imaged under the same conditions used in live cell imaging. Using the

calibration curve, F factor and fluorescence intensity from FAM labeled OMA (Au NR free)-functionalized coverslips (*Appendix*, Figure A5.9d), FAM density was estimated to be ~2,000 molecules μm^{-2}. Note, because the FAM-azide reaction concentration is ten times lower than the cRGDfK peptide concentration used for cell experiments, the absolute RGDfK peptide density should be much higher than 2,000 molecules μm^{-2}, and this value represents the lower bound estimate.

5.4.9 Estimation of OMA nanoparticle collapse-driven forces using molecular tension sensor

To estimate the force applied during OMA nanoparticle collapse, we immobilized OMA nanoparticles onto a surface functionalized with DNA-based molecular tension probes that were recently developed in our lab.[12, 28-29] The DNA tension sensor consists of three components: 1) a lower ssDNA strand modified with a molecular quencher (BHQ1) at the 3′ end, 2) an upper ssDNA strand modified with a Cy3B dye as fluorescence reporter at the 5′ end, 3) and a bridging hairpin duplex flanked by two complementary ssDNA arms that brings the BHQ1 and Cy3B into close proximity. Due to the high quenching efficiency (> 95%) between BHQ1 and Cy3B dye, minimal fluorescence is detected when the hairpin is folded. However, when sufficient external forces are applied to the two ends of DNA, the hairpin structure becomes unfolded due to force, which effectively results in a physical separation of Cy3B dye away from BHQ1. This increased distance between dye and quencher is accompanied by a significant amount of fluorescence increase (~10-30 fold) due to de-quenching of the dye. Therefore, this method enables force measurements in real-time. Here, we used a DNA hairpin that has

been experimentally calibrated to have a $F_{1/2}$ of ~13 pN, which indicates that 50% of harpins will unfold at a force=13 pN.

To immobilize the DNA tension sensor to the coverslip, we adapted a previously published protocol for AuNP tension sensor.[28] Initially, 9 nm spherical AuNPs were randomly anchored to a lipoic acid modified glass coverslip. To efficiently attach the DNA tension sensors onto the AuNP coverslip with high coverage, we modified the sensor with a thiol group at the 5' end of the lower ssDNA and directly incubated the sensor construct to the AuNP surface. Typically, 300 nM thiolated DNA hairpins in 1 M NaCl solution were incubated with the AuNP surface overnight. Note, all hairpin samples were pre-folded by applying anannealing cycle in PCR thermocycler. On the 3′ end of the upper ssDNA, we added an additional biotin group available to bind to streptavidin, which provides a link for the tension sensor to ultimately bind to the biotinylated OMA particles.

Upon NIR illumination of particles, we observed a reversible increase in fluorescence that coincided with NIR illumination. DNA unfolding could be repeated for hundreds of cycles until photobleaching of the force-reporting dye occurred. This suggested that the particle collapse exerts a force that is greater than 13 pN (force response threshold), but below the ~50 pN force required to shear DNA duplexes (*Appendix*, Figure A5.6).

5.4.10 Simulations

Calculations of the OMA particle temperature and heat distribution were performed by finite element simulation (Comsol Multiphysics, Burlington MA). In all the simulations, the NIR laser power was held constant at 35 mW but with different radius of the laser

spot (3, 5, 7, 10 μm, respectively). In these simulations, we assume that during the transient laser heating period (10 msec), the temperature of the OMA particle reaches steady state conditions. Thus, we calculate the temperature distribution in the nanorod and polymer at steady state to determine the maximum temperatures that would be observed during the illumination cycle. We also assume that the nanorod is located exactly at the center of polymer and the laser illumination provides a constant and uniform heat generation that dissipates uniformly from the gold nanorod. The absorption cross section of Au NR was estimated at 20,000 nm^2 based on literature precedent.[30] The heat capacity and thermal conductivity of the polymer hydrogel is assumed to be equivalent to that of water.[30] The value of thermal conductivity of gold nanorod was set to 317 W mK^{-1}.[31] Note that the power density of 113 μW $μm^{-2}$ (35 mW, the radius of the laser spot was 10 μm, 100% duty cycle) is 10 fold greater than that used for cell stimulation because a 100% duty cycle (steady state illumination) is assumed for the energy input calculation.

5.4.11 Surface preparation

Glass coverslips (No. 2–25mm diameter, VWR) were sonicated in Nanopure water (18.2 mΩ) for 10 min and then etched in piranha for 10 min - please take caution - piranha is extremely corrosive and may explode if exposed to organics. The glass coverslips were then washed twice in a beaker of Nanopure water (18.2 mΩ) and placed into three successive wash beakers containing ethanol and left in a final fourth beaker containing 1% 6-azidosulfonylhexyl-triethoxysilane (Gelest, Inc.) in ethanol for 6 hours. The azide functionalized substrates were then immersed in the ethanol three times and subsequently rinsed with ethanol and dried under N_2. To covalently immobilize the

OMAs nanoparticles (or pNIPMAm particles lacking the Au NR core)onto the azide functionalized glass substrates, a 50 μL solution containing 10 μL of 1 nM OMA nanoparticles, 10 μL of 10 mM ascorbic acid, 10 μL of 10 mM Cu (II)-TBTA(55% DMSO), and 20 μL of DMSO were added onto one azide modified glass coverslip and then covered using a second azide functionalized glass coverslip. The sandwiched coverslips were sealed in a secondary petri dish, and the reaction was allowed to proceed for 12 hr at room temperature. The coverslips were then rinsed with ethanol and dried under a stream of N_2. This procedure generated coverslips coated with a monolayer of covalently immobilized OMA particles. To further modify OMA particles with the cyclic Arg-Gly-Asp-d-Phe-Lys c(RGDfK) peptide, a 50 μL solution containing 2 μL of 318 mM RGD-N_3, 5 μL of 10 mM ascorbic acid, 5 μL of 10 mM Cu (II)-TBTA (55% DMSO), and 40 mL of 55% (by volume) DMSO was sandwiched between two OMA-functionalized substrates. This reaction was allowed to proceed at 50 °C for 3 h prior to rinsing with ethanol and drying with nitrogen.

To prepare Au NRs lacking the polymer shell, the CTAB and NaOL surfactants coating the AuNRs were exchanged with 1 mM alkyne terminated PEG thiol (Catalog number: PG2-AKTH-1k, 1000 g/mol, Nanocs, USA) in a 1 ml AuNR solution (described in *Gold nanorod preparation*). To allow for more complete ligand exchange, the solution was sonicated for 3 min and left at room temperature for 12 hr. Subsequently, the AuNR solution was purified by centrifugation at 5,000 rpm for 10 min, removing the supernatant, and then redispersing in 25 μl of deionized water. These Au NRs were immobilized onto azide-functionalized glass coverslips by placing a 70 μL solution containing 25 μl of Au NRs modified with the alkyne terminal group, 5 μL of 10 mM

ascorbic acid, 5 μL of 10 mM Cu(II)-TBTA(55% DMSO), and 35 μL of DMSO between two coverslips. The sandwiched coverslips were sealed in a secondary petri dish, and the reaction was allowed to proceed for 12 hr at room temperature. The coverslips were then rinsed with ethanol and dried under a stream of nitrogen. The coverslips were subsequently incubated with 500 μL of 100 μg ml^{-1} human fibronectin (Sigma-Adrich) for 1 hr. Fibronectin enhanced cell binding to the bare AuNR surface to allow for control experiments. Coverslips were rinsed with sterile PBS prior to seeding cells and conducting experiments.

5.4.12 Synthesis of RGDfK-N_3

500 μg of cRGDfK peptide (Peptides International, MW: 603.68) was reacted with 1.2 mg azide-NHS linker (Thermo Scientific. MW: 198.14) in 20 μL DMF. To this reaction mixture, 0.1 μL of neat triethylamine was added as an organic base and the reaction was allowed to proceed for 12 hr at room temperature. The product was purified by reverse phase HPLC (flow rate 1 ml/min; solvent A: 99.5% DI water, 0.5% TFA; solvent B: 99.5% acetonitrile 0.5% TFA; initial condition was 10% B with a gradient of 1% per min). The final RGDfK-N_3 product was verified by MALDI-TOF.

5.4.13 Cell culture and transfection

NIH/3T3 fibroblast cells were cultured in Dulbecco's Modified Eagle's Medium (DMEM) supplemented with 10% Cosmic Calf Serum (Mediatech), HEPES (9.9 mM, Sigma), sodium pyruvate (1 mM, Sigma), L-glutamine (2.1 mM, Mediatech), penicillin G (100 IU ml^{-1}, Mediatech) and streptomycin (100 μg ml^{-1}, Mediatech) and were incubated at 37 °C with 5% CO_2. Cells were passaged at 60-80% confluency and plated at a density

of 10% using standard cell culture procedures. All cell transfection was performed in a 24-well plate. All procedures are based on a standard protocol provided by Life Technologies (Carlsbad, CA). Briefly, 4×10^4 cells were plated in each well one day before transfection. During transfection, 0.5-1g DNA was mixed with Lipofectamine LTX with Plus™ Reagent for each well and incubated for 24-48 hr before imaging.

5.4.14 Microscopy and optomechanics experiments

Transfected NIH 3T3 cells were cultured on a monolayer of OMA nanoparticles modified with cyclic Arg-Gly-Asp-d-Phe-Lys c(RGDfK) with a density of 2,000 peptides per μm^2 for 12 hr. Live cells were imaged in standard cell imaging buffer (Hank's balanced salt, pH 7.4, 10 mM HEPES without phenol red) at 37 °C. During imaging, physiological temperature was maintained with a warming apparatus consisting of a sample warmer and an objective warmer (Warner Instruments 641674D and 640375). The microscope was Nikon Eclipse Ti driven by the Elements software package. The microscope features an Evolve electron multiplying charge coupled device (EMCCD; Photometrics), an Intensilight epifluorescence source (Nikon), a CFI Apo 100× (numerical aperture (NA) 1.49) objective (Nikon) and a TIRF launcher with three laser lines: 488 nm (10 mW), 561 (40 mW), and 638 nm (20 mW). The experiments used the following Chroma filter cubes: TIRF 488, TRITC, FITC and reflection interference contrast microscopy (RICM). For optomechanics experiments, a near-infrared diode laser (Schäfter+Kirchhoff, Hamburg, Germany) was mounted using the standard dark-field condenser accessory available from Nikon. The NIR laser wavelength was 785 nm ± 10 nm, while the laser output maximum power was 53 mW. The minimum size (diameter) of the focused spot was 6 μm. The laser modulation frequency was controlled by a

frequency generator following the instructions provided by the manufacturer. Two additional NIR cutoff filters (product number: 87-745, 47-291, Edmund optics, USA) were included into the optical path to eliminate NIR bleadthrough to the EMCCD. Using this setup, we simultaneously illuminated the sample with a pulsed NIR source (10 Hz, 10% duty cycle) while recording FAs dynamics for the cell.

5.4.15 Calcium imaging

To modify OMA surface with peptide-major histocompatibility complex (pMHC) from the OVA model. The amine functionalized OMA particles were incubated with NHS-biotin (Thermo Fisher) at 2 mg ml^{-1} in DMSO (Sigma) overnight. Subsequently, the substrates were washed with EtOH and dried under a stream of nitrogen. This was then followed by incubation with streptavidin (1 μg ml^{-1}, 1 hour and room temperature). After rinsing with PBS, the substrates were incubated with the biotinylated H-2K(b) monomers (80 μg ml^{-1}, 1 hour, room temperature). After final rinsing with PBS, the substrates were assembled into the cell imaging chamber (Life Technologies), replaced with hank's balanced salt imaging buffer (Sigma) and used immediately for cell experiment. Here, biotinylated H-2K(b) monomers were provided by the National Institutes of Health Tetramer Core Facility at Emory University. Monomers are comprised of the cognate chicken ovalbumin 257-264 epitope SIINFEKL (N4) peptide loaded in the alpha chain of mouse H-2K(b) that is complexed with beta-2-microglobulin (b2m) from mouse origin.

Freshly purified OT1 cells (n = 1×10^6) were centrifuged to remove the RPMI media and re-suspended in 3 ml of hank's imaging buffer. 10 ml of 1 mM of fura-2/Am in DMSO was added into the cell suspension. The solution was kept at 37 °C for 30 min.

Afterwards, cells were pelleted by centrifugation at 1,200 rpm for 4 min and re-suspended in 3 ml of imaging buffer for an additional 15 min. This step is to ensure full de-esterification of the fura-2/Am. Then, the cells were again pelleted and re-suspended in 1 ml of imaging buffer and prepared for seeding on the OMA surface. The cells were incubated for 20 mins before stimulation.

For the calcium imaging, the microscope employed a Nikon CFI S Fluor 100x oil objective, a Chroma 340 excitation filter set (ET340x, T400lp and ET510/80m) and Chroma 380 excitation filter set (ET380x, T400lp and ET510/80m). During the experiment, the fluorescence images were acquired by using the 340 nm and 380 nm filter sets sequentially. Afterwards, ImageJ was used to generate a mask for both channels excited by 340 nm and 380 nm. Finally, the fura-2 ratio (I340/I380) was calculated by using the image calculator function in ImageJ.

5.4.16 Determination of F-actin displacement using TIRF-based nanometry

The evanescent field intensity in TIRF exponentially decays with a predictable function,[32]

$$I = I_0 e^{-\frac{z}{d}} \quad \text{and} \quad d = \frac{\lambda}{4\pi\sqrt{n_1^2 \sin\theta^2 - n_2^2}}$$

where I_0 is the intensity at $z = 0$, n_1 and n_2 are the indices of refraction of the glass coverslip and the sample, respectively, λ is the excitation wavelength, and θ is the angle of incidence. Therefore, one can infer the height changes of cellular structures, as long as the number of fluorophores remains fixed.[32] In our experiments, we assumed that n_1 (glass) = 1.515, n_2 [33] =1.37, λ= 488 nm, θ= 70° ~78°. Experimentally, we found that the TIRF intensity of F-actin increased by 70% ±12% under steady-state NIR illumination

(*Appendix*, Figure A5.14). Using these parameters, and assuming an initial height of the F-actin at 220 nm, and fixed number of GFP emitters, we were able to estimate the change in height for the F-actin network. The height changes of the F-actin network are estimated to range between 95–115 nm in response to OMA particle collapse. Note that the n_2 is assumed to remain constant. However, the index of refraction for pNIPMAm is known to increase following collapse.[30] An increase in n_2 will reduce the value of I. Therefore, the calculated decrease in z, represents the minimum displacement.

5.5 References

1. Vogel, V.; Sheetz, M., Local force and geometry sensing regulate cell functions. *Nat Rev Mol Cell Biol* **2006,** *7* (4), 265-75.

2. Dufrene, Y. F.; Evans, E.; Engel, A.; Helenius, J.; Gaub, H. E.; Muller, D. J., Five challenges to bringing single-molecule force spectroscopy into living cells. *Nat Methods* **2011,** *8* (2), 123-7.

3. Riveline, D.; Zamir, E.; Balaban, N. Q.; Schwarz, U. S.; Ishizaki, T.; Narumiya, S.; Kam, Z.; Geiger, B.; Bershadsky, A. D., Focal contacts as mechanosensors: externally applied local mechanical force induces growth of focal contacts by an mDia1-dependent and ROCK-independent mechanism. *J Cell Biol* **2001,** *153* (6), 1175-86.

4. Charras, G. T.; Horton, M. A., Single cell mechanotransduction and its modulation analyzed by atomic force microscope indentation. *Biophysical Journal* **2002,** *82* (6), 2970-81.

5. Wang, Y. X.; Botvinick, E. L.; Zhao, Y. H.; Berns, M. W.; Usami, S.; Tsien, R. Y.; Chien, S., Visualizing the mechanical activation of Src. *Nature* **2005,** *434* (7036), 1040-1045.

6. Tseng, P.; Judy, J. W.; Di Carlo, D., Magnetic nanoparticle-mediated massively parallel mechanical modulation of single-cell behavior. *Nature Methods* **2012,** *9* (11), 1113-+.

7. Etoc, F.; Lisse, D.; Bellaiche, Y.; Piehler, J.; Coppey, M.; Dahan, M., Subcellular control of Rac-GTPase signalling by magnetogenetic manipulation inside living cells. *Nature Nanotechnology* **2013,** *8* (3), 193-8.

8. Sniadecki, N. J.; Anguelouch, A.; Yang, M. T.; Lamb, C. M.; Liu, Z.; Kirschner, S. B.; Liu, Y.; Reich, D. H.; Chen, C. S., Magnetic microposts as an approach to apply forces to living cells. *Proceedings of the National Academy of Sciences of the United States of America* **2007,** *104* (37), 14553-14558.

9. Levskaya, A.; Weiner, O. D.; Lim, W. A.; Voigt, C. A., Spatiotemporal control of cell signalling using a light-switchable protein interaction. *Nature* **2009,** *461* (7266), 997-1001.

10. Wu, Y. I.; Frey, D.; Lungu, O. I.; Jaehrig, A.; Schlichting, I.; Kuhlman, B.; Hahn, K. M., A genetically encoded photoactivatable Rac controls the motility of living cells. *Nature* **2009,** *461* (7260), 104-U111.

11. Pastrana, E., Optogenetics: controlling cell function with light. *Nature Methods* **2011,** *8* (1), 24-25.

12. Zhang, Y.; Ge, C.; Zhu, C.; Salaita, K., DNA-based digital tension probes reveal integrin forces during early cell adhesion. *Nature Communications* **2014,** *5*.

13. Wang, X.; Ha, T., Defining single molecular forces required to activate integrin and notch signaling. *Science* **2013,** *340* (6135), 991-4.

14. Jurchenko, C.; Chang, Y.; Narui, Y.; Zhang, Y.; Salaita, K. S., Integrin-generated forces lead to streptavidin-biotin unbinding in cellular adhesions. *Biophysical Journal* **2014,** *106* (7), 1436-46.

15. Oakes, P. W.; Beckham, Y.; Stricker, J.; Gardel, M. L., Tension is required but not sufficient for focal adhesion maturation without a stress fiber template. *Journal of Cell Biology* **2012,** *196* (3), 363-374.

16. Shaw, S. K.; Ma, S.; Kim, M. B.; Rao, R. M.; Hartman, C. U.; Froio, R. M.; Yang, L.; Jones, T.; Liu, Y.; Nusrat, A.; Parkos, C. A.; Luscinskas, F. W., Coordinated redistribution of leukocyte LFA-1 and endothelial cell ICAM-1 accompany neutrophil transmigration. *Journal of Experimental Medicine* **2004,** *200* (12), 1571-1580.

17. Coyer, S. R.; Singh, A.; Dumbauld, D. W.; Calderwood, D. A.; Craig, S. W.; Delamarche, E.; Garcia, A. J., Nanopatterning reveals an ECM area threshold for focal adhesion assembly and force transmission that is regulated by integrin activation and cytoskeleton tension. *Journal of Cell Science* **2012,** *125* (21), 5110-5123.

18. Mih, J. D.; Marinkovic, A.; Liu, F.; Sharif, A. S.; Tschumperlin, D. J., Matrix stiffness reverses the effect of actomyosin tension on cell proliferation. *Journal of Cell Science* **2012,** *125* (24), 5974-5983.

19. Huang, X. H.; El-Sayed, I. H.; Qian, W.; El-Sayed, M. A., Cancer cell imaging and photothermal therapy in the near-infrared region by using gold nanorods. *Journal of the American Chemical Society* **2006,** *128* (6), 2115-2120.

20. Iskratsch, T.; Wolfenson, H.; Sheetz, M. P., Appreciating force and shape-the rise of mechanotransduction in cell biology. *Nat Rev Mol Cell Biol* **2014,** *15* (12), 825-33.

21. Kim, S. T.; Takeuchi, K.; Sun, Z. Y.; Touma, M.; Castro, C. E.; Fahmy, A.; Lang, M. J.; Wagner, G.; Reinherz, E. L., The alphabeta T cell receptor is an anisotropic mechanosensor. *J Biol Chem* **2009,** *284* (45), 31028-37.

22. Liu, B.; Chen, W.; Evavold, Brian D.; Zhu, C., Accumulation of Dynamic Catch Bonds between TCR and Agonist Peptide-MHC Triggers T Cell Signaling. *Cell* **2014,** *157* (2), 357-368.

23. Ye, X. C.; Zheng, C.; Chen, J.; Gao, Y. Z.; Murray, C. B., Using Binary Surfactant Mixtures To Simultaneously Improve the Dimensional Tunability and Monodispersity in the Seeded Growth of Gold Nanorods. *Nano Letters* **2013,** *13* (2), 765-771.

24. Das, M.; Sanson, N.; Fava, D.; Kumacheva, E., Microgels loaded with gold nanorods: Photothermally triggered volume transitions under physiological conditions. *Langmuir* **2007,** *23* (1), 196-201.

25. Contreras-Caceres, R.; Pacifico, J.; Pastoriza-Santos, I.; Perez-Juste, J.; Fernandez-Barbero, A.; Liz-Marzan, L. M., Au@pNIPAM Thermosensitive Nanostructures: Control over Shell Cross-linking, Overall Dimensions, and Core Growth. *Advanced Functional Materials* **2009,** *19* (19), 3070-3076.

26. Tang, F.; Ma, N.; Wang, X.; He, F.; Li, L., Hybrid conjugated polymer-Ag@PNIPAM fluorescent nanoparticles with metal-enhanced fluorescence. *Journal of Materials Chemistry* **2011,** *21* (42), 16943-16948.

27. Galush, W. J.; Nye, J. A.; Groves, J. T., Quantitative fluorescence microscopy using supported lipid bilayer standards. *Biophysical Journal* **2008,** *95* (5), 2512-2519.

28. Liu, Y.; Yehl, K.; Narui, Y.; Salaita, K., Tension Sensing Nanoparticles for Mechano-Imaging at the Living/Nonliving Interface. *Journal of the American Chemical Society* **2013,** *135* (14), 5320-5323.

29. Stabley, D. R.; Jurchenko, C.; Marshall, S. S.; Salaita, K. S., Visualizing mechanical tension across membrane receptors with a fluorescent sensor. *Nature Methods* **2012,** *9* (1), 64-67.

30. Rodriguez-Fernandez, J.; Fedoruk, M.; Hrelescu, C.; Lutich, A. A.; Feldmann, J., Triggering the volume phase transition of core-shell Au nanorod-microgel nanocomposites with light. *Nanotechnology* **2011,** *22* (24), 245708.

31. Ekici, O.; Harrison, R. K.; Durr, N. J.; Eversole, D. S.; Lee, M.; Ben-Yakar, A., Thermal analysis of gold nanorods heated with femtosecond laser pulses. *Journal of Physics D-Applied Physics* **2008,** *41* (18).

32. Saffarian, S.; Kirchhausen, T., Differential evanescence nanometry: Live-cell fluorescence measurements with 10-nm axial resolution on the plasma membrane. *Biophysical Journal* **2008,** *94* (6), 2333-2342.

33. Jiang, T.; Xu, C.; Liu, Y.; Liu, Z.; Wall, J. S.; Zuo, X.; Lian, T.; Salaita, K.; Ni, C.; Pochan, D.; Conticello, V. P., Structurally Defined Nanoscale Sheets from Self-Assembly of Collagen-Mimetic Peptides. *Journal of the American Chemical Society* **2014,** *136* (11), 4300-4308.

34. Xiong, J. P.; Stehle, T.; Diefenbach, B.; Zhang, R.; Dunker, R.; Scott, D. L.; Joachimiak, A.; Goodman, S. L.; Arnaout, M. A., Crystal structure of the extracellular segment of integrin alpha Vbeta3. *Science* **2001,** *294* (5541), 339-45.

5.6 Appendix

Technique	***Observation***	***Experimental condition***
sCMOS high-speed fluorescence measurements recording particle dynamics **(Figure 5.1f)**	<100 nm decrease in particle diameter (FWHM)	NIR illumination: 11 μW μm^{-2}, 10 Hz frequency,10% duty cycle. Conditions: water, 37 °C.
Liquid cell temperature-controlled AFM measurements **(Figure 5.1c and d)**	~120 nm decrease in particle diameter (FWHM)	Steady state temperature control Conditions: water, variable temperature
SIM microscopy **(Supplementary Fig. 3)**	~100 nm decrease in particle diameter (FWHM)	Continuous NIR illumination, 11 μW μm^{-2} Conditions: water, 37 °C
TIRF-based nanometry **(Supplementary Fig. 14)**	100 nm ± 10 nm decrease in particle height	NIR illumination condition: 11 μW μm^{-2}, 10 Hz frequency, 10% duty cycle. Conditions: HEPES buffer, 37 °C

Table A5.1 OMA particle size change determination.

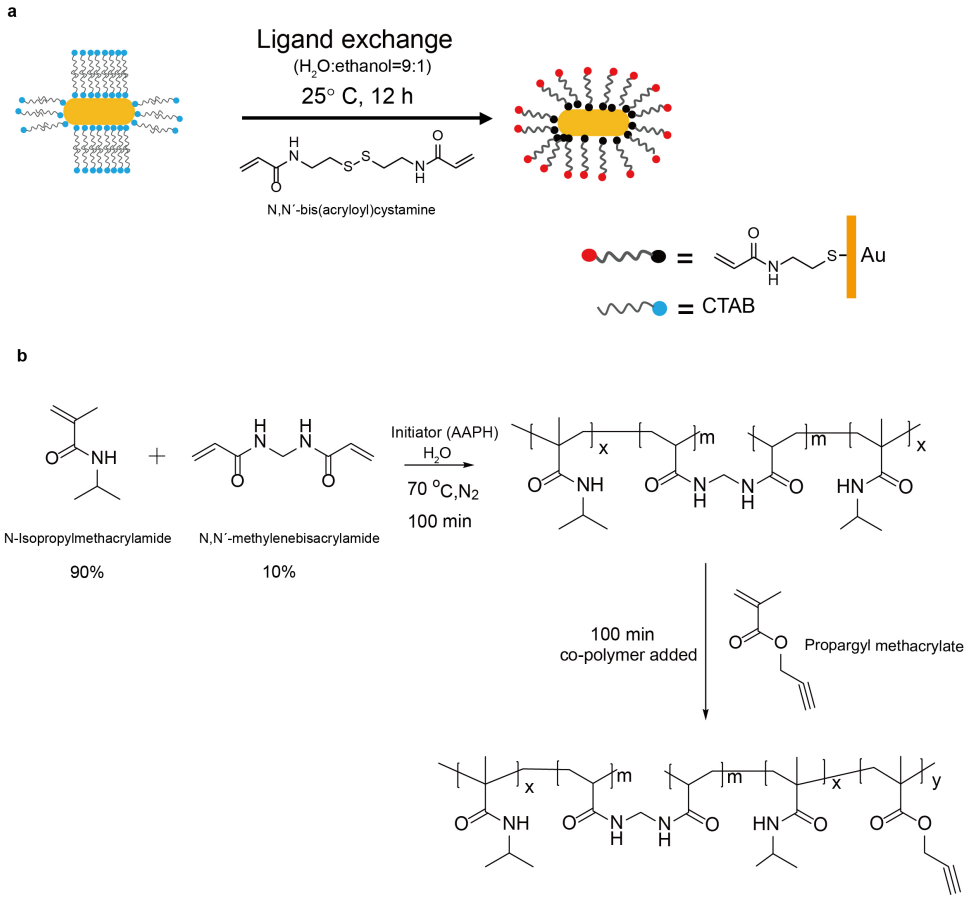

Figure A5.1 Schematic illustration of the preparation of pNIPMAm coated gold nanorods through a two-step procedure. (a) Surface functionalization of gold nanorods with alkene functional groups using N,N′-bis(acryloyl)cystamine [34]. (b) Synthetic procedure for polymerization of gold nanorods coated with pNIPMAm polymer. For more details, see materials and methods.

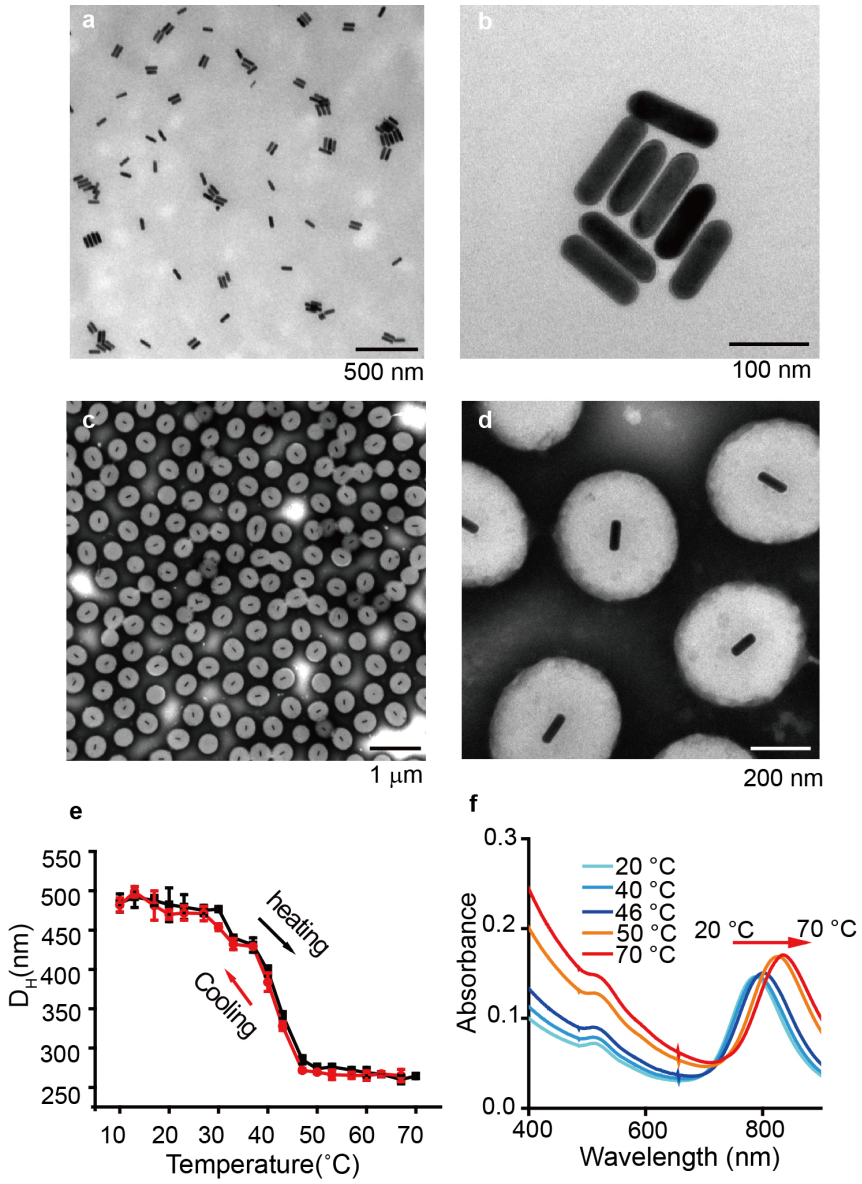

Figure A5.2 Characterization of OMA particles. (a, b) Representative TEM images of the gold nanorods (~25 nm × 100 nm) with a LSPR maxima at 785 nm. (c, d) Representative TEM images of OMA nanoparticles. Please note that because TEM is conducted under vacuum, TEM images may underestimate the size of the hydrated polymer shell. (e) Temperature-controlled DLS measurements reporting the hydrodynamic diameter of OMA nanoparticles as a function of temperature. (f) Temperature-dependent vis-NIR absorption spectra of OMA nanoparticles (from 20 to 70°C). At T>42 °C, the Vis-NIR spectra showed an increase in extinction for λ<650 nm, accompanied by a red shift and enhancement in the NIR λ_{max}. The shift in the NIR peak is driven by an increase in the refractive index of the polymer shell following particle collapse, while the increase in extinction at λ<650 nm is likely due to additional scattering above the phase-transition temperature.

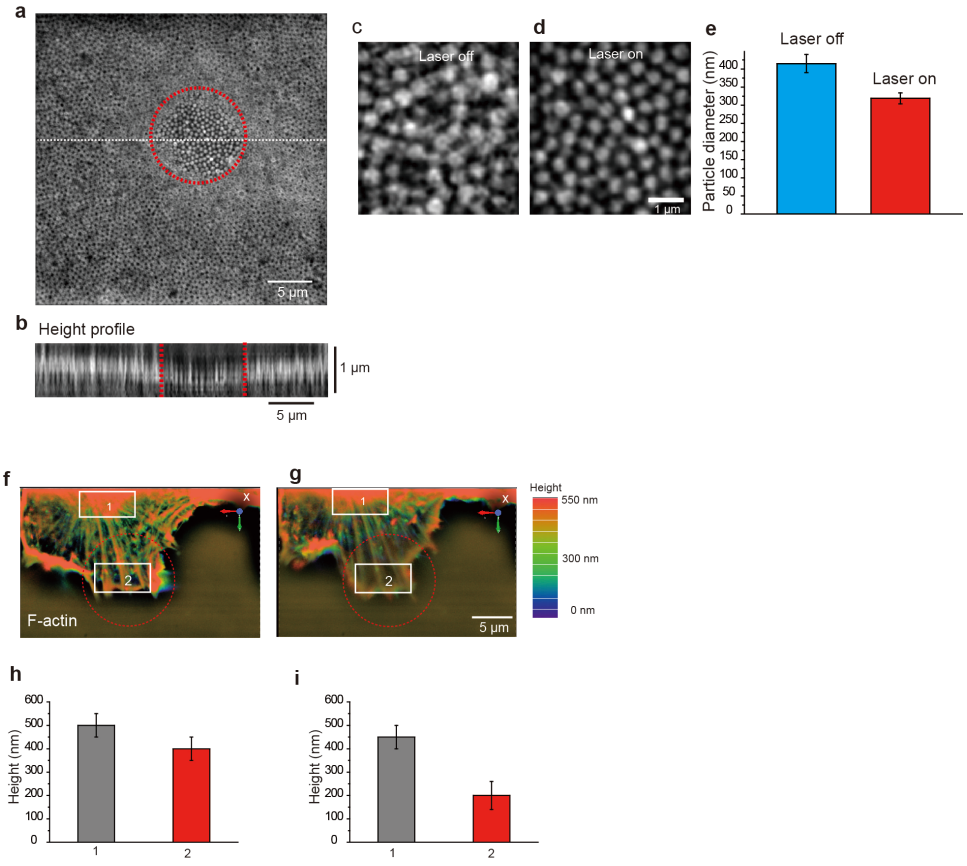

Figure A 5.3 3D-SIM of OMA particles and the F-actin network upon NIR illumination. (a) Representative 3D-SIM image of OMA nanoparticles labeled with Alexa 488 and irradiated using a 785 nm NIR laser at 113 μW μm^{-2}. The image is taken from a single z-position where the collapsed particles (within dotted red circle) were optimally focused. Data was collected in DI water at room temperature. The final 3D image was reconstructed from a stack of 27 individual SIM images starting from the coverslip with 50 nm step size (each 2D SIM image was reconstructed from 15 acquisitions). (b) Side view of a single *x*-*z* cross-section cut through the white dashed line shown in a. (c-d) Representative zoom-in SIM images of OMA nanoparticles before and after NIR illumination. (e) Plot displaying the FWHM of OMA particles (from n=10 particles for each group) before and after NIR illumination. (f-g) 3D SIM images of a live NIH 3T3 cell expressing LifeAct-mCherry before and after OMA actuation (111 μW μm^{-2}, 100% duty cycle). The red dashed circle represents the region of NIR illumination. (h-i) Plots display the average heights of F-actin network from the denoted regions of interest 1 and 2 indicated by white boxes in f and g. The error bar for each data point represents the standard deviation of heights measured by line scan analysis from n= 5 lines.

Note that there is minimal actin recruitment within the region of illumination (red dashed circle) in g. This is because the 3D-SIM experiments were conducted using steady state illumination (100% duty cycle, 0 Hz). As indicated in the main text and Supplementary Fig. 16 and 17, cyclic mechanical stimulation is required for actin recruitment and FA growth.

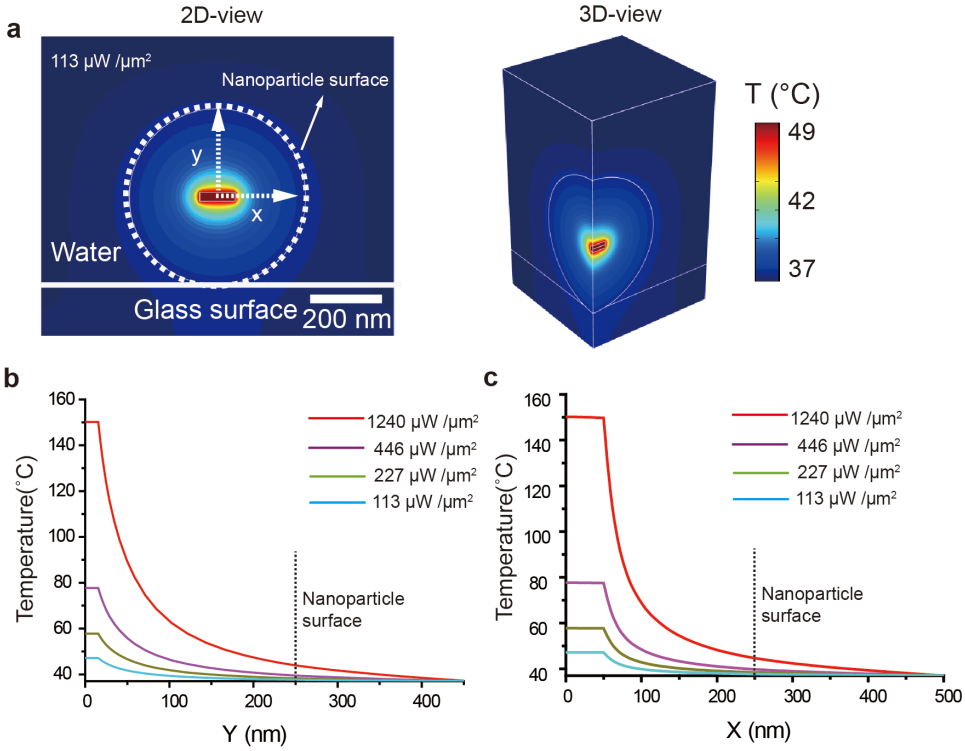

Figure A5.4 3D-finite element simulation of the heat distribution in a OMA nanoparticle irradiated with 785 nm IR laser beam. (a) 3D-finite element simulation of the heat distribution in a OMA nanoparticle irradiated with 785 nm IR laser beam at a power density of 113 μW μm^{-2} in water. (b, c) Plots showing cross-sectional temperature profiles along the short (Y) and long (X) axis of a single Au nanorod irradiated with 785 nm IR laser beam for four different power densities (1240, 446, 227,113 μW μm^{-2}).

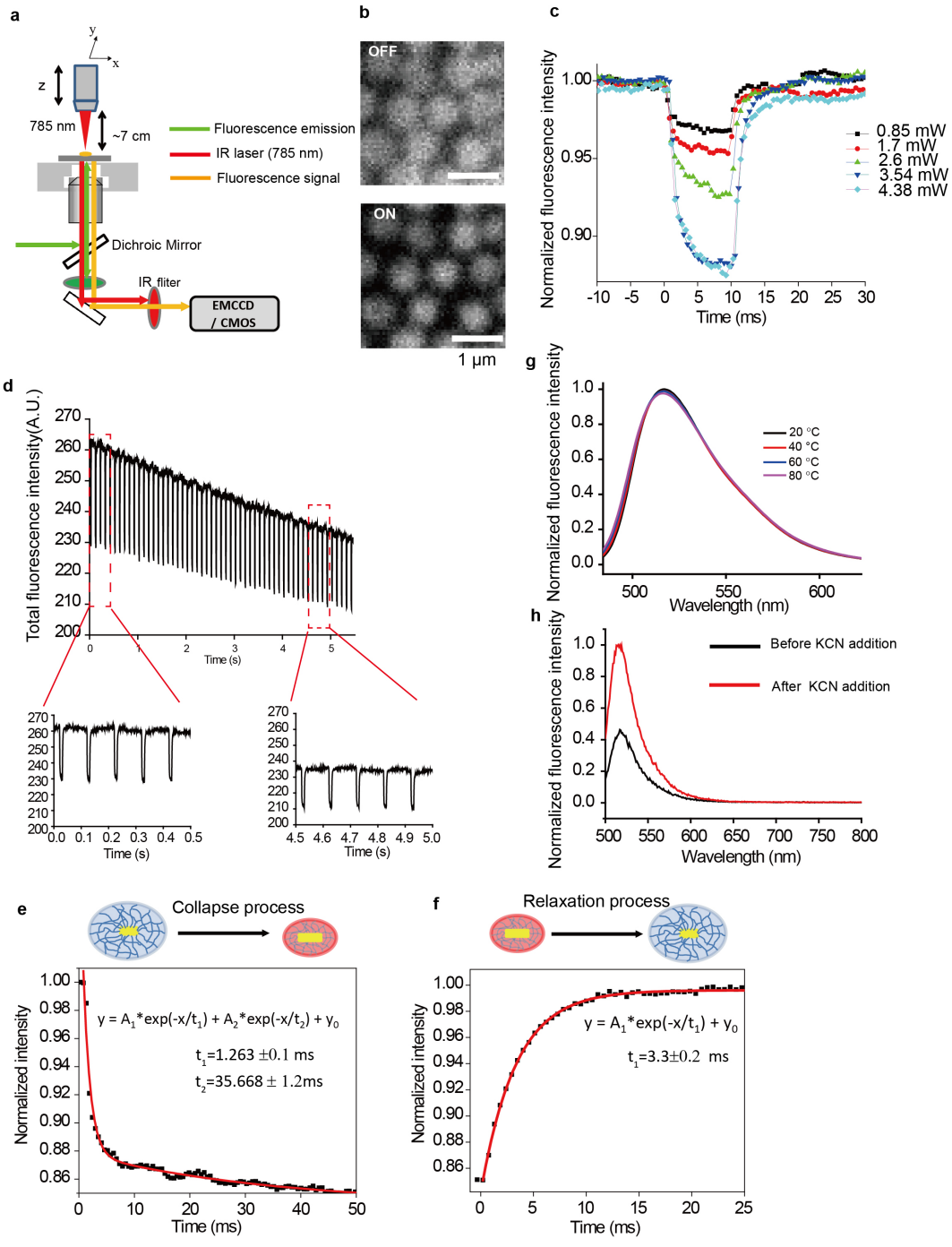

Figure A5.5 Determination of the collapse and relaxation dynamics of OMA nanoparticles. (a) Schematic of the experimental setup used for controlling the collapse of OMA nanoparticles. A near-infrared diode laser (Schäfter+Kirchhoff, Hamburg, Germany) was mounted using the standard darkfield condenser accessory provided by Nikon. (b) Representative fluorescence images of OMA nanoparticles labeled with Alexa 488 and captured by a sCMOS camera (Zyla 4.2 sCMOS, Andor Technologies Ltd., UK) at 1800 fps while NIR laser was switched between the on and off state. Data was collected in DI water at 37°C. (c) Fluorescence versus time plot showing kinetics of

OMA particle collapse and subsequent relaxation when the surface was excited at different NIR laser power intensities (10 Hz, 10% duty cycle). (d) A plot showing the total fluorescence intensity of OMA nanoparticles as a function of time while the NIR laser is operating at 10 Hz frequency and 10% duty cycle. OMA particle collapse and subsequent relaxation was highly reversible and could be sustained for at least 10^6 cycles (See materials and methods). (e) A biexponential decay fit of a typical NIR-induced polymer collapse in the time domain of 0–50 ms where the τ_1 and τ_2 were 1.2 and 35 ms, respectively. (f) The particle collapse relaxation process can be fit to a single-exponential rise, τ_1 which was 3.3 ms. (f) Alexa fluor 488 fluorescence temperature dependence in the range of 20–80 °C in Milli-Q water. The results show that Alexa fluor 488 is a temperature independent dye. (g) Normalized fluorescence intensity of OMA nanoparticles labeled with Alexa fluor 488 dye before (black) and after (red) dissolution of the gold nanorods. Taken together, this indicates that the ~15% decrease in fluorescence in Fig. 1f and Supplementary Fig. S5c, d, e and f is primarily due to quenching by the Au nanorod core upon particle collapse.

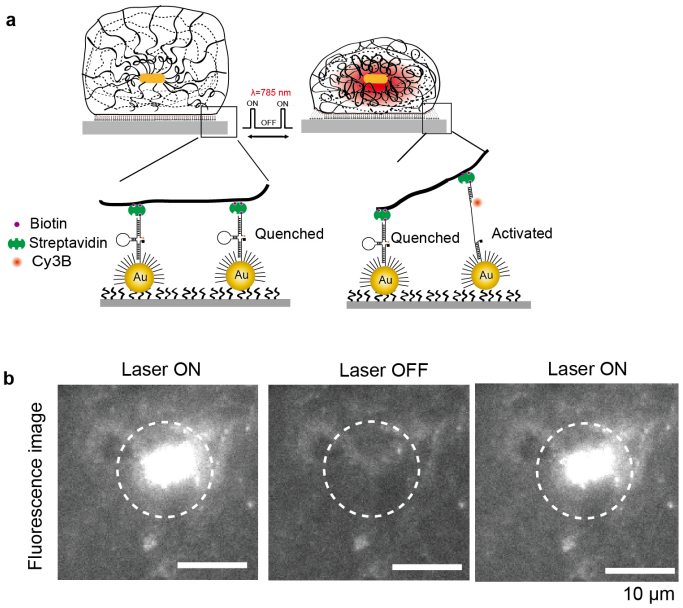

Figure A5.6 Estimation of OMA nanoparticle collapse-driven force using molecular tension sensor. (a) Schematic showing the approach used to estimate the force generated by OMA nanoparticle collapse using DNA hairpin based molecular tension sensor. (b) Representative fluorescence images of DNA-AuNP tension sensor while NIR laser was switched between the on and off state.

Note that temperature measurements confirm that DNA unfolding was mechanically driven and not thermal (melting temperature of hairpin= 81.3 °C). This suggests that the particle collapse exerts a force per ligand that is greater than 13 pN (force response threshold), but below the ~50 pN force required to shear DNA duplexes.

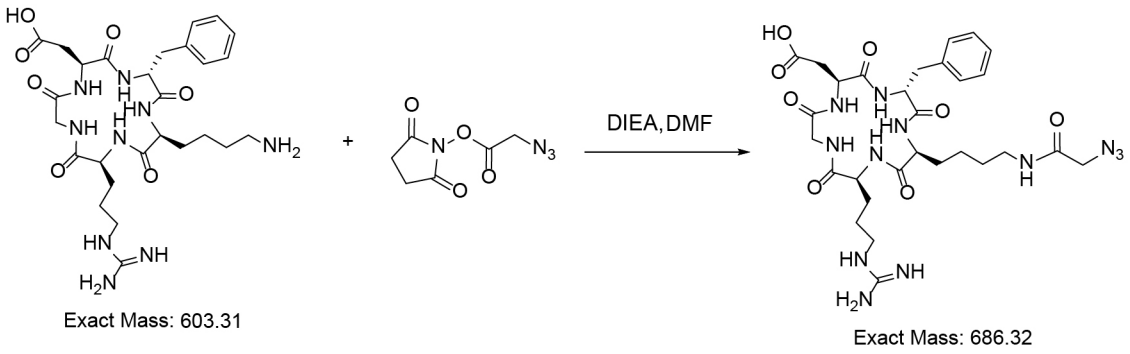

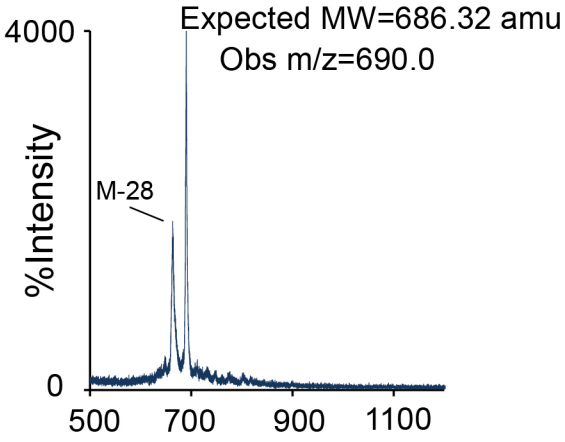

Figure A5.7 Synthesis of cRGDfK-azide ligand. Schematic showing the chemical synthesis of cRGDfK-azide ligand and MALDI-TOF spectrum of product. The mono-azide functionalized cRGDfK product exhibits two distinct peaks in their mass spectra when analyzed using reflector mode: the parent ion ([M+]) peak and a second peak corresponding to the in-source expulsion of N_2 ([M-28]) (See materials and methods).

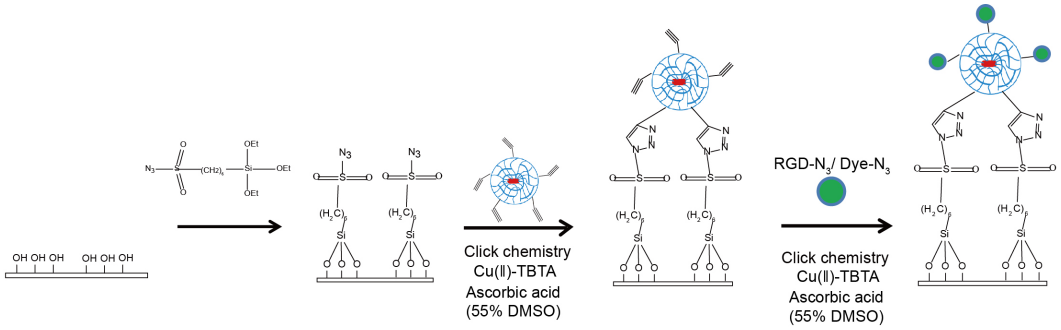

Figure A5.8 OMA nanoparticles surface preparation. Schematic showing the protocol for covalent immobilization of OMA nanoparticles on glass coverslips (See materials and methods).

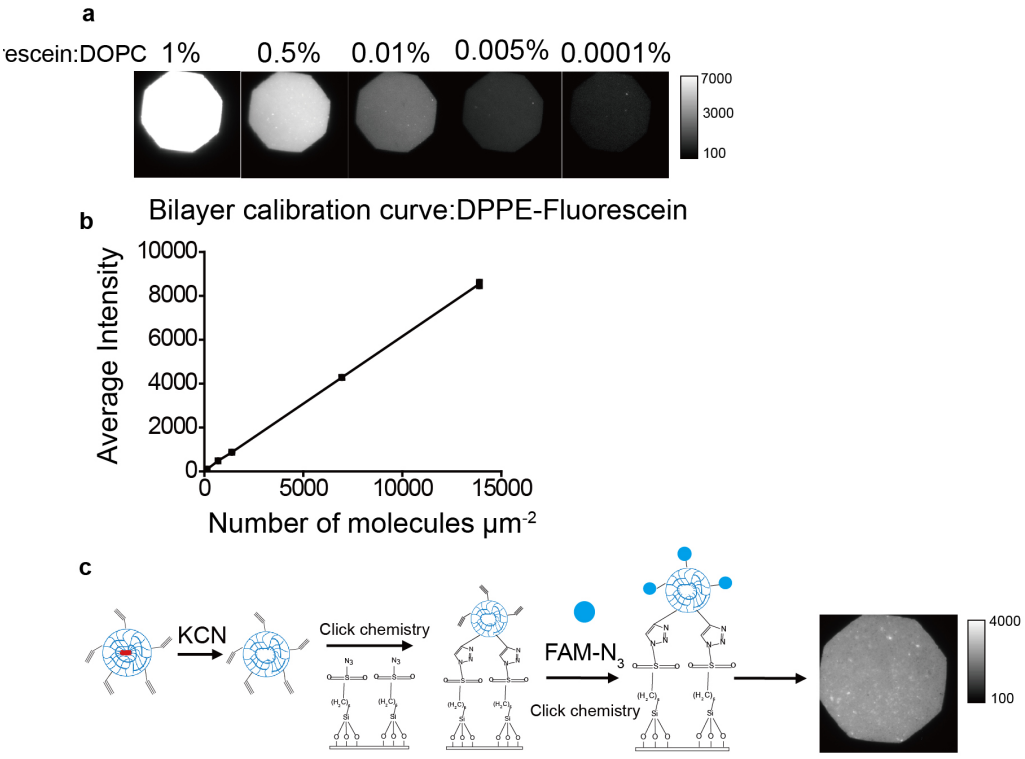

d

Scaling factor (FAM-N_3:Fluorescein)	1.5
RGD density	> 2,000 molecules μm^{-2}

Figure A5.9 Determination of cRGDfK peptide density on OMA nanoparticles surface. (a) Representative fluorescence images from DOPC supported lipid membranes doped with 1% to 0.0001% DPPE-fluorescein. (b) A plot showing the calibration curve relating the fluorescence intensity of DPPE-fluorescein doped supported lipid membranes to the molecular density. (c) Scheme showing the procedure used to measure the average molecules density of FAM molecules on OMAs (Au NR free) surface. (d) Using the calibration curve, F factor, and fluorescence intensity from FAM labeled OMA (Au NR free) functionalized coverslips; FAM density was estimated to be ~2,000 molecules μm^{-2}. Note that the absolute cRGDfK peptide density should be much higher than 2,000 molecules μm^{-2} since the cRGDfK peptide concentration is ten times greater than the FAM azide concentration during the click reaction to functionalize particles (See materials and methods).

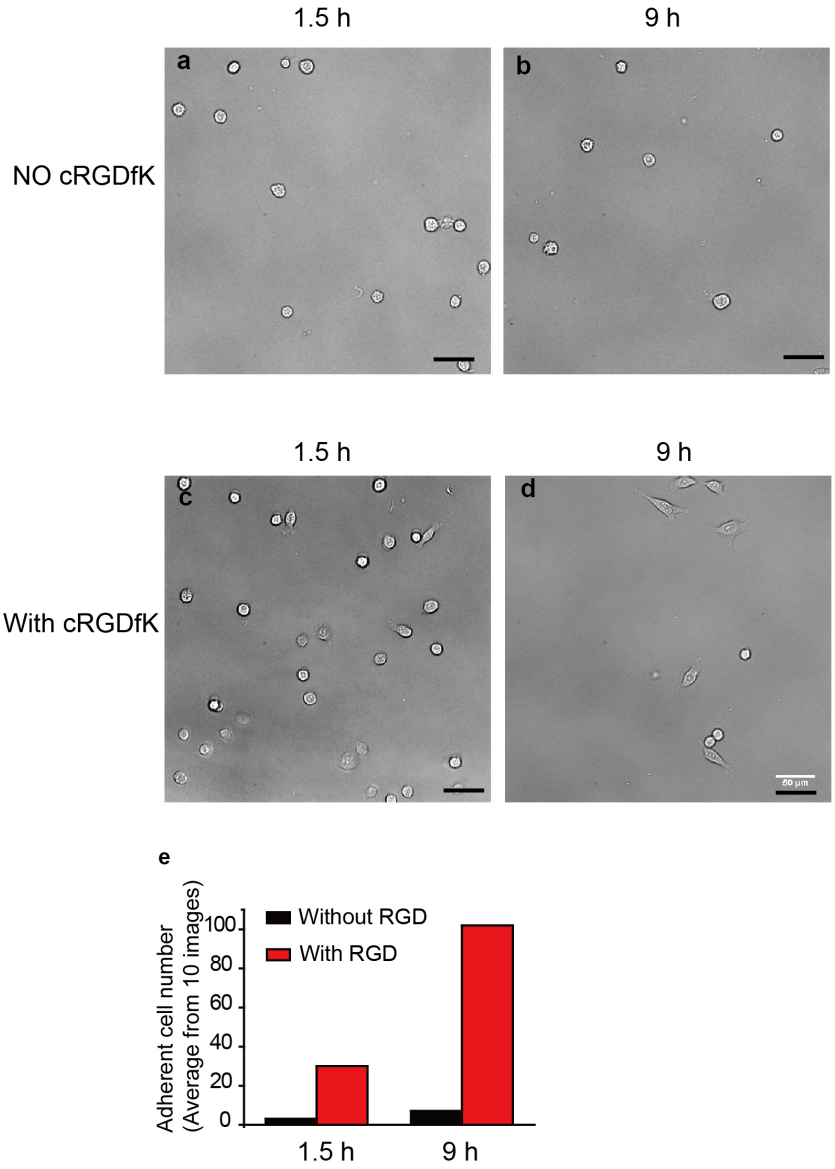

Figure A5.10 Representative bright field images of NIH 3T3 cells cultured onto OMA particles surface with and without cRGDfK peptide. (a, b) Representative bright field images of NIH 3T3 cells cultured onto OMA nanoparticles surface lacking cRGDfK peptide. (c, d) Representative bright field images of NIH 3T3 cells cultured onto cRGDfK modified OMA nanoparticles surface. (e) The histogram displays the total number of spread of cells (from 10 images) onto OMA nanoparticles surfaces modified with (red) and without (black) cRGDfK at two time points.

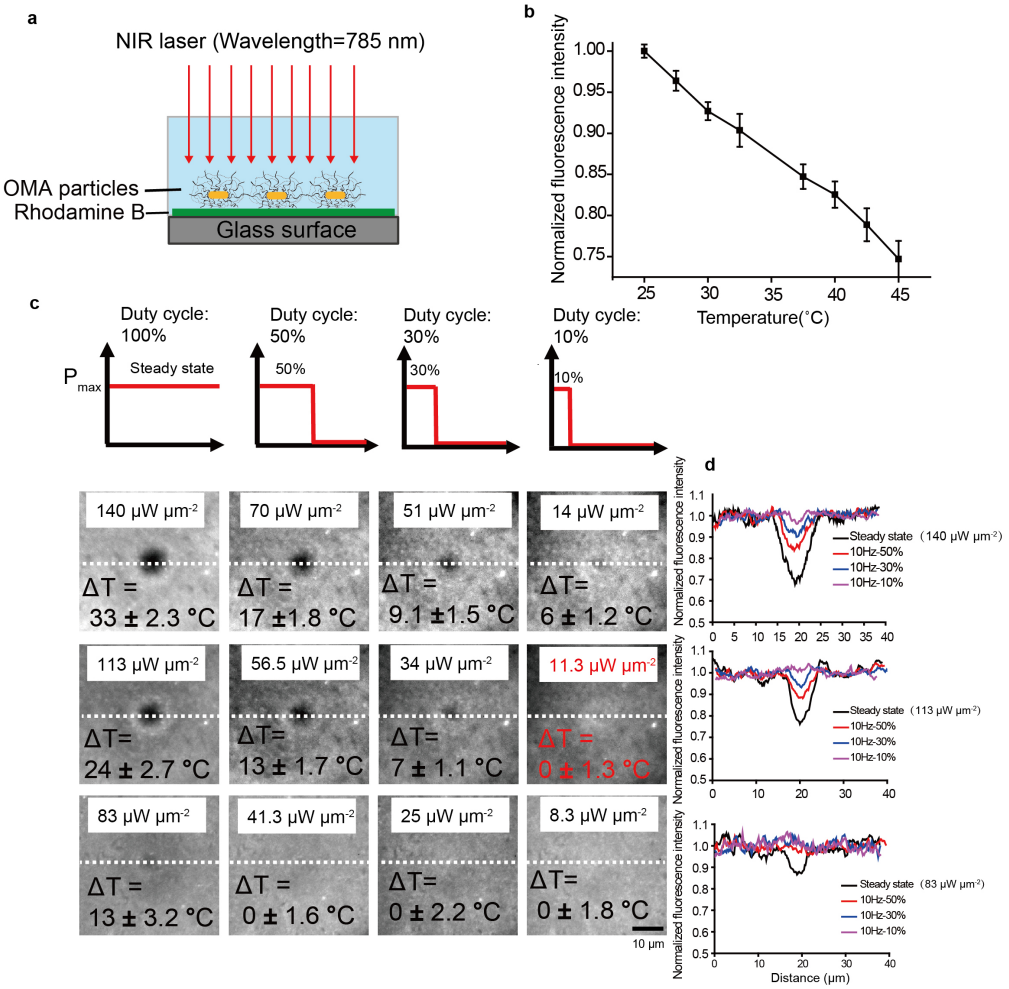

Figure A5.11 Determination of OMA surface temperature. (a) A schematic showing the procedure used to measure the average temperature of OMA nanoparticles as a function of the NIR laser power intensity and duty cycle. First, a thin film of Rhodamine B was prepared by spin coating the glass slide with a 1 μM Rhodamine B aqueous solution. The slide was then allowed to dry slowly at ambient conditions for ~10 min. Subsequently, a few drops of a solution containing 0.1 nM OMA nanoparticles was deposited onto the Rhodamine B coated glass surface. The sample was then allowed to fully dry and then mounted into a sample holder for NIR illumination experiments in PBS. (b) Normalized fluorescence intensity of Rhodamine B as a function of temperature. The fluorescence curve shows that the fluorescence intensity decreases ~ 1% when temperature increases 1 °C. Data was obtained using a spectrophotometer in PBS. (c) Fluorescence images of Rhodamine B film coated with OMA nanoparticles and excited using different NIR laser power intensities and duty cycles. (d) The plot shows the normalized fluorescence intensity line scan profiles of images in (c) across the illumination area indicated by the dashed white line. Note that, at the illumination condition for cell stimulation (3.5 mW, 10% duty cycle, 10 Hz, 11.3 μW μm^{-2}, the laser spot radius is 10 μm), no detectable increase in equilibrium surface temperature was observed.

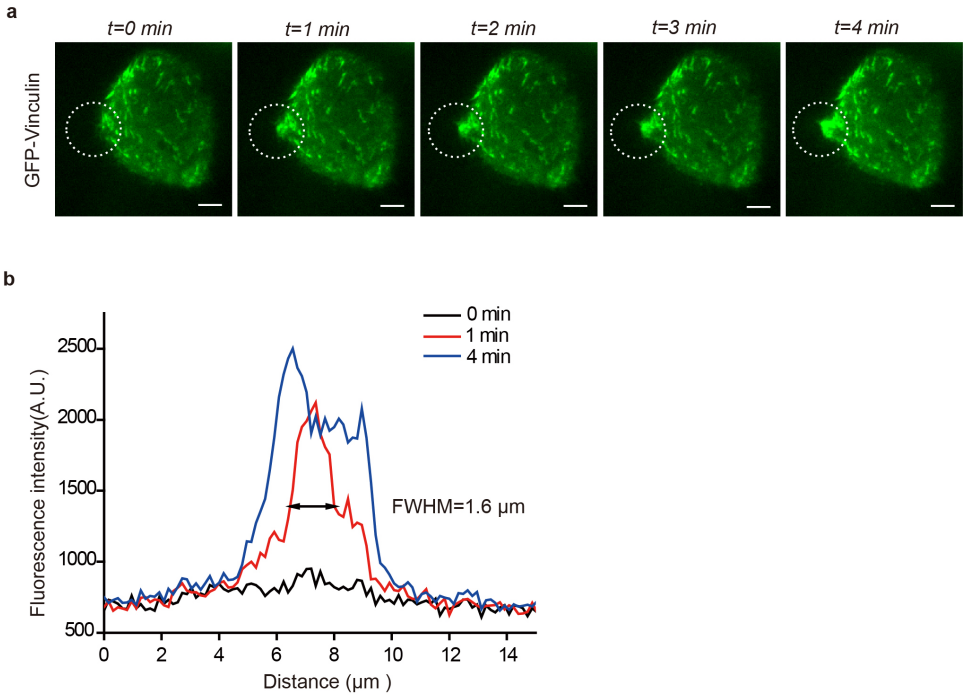

Figure A5.12 Optomechanical actuation of integrin leads to GFP-vinculin recruitment. (a) Representative time-lapse TIRF images of GFP-Vinculin transiently transfected in 3T3 cells that were cultured on OMA nanoparticles displaying the cRGDfK peptide. NIR illumination (red dashed circle, 10 Hz, 10% duty cycle, power density = 11.3 μW μm^{-2}) leads to rapid recruitment of GFP-vinculin. Scale bars, 5 μm. (b) Plot represents the fluorescence intensities profiles (dashed white line) across the illumination area at different time points.

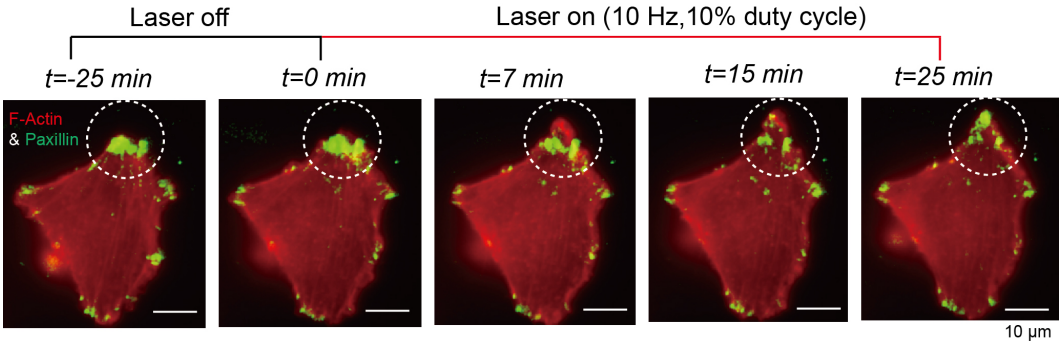

Figure A5.13 Simultaneous tracking of paxillin and actin following OMA stimulation. Representative time-lapse dual-color fluorescence images of Life-Act mcherry actin (red) and GFP-paxillin (green) transiently transfected NIH 3T3 cells upon NIR illumination (white dashed circle, 11.3 μW μm^{-2}, 10 % duty cycle). Before stimulation (-25 min – 0 min), minimal changes in the actin and paxillin signal was observed. Following NIR stimulation (at t = 0 min), the cell membrane rapidly protruded toward the NIR illumination region as shown by the accumulation of Life-act mcherry within the dotted white circle (t = 7 min). At t = 15 min, puncta of GFP-paxillin were observed within the newly protruding region of the cell, thus indicating the formation of nascent focal adhesions. These nascent focal adhesions continued to grow as the NIR stimulus was maintained (t = 25 min). These dual-color fluorescence images show that the F-actin polymerization precedes the recruitment of paxillin and FA maturation upon OMA actuation.

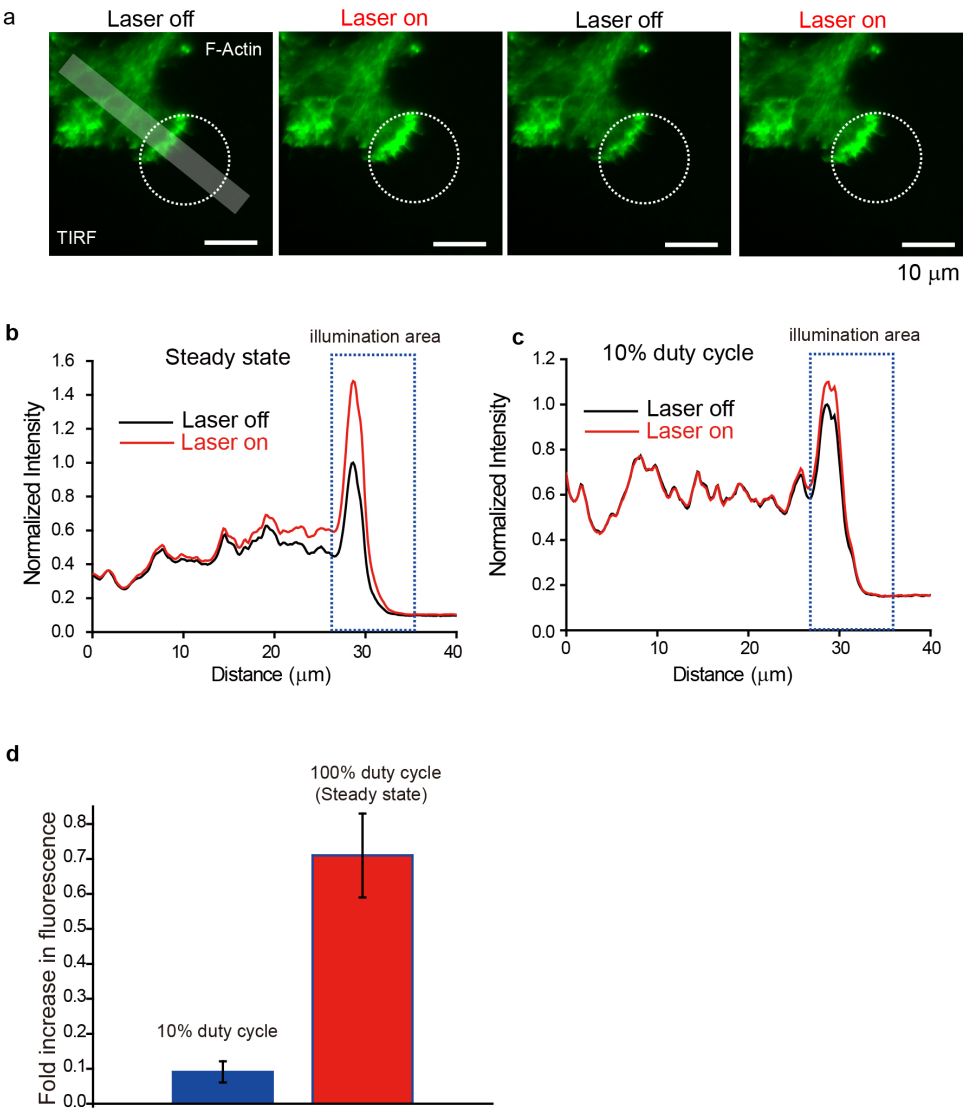

Figure A5.14 Determination of F-actin displacement using TIRF-based nanometry. (a) Representative TIRF images of GFP-LifeAct transiently transfected 3T3 cells that were cultured on OMA nanoparticles when the NIR laser (red dashed circle, 111 μW μm^{-2}, 100% duty cycle) was switched on and off. The acquisition time was 1 s. (b-c) Plots show fluorescence line scan analysis from the region denoted by the gray rectangle in the TIRF image shown in (a). The red and black profiles represent the TIRF intensity when NIR was switched on and off. The NIR laser was operated at 100% duty cycle in (b), and at 10% duty cycle in (c). The illumination area was indicated by dashed blue rectangle. (d) Plot displays the average fold increase in TIRF signal in the illumination area when OMA nanoparticles were excited by NIR laser with 10% duty cycle and 100% duty cycle, respectively. The error bar for each data point represents the standard deviation of cell response from n= 6 cells.

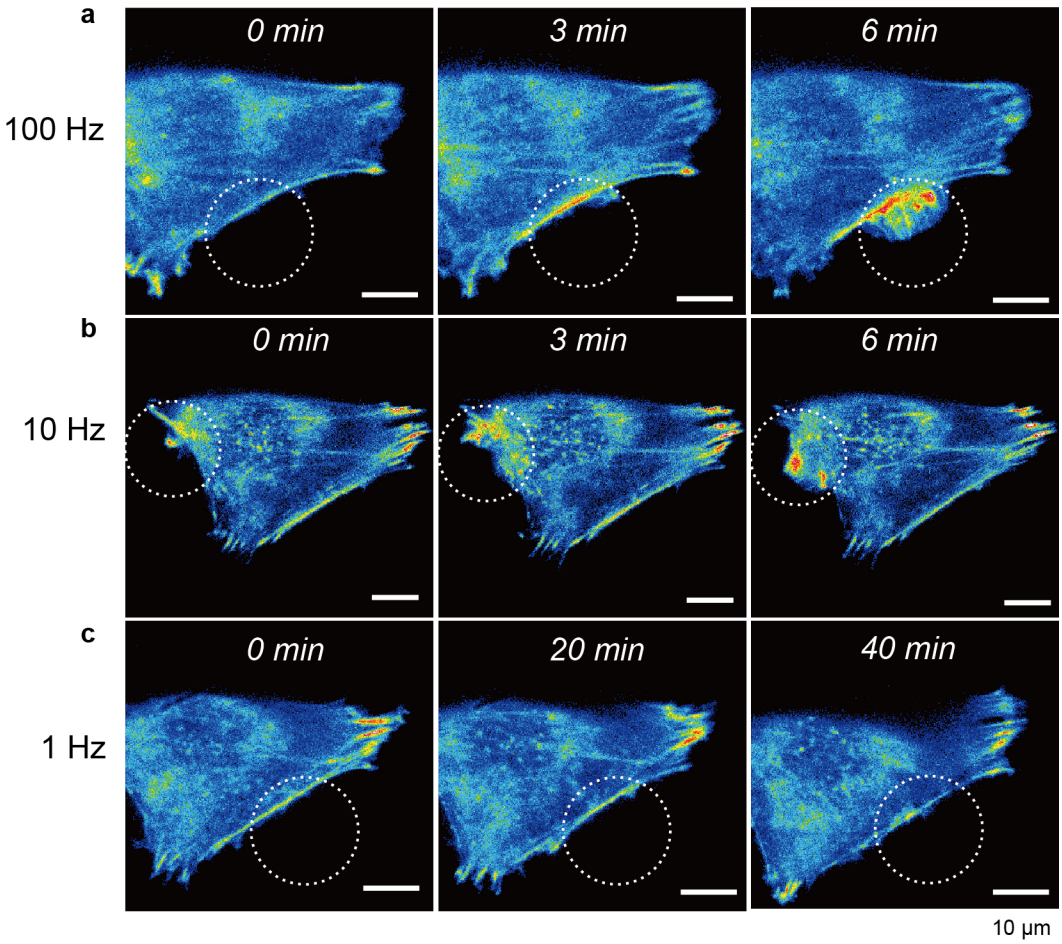

Figure A5.15 Cell response to NIR illumination frequencies from 1 Hz to 100 Hz. Representative time-lapse fluorescence images of Life-act-mCherry transiently transfected NIH 3T3 cells upon NIR illumination at different frequencies from 1 Hz to 100 Hz. Cells were cultured overnight prior to stimulation.

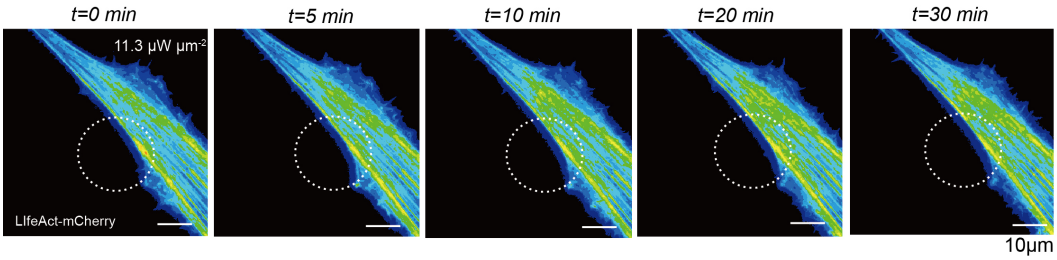

Figure A5.16 Cell response to continuous NIR illumination. Representative time-lapse fluorescence images of LifeAct-mCherry transiently transfected NIH 3T3 cells upon continuous NIR illumination (power density = 11.3 μW μm^{-2}, the duty cycle is 100%). No significant change in F-actin was observed under these experimental conditions. This suggests an important role in cyclic application of mechanical stimulus for driving integrin activation.

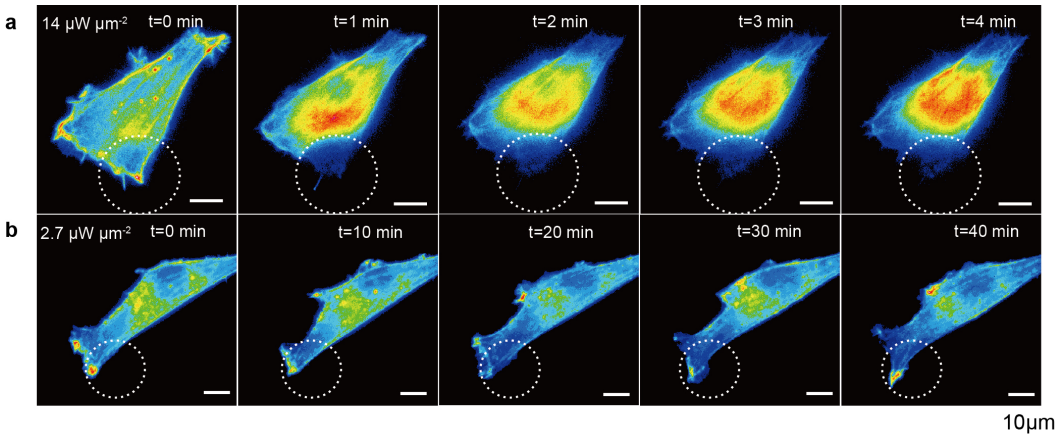

Figure A5.17 Cell response to high and low intensity NIR illumination. Representative time-lapse fluorescence images of Life-act mcherry transiently transfected NIH 3T3 cells cultured on OMAs surface upon high (14 μW μm^{-2}) (a), and low intensity (2.7 μW μm^{-2}) (b) NIR illumination. Scale bars: 10 μm.

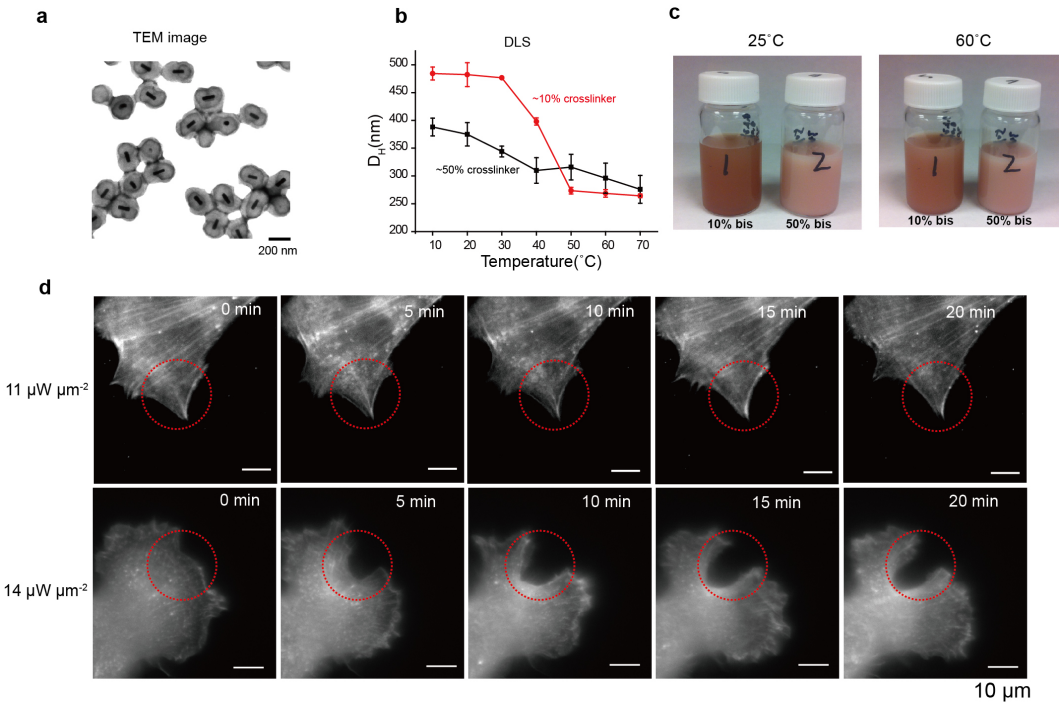

Figure A5.18 Control OMA particles synthesized with 50% crosslinking *N,N'*-Methylenebis(acrylamide) to test potential thermal effects. (a) Representative TEM image of Au nanorod core-NIPMAm shell nanoparticles generated using a 50% cross-linker concentration (N,N-Methylenebisacrylamide). (b) Temperature-controlled DLS measurements reporting the hydrodynamic diameter of core-shell nanoparticles with 10% cross-linker (red) and 50% cross-linker concentration (black) as a function of temperature. (c) Photographs of aqueous solutions containing core-shell nanoparticles with 10% and 50% crosslinker concentration at different temperatures. (d) Representative time-lapse fluorescence images of Lifeact-mCherry transiently transfected NIH 3T3 cells cultured on the 50% cross-linker concentration particles upon NIR illumination with different laser power densities. Cells were cultured overnight prior to stimulation. The duty cycle was 10% and actuation frequency was 10 Hz in these experiments.

The cross-linker concentration in thermo-responsive polymers can strongly alter their properties[23]. The increased crosslinking density significantly reduced the swelling ratio of polymer particles as shown in the temperature controlled DLS measurement (b). The average hydrodynamic diameter of the core-shell nanoparticles with 50% crosslinker was reduced from 370 ± 20 nm to 260 ± 30 nm. This volume transition is significantly reduced compared with particles crosslinked with 10% *N,N'*-methylenebisacrylamide. The dampened volume transition is also shown in (c). Importantly, core-shell particles with 50% crosslinker failed to display an increase in actin localization regardless of the NIR intensity tested.

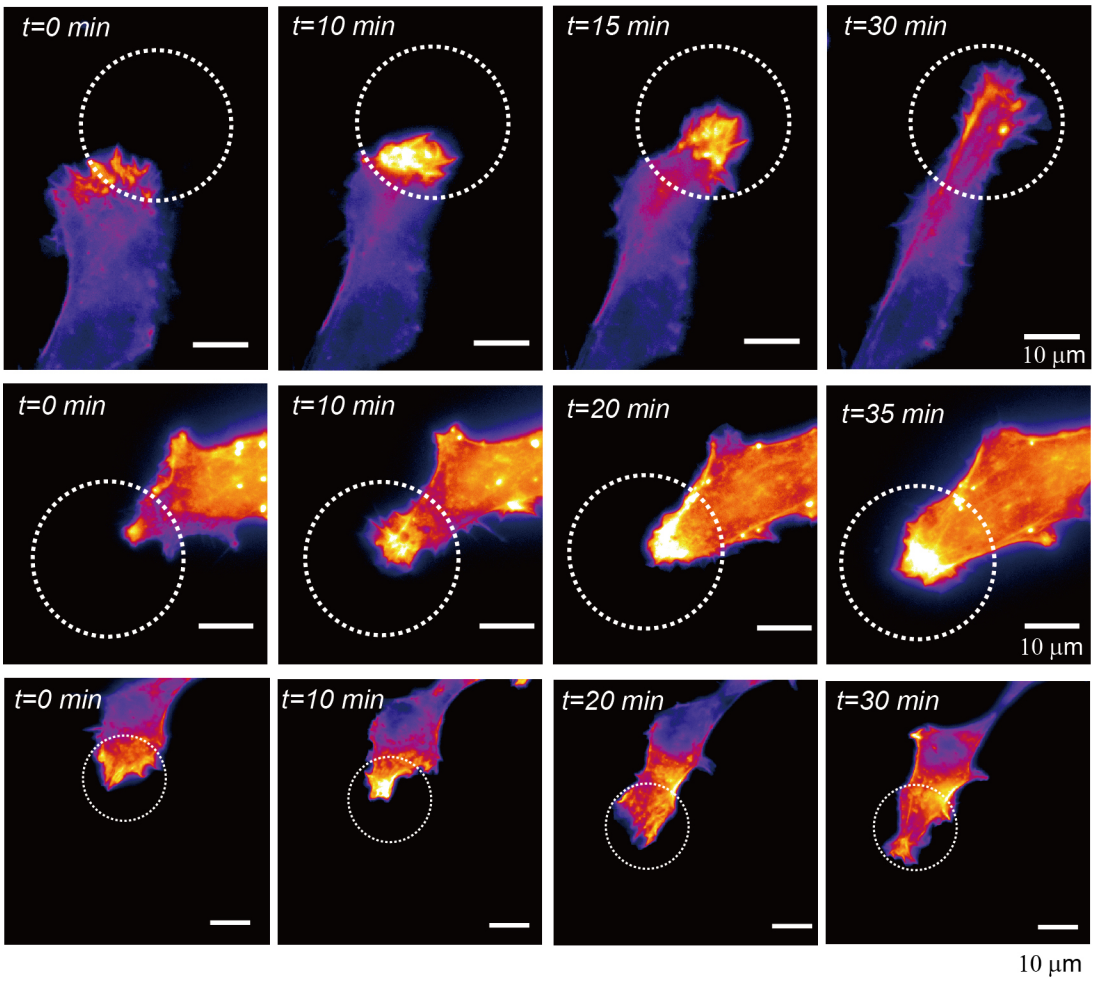

Figure A5.19 OMA control of NIH 3T3 cell migration. Representative fluorescence images taken from time-lapse videos of OMA control of NIH 3T3 cell migration. Cells were transfected with Life-Act mCherry. The white dashed circle represents the region of NIR illumination.

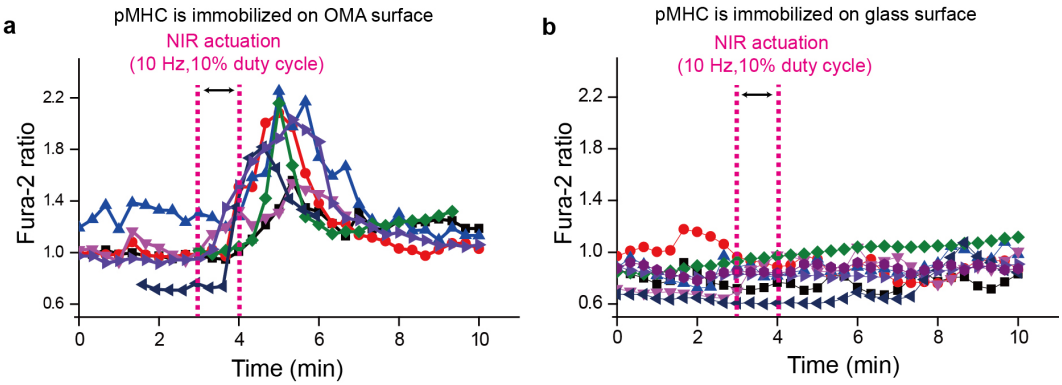

Figure A5.20 Quantitative analysis of fura-2 ratio rise for T cells on different surfaces upon NIR stimulation. (a-b) Plots depicting a histogram showing the quantitative analysis of fura-2 ratio rise for different T cells upon OMA stimulation as depicted in (Figure 5.2e) and (Figure 5.2g). *n*= 7 cells for each plot.

Supplementary Note

Upon OMA particle collapse, the polymer will increase in stiffness and the density of the RGD ligands will also likely increase. Note however that the collapsed state of the OMA particles is transient persisting for 10 ms within each 100 ms time window (one period). This indicates that the NIR illumination in our experiments causes a transient change to the rigidity of the particle and the density of RGD. Given that the Young's modulus of PNIPMAm is reported to increase from 100 kPa to 600 kPa upon collapse[32], this equates to a change in the rigidity of the surface from 100 to 150 kPa (10%× 600 + 90%×100). Based on literature precedent, an increase in rigidity from 100 to 150 kPa is insignificant, and will not impact cell response[33-35]. In addition, NIR illumination is tuned such that each particle is partially collapsed and surface temperature of the OMA particles does not exceed the LCST. Therefore, the stiffness is likely less than 150 kPa during NIR actuation.

In regards to the change in RGD density, we measured the RGD density and determined that it is more than 2,000 peptides μm^{-2} (Figure A5.9) which is 5 fold greater than the threshold required to trigger FA formation[36]. Based on literature precedent there is minimal difference in cell response to densities that exceed this threshold value[36]. Therefore, it is highly unlikely that a transient increase in RGD density would drive the cell response.

Finally, ROCK inhibitor studies (Figure 5.2b) show that the cell response is maintained, further confirming that the mechanism is independent of cell stiffness sensing mechanisms.

Taken together, these lines of evidence indicate that the change in RGD density and change in particle stiffness do not contribute to the observed cell response.

Chapter 6: Summary and Perspective

6.1 Summary

This thesis mainly focuses on the technological development of several gold nanoparticle (AuNP)-based tension probes and their application in cell biology and molecular biophysics. Compared to previous generations of MTFM probes,[1-2] AuNP tension probes provide excellent sensitivity, robust stability and broad dynamic range for measuring receptor-mediated forces such as integrin and TCR.[3-6]

Integrin-mediated focal adhesions were studied as a model system to validate the new force sensing probes.[7-8] Importantly, neither TFM nor SMFS methods can reveal the forces transmitted through single integrin receptors during the processes of their activation and the formation of focal adhesions. Jurchenko et al. discovered that integrin forces were strong enough to dissociate the biotin-streptavidin bond, rupturing the first generation of MTFM probes from the substrate.[9] To address this problem, we developed a new type of AuNP-based probes that were immobilized on surfaces through the gold-sulfur interaction,[3] which can withstand forces that exceeds ~1 nN.[10] With these probes, integrin forces were visualized from their initial spreading to the formation of mature focal adhesions. Importantly, this study marked the first example of using molecular tension probes to provide pN tension maps of integrin forces.

Over the past two decades, the Chen lab has published a series of hallmark papers showing that cell life, apoptosis[11] and stem cell differentiation[12] could be geometrically controlled by integrin-mediated cell adhesions. By developing micropatterned TFM and mPADs, they discovered that critical kinase activities are highly influenced by local stress due to cell cytoskeleton remodeling.[13-14] Spatz and colleagues pursued a similar question but at the nanoscale. They probed how the nanoscale organization of integrin

ligands modulates cell adhesions and found that the cells only form stable focal adhesions on substrates with a minimal ligand spacing of 50-60 nm.[15-17] Several structural models have been proposed to explain this observation.[18-19] However, it remains elusive whether mechanical force transmission could be altered by the nanoscale organization of integrin ligands, which was a question beyond the spatial resolution of TFM and mPADs.

To answer this question, we combined AuNP-based tension probes with recently developed bottom-up assembly techniques to arrange gold nanoparticles into periodic hexagonal arrays with spacings that range from 20 to 150 nm.[4] With these nanopatterned probes, we measured mechanical forces across individual integrin receptors that were confined to specific geometries and spacings. Our results suggest that integrin receptors are coupled with cytoskeletal forces in order to physically sense the nanoscale density of their ECM ligands. This work also represents a technical advance that bridges the field of mechanical force sensing and nanolithography. Because clustering is a very common behavior during the activation of many surface receptors, such as TCR and EGFR signaling pathway,[20-21] this strategy will likely become the workhorse tool in studying the complex relationships between nanoscale receptor clustering and their force transmission.

TCR-mediated mechanotransduction is another topic of great significance in immunology and cell biology.[22] An increasing number of studies suggest that T-cells mechanically interpret the specificity and binding kinetics to antigen and transduce this information into function.[23-26] However, the major challenge in these experiments is the requirement that the experimenter externally applies the force to the TCR, thus the innate TCR forces and their physiological consequences remain unknown. Therefore, the physical model of T cell activation still remains untested due to the lack of methods that

can quantify T cell generated forces at the level of single TCRs and to correlate these forces with T cell functional responses. Although PEG-based probes have been successfully applied in measuring integrin forces, they are less sensitive in the study of TCR forces. The "analogue" nature of PEG spring likely limits the fluorescence intensity in response to forces in the low pN range. To address this issue, we created a class of ultrasensitive tension probes that display up to 100-fold fluorescence enhancement upon activation.[27] These probes are created by combining recently developed DNA hairpin tension probes with AuNP-based probes.[3, 28] With this enhanced sensitivity, we generated the first pN tension maps of individual TCR-pMHC complexes during T cell activation. A mechano-chemical signaling crosstalk between adhesion molecules such as LFA-1 and TCR was observed during T cell surveillance. Most importantly, our results showed that naïve CD8+ T cells maintain an essential level of TCR force at 12-19 pN for enhanced antigen fidelity, experimentally validating the biophysical mechanisms of antigen discrimination.

Although force measurement techniques have revolutionized the field of mechanobiology, these methods do not determine a causal relationship between mechanical forces and subsequent biological events. To address this problem in multiple cellular processes, such as cell adhesion, membrane protrusion, and cell migration, we developed optomechanical actuator approaches.[29] This novel mechanoactuator efficiently converts NIR illumination into pN forces that can be specifically delivered to surface receptors of interests. With this tool, we mechanically triggered the activation of naïve CD8 T cells within minutes, demonstrating its high modularity and potential in the study of cell mechanotransduction at interfaces.

6.2 Perspective

In the coming years, while the biological community will likely use MTFM as a workhorse tool in the field of mechanotransduction, chemists will continue developing improvements that broadens its scope. There are a number of synthetic developments that can be envisioned, which will likely improve upon the current molecular tension probe design.

First, many photo-physical and-chemical limitations of current MTFM probes require the development of alternative spectroscopic readouts. FRET-based tension probes employ organic dyes as molecular reporter in most of the aforementioned studies. However, it significantly suffers from photobleaching, oxidation, and an upper distance limit of ~10 nm.[30] Compared to organic dyes, quantum dots display improved brightness and superior photostability.[31] Furthermore, large plasmonic nanoparticles (>20 nm) comprised of gold[32] and silver[33] have also been utilized as spectroscopic rulers. In these cases, the distance between two nanoparticles can be easily quantified by the peak shifts due to their surface plasmonic coupling. The advantages of this method include a stable scattering signal that is orders of magnitude brighter than organic dyes, thus potentially boosting the temporal resolution and enabling long term force imaging without photobleaching.

Rupture or unfolding the spring of any MTFM probes (DNA hairpin, biotin-streptavindin, PEG extension, protein unfolding) depends linearly on the logarithm of force loading rate.[34] None of the molecular tension probes take this factor into account for the estimation of cellular forces, even though they are most likely calibrated at different loading-rates. So far, the loading rate of cellular contractile forces is still a black box,

which makes it less meaningful to compare the absolute value of forces acquired using different probes or from different proteins. To address this issue, it is of vital importance to either develop molecular tension probes that are minimally loading-rate dependent or develop a method that can quantify the loading rate of cellular forces in their physiological conditions.

Compared to other force sensing techniques such as TFM, current MTFM probes can only report the magnitude rather than the direction of cellular forces, which is a very undesirable situation. With only the knowledge of force magnitude, the mechanics can be identical in distinct processes such as actin polymerization and myosin contractility, where forces are possibly exerted in two opposite directions.[35-36] Recently, several novel strategies using polarization and defocused fluorescence microscopy have been successfully developed to report the dipole moment of organic dyes.[37-38] Assuming that cellular tension modulates the polarization of the fluorophore emission, these fluorescent tension probes could be transformed into force reporters by employing anisotropic imaging methods.

Lastly, developing appropriate chemistry to decorate 3D polymer matrices with MTFM probes is one of the most urgent and challenging tasks.[39] The natural ECM in tissue is a complex 3D fibrous meshwork with fibers and gaps providing complex biochemical and physical cues, which are very different from uniformly coated 2D surfaces.[40] Many cellular processes such as cell migration and differentiation are profoundly altered by 3D culture. For example, it remains unclear how integrin-mediated focal adhesions or equivalent structures form in a 3D environment and what magnitude of

mechanical forces is generated through these structures. Therefore, it is highly desirable to redesign MTFM probes for mechanosensing at 3D topographies.

6.3 Other contributions

Besides the studies presented in this thesis, I have made contributions to a number of other publications, which are listed below.

1. **Liu, Y.**; Ma. V.P.; Galior, K.; Zhang, Y.; Chang, Y.; Salaita, K. Developing Fluorescent Reporters for Molecular Forces at the Cell Surface. ***Accounts of Chemical Research*** (*Invited Review*), *To be submitted*

2. Galior, K.; **Liu, Y.**; Su, H.; Ma, V.P.; Wongtrakool, C.; Salaita, K. Using molecular tension probes to study the mechanopharmacology of asthmatic smooth muscle cells. *In preparation*

3. Ma. V.P.*; **Liu, Y.***; Blanchfield, J.L.; Galior, K.; Salaita, K. Ratiometric tension probes for mapping receptor forces and clustering at intermembrane junctions. *Nano Letters* **2016**, 16(7), 4552-4559

4. **Liu, Y.**; Blanchfield, J. L.; Ma, V.P.; Andargachew, R.; Galior, K.; Liu, Z.; Evavold, B.; Salaita, K. DNA-based Nanoparticle Tension Sensors Reveal that T-cell Receptors Transmit Defined pN Forces to Their Antigens for Enhanced Fidelity. *Proc. Natl. Acad. Sci. USA,* **2016**, 113 (20), 5610-5615

   Highlighted by *ScienceDaily*, “T cells use 'handshakes' to sort friends from foes”.

   Highlighted by *Chemical & Engineering News* 2016, 94(20), p.12, “T cells Tug on Antigens”.

5. Ma, V. P.; **Liu, Y.**; Yehl, K.; Galior, K.; Zhang, Y.; Salaita, K. The Mechanically-induced Catalytic Amplification Reaction for Readout of Receptor-Mediated Cellular Forces. *Angew. Chem. Int. Ed.* **2016**, 55 (18), 5488-5492

   Highlighted by *Nature Methods* **2016** 13, 466-467, "PCR for Cellular Forces".

6. Liu, Z.*; **Liu, Y.***; Yuan, Y.; Seyf, H.; Henry, A.; Mattheyses, A.; Yehl, K.; Zhang, Y.; Huang, Z.; Salaita, K. Nanoscale Optomechanical Actuators for Controlling Mechanotransduction in Living Cells. *Nature Methods* **2016**, 13, 143-146

7. Yehl, K.; Mugler, A.; Vivek, S.; **Liu, Y.**; Zhang, Y.; Fan, M; Weeks, E.; Salaita, K. High-speed DNA-based rolling motors powered by RNase H. *Nature Nanotechnology* **2016**, 11, 184-190

   Highlighted by *Chemistry World,* "Speedy DNA nanomachines are on a roll", Dec 9, **2015**

   Highlighted by *Phys.org*

   Highlighted by *Nanowerk*

8. Galior, K.*; **Liu, Y.***; Yehl, K.; Vivek, S.; Salaita, K. Titin-based Nanoparticle Tension Sensors Map High-Magnitude Integrin Forces within Focal Adhesions. *Nano Letters* **2015**, 16 (1), 341-348

   Highlighted by *Faculty of 1000 Prime*

9. **Liu, Y.**; Medda, R.; Liu, Z.; Galior, K.; Yehl, K.; Cavalcanti-Adam, E.A.; Spatz, J.P.; Salaita, K. Nanoparticle Tension Probes Patterned at the Nanoscale: Impact of integrin clustering on force transmission. *Nano Letters* **2014**, 14(10), 5539-5546

   Highlighted by *ScienceDaily*

   Highlighted by *Phys.org*

10. Jiang, T.; Xu, C.; **Liu, Y**.; Liu, Z.; Wall, J.; Zuo, X.; Lian, T.; Salaita, K.; Ni, C.; Pochan, D.; Conticello, V. Structurally Defined Nanoscale Sheets from Self-Assembly of Collagen-Mimetic Peptides. *J. Am. Chem. Soc*. **2014**, 136 (11), 4300–4308

11. Zheng, W.; **Liu, Y**.; Yehl, K.; West, A.; Schuler, E.; Kindt, J.; Salaita, K. Quantum Dots Encapsulated within Phospholipid Membranes: Phase-Dependent Structure, Photostability, and Site-Selective Functionalization, *J. Am. Chem. Soc*. **2014**, 136, 1992–1999

12. **Liu, Y**.; Yehl, K.; Narui, Y.; Salaita, K. Tension Sensing Nanoparticles for Mechano imaging at the Living/non-Living Interface. *J. Am. Chem. Soc.* **2013**, 135 (14), 5320–5323

   Highlighted by *Faculty of 1000 Prime*

   Highlighted by *Lab Tools*, *The Scientist Magazine, September Issue, 2013*

   Highlighted by Emory Featured Innovation

6.4 References

1. Stabley, D. R.; Jurchenko, C.; Marshall, S. S.; Salaita, K. S., Visualizing mechanical tension across membrane receptors with a fluorescent sensor. *Nature Methods* **2012,** *9* (1), 64-U172.

2. Jurchenko, C.; Chang, Y.; Narui, Y.; Zhang, Y.; Salaita, Khalid S., Integrin-Generated Forces Lead to Streptavidin-Biotin Unbinding in Cellular Adhesions. *Biophysical Journal* **2014,** *106* (7), 1436-1446.

3. Liu, Y.; Yehl, K.; Narui, Y.; Salaita, K., Tension Sensing Nanoparticles for Mechano-Imaging at the Living/Nonliving Interface. *Journal of the American Chemical Society* **2013,** *135* (14), 5320-5323.

4. Liu, Y.; Medda, R.; Liu, Z.; Galior, K.; Yehl, K.; Spatz, J. P.; Cavalcanti-Adam, E. A.; Salaita, K., Nanoparticle Tension Probes Patterned at the Nanoscale: Impact of Integrin Clustering on Force Transmission. *Nano Letters* **2014,** *14*, 5539-5546.

5. Galior, K.; Liu, Y.; Yehl, K.; Vivek, S.; Salaita, K., Titin-Based Nanoparticle Tension Sensors Map High-Magnitude Integrin Forces within Focal Adhesions. *Nano Letters* **2016,** *16* (1), 341-8.

6. Ma, V. P. Y.; Liu, Y.; Blanchfield, L.; Su, H. Q.; Evavold, B. D.; Salaita, K., Ratiometric Tension Probes for Mapping Receptor Forces and Clustering at Intermembrane Junctions. *Nano Letters* **2016,** *16* (7), 4552-4559.

7. Polacheck, W. J.; Chen, C. S., Measuring cell-generated forces: a guide to the available tools. *Nat Methods* **2016,** *13* (5), 415-23.

8. Iskratsch, T.; Wolfenson, H.; Sheetz, M. P., Appreciating force and shape-the rise of mechanotransduction in cell biology. *Nat Rev Mol Cell Biol* **2014,** *15* (12), 825-33.

9. Jurchenko, C.; Chang, Y.; Narui, Y.; Zhang, Y.; Salaita, K. S., Integrin-generated forces lead to streptavidin-biotin unbinding in cellular adhesions. *Biophysical Journal* **2014,** *106* (7), 1436-46.

10. Grandbois, M.; Beyer, M.; Rief, M.; Clausen-Schaumann, H.; Gaub, H. E., How Strong Is a Covalent Bond? *Science* **1999,** *283* (5408), 1727-1730.

11. Chen, C. S.; Mrksich, M.; Huang, S.; Whitesides, G. M.; Ingber, D. E., Geometric control of cell life and death. *Science* **1997,** *276* (5317), 1425-8.

12. McBeath, R.; Pirone, D. M.; Nelson, C. M.; Bhadriraju, K.; Chen, C. S., Cell shape, cytoskeletal tension, and RhoA regulate stem cell lineage commitment. *Dev Cell* **2004,** *6* (4), 483-95.

13. Fu, J. P.; Wang, Y. K.; Yang, M. T.; Desai, R. A.; Yu, X. A.; Liu, Z. J.; Chen, C. S., Mechanical regulation of cell function with geometrically modulated elastomeric substrates. *Nature Methods* **2010,** *7* (9), 733-U95.

14. Nelson, C. M.; Jean, R. P.; Tan, J. L.; Liu, W. F.; Sniadecki, N. J.; Spector, A. A.; Chen, C. S., Emergent patterns of growth controlled by multicellular form and mechanics. *Proceedings of the National Academy of Sciences of the United States of America* **2005,** *102* (33), 11594-11599.

15. Arnold, M.; Cavalcanti-Adam, E. A.; Glass, R.; Blummel, J.; Eck, W.; Kantlehner, M.; Kessler, H.; Spatz, J. P., Activation of integrin function by nanopatterned adhesive interfaces. *Chemphyschem* **2004,** *5* (3), 383-388.

16. Cavalcanti-Adam, E. A.; Volberg, T.; Micoulet, A.; Kessler, H.; Geiger, B.; Spatz, J. P., Cell spreading and focal adhesion dynamics are regulated by spacing of integrin ligands. *Biophysical Journal* **2007,** *92* (8), 2964-2974.

17. Huang, J.; Gräter, S. V.; Corbellini, F.; Rinck, S.; Bock, E.; Kemkemer, R.; Kessler, H.; Ding, J.; Spatz, J. P., Impact of Order and Disorder in RGD Nanopatterns on Cell Adhesion. *Nano Letters* **2009,** *9* (3), 1111-1116.

18. Coussen, F.; Choquet, D.; Sheetz, M. P.; Erickson, H. P., Trimers of the fibronectin cell adhesion domain localize to actin filament bundles and undergo rearward translocation. *Journal of Cell Science* **2002,** *115* (12), 2581-2590.

19. Meyer, R. K.; Aebi, U., Bundling of Actin-Filaments by Alpha-Actinin Depends on Its Molecular Length. *Journal of Cell Biology* **1990,** *110* (6), 2013-2024.

20. Grakoui, A.; Bromley, S. K.; Sumen, C.; Davis, M. M.; Shaw, A. S.; Allen, P. M.; Dustin, M. L., The immunological synapse: A molecular machine controlling T cell activation. *Science* **1999,** *285* (5425), 221-227.

21. Salaita, K.; Nair, P. M.; Petit, R. S.; Neve, R. M.; Das, D.; Gray, J. W.; Groves, J. T., Restriction of Receptor Movement Alters Cellular Response: Physical Force Sensing by EphA2. *Science* **2010,** *327* (5971), 1380-1385.

22. Ma, Z. Y.; Finkel, T. H., T cell receptor triggering by force. *Trends in Immunology* **2010,** *31* (1), 1-6.

23. Kim, S. T.; Takeuchi, K.; Sun, Z. Y.; Touma, M.; Castro, C. E.; Fahmy, A.; Lang, M. J.; Wagner, G.; Reinherz, E. L., The alphabeta T cell receptor is an anisotropic mechanosensor. *J Biol Chem* **2009,** *284* (45), 31028-37.

24. Liu, B.; Chen, W.; Evavold, Brian D.; Zhu, C., Accumulation of Dynamic Catch Bonds between TCR and Agonist Peptide-MHC Triggers T Cell Signaling. *Cell* **2014,** *157* (2), 357-368.

25. Hong, J.; Persaud, S. P.; Horvath, S.; Allen, P. M.; Evavold, B. D.; Zhu, C., Force-Regulated In Situ TCR-Peptide-Bound MHC Class II Kinetics Determine Functions of CD4+ T Cells. *Journal of Immunology* **2015,** *195* (8), 3557-64.

26. Das, D. K.; Feng, Y.; Mallis, R. J.; Li, X.; Keskin, D. B.; Hussey, R. E.; Brady, S. K.; Wang, J. H.; Wagner, G.; Reinherz, E. L.; Lang, M. J., Force-dependent transition in the T-cell receptor beta-subunit allosterically regulates peptide discrimination and pMHC bond lifetime. *Proc Natl Acad Sci U S A* **2015,** *112* (5), 1517-22.

27. Liu, Y.; Blanchfield, L.; Ma, V. P. Y.; Andargachew, R.; Galior, K.; Liu, Z.; Evavold, B.; Salaita, K., DNA-based nanoparticle tension sensors reveal that T-cell receptors transmit defined pN forces to their antigens for enhanced fidelity. *Proceedings of the National Academy of Sciences of the United States of America* **2016,** *113* (20), 5610-5615.

28. Zhang, Y.; Ge, C.; Zhu, C.; Salaita, K., DNA-based digital tension probes reveal integrin forces during early cell adhesion. *Nature Communications* **2014,** *5*, 5167.

29. Liu, Z.; Liu, Y.; Chang, Y.; Seyf, H. R.; Henry, A.; Mattheyses, A. L.; Yehl, K.; Zhang, Y.; Huang, Z.; Salaita, K., Nanoscale optomechanical actuators for controlling mechanotransduction in living cells. *Nat Meth* **2016,** *13* (2), 143-146.

30. Roy, R.; Hohng, S.; Ha, T., A practical guide to single-molecule FRET. *Nature Methods* **2008,** *5* (6), 507-516.

31. Resch-Genger, U.; Grabolle, M.; Cavaliere-Jaricot, S.; Nitschke, R.; Nann, T., Quantum dots versus organic dyes as fluorescent labels. *Nature Methods* **2008,** *5* (9), 763-775.

32. Liu, G. L.; Yin, Y. D.; Kunchakarra, S.; Mukherjee, B.; Gerion, D.; Jett, S. D.; Bear, D. G.; Gray, J. W.; Alivisatos, A. P.; Lee, L. P.; Chen, F. Q. F., A nanoplasmonic molecular ruler for measuring nuclease activity and DNA footprinting. *Nature Nanotechnology* **2006,** *1* (1), 47-52.

33. Rong, G. X.; Wang, H. Y.; Reinhard, B. M., Insights from a Nanoparticle Minuet: Two-Dimensional Membrane Profiling through Silver Plasmon Ruler Tracking. *Nano Letters* **2010,** *10* (1), 230-238.

34. Bustamante, C.; Chemla, Y. R.; Forde, N. R.; Izhaky, D., Mechanical processes in biochemistry. *Annu Rev Biochem* **2004,** *73*, 705-48.

35. McGrath, J. L.; Schwartz, I.; Ehrenberg, M.; Bindschadler, M., The role of substrate curvature in actin-based pushing forces. *Molecular Biology of the Cell* **2004,** *15*, 146A-146A.

36. Raucher, D.; Sheetz, M. P., Cell spreading and lamellipodial extension rate is regulated by membrane tension. *Journal of Cell Biology* **2000,** *148* (1), 127-136.

37. Bohmer, M.; Enderlein, J., Orientation imaging of single molecules by wide-field epifluorescence microscopy. *Journal of the Optical Society of America B-Optical Physics* **2003,** *20* (3), 554-559.

38. Forkey, J. N.; Quinlan, M. E.; Goldman, Y. E., Measurement of single macromolecule orientation by total internal reflection fluorescence polarization microscopy. *Biophysical Journal* **2005,** *89* (2), 1261-1271.

39. Doyle, A. D.; Yamada, K. M., Mechanosensing via cell-matrix adhesions in 3D microenvironments. *Experimental Cell Research* **2016,** *343* (1), 60-66.

40. Rhee, S., Fibroblasts in three dimensional matrices: cell migration and matrix remodeling. *Experimental and Molecular Medicine* **2009,** *41* (12), 858-865.